Solar Energy at Urban Scale

# Solar Energy at Urban Scale

Edited by
Benoit Beckers

*Series Editor*
*Piotr Breitkopf*

ISTE WILEY

First published 2012 in Great Britain and the United States by ISTE Ltd and John Wiley & Sons, Inc.



ISTE Ltd
27-37 St George's Road
London SW19 4EU
UK

www.iste.co.uk

John Wiley & Sons, Inc.
111 River Street
Hoboken, NJ 07030
USA

www.wiley.com



Library of Congress Cataloging-in-Publication Data

Solar energy at urban scale / edited by Benoit Beckers.
p. cm.
Includes bibliographical references and index.
ISBN 978-1-84821-356-2
1. Solar energy. 2. Urban climatology. 3. Environmental engineering. 4. City planning. I. Beckers, Benoit, 1969-
TJ810.S61815 2012
690.028'6--dc23

2012009827

British Library Cataloguing-in-Publication Data
A CIP record for this book is available from the British Library
ISBN: 978-1-84821-356-2

Printed and bound in Great Britain by CPI Group (UK) Ltd., Croydon, Surrey CR0 4YY

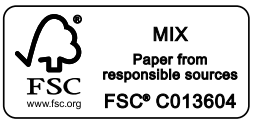

# Table of Contents

# Introduction

Since ancient times, despite the noise, the overcrowding, the fire hazards, and the epidemics, to live in the center of a large city has been considered a privilege. Kings, architects, and philosophers have imagined the ideal city as the city that would address the most private of activities, public life, and large parties. Foremost, an ideal city is the city that would overcome the vagaries of the weather – wind, cold, heat, and light – and would allow living to the rhythm of civilized society. Athens, Rome, Constantinople, Chang'an, Baghdad, Paris, London, Manhattan, or Brasilia were the greatest accomplishments of their time regarding the quality of life in common.

However, at the turn of the 20th Century, the simultaneous occurrences of elevators, automobiles, and cheap energy – oil and electricity – sharply, and simultaneously, increased the number of floors of downtown buildings and the radius of urban sprawl. In the center, the old buildings were left in the perpetual shade of skyscrapers, and many thousands of hectares of residential areas and roads covered the former farmland.

Today, throughout the world, a crop area equivalent to that of Italy is taken over each year by cities. Several countries, which were previously food exporters, find themselves unable to feed their own population. Entire metropolises depend largely on energy, out of which a huge amount is being consumed for transportation and air conditioning.

Thus, the densification of cities has become a necessity for future generations. However, the inhabitants of pre-industrial cities probably might never have reached the million mark, and the following steps were built on the illusion of inexhaustible fossil fuels. To allow tens of millions of people to live together comfortably and sustainably on a small area, better knowledge of urban physics is indispensable.

This book offers a state of the art as complete as possible around a single element of this physics: solar energy. The idea is to better highlight the different aspects of the problem, their necessary links, the latest advances, and the perspectives from different fields of physics, engineering, and architecture.

This book is organized into four main parts. The first part (measures and models of solar irradiance) processes the input data, such as the data recorded from satellites and ground stations, or recomposed from "sky" models. It describes the radiation emitted by the Sun, until it reaches the urban canopy.

The second part (radiative contribution to the urban climate) describes how this radiation is involved in the urban climate, interacting with buildings and vegetation.

The third part (light and heat modeling) explores the various components of numerical models developed to simulate the radiative exchanges at the urban scale.

The fourth part (urban planning) describes the inclusion of radiation in the process of regulation and in urban planning, in tropical latitudes, in arid climates, in Mediterranean countries and, finally, in cold temperate and northern zones.

The decision to write this book was taken after a workshop held at the Compiègne University of Technology. At this meeting, the participants expressed their interest in a general book covering the whole problem. From the core of speakers at the workshop, a well-established group of contributors was formed to show the recent and future progress in the field of solar energy at the urban scale. This is a research book. However, throughout the world, we feel the need for highly skilled engineers and planners to quantify energy and to apply such calculations to real cases of new districts or districts of regeneration. We hope this book will serve as the first complete reference on the subject, and find its place in the corresponding programs of the faculties of engineering and architecture.

# The Authors

Dr. **Daniel G. Aliaga** is an Associate Professor of computer science at Purdue University. Dr. Aliaga's research is in 3D computer graphics but overlaps with computer vision and with visualization. He focuses on (i) 3D urban modeling, (ii) projector-camera systems, and (iii) 3D digital fabrication. To date, Prof. Aliaga has published over 70 peer-reviewed publications, several patents on 3D acquisition, and served on over 35 program committees, on numerous NSF panels, and on the editorial board of *Graphical Models*. His research has been completely or partially funded by NSF, MTC, Microsoft Research, Google, and Adobe Inc.

Professor **Viorel Badescu** is a scientist presently affiliated with Candida Oancea Institute at Polytechnic University of Bucharest. His mainstream scientific contribution consists of more than 200 papers and 30 books related to statistical physics and thermodynamics, the physics of semiconductors, and various aspects of terrestrial and space solar energy applications. In addition, he has theorized on present-day Mars meteorology and Mars terraforming and on several macro-engineering projects. He is a corresponding member of Romanian Academy.

After obtaining an engineering degree in physics from University of Liège in 1992, **Benoit Beckers** joined the Architecture Superior School of the Polytechnic University of Catalonia in Barcelona, starting with personal research on the following subjects: solar radiation and natural light in architectural and urban projects, geometrical methods in numerical simulation, and wave perception in their physical and cultural environment. In 2008, he joined the Compiègne University of Technology, France, as an associate professor. He is the originator and one of the main designers of the Heliodon software devoted to daylight and solar radiation simulation in architecture.

After graduating as an engineer in physics from the University of Liège in 1966, **Pierre Beckers** joined the Aerospace Laboratory (LTAS, Laboratoire de Techniques

Aéronautiques et Spatiales) of the same university. He devoted his research to finite element models in structural mechanics, computer programs for finite element applications, computer graphics, data visualization, and CAD. Pierre Beckers is one of the main designers of the SAMCEF finite element systems, currently marketed by the Samtech Company founded in 1986. He is now Emeritus Professor at the University of Liège.

**Grega Bizjak**, PhD, is an associated professor and Head of Laboratory of Lighting and Photometry at Faculty of Electrical Engineering, University of Ljubljana. He is active in the field of lighting and photometry as well as in the field of electrical power engineering. His main research interests in lighting are energy-efficient indoor and outdoor lighting, use of daylight, LEDs in lighting applications, and photometry. Prof. Bizjak is the president of Slovenian National Committee of CIE and representative of Slovenia in CIE Division 2.

**Philippe Blanc** graduated from the Ecole Nationale Supérieure des Télécommunications de Bretagne (France) in 1995 with a specialization in signal and image processing. In 1999, he obtained a PhD in signal, automatic and robotics from the MINES ParisTech. He worked for nine years in the Research Department of Thales Alenia Space in projects related to Earth observation and spaceborne systems. Since 2007, he has been working as a senior scientist at the Center for Energy and Processes of MINES ParisTech, in Sophia Antipolis. He is the head of the research group “Observation, Modeling, Decision”.

**Guedi Capeluto** is an architect and an associate professor at the Faculty of Architecture and Town Planning, Technion – Israel Institute of Technology. He has developed several design tools for energy-conscious and sustainable architectural design in a twofold level: building and urban scale. His research is focused on sustainable architecture, intelligent buildings, daylighting, daylight access, and solar rights in urban design. He is in charge of teaching lighting at both the undergraduate and graduate levels. He also teaches at a solar bio-climatic architectural design studio.

**Tom van Eekelen** studied aerospace engineering at the Technical University in Delft (the Netherlands), where he specialized in structural engineering. After working at the University, he started working for Samtech where he developed nonlinear mechanics models/solutions in Meccano. Now he is in charge of all the thermal developments in SAMCEF Thermal, which includes functionalities such as thermal radiation and charring ablators.

**Bella Espinar** received her master’s degree in physics from the University of Granada, Spain, in 2002, and her PhD in applied physics from the University of Almeria, Spain, in 2009. She is experienced in solar radiation measurement,

uncertainty analysis and quality control assessment, atmospheric optics, and development of methods exploiting Earth observation data and models. She has participated in several European contracts in relation with solar resource as well as photovoltaic production and smart grids. Currently, she is working at the Center for Energy and Processes of MINES ParisTech, on Earth observation data for solar resource assessment and meteorology for energy.

**George Janes** founded George M. Janes and Associates in 2008 after spending six years as executive director of the Environmental Simulation Center (ESC), New York. He is one of the region's experts on the intersection of planning with technology and writes and speaks widely on the topic. He has worked as a planner in the public, not-for-profit, and private sectors with a focus on how technology can be used to make better planning decisions. Previously, Mr. Janes managed the development of several of IBM's simulation modeling programs including Community, viz, a planning decision-support system that links visual simulation with local land use decision-making; and TRANSIMs, the next-generation traffic simulation developed by Los Alamos National Laboratory and commercialized by IBM.

**Pierre Kastendeuch** is a lecturer at the Faculty of Geography and Planning (University of Strasbourg). He is a member of the Laboratoire des Sciences de l'Image, de l'Informatique et de la Télédétection (UMR 7005 du CNRS).

**Matej Kobav**, PhD, is a teaching assistant at the Laboratory of Lighting and Photometry at the Faculty of Electrical Engineering, University of Ljubljana. He is active in the fields of lighting and photometry as well as in the field of electrical power engineering. His main research interest in lighting includes use of daylight and energy-efficient indoor and outdoor lighting and photometry. M. Kobav is the representative of Slovenia in CIE Division 3.

**John Mardaljevic** is a reader in Daylight Modeling at De Montfort University, Leicester, UK. His first significant contribution in the field of daylight modeling was the validation of the radiance lighting simulation program under real sky conditions. This helped in the establishment of the radiance system as a de facto standard worldwide for lighting simulation. Mardaljevic went on to pioneer the development and application of what has come known as climate-based daylight modeling. Mardaljevic served on the panel for the 2008 revision of British Standard 8206: Daylight in Buildings. He leads the CIE Technical Committee 3-47: Climate-Based Daylight Modeling, and in 2010 he was appointed as "UK Principal Expert on Daylight" for the European Committee for Standardisation CEN/TC 169 WG11.

Professor **Frédéric Monette** has more than 20 years of experience in the field of environmental engineering and water treatment. After obtaining his undergraduate

(1989) and PhD (1999) degrees in civil engineering at the École Polytechnique de Montréal, he worked as a research assistant at UQAM from 1991 to 2004, where he cofounded the Station Expérimentale de Procédés Pilotes en Environnement laboratory in 1994. In 2004, he began his academic career at École de Technologie Supérieure de Montréal. His more recent research interest focuses on urban environmental engineering.

**Marjorie Musy** is a researcher at CERMA Laboratory of Architectural and Urban Ambient Environment in Nantes, and at the Institute for Research on Urban Sciences and Techniques, IRSTV (France). Her research activity focuses on urban microclimate modeling, impacts of urban vegetation, impacts of urban form, building energy consumption, and natural ventilation of buildings. She is in charge of VegDUD project founded by French Research Agency.

**Edward Ng** is an architect and a Professor at the Chinese University of Hong Kong (CUHK). He has practiced as an architect, as well as lectured in various universities around the world. Environmental and sustainable design is professor Ng's specialty. He was the director of the CIE-IDMP research class station at CUHK in Hong Kong. He is director of the MSc Sustainable and Environmental Design Program at CUHK. As an environmental consultant to the Hong Kong government, he developed the performance-based daylight design building regulations and the Air Ventilation Assessment (AVA) Guidelines.

Dr. **Marius Paulescu** is an Associate Professor at the Physics Department of the West University of Timisoara (Romania). His main research activity is in the field of solar energy conversion, covering the whole range from quantum solid-state physics applied to electronic devices to solar radiation modeling and solar architecture. A core involvement was the designing and placing into operation in 2008 of the first Romanian station outfitted for systematic monitoring of solar irradiance on tilted surfaces.

**Théo Pirard** has graduated in history and education from the Catholic University of Louvain. Since 1969, he is chronicler for news concerning space research and technology for many periodicals in Belgium, France, UK, USA, and for various Web sites (ESA Belgium, Wallonie Espace). He participated in the educational program of the Euro Space Center/Belgium, the Space Expo in Kourou (French Guyana), and the Space Hall of "Musée de l'Air et de l'Espace Le Bourget (Paris)". He is co-author of several books such as *Emerging Space Powers, The New Space Programs of Asia, the Middle East and South-America*, with Brian Harvey, Henk H. F. Smid, and Theo Pirard, Springer Praxis Books, 2010.

Chapter 1

# The Odyssey of Remote Sensing from Space: Half a Century of Satellites for Earth Observations

The operational venture of remote sensing spacecraft started in 1960 following two separate paths: the civilian weather observatories using television (TV) cameras for low-resolution images as well as the military spy satellites with high-resolution photographic films returning to Earth in recoverable capsules. The community of meteorological forecasters was the first one to use the dimension of space to embrace atmospheric changes and weather conditions on a global scale. The intelligence services of the USA and the Soviet Union (now Russia) used powerful telescopes to take precise pictures revealing many details on the ground. The problem for the early remote sensing from space, using optical systems, was that cloud cover prevents the satellites from taking useful photographs much of the time.

As spy satellites were able to observe the military operations in an adversery's camps, the world of the 1960s was saved from the catastrophic move of a "Cold War" between two nuclear powers of this time toward a severely "hot conflict" which would have impacted the survival of the whole planet! Half a century later, today's world is saved from the environmental tragedy of global climate change, mainly due to the images (collected every hour) and continuous data, which are currently collected by Earth observation (EO) satellites. Space, along with processing systems, is our new dimension for control of the globe for environmental and security purposes. Among the priorities to develop space as an asset serving the

Chapter written by Théo PIRARD.

*Solar Energy at Urban Scale* Benoit Beckers

citizens of the world, the European Union (EU) has, along with the civilian Galileo constellation for geo-positioning, deployed the Global Monitoring for Environment and Security (GMES) program. It consists of five different Sentinel families of operational spacecraft and sensors in orbit, all "made in Europe".

### 1.1. To improve the weather forecasts

To see our planet from space has been a dream since the beginning of the space age. It is still the purpose of most of the student teams, which are currently developing low-cost CubeSats (1–2 kg) for technological education. The first remote sensing satellites, with low-resolution imaging capabilities, were dedicated to meteorological observations. Using TV-type cameras, they are able to monitor the evolution of the clouds reflecting the sunlight. The weather satellite system, designed and operated for the continuous imaging survey of the globe, was based on the Television Infrared Observation Satellite (TIROS), developed by the National Aeronautics and Space Administration (NASA). The spin-stabilized Tiros-1 satellite was launched on April 1, 1960, and was operational for only 78 days in the 700 km altitude range. It opened the way to permanent operations with more reliable and more sophisticated spacecraft for weather forecasts. Some of its essential features remain unchanged in its later versions used even today, by Russian, European, Chinese, Japanese, Indian, and Korean meteorological satellites.

Before the advent of satellites, weather bureaus collected data from weather stations, ships, buoys, and balloons disseminated around the globe. The satellites are more expensive than these ground systems, but they can collect more globally instantaneous information with innovative sensors (spectrometers, sounders, etc.) for a larger field of vision. The information thus collected has to be updated and enhanced by *in situ* observations. Nowadays, weather satellites show the parameter by which the weather on the far side of the world would affect our meteorological conditions in a span of 4 or 5 days' time. Sequences of pictures from geosynchronous satellites – positioned on a circular orbit at approximately 35,800 km above the equator – show cloud formations in the Pacific Ocean traveling all the way across Canada before reaching Europe. With the amount of data collected by polar satellites regarding the atmospheric phenomena – in sun-synchronous orbit between 500 and 1,000 km of altitude – and their quick processing by powerful computers, it is possible to establish accurate weather forecasts for one week in advance.

The principle of remote sensing by optical satellites is to record with accurate precision the intensity of the Sun's reflected light on the surface of the Earth. The number of pixels in the image taken by the camera dictates the graininess or resolution, namely the ability to blow it up and observe greater detail. The more pixels in an image, the more you can magnify it without making it grainy. On the

other hand, the more pixels in a camera, the fewer the images you can store in the memory and consequently the more capacity you need to transmit it over the network for processing. The resolution hence obtained is on par with the swath: if the images have to capture some critical details, you will reduce the angle of view required to observe the desired areas. The camera fixed on the Tiros works on the principle of TV-type cathode-ray tube technology, with wide-angle capability. The images obtained show only a few details: the smallest features visible in weather images typically being 1 km in size. This lack of detail in the images obtained is a constraint due to the limited frequency bandwidth of the satellite to transmit such images to small ground receivers.

The US weather satellites, both in sun-synchronous and geosynchronous orbits, are owned and operated by the National Oceanic and Atmospheric Administration (NOAA) under the authority of the Department of the Interior. In parallel, the Department of Defense (DOD) had its own polar weather satellites within the Defense Meteorological Satellites Program. To reduce expenditure, an attempt was recently made to combine the weather programs of both the DOD and NOAA. However, the objective is still yet to be realized. In Europe, the first weather satellite Meteosat-1 was developed and operated in geosynchronous orbit by the European Space Agency (ESA). Once it became operational, the Meteosat system was transferred to the intergovernmental Eumetsat organization that owns and operates the satellites and the associated satellite control and data processing facilities. Other geosynchronous satellites for weather observations, indigenously manufactured, are used in Russia by Roskomgidromet, in Japan by the Japan Meteorological Agency (JMA), in India by the Indian Space Research Organization (ISRO), and in China by the China Meteorological Administration (CMA). The observations thus recorded are complemented by images and data obtained from polar spacecraft, also built by these countries.

### 1.2. Technological challenges to spy and to map from orbit

Satellites fly across the sky unhindered by borders, typically in the range of 200–800 km above ground level. In the mid-1950s, the American Central Intelligence Agency (CIA) used a fleet of U-2 spy planes over the large airspace of the then Soviet Union (Russia). On May 1, 1960, one of its high-altitude aircraft was shot down by a Soviet missile, creating great tension between the two superpowers of the time. After this Cold War incident, CIA/DOD decided to move ahead with its space “segment” through the reconnaissance Corona/Key Hole (KH) program. With the deployment of military spacecraft using photographic cameras, whose films are placed in return capsules for mid-air recovery, high-resolution images of the Soviet, Chinese, North Korean, and Cuban territories became a reality. The first successful recovery was thus made with the Discoverer-13 mission on

August 19, 1960. The Corona "top secret" imagery was officially declassified in February 1995. It is available from the impressive data center of the US Geological Survey (USGS)/Department of Interior or www.usgs.gov, along with high-resolution multispectral data of other governmental EO satellites.

The impetus for the development of military reconnaissance systems in orbit was provided by the National Reconnaissance Office (NRO) that was created secretly in September 1961. Its creation was kept so secretive that its existence was only revealed to the public, more than 30 years later in 1992! This unit of the DOD is located in Chantilly (Virginia). In September 2011, it celebrated 50 years of vigilance from the sky with a temporary exhibition of "declassified" heavy spacecraft for very high resolution imagery: KH-7/Gambit (1963–1967), KH-8/Gambit-3 (1966–1984), and KH-9/Hexagon (1971–1986) were capable of detecting objects of up to 10 cm in length! For reconnaissance activities from space, some of the US satellites also use opto-electronic systems for digital high-resolution imagery. The Satellite and Missile Observation System (SAMOS) spacecrafts were launched from January 1961 to November 1962. Their *modus operandi* was to capture an image and to develop the film on board the satellite, and then to scan the image electronically for transmission via telemetry. This last alternative was proven to be unnecessary based on the comparison with the excellent-quality photographic materials collected with recoverable capsules. However, the usage of the SAMOS spacecrafts was particularly useful in going a step forward with the utilization of digital cameras for quickly mapping large territories and isolated areas with great accuracy. To be optimistic, there is a possibility to synchronize the same feature to combine two images to give a three-dimensional (3D) view of the imagery in question.

This 3D vision was demonstrated by a series of Moon mapping observatories, which benefited from access to classified spy satellite technology because of a secret agreement between NASA and the NRO. Five automated Lunar Orbiters were developed and operated by NASA to map the Moon surface for landing sites in preparation of the manned Apollo expeditions. Put into lunar orbit between August 1966 and August 1967, the robots of NASA photographed 99% of the Moon with resolution as low as 1 m for some areas. Their advanced system to take high-quality pictures was provided by an Eastman Kodak camera and derived from instruments designed for the U-2 spy plane. The on-orbit–developed film was scanned by a photomultiplier for transmission to Earth.

Today, photography is a significant player in the digital revolution. The technology used in the camera of a remote sensing satellite is the same technology we have in a digital camera or a cell phone. It uses a charge-coupled device (CCD), which is a form of solid-state electronics similar to the computer chip, which turns light reflectance into an electrical message. Such a technology reduces the mass of the optical sensor and makes it more compact. You may find miniaturized cameras

on a small satellite. However, to focus on specific targets for high-resolution pictures, you need to innovate with new types of telescopes. The pioneering EO satellite systems during the 1960s used mostly optical devices for multispectral remote sensing. Their successful development of new applications had to challenge some critical aspects in space: the stability of the platform, the agility of the spacecraft, the quick processing of the imagery, and the corrective action related to the atmospheric disturbances on detailed pictures of precise ground items.

The altitude control of a satellite in orbit is particularly crucial for very high resolution remote sensing from space. The platform of a satellite is equipped with star trackers and reaction wheels (gyroscopes), even with micro-thrusters to point the sensors to the targeted areas. The satellite has to compensate its 7.5 km $s^{-1}$ – in 600 km circular orbit – similar to a photographer panning to snap a moving target. The satellite, to view them and to reveal ground changes (illumination, colors, etc.) from different angles, must be very agile to roll itself to 25° side-to-side and 55° along its path. It has to work as a very reactive photographer to get the best vision of an object of an event. The accuracy of the pointing system is an essential prerequisite to achieve a successful campaign of Earth observations from space. The large quantity of data, acquired with multispectral and, especially, hyperspectral sensors, require powerful recorders or memories to store them on board, as well as ground computers to process them.

Image processing has to consider the fact that Earth's atmosphere is constantly moving due to thermal gradients within it. The Earth's atmosphere limits how satellites can record data in several ways. The atmosphere is turbulent not only when there are clouds, fog, smoke, and gas pollution but also with a clear sky during the daytime. Astronomers who observe the sky with high-performance telescopes know the effect of the atmosphere on a perfect vision of a celestial phenomenon. When viewing the stars, we observe the twinkling of starlight that is due to the shimmering effect of the atmosphere. In the same fashion, the atmospheric turbulence puts limits on the accuracy of observations of Earth from orbit. The atmospheric turbulence has a serious effect on the resolution level attained at the decimeter level.

The quality of a satellite image is not determined by a simple resolution value in meters or centimeters. A resolution of 10 cm is probably the best that spy satellites can attain, but that does not come close to reading the headlines or the number plate nor even detecting the golf ball. A 10 cm resolution does not mean that two objects 10 cm apart will always be recognized as two objects and that two objects 8 cm apart will always be recognized as a single larger object. The ability to detect the small gap between two objects will depend on facts such as the Sun's lighting conditions, the shapes and surfaces of the objects, shadowing in the gap, and the color and sheen contrast between the objects and between them and the gap. A gap of 1 cm between two objects would hardly ever be detected.

Cloud cover is another aspect in the atmosphere that significantly prevents the satellites from taking useful photographs much of the time. In the late 1970s the first radar spy satellite appeared that was able to see through the clouds, both during day and night. NASA tested the first radar satellite with the launch of Seasat in June 1978 to demonstrate the feasibility of a global satellite monitoring of oceanographic phenomena. It was operated, for only a few weeks, until October 1978, when a massive short circuit damaged its electrical system. The Synthetic Aperture Radar (SAR), with "phased array" antenna, transmits beams or pulses of microwave energy – in UHF-band, L-band, C-band, or X-band frequencies – and records the echoes or returning reflections on the ground.

The radar principle is used to form an image by utilizing the time delay of the backscattered signals. This electronically active approach for remote sensing observations needs high-power systems on board the satellites: large panels of solar cells, even nuclear reactors (as was the case for many radar satellites of the former Soviet Union). Outside the military spy satellites of the DODs of the United States, China, Japan, Germany (SAR-Lupe), Italy (dual-use Cosmo-SkyMed), India, and Israel, there are civilian and commercial radar satellites in operation throughout the world: Europe, through ESA, with the European Remote Sensing (ERS) (launched in 1991 and in 1995) and Envisat (still operational since 2002), and Canada with Radarsat (since 1995), Infoterra with TerraSAR-X and TanDEM-X.

### 1.3. Toward global environmental observers in space

In the mid-1960s, NASA began to plan the deployment, for civilian purposes, of a land remote sensing system. In 1965, the USGS office proposed the idea of a remote sensing satellite program to gather facts about the natural resources of our planet. Concurrently, the US DOD feared that this civilian program would compromise the secrecy of its reconnaissance missions. In 1967, the US Department of the Interior attempted to become the lead agency for such a system by announcing the Earth Resources Observation Satellite (EROS) program, focusing primarily on satellite imagery for mapping and geology. This attempt failed, leaving NASA in its clear role of research and development agency to refine its effort, under the name of the Earth Resources Technology Satellite (ERTS). Referred to as the Landsat system in 1975, it aims at collecting data of 80 m resolution along a 185 km wide swath in four spectral bands that were found particularly useful for geological survey and for environmental monitoring: green (0.5–0.6 μm) for vegetation imaging, red (0.6–0.8 μm) for imaging of man-made objects, blue (0.4–0.5 μm) for deep water imaging, and near-infrared (IR) (0.8–1.1 μm) for vegetation and soil moisture observations. These bands are the key wavelengths for most of the current EO satellites for civilian purposes.

ERTS-1 or Landsat-1 was a modified Nimbus-type meteorological satellite. Launched on July 23, 1972, it heralded a new age of land remote sensing from space. Until then, this dimension was intensively used by meteorological services and by military intelligence. Put in 917 km altitude sun-synchronous orbit, the environmental observatory of NASA remained operational until January 1978. This stabilized, Earth-oriented platform was designed to carry two optical devices: a three-camera Return Beam Vidicon (RBV) system and a four-channel MultiSpectral Scanner (MSS) which acquired some 300,000 images with a resolution of 80 m and with a swath width of 185 km.

Similar to Landsat-1, Landsat-2 and Landsat-3 with MSS and an enhanced vidicon camera were launched in 1975 and 1978 respectively: they demonstrated that NASA has a long-term vision for Earth observation. The main objective of the Landsat program was to make the data widely available to nearly all potential users regardless of political affiliation. During the Cold War, at the opposite end of the secrecy surrounding the military Corona program, Landsat data played an important role in demonstrating the open exchange of information and ideas, for new applications, to the world community. This openness represented a great change in the strategy of the USA in geo-information services. It pushed ahead a political strategy toward global transparency, to face the worldwide changes of life conditions on the "spaceship Earth" with more than 7 billion inhabitants!

In the mid-1970s, NASA began developing the more capable Thematic Mapper (TM), derived from the MSS instrument, for the Landsat-4 and Landsat-5 missions with heavier spacecraft using a new design. This new multispectral sensor collects 30 m resolution data in the visible and the near-IR spectral bands along the same 185 km swath. In 1979, the White House decided that the Landsat system, now ready for operational status, would be transferred for control to the NOAA that operates the geostationary and polar weather satellites of the USA. Because of budgetary constraints and to ensure continuity of Landsat observations, a decision was taken in 1984 to transfer the operational control of the system to a private firm: the Earth Observation Satellite Company (EOSAT) won the competitive bidding process and took over Landsat activities. In the meantime, in 1982, France (along with Belgium and Sweden) decided to go ahead with the commercial SPOT Image company that established as a worldwide distributor of products and services using imagery from the EO satellites. In 1983, SPOT Image opened a subsidiary close to Washington, D.C.

EOSAT had to face a long-term funding dispute among Congress, the federal administration, NOAA, NASA, and the USGS. Even though the US government as a whole was, and still remains, the largest customer for the Landsat-type data, no single agency was willing to commit sufficient operating funds to continue the sustainable management of system operations. At the end of 1992, EOSAT ceased processing the

Landsat data. This lack of commitment to a continuously operated remote sensing system undercut what little confidence space imagery customers had in the Landsat system. Efforts to get the DOD as a partner for 5 m resolution observations were unsuccessful. Even by early 1994, the question of whether NASA or some other agency would operate the Landsat system had not been answered. By 1998, the NOAA hardly had any role in Landsat, and consequently the USGS was given the entire operational role. Nowadays, the Landsat system is managed by the USGS for data processing, storage, and distribution, while the development of new remote sensing satellites for governmental purposes is under the responsibility of NASA.

The privatization experiment failed for the Landsat system. However, the long experience gained working with the Landsat data demonstrated the usability of land remote sensing and ultimately led to a new, more sustainable thrust toward a marketplace of remote sensing data and information. The Landsat images, archived in the USA by the USGS and at Landsat receiving stations around the world, are a unique resource for global change research and applications in agriculture, cartography, geology, forestry, regional planning, surveillance, education, and national security. With Landsat-5, launched on March 1, 1984, the USGS collected images with its TM instrumentation until November 2011. After 27 years of operations, it decided to stop acquiring the Landsat-5 data due to a rapidly degrading electronic component. After the loss of the Landsat-6 due to launch failure, there is Landsat-7, the most important one of the series, in sun-synchronous orbit since mid-April 1999. Described by NASA as the most accurately calibrated Earth-observing satellite, the 2.2 t spacecraft uses an Enhanced Thematic Mapper (ETM+) for 15 m resolution images in panchromatic mode (0.5–0.9 μm) and for 30 m resolution observations in three visible bands (0.45–0.69 μm), two near-IR (0.77–0.9 μm, 1.55–1.75 μm), and one mid-IR (2.08–2.35 μm), for 60 m resolution data in thermal IR (10.4–12.5 μm).

Since 1985, the governmental Landsat system is rivaled continuously by the commercial Satellite Pour l'Observation de la Terre (SPOT) system of France. It is managed by the French SPOT Image company, now part of Astrium GEO-Information Services. The 1.8 t SPOT-1, jointly developed by France, Sweden, and Belgium, was launched on February 22, 1986: it carried two high-resolution visible (HRV) imaging instruments for 10 m resolution (panchromatic) and 20 m resolution multispectral (0.5–0.9 μm) bands. It was followed by identical satellites, SPOT-2 in January 1990 and SPOT-3 in September 1993. SPOT Image currently operates, respectively, since March 1998 and May 2002, the enhanced 2.76 t SPOT-4 with two HRV infrareds (HRVIRs) for 10 m observations, as well as 3 t SPOT-5 with high-resolution stereoscopic (HRS) imager for stereo pairs of 5 m resolution. Also onboard, the SPOT-4 and SPOT-5 satellites, the Vegetation-1 and Vegetation-2 spectrometers, financed by the European Commission, are "hosted-payloads" to view the globe with a resolution of 1 km and 2,250 km-wide swath for the daily

monitoring of natural resources and oceanographic features. Their data are processed and archived at VITO, Mol (Belgium). With the dual-use (civilian–military) Pleïades HR system – first of the two satellites launched in December 2011, Astrium GEO-Information Services will have access to Earth images having a resolution of less than 1 m. This imagery is combined with stereoscopic or 3D radar data of TerraSAR-X and TanDEM-X satellites operated by Infoterra, a subsidiary of Astrium.

### 1.4. The digital revolution of the ICTs for GIS applications

EO satellites are emblematic of the information age technologies, with (information and communication technologies (ICTs)) whose quick development and innovating expansion marked the start of this new millennium. Their permanent exploitation promises to bolster global transparency by offering an unprecedented access to accurate and timely digital information on our current resources and for our sustainable development. Higher resolution imagery represent a new source of information, which requires, for its applications, new processing systems (computers and software). The new commercial Earth-observatory enterprises are making the transition from being primarily providers of satellite imagery data to offering geospatial information products and services tailored to a broad range of traditional and new customers. Because this is the most promising business, a successful transition would secure them an integral role in the knowledge-based economy.

One of the biggest driving forces for the usability of data remotely sensed by a satellite is the advent of the Geographical Information System (GIS), which intensively exploits the digital content of global viewing from space. Commercial observations of Earth now blur the long-standing differences between civil and military imaging satellites. The distinction between civilian (government-owned) and commercial (government licensed and privately owned) observation satellites is becoming less clear-cut. The new Earth observers or explorers show the performances of the spy satellites, which were designed, developed, and operated in the 1960s. A confluence of trends – political, technological, and economic – has encouraged entrepreneurial firms and emerging nations to enter the nascent Earth-observation data marketplace. The end of US–Soviet confrontation had the effect of relaxing the earlier Cold War restrictions on satellite imaging technologies and expanding public access to higher resolution images. The applications Google Earth and Microsoft Bing Maps (Virtual Earth) offered via internet for every personal computer gives a static high-resolution picture of ground aspects, as viewed in the previous three years. The next step will be a dynamic view based on satellite images made some hours before, like the meteorological observations from various orbits. A restriction still exists in the policy of the USA: not to release imagery with resolution of <0.50 m without governmental permission, because of strategic

reasons. However, the international competition will oblige the US administration to relax its constraints.

Technological push in a world without frontiers spurred greater industrial interest in developing commercial observation satellites and marketing high-quality imagery products. Advances in satellite and optical sensor technologies allow the development of imaging satellites that are substantially smaller, cheaper, more compact, and more agile than the relatively large and expensive EO satellites of the previous decades. Equally important has been a rapid improvement in enabling technologies that reduce the technical gap and cost barriers for a potentially broader range of customers. The American Landsat and French SPOT spacecraft were the first civilian remote sensing satellites, which captured public attention when they returned in 1986 images revealing the real dramatic impact of the Chernobyl reactor disaster, despite the blackout imposed by the Soviet officials. The contribution to transparency at a global scale does not depend on a single satellite system, but arises from the cumulative impact of a growing constellation of commercial and civilian observation satellites.

Since the beginning of this century, we see a plethoric development of EO satellites around the world. Many small, compact, and agile satellites are capable of Earth imaging with the conventional four-band sensors, for resolutions, which show useful details from 5 to 20 m. The international access, through broadband internet, to a large number of observations using various types of imaging sensors (electro-optical, radar, thermal IR, etc.) will substantially enhance global transparency, through the multidisciplinary approach, on the sustainable growth of spaceship Earth. The international competition in providing geospatial information products and services is likely to be fierce because many EO satellites are focused on establishing a niche in the developing market for satellite imagery. Outside the American commercial operators, such as DigitalGlobe and GeoEye, Europe, India, and China appear as the leaders in remote sensing activities with a constellation of EO satellites. At the same time, countries such as Israel (with Imagesat), Brazil (cooperating with China), Argentina (with NASA), South Korea and Taiwan (with European industries), and United Arab Emirates led by Dubai (with South Korean technology) are making substantial progress in the manufacturing and exploitation of remote sensing satellites.

The plethora of EO satellites in our skies means that the solar illumination of our planet will be constantly measured from space. The EO satellites are indispensable tools to permanently monitor the global changes and their causes and effects. Particularly at this time, with an environment seriously affected by the dramatic changes in the atmosphere and in the oceans, by natural disasters due to the climatic conditions and geological phenomena, some crucial decisions must be urgently taken and seriously applied concerning the management of the natural

resources and the growth of human activities at the global scale. Significant pollution from the burning of vegetation, forestry destruction, volcanic eruptions, and ozone depletion show that the Earth is dramatically changing because of strong energy consumption in the industrialized areas and intense land use in the populated countries. World summits about the health of the Earth, held at Rio in 1992, at Kyoto in 1997, then in Dubai in 2011, established political protocols to develop vital solutions for sustainable humankind at a global scale.

On July 31, 2003, the first Earth Observation Summit, with high-level delegates from 30 countries and 22 international organizations, took place in Washington, D.C. to push ahead the real solutions for the efficient exchange of information. The day after, the Group on Earth Observation (GEO) was established to develop a 10-year plan for the implementation of a comprehensive, coordinated, and sustained network of remote sensing and data processing systems. On February 16, 2005, during the third Earth Observation Summit that took place in Brussels, representatives of some 60 countries and 40 international organizations endorsed a 10-year plan with concrete steps toward comprehensive cooperation in Earth observations: they agreed on a worldwide strategy to set up the Global Earth Observation System of Systems (GEOSSs) to meet user needs, especially in the developing world, for social and economic benefits.

New advanced technologies, in parallel with new challenges for data processing activities, will allow the vertical profiles of the atmospheric chemistry, the hyperspectral views of land features, and ocean changes. For the next decade, some satellite manufacturers have on the drawing board the development of geosynchronous remote sensing satellites using adaptative optics to track the birth of a tornado, to spot the area of a sudden forest fire, and to locate and monitor "live" the impact of floods. Hyperspectral (>100 spectral bands) and high-resolution (up to 0.2 m) Earth observations are becoming the new challenges of remote sensing satellites. The great variety, in the near future, of EO satellites using optical and electronic sensors means a growing investment in space technology and in data processing.

To avoid too large a number of duplicated efforts through commercial competition, some international coordination between the players in the market of remote sensing missions is necessary harmonize systems in orbit, terminals on the ground, and methods in imagery analysis for the future of life on our planet. The United Nations organization is encouraging the transfer of technologies, of data, and of software for Earth observations from the Northern industrialized countries to Southern developing areas. Open and free access to remote sensing data reduces the business of products and services from space. This poses a dramatic challenge to the satellite industries, which are operating EO satellites for commercial purposes. Europe's initiative of GMES – a joint program of the ESA and of the EU and part of

the GEOSS Plan – has to review all opportunities that are taking place around the planet. ESA is pushing ahead the development of experimental Earth Explorers and the five families of operational Sentinel observatories as the continuation of the successful Envisat mission. Priority is given to the modular approach of miniaturized multipurpose platforms, which demonstrate how powerful are the integrated applications, such as synergies between satellite remote sensing and positioning products. The concept of global constellations for Earth observations, developed and promoted by Surrey Satellite Technology Limited in Guildford (UK), is becoming the reference for a great variety of remote sensing satellites throughout the world.

## 1.5. Suggested reading

[BAK 01] BAKER J.C., O'CONNELL K.M., WILLIAMSON R.A. (eds.), *Commercial Observation Satellites – At the Leading Edge of Global Transparency*, RAND/ASPRS, p. 645, 2001.

[NOR 10] NORRIS P., *Watching Earth from Space – How Surveillance Helps Us and Harms Us*, Springer-Praxis, p. 284, 2010.

For further information about Earth observation satellites: see http://directory.eoportal.org/; http://www.eohandbook.com/

# Chapter 2

# Territorial and Urban Measurements

Solar radiation, in the broad sense, refers to the radiation emitted by the Sun with a spectral wavelength range of about 0.28–4 μm. Broad band measurements in this range are currently made and are further described in this chapter. The chapter is organized as follows. Section 2.1 summarizes the fundamentals and the main radiometric quantities of solar radiation. Section 2.2 is dedicated to radiometry instrumentation and data quality control. The main concepts and instruments presented in this section apply to both territorial and urban measurements. The specificity of the radiometry in urban environments is portrayed in section 2.3, and section 2.4 contains the main conclusions.

## 2.1. Solar radiation at the Earth's surface

The Sun has a diameter of 1.39 million km. It subtends an angular diameter of about 0.52° at an average distance between the Sun and the Earth that is of 149 million km. The Sun is very often modeled as a point radiation source. At this level of approximation, a beam of nearly parallel rays strikes the top surface of the Earth's atmosphere. This beam is referred to as extraterrestrial radiation (ETR). ETR fluctuates about 6.9% during a year (from 1,412 $Wm^{-2}$ in January to 1,321 $Wm^{-2}$ in July) due to the Earth's varying distance from the Sun. Figure 2.1 shows the spectral distribution of ETR (i.e. the extraterrestrial solar spectrum) at the mean Sun–Earth distance. The graph is plotted for low resolution with data from [GUE 08] and is detailed enough for many solar energy applications. It is available online at http://rredc.nrel.gov/solar/spectra/am0, along with other reference radiation spectra.

Chapter written by Marius PAULESCU and Viorel BADESCU.

*Solar Energy at Urban Scale* Benoit Beckers

The spectral integration of the extraterrestrial spectrum over all wavelengths (i.e. between zero and infinity) defines the solar constant $G_{SC}$. Thus, $G_{SC}$ is the solar energy flux incoming on a unitary surface area perpendicular to the Sun's rays at the mean Sun–Earth distance. Since the Sun's radiance varies slightly over short and long periods [FRÖ 91], the solar constant does not remain steady over time. There is a variation about ±1 $Wm^{-2}$ around the mean solar constant during a typical solar cycle of 11 years [GUE 08]. Based on the data collected over 25 years from terrestrial and space observations, the actual best estimate of the average solar constant is $G_{SC}$ = 1,366.1 $Wm^{-2}$ [GUE 04].

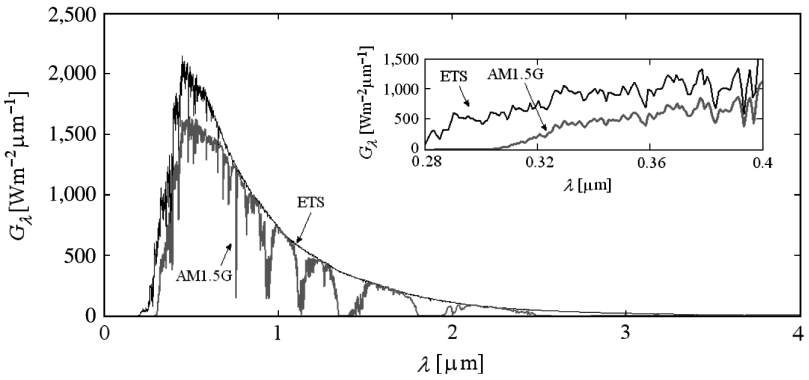


**Figure 2.1.** *Extraterrestrial solar spectrum (ETS) and terrestrial standard solar spectrum AM1.5G. A detail of ultraviolet spectrum is presented inset. $G_\lambda$ is the extraterrestrial spectral energy flux density, $\lambda$ is the photon wavelength, and AM1.5G stands for the standard air mass 1.5 global solar spectrum*

When the ETR passes through the Earth's atmosphere, its spectral distribution is modified by absorption and scattering processes. While scattering occurs for the whole wavelength spectrum, atmospheric gases absorb solar radiation selectively. Most of the ETR shortwave photons (wavelength $\lambda < 0.3$ μm) are filtered out by the ozone layer. Unlike the visible band, where a relatively low absorption occurs, the infrared (IR) absorption is strong due to the vibration–rotation bands of water vapor. The complex effect experienced by the ETR spectral distribution when passing through the Earth's atmosphere is illustrated in Figure 2.1, which displays the air mass 1.5 global (AM1.5G) radiation spectrum defined by the Commision Internationale de l'Eclairage (CIE) and the American Society for Testing and Materials (ASTM) for terrestrial use of photovoltaic solar cells. The standards assume that the receiving surface is tilted 37° toward the equator and the solar zenith angle is 48°19′; also, the total ozone column content is 0.34 cm·atm, the Angstrom turbidity coefficient at 0.5 μm wavelength is 0.084, and the water vapor

column content is 1.42 g.cm$^{-2}$. (If the air mass (AM) is approximated by the inverse of the zenith angle cosine, then $1/\cos(48°19') = 1.5$. This value gives us the acronym AM1.5).

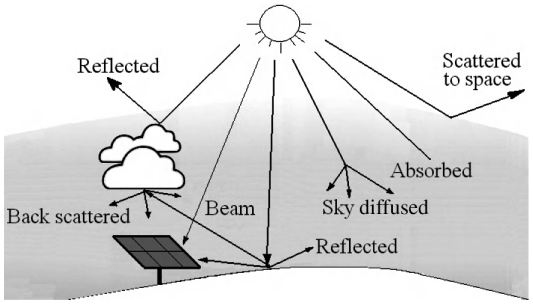


**Figure 2.2.** *Extraterrestrial solar radiation shared out by the atmosphere and ground*

As a result of its passage through the atmosphere, the ETR is separated into different components, schematically indicated in Figure 2.2. The direct component of solar radiation is that part of ETR that directly reaches the Earth's surface. Scattering of the ETR in the atmosphere generates the diffuse component. A part of the solar radiation that is reflected by the ground may also be present in the total solar radiation. More precisely, the following quantities associated with solar radiation are commonly measured:

*Direct beam irradiance* ($G_b$) is the energy flux density of the solar radiation incoming from the solid angle subtended by the Sun's disk on a unitary surface area perpendicular to the Sun's rays (units: Wm$^{-2}$).

*Direct horizontal irradiance* ($G_h$) differs from the direct beam irradiance in that it is measured on a flat horizontal plane. Lambert's cosine law states that the beam on a plane surface is directly proportional to the cosine of the incidence angle. Since the incidence angle of the solar beam striking the horizontal ground is equal to the zenith angle $\theta_z$ (Figure 2.3), then

$$G_h = G_b \cos\theta_z \qquad [2.1]$$

*Diffuse irradiance* ($G_d$) represents the energy flux density of the solar radiation incoming from the entire sky "dome" on a horizontal surface (excluding the direct beam coming from the Sun's disk).

*Global irradiance* ($G$) is the sum of the direct horizontal and diffuse components, given as

$$G = G_h + G_d = G_b \cos\theta_z + G_d \qquad [2.2]$$

The term "global" is associated with the fact that the solar radiation is received from the entire $2\pi$ solid angle of the sky dome. Equation [2.2] describes the basic relationship between the horizontal solar irradiance components, which are fundamental for the calibration of solar instruments.

*The total irradiance* ($G_t$) received by a surface tilted with an angle $\beta$ with respect to the horizontal plane (Figure 2.3) is the sum of beam flux density, diffuse flux density, and the additional flux density $G_r$ of the solar radiation reflected from the ground. Use of equation [2.2] yields (Figure 2.3)

$$G_t = G_b \cos\theta + R_d G_d + G_r \qquad [2.3]$$

where $\theta$ is the incidence angle (i.e. the angle between the direction of beam radiation and the normal to the surface, see Figure 2.3); $R_d$ is a correction coefficient taking into account the anisotropic scattering and the fact that in some cases just a part of the whole hemispherical sky is viewed from the receiver; and $G_r$ is the flux density of radiation reflected by the ground that is intercepted by the tilted surface. There are many works devoted to the evaluation of $R_d$, which is considered the major potential source of errors in equation [2.3]. The ground reflected component $G_r$ may also be a cause of errors, though of lesser importance. The simplest $R_d$ model considers diffuse irradiance to be isotropic distributed in the sky [LIU 60], while the more realistic models consider diffuse irradiation to be anisotropic [PER 87].

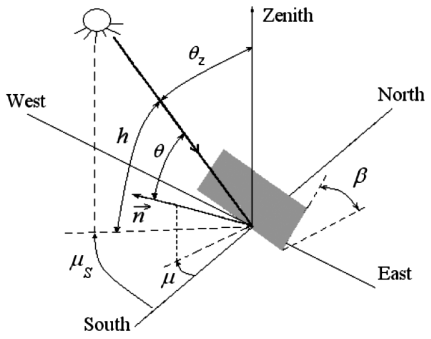


**Figure 2.3.** *Angles describing the position of the Sun: $\theta_z$ – zenith angle; $h$ – elevation angle; $\mu_S$ – azimuth angle. Angles describing the position of a surface: $\beta$ – slope angle; $\mu$ – surface azimuth angle. The incidence angle $\theta$ represents the angle between the direction of the Sun and the normal to the surface $\vec{n}$*

By summing up over a finite time period $\Delta t = t_2 - t_1$, we obtain the solar irradiation components

$$H = \int_{t_1}^{t_2} G(t)\,dt \qquad [2.4]$$

usually measured in $Jm^{-2}$ or $Whm^{-2}$. In equation [2.4], $G(t)$ stands for any of the above solar irradiance components and, consequently, $H$, refers to the corresponding solar irradiation component.

For proper characterization of the radiative regime, the state of the sky should be assessed. Two quantities are commonly used to describe the state of the sky. The most usual indicator is the total cloud cover amount $C$ (sometimes called point cloudiness), which represents the fraction of the celestial vault covered by clouds (estimated in tenths or oktas). The total cloud cover amount is essentially an instantaneous quantity. A daily averaged total cloud cover amount may be computed. The second quantity indirectly describing the state of the sky is the relative sunshine $\sigma$ (also called sunshine fraction). It is defined as $\sigma \equiv s/S$ , where $S$ is the length of a given time interval and $s$ is the bright sunshine duration during that interval.

Radiometry is the science that studies the measurement of electromagnetic radiation. The specific device for measuring the energy flux of electromagnetic radiation is referred to as radiometer. Radiometers have been developed to measure the energy flux of different components of the terrestrial solar radiation, as described in the following section.

## 2.2. Instrumentation

Each of the quantities defined in section 2.1 is measured with specific techniques and devices. Sensors' temperature fluctuation (the sensors are placed outdoors and their temperature may vary between −20°C and 70°C), wind, and rain are the factors that influence solar irradiance measurements. The minimization of these perturbations is a difficult task in solar radiometers engineering. In the following, we present the instrumentation used to measure various solar irradiances at ground surface. Also, the accuracy of these measurements is discussed in relation to instrumentation's performance.

The optical electromagnetic radiation is primarily detected by converting the beam's energy in electric signals that can be measured by employing conventional techniques. Two physical phenomena are involved in this case:

1) *The thermoelectric effect* – It is the occurrence of an electric voltage due to a temperature difference between two regions of the detector, as a result of the incident beam absorption.

2) *The photovoltaic effect* – It is a method of directly generating electrical power by converting the energy flux of optical radiation; this is commonly performed by using semiconductor devices.

The radiometers based on photodetectors provide the simplest and cheapest alternative. A response time of about 10 μs makes these sensors appropriate for measuring fast alternating solar irradiance as in [TOM 10]. Owing to the limitations introduced by the spectral character during photons absorption in semiconductor materials, such radiometers are also used for narrowband measurements. The wavelength corresponding to maximum absorption depends on the material of the sensor and the characteristics of the semiconductor junction. Photodiode shortwave sensors with peak sensitivities between 0.55 μm and 0.8 μm are available for general use. But this non-uniform and limited spectral response of semiconductor sensors is the major drawback of such photodetector-based radiometers, which makes them inadequate for highly-accurate broadband measurements. Owing to their nearly constant spectral sensitivity for the whole solar spectral range, radiometers equipped with thermal sensors are widely used to measure broadband solar irradiance.

### 2.2.1. *Fundamentals of solar irradiance measurements*

Let us consider a thermal receiver (TR) with mass $m$, specific heat $C$, and the absorption coefficient $\alpha$. An optical beam with the spectral density of energy flux $G_\lambda$ is normally incident to a plane surface of TR. The incident energy on the TR surface of area $A$ during the infinitesimal time interval $dt$ is:

$$\left( \int_0^\infty G_\lambda d\lambda \right) A dt = GA dt \qquad [2.5]$$

while the energy absorbed by the TR is $\alpha GA dt$. A fraction of this energy is used to augment the TR temperature, while the other fraction is the heat loss toward the environment. Let us assume that during the time span $dt$, the TR temperature increases from the ambient temperature $T_a$ to $T = T_a + dT$. Also, the heat loss by convection is $k\left(T - T_a\right)dt$. The heat transfer coefficient $k$ is a complicated function of $A$, $T$, and $T_a$. However, in many situations, using a constant $k$ value is a good approximation. The loss by thermal radiation is small and can be neglected in the first instance. Thus, the balance thermal energy equation is given by:

$$GA\alpha dt = mCdT + k\left(T - T_a\right)dt \qquad [2.6]$$

Equation [2.6] can be integrated to obtain the solution:

$$GA\alpha - k\left(T - T_a\right) = c\,\mathrm{e}^{-\frac{kt}{mC}} \qquad [2.7]$$

The value of the integration constant $c$ is obtained from the initial condition: at time $t = 0$, the TR temperature equals the ambient temperature, i.e. $T(0) = T_a$; this gives $c = GA\alpha$. The time evolution of TR temperature can be calculated in this manner:

$$T = T_a + \frac{GA\alpha}{k}\left(1 - \mathrm{e}^{-\frac{kt}{mC}}\right) \qquad [2.8]$$

Let us assume a constant incident optical energy flux. Then, after a long time interval, the steady state will be reached. The steady-state TR temperature is given by:

$$T_m = T_a + \frac{GA\alpha}{k} \qquad [2.9]$$

The radiometers require a time for responding to change in the incident radiation. The response time is a radiometer quality indicator (see Table 2.2) and is defined as the time for the output signal to reach 95% of the final value following a step-change in irradiance. Obviously, the response time of a radiometer has to be as short as possible. As a result, the time $\tau = mC/k$ during which the system described by equation [2.8] relaxes to steady state has to be small. Note that increasing the value of $k$ in equation [2.9] yields a higher temperature amplitude $T_m - T_a$, which, in turn, diminishes the precision in measuring $T_m$. Consequently, the only way to obtain a shorter $\tau$ value is by diminishing the product $mC$.

Let us now assume that the optical flux is suppressed after the system reaches the steady state. The balance equation [2.6] becomes

$$0 = mCdT + k\left(T - T_a\right)dt \qquad [2.10]$$

with the solution

$$T = T_a + \frac{GA\alpha}{k}\mathrm{e}^{-\frac{kt}{mC}} \qquad [2.11]$$

The system reversibility is expressed by [2.11], i.e. for time $t$ longer than $\tau$, the system turns back to the initial state, $T = T_a$. The most important result of

this section is equation [2.9], which shows a linear dependence between the TR temperature and the optical energy flux density $G$. Equation [2.9] is the basic equation providing the solar irradiance measurement.

### 2.2.2. *Solar radiometers*

#### 2.2.2.1. *Pyrheliometers*

A pyrheliometer is a broadband instrument that measures the direct beam component $G_b$ of solar radiation. Consequently, the instrument should be permanently pointed toward the Sun. A two-axis Sun tracking mechanism is quite often used for this purpose. The detector is a multijunction thermopile placed at the bottom of a collimating tube (Figure 2.4(a)) that is provided with a quartz window to protect the instrument. The detector is coated with optical black paint (acting as a full absorber for solar energy in the wavelength range of 0.280–3 μm), and its temperature is compensated to minimize sensitivity to ambient temperature fluctuations. The pyrheliometer aperture angle is 5°. Consequently, radiation received from the Sun from a limited circumsolar region is measured, but all diffuse radiation originating from the rest of the sky is excluded.

A readout device is used with pyrheliometers (or other radiometers) to give the present value of direct beam irradiance. It is scaled to the sensitivity of a particular instrument to display the value directly in SI units, $Wm^{-2}$.

#### 2.2.2.2. *Pyranometers*

Pyranometers are broadband instruments that measure global solar irradiance incoming from a $2\pi$ solid angle on a planar surface. A typical pyranometer is schematically represented in Figure 2.4(b). It consists of a white disk for limiting the acceptance angle to 180° and two concentric hemispherical transparent covers made of glass. The domes shield the sensor from thermal convection, protect it against weather threat (rain, wind, and dust), and limit the spectral sensitivity of the instrument in the wavelength range of 0.29–2.8 μm. A small cartridge of silica gel inside the dome absorbs water vapor.

A pyranometer can be used to measure the diffuse solar irradiance $G_d$, provided the contribution of the direct beam component is eliminated. A small shading disk should be mounted on an automated solar tracker to ensure that the pyranometer is continuously shaded. Alternatively, a shadow-ring may prevent the direct component $G_b$ reaching the sensor for a whole day. As the daily maximum Sun elevation angle changes day-by-day, it is necessary to change periodically (days lag) the height of the shadow-ring. On the other hand, since the shadow-ring intercepts part of the diffuse radiation, it is necessary to correct the measured values. The

percentage of diffuse radiation intercepted by the shadow-ring varies during the year with respect to its position and atmospheric conditions [SIR 87].

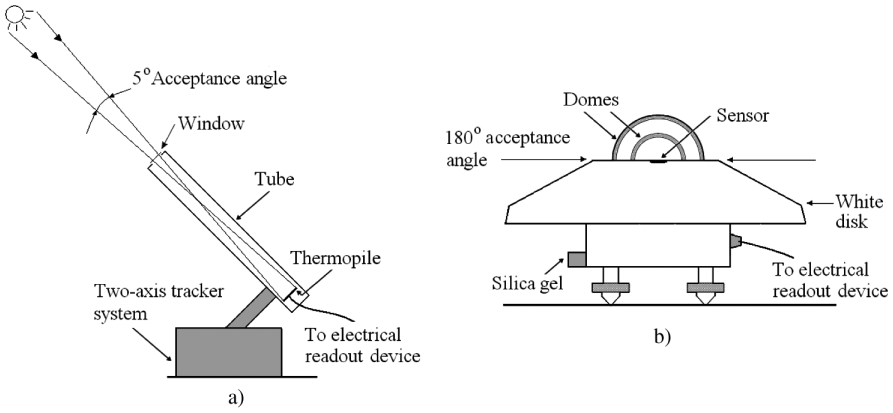


**Figure 2.4.** *Schematic of a pyrheliometer (a) and pyranometer (b)*

Figure 2.5 shows two solar radiation measurement devices in operation [SOL 11]. The first device, LPPYRA 05 [DEL 11], is a double pyranometer, i.e. it is manufactured by mounting two pyranometers in the same housing: one measures the global solar irradiance while the other measures the ground reflected radiation $G_r$. The ensemble measures the net global radiation as well as the ground albedo. The second device, LPPYRA 12 [DEL 11], is equipped with a shadow-ring and measures the diffuse solar irradiance $G_d$. The pyranometer base is mounted parallel to the ground while the shadow-ring is positioned such that its axis is parallel to the Earth's axis.

**Figure 2.5.** *First-class pyranometers mounted on the Solar Platform of the West University of Timisoara, Romania: LPPYRA 05 measuring global and ground reflected solar irradiance (left) and LPPYRA 12 equipped with shadow band measuring the diffuse solar irradiance (right)*

Two types of pyranometer sensors are commercially available: the black-and-white sensor [FIS 11] (Figure 2.6, left) and the thermopile sensor [DEL 11] (Figure 2.6, right).

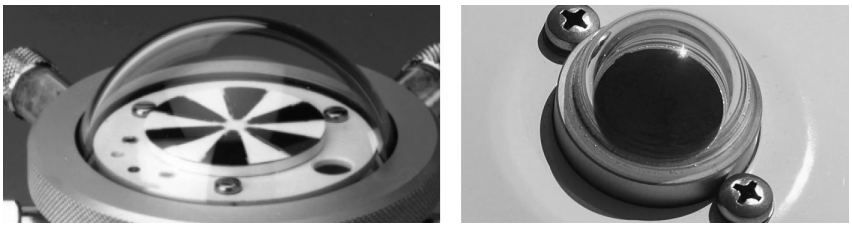

**Figure 2.6.** *Pyranometer sensors: black and white (details from [FIS 11]) (left) and thermopile [DEL 11] (right)*

First, the operation of the black-and-white sensor is considered. The temperatures of the black and white surfaces may be derived using equation [2.9].

$$T_{black(white)} = T_a + G\frac{A\alpha_{black(white)}}{k} \qquad [2.12]$$

The temperature difference $\Delta T = T_{black} - T_{white}$ between these surfaces is mainly due to the difference in the absorption coefficient values:

$$\Delta T = G\frac{A}{k}(\alpha_{black} - \alpha_{white}) \qquad [2.13]$$

Equation [2.13] shows that $\Delta T$ is proportional to the energy flux density $G$ incident on the sensing surfaces. The temperature difference $\Delta T$ is measured, and $G$ is finally obtained from equation [2.13]. The ambient temperature $T_a$ does not figure in equation [2.13]. In practice, the influence of ambient temperature is cancelled by proper sensor design.

Second, the thermopile sensor is considered. Equation [2.9] is applicable for this case as well. However, the thermopile device uses the Seebeck effect to create a difference of electric potential based on the temperature difference $\Delta T$. A thermopile consists of a fairly large number of thermocouples (between 20 and 40) mounted in series to increase the output signal. The cold junctions of the thermopile are intimately connected to the body of the instrument, which remains at the ambient temperature due to its large mass and large thermal capacity. The hot junctions are bonded to a layer of black paint, which is a strong solar radiation

absorber. The absorbed radiation increases the temperature of the hot junction. The temperature gradient between the hot and the cold junctions generates a voltage proportional to the incident radiation. Typically, an incident solar energy density flux of 1,000 $Wm^{-2}$ produces a temperature difference of 5°C, resulting in an output signal of 5 mV.

#### 2.2.2.3. *World radiometric reference*

The World Radiometric Reference (WRR) is the measurement standard representing the SI unit of irradiance. It was introduced to ensure worldwide homogeneity of solar radiation measurements The WRR is maintained and operated by the World Radiation Center (WRC) at Physikalisch–Meteorologisches Observatorium Davos, Switzerland [PMO 11]. The WRR has been used since 1979 by the World Meteorological Organization (WMO) and other communities for measurements of direct solar irradiance. The WRR is obtained from the weighted mean of the measurements of 15 very accurate absolute cavity radiometers of 10 different types. Absolute cavity radiometers absorb photons on a blackened conical receiver and are electrically self-calibrating. They have an estimated accuracy of 0.3% and stability larger than 0.01% per year [FRÖ 91]. To guarantee the long-term stability of the reference, a group of six absolute pyrheliometers of different designs are used presently as the World Standard Group (WSG) (Figure 2.7).

#### 2.2.2.4. *Radiometers calibration and uncertainty*

According to [WMO 08], the radiometers are classified by using various criteria: the type of variable to be measured, the field of view, the spectral response, the main use, and so on. The most important types of radiometers are listed in Table 2.1.

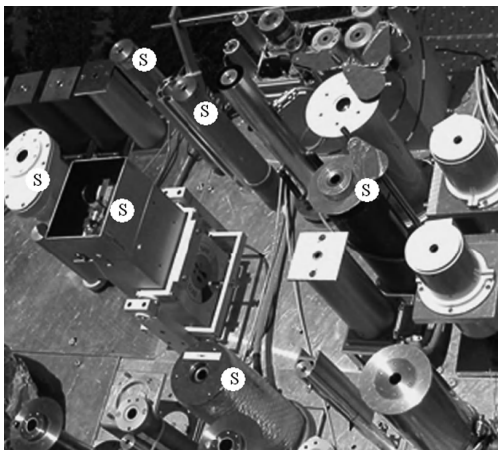


**Figure 2.7.** *The WSG pyrheliometers are marked by "S". After [GUE 08]*

| Instrument | Parameter to be measured | Main use | Acceptance angle (sr) |
|---|---|---|---|
| Absolute pyrheliometer | Direct beam solar irradiance | Primary standard | $5 \times 10^{-3}$ |
| Pyrheliometer | Direct beam solar irradiance | Secondary standard network | $5 \times 10^{-3}$ |
| Pyranometer | Global, diffuse, and reflected solar irradiance | Working standard network | $2\pi$ |

**Table 2.1.** *Different category of pyrheliometers and pyranometers (after [WMO 08])*

Self-calibrating absolute pyrheliometers [RED 96] are used as the primary standard, the other radiometers being calibrated against an absolute instrument. The uncertainty of the measured value depends on factors, such as:

– *resolution*: the smallest change in the radiation quantity that can be detected by the instrument;

– *non-linearity of response*: the change in sensitivity associated with the incident irradiance level;

– *deviation of the directional response*: the cosine response and azimuth response;

– *time constant of the instrument*: the time taken to reach 95% of the final value;

– *changes in sensitivity due to changes in weather variables*: variables such as temperature, humidity, pressure, and wind;

– *long-term drifts of sensitivity*: defined as the ratio of electrical output signal to the irradiance applied.

All the aforementioned uncertainties should be known for a well-characterized instrument. Certain instruments perform better for particular climates, irradiances, and solar positions; therefore, instruments should be selected according to their end use.

The pyranometer calibration consists of setting up one or more calibration factors and their dependence on environmental conditions, such as temperature, irradiance level, spectral and angular distribution of irradiance, and inclination of instrument. There are a variety of methods for calibrating the pyranometers, based on radiation coming from the Sun or from the laboratory sources. A short list is as follows:

– In the field, using equation [2.2], where a standard pyrheliometer gives the direct beam solar irradiance and a shaded standard pyranometer gives the diffuse irradiance.

– In the field, by comparison with a standard pyranometer, using the Sun as a radiation source and the same conditions of exposure.

– In the laboratory, by comparison with a similar pyranometer previously calibrated in the field, using an artificial radiation source.

#### 2.2.2.5. *Classification of pyranometers*

The accepted classification of pyranometers with respect to their quality is defined by the International Standard ISO 9060/1990 that is also adopted by WMO [WMO 08]. ISO 9060 standard distinguishes between the three classes of pyranometers: the best is (somewhat improperly) called *secondary standard*, the second best is called *first class*, and the third best is called *second class*. Table 2.2 summarizes the characteristics of secondary standard and first class pyranometers.

### 2.2.3. *Sunshine duration measurements*

According to [WMO 08], sunshine duration during a given period is defined as the sum of the time spans for which the direct solar irradiance exceeds the threshold of 120 $Wm^{-2}$. In practice, the following two methods are widely used for measuring sunshine duration:

*Burning card method*: This method is based on the Campbell–Stokes sunshine recorder and consists of a solid glass sphere that focuses a direct beam of solar radiation onto a card that is burnt.

*The pyranometric method*: This method implies the measurement of the global and diffuse solar irradiance; the direct solar irradiance is derived by subtraction, which is then compared with the WMO threshold.

#### 2.2.3.1. *Burning card method*

The Campbell–Stokes recorder was invented by J.F. Campbell in 1853 and later modified by Sir G.G. Stokes in 1879. The original design is still in use with very little change, being probably the most common sunshine recorder in use nowadays.

The Campbell–Stokes sunshine recorder basic setup consists of a glass sphere mounted concentrically in a spherical bowl (Figure 2.8). The support can be adjusted such that the axis of the sphere may be inclined to the angle of the local latitude. A series of grooves are engraved on the spherical bowl segment to hold the recording card. The glass sphere focuses the direct beam solar radiation on to the

card, burning a trace whenever the Sun is shining. The position and length of the trace indicate the starting time and duration of the sunshine interval.

| ISO specification | Secondary standard | First class |
|---|---|---|
| WMO characteristics | High quality | Good quality |
| Response time (to reach 95% of the final value) | <15 s | <30 s |
| Zero off-set response: | | |
| Response to 200 $Wm^{-2}$ net radiation | 7 $Wm^{-2}$ | 15 $Wm^{-2}$ |
| Response to 5°$Ch^{-1}$ change in ambient temperature | ±2 $Wm^{-2}$ | ±4 $Wm^{-2}$ |
| Resolution | ±1 $Wm^{-2}$ | ±5 $Wm^{-2}$ |
| Stability (change in sensitivity per year) | ±0.8% | ±1.5% |
| Linearity (deviation from sensitivity at 500 $Wm^{-2}$ over 100–1,000 $Wm^{-2}$ irradiance range) | ±0.5% | ±1% |
| Directional response for beam radiation (error due when assuming that the normal incidence response at 1,000 $Wm^{-2}$ is valid for all directions) | ±10 $Wm^{-2}$ | ±20 $Wm^{-2}$ |
| Spectral selectivity (deviation of the product of spectral absorbance and transmittance, respectively, from the mean) | | |
| ISO (0.35–1.5 μm) | ±3% | ±5% |
| WMO (0.3–3 μm) | ±2% | ±5% |
| Temperature response (maximum relative error due to any change of ambient temperature within a 50°C interval) | ±2% | ±4% |
| Tilt response (percentage deviation from horizontal response when the tilt is changed from horizontal to vertical at 1,000 $Wm^{-2}$) | ±0.5% | ±2% |
| Achievable uncertainty, 95% confidence level | | |
| WMO hourly totals | 3% | 8% |
| WMO daily totals | 2% | 5% |

**Table 2.2.** *Characteristics of pyranometers, ISO 9060 standard*

**Figure 2.8.** *Typical Campbell–Stokes sunshine recorder (Image credit: http://commons.wikimedia.org/wiki/File:Heliografo.jpg)*

The errors of this recorder are mainly due to the dependence of burning initiation on the card's temperature and humidity as well as to the overburning effect, especially in case of broken clouds [KER 04].

2.2.3.2. *Pyranometric method*

The pyranometric method to measure the duration of sunshine is based on the fundamental correlation equation [2.2] between the direct radiation $G_b$, diffuse radiation $G_d$, and global radiation $G$. By using measurements of $G$ and $G_d$, the WMO sunshine criterion can be expressed as:

$$\xi(t) = \begin{cases} 1 & \text{if} \quad \left(G - G_d\right) \big/ \cos\theta_z > 120\ \text{Wm}^{-2} \\ 0 & \text{otherwise} \end{cases} \qquad [2.14]$$

where $\theta_z$ is the Sun zenith angle and $\xi$ stands for the sunshine number [BAD 02], which is a Boolean variable stating whether the Sun is covered by clouds or not. Statistical properties of the sunshine number are investigated in [BAD 11], while methods to quantify the fluctuations of solar radiative regime by using the sunshine number are reported in [PAU 11]. Figure 2.9 depicts a sample of global and diffuse solar irradiance recorded on the Solar Platform of the West University of Timisoara [PAU 10] during October 1, 2010 along with the sunshine number.

The sunshine duration during a time interval $\Delta t$ is obtained by multiplying $\Delta t$ by the mean sunshine number $\overline{\xi}$ during $\Delta t$.

The errors in the pyranometric method stem from the errors of measuring global and diffuse solar irradiance, which are amplified at higher zenith angles (see equation [2.14]). Choosing a high-quality pyranometer is of primary importance to reduce the uncertainty level of the results. Usage of shading rings has, as a

consequence, under-evaluated the incident diffuse of solar energy. Hence, corrections are made to the measurements to diminish this negative effect.

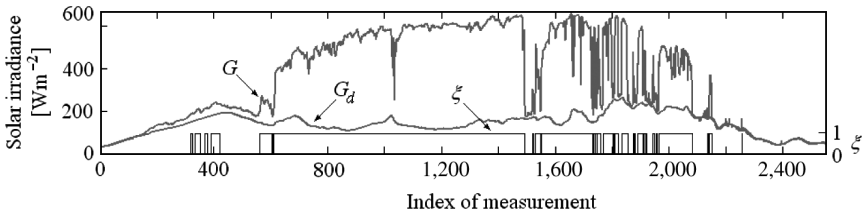


**Figure 2.9.** *Global (G) and diffuse ($G_d$) solar irradiance on October 1, 2010 recorded at four samples per minute [PAU 10] on the Solar Platform of the West University of Timisoara, Romania. The variation of the sunchine number is also shown*

### 2.2.4. *Data quality assessment*

The quality control of solar radiation data includes the following three stages:

1) Quality assurance: It includes measures taken prior to sensor operation in the field as well as proper selection and installation of the instruments and regular calibrations and maintenance.

2) Real-time automatic assessment tests during measurement process.

3) Retrospective data analysis.

The first stage is very important since a datum once acquired remains the same forever. Chapters 7 and 8 of the WMO Guide to Meteorological Instruments and Methods of Observation [WMO 08] provide guidance for carrying out accurate solar radiation measurements. Also, [WMO 86] gives a detailed description of instruments currently used in solar radiation measurements and the principles according to which they operate.

Real-time quality assessment can be performed to indicate whether a data value is missing, reasonable, too small, or too large. For instance, following [GUE 08], certain questions to be answered are as follows: Does the direct beam solar irradiance lie between zero and the extraterrestrial value? Does the measured solar irradiance lie between zero and a maximum expected value? Is the diffuse component greater than the estimated Rayleigh diffuse component? However, such physical tests cannot replace a proper quality assurance.

In addition to testing physical limits, a quality control criterion may rely on the repetitiveness in the observed data. For instance, global irradiance must equal the sum of diffuse and beam irradiance (see equation [2.2]).

Retrospective quality control is performed by testing data against reliable physical models. A review of the procedures for quality assessment of solar irradiation data may be found in [YOU 05].

### 2.2.5. *Data availability*

Compared to the needs, there are very few stations equipped for monitoring solar radiation. Most countries worldwide set up national networks contributing to the World Radiation Data Center (WRDC) located at the Main Geophysical Observatory, St. Petersburg, Russia. WRDC serves as a central depository for solar radiation data collected over 1,000 stations throughout the world. The majority of data available from 1964 to 1993 are freely accessible at http://wrdc.mgo.nrel.gov/ and the data from 1994 till date are also freely accessible at http://wrdc.mgo.rssi.ru/.

## 2.3. Radiation measurements in urban environment

Shortwave and longwave incoming and outgoing radiation fluxes are affected by the special properties of the atmosphere and surface of cities. Thus, the features of solar radiation incident in cities may be different from those of the neighboring territorial areas. However, very few systematic recordings of solar global radiation measurements exist in built-up urban areas. In this section, we first present the main differences between territorial and urban areas in terms of description scales. Next, a classification of urban zones is presented. Finally, the main characteristics of radiation measurements in the urban environment are briefly outlined.

### 2.3.1. *Description scales*

The concept of description scale is of fundamental importance in meteorological applications. Three horizontal scales are usually considered when the urban environment is described [OKE 84, WMO 08].

1) *The microscale*, which does not exceed a few hundred meters in size and is related to particular urban constituents such as trees, gardens, buildings, and streets. The horizontal microclimatic effects of an urban constituent persist for some distance away from their source and are then mixed by the action of turbulent eddies.

2) *The local scale*, which is typically one to a few kilometers in size. It includes landscape features such as topography, but the microscale effects are averaged. It is useful in describing the climate of urban environments that are similar from some points of view (e.g. in terms of size and spacing of buildings).

3) *The mesoscale*, which is typically tens of kilometers in size and may include a whole city. It is useful in describing the way that a town influences the weather.

The basic vertical scale when describing the climate of urban areas is of the order of the urban canopy layer (UCL), which is the place where vertical exchanges of momentum, heat, and moisture occur. The UCL thickness is roughly equivalent to the mean height $z_H$ of buildings and trees in a given area. The vertical microclimatic effects of an urban constituent persist on the so-called roughness sublayer (RSL) of blending height $z_r$. Rough estimates for $z_r$ are between $1.5 \cdot z_H$ for densely built area and more than $4 \cdot z_H$ for low-density areas [GRI 99]. Measurement devices placed above the RSL receive a spatially averaged signal that is representative of the local scale. To measure microlocal effects, the device should be placed at a height lower than $z_r$.

Other height restrictions are related to the internal boundary layer generated by each local-scale surface type. They depend on the distance around the measurement site where the urban terrain shows similar features [WMO 08]. These restrictions have weaker effects on radiation measurements and are not described here.

### 2.3.2. *Urban site description*

The urban areas affect the atmospheric environment through four of their basic features: (i) morphology (described by sizing and spacing of buildings and streets), (ii) skin properties (described by the relative ratios of built-up, paved, vegetated, or water-covered surface areas), (iii) body properties (described by the existing natural or man-made materials), and (iv) urban physiology (described by the sink and sources of heat, humidity, and pollutants, due to natural phenomena and human activity). The surfaces of various parts of cities can be classified in terms of these four features. Ellefsen [ELL 91] developed a set of urban terrain zone types that can be used to describe urban structure for roughness, airflow, radiation access, and screening.

For solar radiation measurements, the simpler scheme shown in Table 2.3 is more useful. It takes into account the aspect ratio $Z_H/W$, where $W$ is the average spacing between the main roughness elements (building and trees). In the city center, $Z_H/W$ is the street "canyon" height/width. The aspect ratio is known to be related to solar shading and longwave radiation screening [OKE 81]. In addition, Table 2.3 takes into account the percentage built, which is the average proportion of ground plan covered by built features such as buildings and roads (the rest of the area is occupied by pervious cover, i.e. green space, water, and other natural surfaces). The percentage built is related to the optical properties of the urban skin. It is also connected to the urban zone surface permeability in terms of the moisture status of the ground and the humidification and evaporative cooling potential.

### 2.3.3. *WMO recommendations*

The same instruments used for solar radiation measurement are also used in territorial and urban areas. However, the standard guidelines for territorial measurements cannot be followed in the urban environment. This is mainly due to the obstruction of radiation exchange by buildings and trees as well as to the existence of artificial surface cover. Since every measurement site has specific features, stating rigid recommendation rules is of little utility in urban areas. In this context, it is often necessary to perform measurements in a closer range than is usually done for territorial areas, to accept exposure over non-standard surfaces at non-standard heights, or to split the observations between two or more locations. WMO [WMO 08] recommends applying guiding principles rather than rules and to retaining a flexible approach. A summary of recommendations follows.

#### 2.3.3.1. *Scope of measurements and measurement site selection*

Knowledge of *global* solar radiation is of primary importance in the study of urban climate. Also, information on solar radiation is useful for solar energy applications, daylight levels in buildings, legislated rights to solar exposure, and other fields. Therefore, the measurement of *global* solar radiation has a high priority among the radiometric variables. Other incoming radiation fluxes of interest are *direct* and *diffuse* solar radiation, *UV* solar radiation, and *longwave atmospheric* radiation. They have applications in estimation of the pollution extinction coefficients (the direct solar radiation), the interior daylighting (the diffuse solar radiation), the depletion by ozone and damage to humans, plants, and materials (UV solar radiation), and the enhancement of the flux by pollutants and the heat island effect (longwave atmospheric radiation). The choice of measuring any of these incoming fluxes depends on the potential applications and sensor costs.

The scope of measurements is of primary importance. Difference should be made between measurements wanting to characterize a particular given site and those aiming to monitor the greatest impact of the city or an urban zone. In the former case, the measurement place is imposed but the latter case is more involved and a few comments on the measurement site selection follow. It is useful to have at our disposal an existing list of urban zones prepared in accordance with the four features described in section 2.3.2. Areas where there is the highest probability of finding maximum effects can be judged initially by referring to that list. The next step is to inspect the map, imagery and photographic evidence and look for areas of reasonably homogeneous urban development without large patches of anomalous structure (such as unusually wet patches in an otherwise dry area, individual buildings that go beyond by more than half the average building height). The measurement place should be sited over surfaces that, within a microscale radius, are representative of the local-scale urban environment. The percentage built category in Table 2.3 is a crude guide to the recommended underlying surface.

| Zone class | Urban climate zone | Aspect ratio $z_H/W$ | Percentage built |
|---|---|---|---|
| 1 | Intensely developed urban with detached close-set high-rise buildings with cladding, e.g. downtown towers | >2 | >90 |
| 2 | Intensely high-density urban with 2–5 storey, attached or very-close-set buildings often of bricks or stone, e.g. old city core | 1–2.5 | >85 |
| 3 | Highly developed, medium-density urban with row or detached but close-set houses, stores, and apartments, e.g. urban housing | 0.5–1.5 | 70–85 |
| 4 | Highly developed, low, or medium-density urban with large low buildings and paved parking, e.g. shopping malls and warehouses | 0.05–0.2 | 70–95 |
| 5 | Medium development, low-density suburban with one- or two-storey houses, e.g. suburban houses | 0.2–0.6 | 35–65 |
| 6 | Mixed use with large buildings in open landscape, e.g. institutions such as hospitals, universities, and airports | 0.1–0.5 (depends on trees) | <40 |
| 7 | Semi-rural development and scattered houses in natural or agricultural areas, e.g. farms and estates | >0.05 (depends on trees) | <10 |

**Table 2.3.** *Urban zone classes. Modified from Table 11.1 of [WMO 08]*

Building roofs may be used for incoming solar radiation measurements. We have to avoid, if possible, short-term obstruction of direct solar radiation impinging on an up-facing radiometer by masts, antennas, flag poles, and similar structures. Such existing obstructions should be fully documented in terms of location and duration before the measurements are made. Excessive reflection from very light-colored walls that may extend above the local horizon should be avoided.

The upper domes of the radiometers should be cleaned on a regular basis (this means daily in heavily polluted areas).

#### 2.3.3.2. *Measurements and corrections*

The rules for territorial measurements should be used for urban sites, when possible. The unobstructed horizon is the most significant requirement in case of incoming solar radiation. The radiometers should be free of vibration and have no

obstruction above the sensor's plane. This includes fixed elements, such as buildings, trees, and hills, as well as ephemeral phenomena, such as pollutant plumes and clouds generated by exhaust vents. Objects subtending angles larger than 10° or those that might intercept the direct radiation at any time should be considered. Obstructions below the elevation of 5° can be neglected since the diffuse radiation below that elevation contributes less than 1% to the diffuse radiation coming from the whole hemispherical vault.

When the direct solar radiation is obstructed, the respective corrections are to be carried out in the record. The diffuse solar radiation can be corrected for obstructions only when records exist for both global and diffuse radiation. First, the diffuse record is to be corrected and then the global record is subsequently adjusted. The correction affects the fraction of the diffuse irradiance coming from the obstructed part of the sky.

## 2.4. Conclusions

In the last decade, the field of solar radiometry has seriously progressed, resulting in significantly improved quality of solar radiation measurement. The uncertainties in the best practical solar radiation data available today are still in the order of 3% in direct beam, 5% in total global horizontal, 3% in diffuse horizontal irradiance measured with a corrected pyranometer, and perhaps 5–20% in sunshine duration, for sunshine recorders. The challenge for solar radiation measurements in the next decades is to reduce the uncertainty in measured data. The rules for territorial measurements should be used for urban sites, when possible. However, the main recommendation is to apply guiding principles rather than rules, and to retain a flexible approach.

## 2.5. Acknowledgments

The authors wish to thank Dr. Cristian Oprea (Romanian National Meteorological Administration) for valuable comments. One author (VB) would like to thank Dr. Bertrand Calpini (MeteoSwiss) for useful WMO references.

## 2.6. Bibliography

[BAD 02] BADESCU V., "A new kind of cloudy sky model to compute instantaneous values of diffuse and global solar irradiance", *Theoretical and Applied Climatology*, vol. 72, pp. 127–136, 2002.

[BAD 11] BADESCU V., PAULESCU M., "Statistical properties of the sunshine number illustrated with measurements from Timisoara (Romania)", *Atmospheric Research*, vol. 101, pp. 194–204, 2011.

[DEL 11] DELTA O.H.M., Pyranometers, albedometers – manuals. Available at: http://www.deltaohm.com/ver2010/uk/index.php. Accessed in August 2011.

[ELL 91] ELLEFSEN R., "Mapping and measuring buildings in the canopy boundary layer in ten US cities", *Energy and Buildings*, vol. 16, pp. 1025–1049, 1991.

[FIS 11] Dual pyranometer. Fischer product data sheet Edition 1, 04/05. Available at: http://www.fischer-barometer.de/datenblaetter/E461121.pdf. Accessed in August 2011.

[FRÖ 91] FRÖHLICH, C., "History of solar radiometry and the World Radiation Reference", *Metrologia*, vol. 28, pp. 111–115, 1991.

[GRI 99] GRIMMOND C.S.B., OKE T.R., "Aerodynamic properties of urban areas derived from analysis of surface form", *Journal of Applied Meteorology*, vol. 38, no. 9, pp. 1262–1292, 1999.

[GUE 04] GUEYMARD C.A., "The sun's total and spectral irradiance for solar energy application and solar radiation models", *Solar Energy*, vol. 76, pp. 423–453, 2004.

[GUE 08] GUEYMARD C.A., MYERS D.R., "Solar radiation measurement: progress in radiometry for improved modeling", Chapter 1 in BADESCU V., *Modeling Solar Radiation at the Earth Surface*, Springer, 2008.

[KER 04] KERR A., TABONY R., "Comparison of sunshine recorded by Campbell–Stokes and automatic sensors", *Weather*, vol. 59, pp. 90–95, 2004.

[LIU 60] LIU B.Y.H., JORDAN R.C., "The interrelationship and the characteristics distribution of direct, diffuse and total solar radiation", *Solar Energy*, vol. 4, pp. 1–19, 1960.

[OKE 81] OKE T.R., "Canyon geometry and the nocturnal heat island: comparison of scale model and field observations", *Journal of Climatology*, vol. 1, no. 3, pp. 237–254, 1981.

[OKE 84] OKE T.R., "Methods in urban climatology", in KIRCHOFER W., OHMURA A., WANNER W. (eds.), *Applied Climatology*,. *Zürcher Geographische Schriften*, vol. 14, pp. 19–29, 1984.

[PAU 10] PAULESCU M., DUGHIR C., TULCAN-PAULESCU E., LASCU M., GRAVILA P., JURCA T., "Solar radiation modeling and measurements in Timisoara, Romania: data and model quality", *Environmental Engineering and Management Journal*, vol. 9, no. 8, pp. 1089–1095, 2010.

[PAU 11] PAULESCU M., BADESCU V., "New approaches to measure the stability of the solar radiative regime", *Theoretical and Applied Climatology*, vol. 103, pp. 459–470, 2011.

[PER 87] PEREZ R., SEALS R., INEICHEN P., STEWART R., MENICUCCI D., "A new simplified version of the Perez diffuse irradiance model for tilted surface", *Solar Energy*, vol. 39, pp. 221–231, 1987.

[PMO 11] PMOD/WRC Physikalisch-Meteorologisches Observatorium Davos/World Radiation Center. Available at: http://www.pmodwrc.ch/pmod.php?topic=wrc. Accessed in August 2011.

[RED 96] REDA I., Calibration of a Solar Absolute Cavity Radiometer with Traceability to the World Radiometric Reference, Tech. Rep. NREL TP-463-20619, National Renewable Energy Laboratory, Golden, Colorado, 1996.

[SIR 87] SIREN K.E., "The shadow band correction for diffuse irradiation based on a two-component sky radiance model", *Solar Energy*, vol. 39, pp. 433–438, 1987.

[SOL 11] Solar Platform of the West University of Timiosoara, Romania. Available online at: http://solar.physics.uvt.ro/srms. Accessed in September 2011.

[TOM 10] TOMSON T., "Fast dynamic processes of solar radiation", *Solar Energy*, vol. 84, pp. 318–323, 2010.

[WMO 86] WMO, Revised Instruction Manual on Radiation Instruments and Measurements, World Meteorological Organization: World Climate Research Programme Publications Series No. 7, WMO/TD No. 149, Geneva, 1986.

[WMO 08] World Meteorological Organization, Guide to Meteorological Instruments and Methods of Observation, No. 8, 7th edition, Chapters 7 and 11, 2008.

[YOU 05] YOUNES S., CLAYWELL R., MUNEER T., "Quality control of solar radiation data: present status and proposed new approaches", *Energy*, vol. 30, pp. 1533–1549, 2005.

# Chapter 3

# Sky Luminance Models

As indicated in the title of the chapter, only the sky models of luminance distribution are explained in the following. Luminance, compared to radiance, is a photometric quantity that is measured in cd $m^{-2}$. Radiance, on the other hand, is a radiometric quantity measured in W $sr^{-1}$ $m^{-2}$. The difference is that luminance considers the human eye, which is not equally sensitive to all wavelengths of light or even electromagnetic radiation. Radiance takes into account all electromagnetic radiations, but only the visible part of luminance. With some approximations, the presented models of luminance distribution may also be used for modeling radiance sky distribution although special radiance distribution models may also be found in the literature.

Sky luminance models generate continuous sky luminance patterns. For more than 100 years, researchers all over the world have been trying to describe and model sky luminance distribution. The first measurements were performed by Schramm [SCH 01] in 1901, by Kaehler [KAE 08] in 1908, and by Kimball and Hand [KIM 21] in 1921. The measurements were performed under overcast skies and the gradual decrease in luminance from zenith to horizon was noted to be in the ratio from 2:1 to 3:1. Moon and Spencer [MOO 42] surveyed and arranged the previous research work, and in 1942 proposed luminance distribution of the overcast sky as a standard. The CIE adopted a simplified version of the proposed standard as a CIE overcast sky only in 1955 [CIE 55].

Parallel to the measurements on overcast skies, in 1929 Pokrowsky [POK 29] found a gradual increase in luminance from zenith to horizon in the case of clear

Chapter written by Matej KOBAV and Grega BIZJAK.

*Solar Energy at Urban Scale* Benoit Beckers

skies in the ratio of 1:3.65 and more. On the basis of the work performed by Boldyrev [BOL 35] in 1935 and Krat [KRA 43] in 1943, Kittler [KIT 67] recommended standard clear sky in 1967. Kittler's proposal was adopted in 1973 as a CIE standard clear sky [CIE 73].

Since then, several different approaches and concepts were used to describe sky luminance distribution under various intermediate skies.

In 2003, CIE adopted a standard "Spatial distribution of daylight" [CIE 03], which describes 15 different sky types (five for overcast skies, five for intermediate skies, and five for clear skies). Here we describe sky models from the past which are now mostly used to model sky luminance distribution using simple parameters such as irradiances. Irradiances (global and diffuse) are measured within International Daylight Measurement Programme (IDMP) stations or could be derived from the images of geostationary satellites [DUM 03]. These satellites provide a continuous coverage of the Earth, taking pictures at least every half hour and with a spatial resolution of 5 km or less. For Western and central Europe, these data are available on a Satel-Light Web server (www.satel-light.com).

The luminance of each point on a sky is common to all models and is defined relative to the luminance of zenith. To shorten the needed calculation procedure, usually the sky dome is divided into an appropriate number of sky patches or elements with assumed uniform luminance. The positions of such sky element as well as the position of the Sun can be described with the help of angles as shown in Figure 3.1.

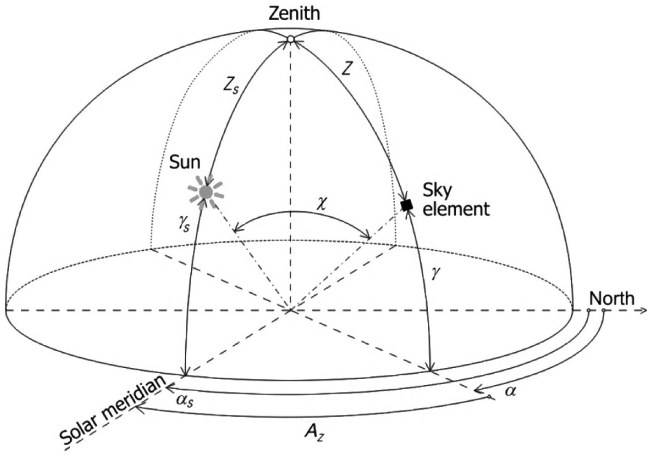


**Figure 3.1.** *Angles defining the position of the Sun and a sky element*

In Figure 3.1, the following angles are noted:

$Z$ zenith angle of a sky element,

$Z_S$ solar zenith angle,

$\gamma$ altitude of a sky element,

$\gamma_S$ altitude of the Sun,

$A_z$ angular difference between azimuth of the Sun and azimuth of the sky element;

$\alpha_S$ solar azimuth,

$\alpha$ azimuth of a sky element.

### 3.1. CIE standard overcast sky (1955)

In 1955, CIE accepted a proposal by Moon and Spencer [MOO 42] for an overcast sky standard with the gradation of ratio between horizontal and zenith luminance $L_H/L_Z$ = 1:3. This means that the luminance of a zenith is three times higher than the luminance of a sky element at unobstructed horizon. Luminance of an arbitrary sky element is defined using the following equation:

$$\frac{L_\alpha}{L_Z} = \frac{1}{3}\left(1 + 2\cos Z\right) \qquad [3.1]$$

where:

$L_\alpha$ luminance of a sky element,

$L_Z$ zenith luminance,

$Z$ zenith angle of a sky element.

As evident from equation [3.1], the luminance of a sky element for this model is not dependent on the azimuth or altitude of the Sun. Hence, this model can only be used for conditions with densely overcast skies, where the Sun is fully shaded by clouds and its position cannot be defined by observing the sky luminance distribution.

### 3.2. CIE standard clear sky (1996)

In 1996, new joint ISO/CIE standard [CIE 96] for sky modeling was published. This standard includes Moon and Spencer's formulation of overcast sky (described in Chapter 1, section 1.3.1) and Kittler's [KIT 67] formulation of clear sky.

This additional clear sky model was defined in the same way as the overcast sky model with an ratio between luminance of an arbitrary portion of sky and zenith luminance. Relative luminance of an arbitrary sky element of a standard clear sky is defined using the following equation:

$$\frac{L_\alpha}{L_Z} = \frac{\left(1 - e^{-0.32/\sin\gamma}\right) \cdot \left(0.91 + 10e^{-3\chi} + 0.45\cos^2\chi\right)}{0.274 \cdot \left(0.91 + 10e^{-3Z_s} + 0.45\cos^2 Z_s\right)} \quad [3.2]$$

where:

$\chi$ angular distance between the sky element and the Sun,

$Z_S$ solar zenith angle,

$\gamma$ altitude of a sky element.

The angular distance (Figure 3.1) between the sky element and the Sun (scattering angle) is defined using the following two equations:

$$\chi = \arccos(\cos Z_S \cdot \cos Z + \sin Z_S \cdot \sin Z \cdot \cos A_z) \quad [3.3]$$

$$A_Z = |\alpha - \alpha_S| \quad [3.4]$$

where:

$A_Z$ angular difference between azimuth of the Sun and azimuth of the sky element,

$\alpha_S$ solar azimuth,

$\alpha$ azimuth of a sky element.

### 3.3. CIE standard general sky

Following the CIE standards [CIE 96], useful models of clear and overcast skies were defined. But in reality, these two types of skies are not so frequent across all locations on Earth. So there was also a need to model some intermediate (partly cloudy) skies. In 1998, Kittler *et al.* [KIT 98] presented the extended sky model that allowed the modeling of different sky types (clear, intermediate, and overcast) with the help of different parameters. From a large number of possible sky types, 15 different sky types of relative luminance distribution were chosen. These chosen sky types were selected based on sky measurements made at the same time in different

locations (Tokyo, Berkeley, and Sydney). The presented formulation of 15 sky types was adopted as a standard general sky model defined in CIE standard [CIE 03] in 2003. In the CIE standard [CIE 03], detailed definitions of daylight conditions can be found that cover five overcast, five intermediate, and five clear skies. With the complex formulation and parameterization, a whole spectrum of different effects of diffuse scattering by the atmosphere and effects of direct sunlight are covered.

Input parameters for the calculation of the relative luminance distribution are the position of the Sun and the parameters *a*, *b*, *c*, *d*, *e*, which describe atmospheric conditions. In Table 3.1, we can find six groups of parameters *a* and *b* that describe gradation function (Figure 3.2) and six groups of parameters *c*, *d*, and *e* that describe indicatrix function (Figure 3.3). If we were to combine all these six gradation groups with all six indicatrix groups, we would end up with 36 sky types. Since the standard [CIE 03] is based on sky scans, the most rare or practically non-occurring sky types were eliminated and only 15 different sky types were included.

In the CIE standard general sky model, the ratio of the luminance of the arbitrary sky element ($L_a$) to the zenith luminance ($L_Z$) is defined with the help of the following equation:

$$\frac{L_\alpha}{L_Z} = \frac{f(\chi)\cdot\phi(Z)}{f(Z_S)\cdot\phi(0)} \qquad [3.5]$$

where:

*f(x)* indicatrix function,

*φ(Z)* gradation function.

The luminance gradation function, $\varphi(Z)$, relates the luminance of a sky element to its zenith angle

$$\varphi(Z) = 1 + a\cdot\exp\left(\frac{b}{\cos Z}\right) \qquad [3.6]$$

where $0 \le Z \le \frac{\pi}{2}$

and at the horizon $\varphi\left(\frac{\pi}{2}\right) = 1$

| CIE sky type | Gradation | Indicatrix | *a* | *b* | *c* | *d* | *e* | Description of luminance distribution |
|---|---|---|---|---|---|---|---|---|
| 1 | I | 1 | 4 | −0.7 | 0 | −1 | 0 | *CIE standard overcast sky, alternative form with steep luminance gradation toward zenith, azimuthal uniformity* |
| 2 | I | 2 | 4 | −0.7 | 2 | −1.5 | 0.15 | Overcast, with steep luminance gradation and slight brightening toward the Sun |
| 3 | II | 1 | 1.1 | −0.8 | 0 | −1 | 0 | Overcast, moderately graded with azimuthal uniformity |
| 4 | II | 2 | 1.1 | −0.8 | 2 | −1.5 | 0.15 | Overcast, moderately graded, and slight brightening toward the Sun |
| 5 | III | 1 | 0 | −1 | 0 | −1 | 0 | *Sky of uniform luminance* |
| 6 | III | 2 | 0 | −1 | 2 | −1.5 | 0.15 | Partly cloudy sky, no gradation toward zenith, slight brightening toward the Sun |
| 7 | III | 3 | 0 | −1 | 5 | −2.5 | 0.3 | Partly cloudy sky, no gradation toward zenith, brighter circumsolar region |
| 8 | III | 4 | 0 | −1 | 10 | −3 | 0.45 | Partly cloudy sky, no gradation toward zenith, distinct solar corona |
| 9 | IV | 2 | −1 | −0.55 | 2 | −1.5 | 0.15 | Partly cloudy, with the obscured Sun |
| 10 | IV | 3 | −1 | −0.55 | 5 | −2.5 | 0.3 | Partly cloudy, with brighter circumsolar region |
| 11 | IV | 4 | −1 | −0.55 | 10 | −3 | 0.45 | White–blue sky with distinct solar corona |
| 12 | V | 4 | −1 | −0.32 | 10 | −3 | 0.45 | *CIE standard clear sky, low illuminance turbidity* |
| 13 | V | 5 | −1 | −0.32 | 16 | −3 | 0.3 | *CIE standard clear sky, polluted atmosphere* |
| 14 | VI | 5 | −1 | −0.15 | 16 | −3 | 0.3 | Cloudless turbid sky with broad solar corona |
| 15 | VI | 6 | −1 | −0.15 | 24 | −2.8 | 0.15 | White–blue turbid sky with broad solar corona |

**Table 3.1.** *15 Standard skies, gradation, indicatrix groups, and parameters defining those groups*

Equation [3.5] requires the value of gradation function at zenith, which is defined as

$$\varphi(0) = 1 + a \cdot \exp b \qquad [3.7]$$

Waveforms belonging to six standard gradation functions are shown in Figure 3.2.

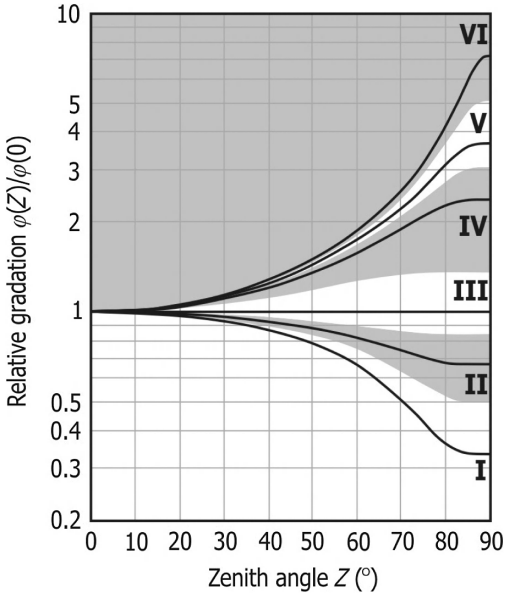


**Figure 3.2.** *Standard gradation function groups*

Similarly, scattering indicatrix function, $f$, relates the relative luminance of a sky element to its angular distance from the Sun as follows:

$$f(\chi) = 1 + c \cdot \left[ \exp(d\chi) - \exp(d\frac{\pi}{2}) \right] + e \cdot \cos^2 \chi \qquad [3.8]$$

Its value at the zenith is given by

$$f(Z_S) = 1 + c \cdot \left[ \exp(dZ_S) - \exp(d\frac{\pi}{2}) \right] + e \cdot \cos^2 Z_S \qquad [3.9]$$

Waveforms belonging to six standard indicatrix functions are shown in Figure 3.3 and the standard indicatrix types are listed in Table 3.2.

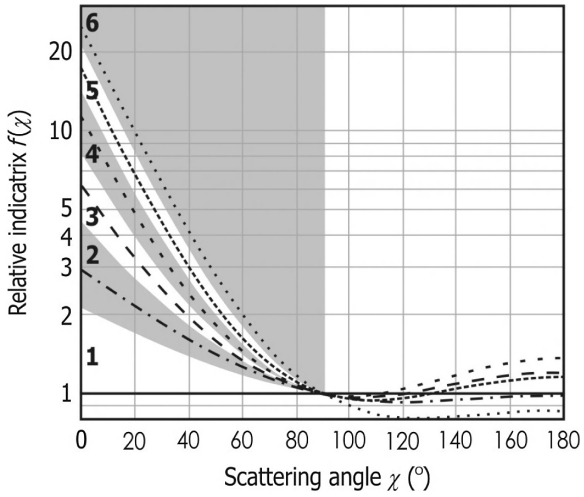


**Figure 3.3.** *Standard indicatrix function groups*

| Indicatrix type | Description | *c* | *d* | *e* |
|---|---|---|---|---|
| 1 | Unity relative scattering indicatrix with a stable uniform course | 0 | −1.0 | 0 |
| 2 | Slightly rising relative scattering indicatrix toward Sun positions | 2 | −1.5 | 0.15 |
| 3 | Rising trend of relative scattering indicatrix toward Sun positions | 5 | −2.5 | 0.30 |
| 4 | Distinct solar corona created by the relative scattering indicatrix | 10 | −3.0 | 0.45 |
| 5 | Steeply rising relative scattering indicatrix toward Sun positions | 16 | −3.0 | 0.30 |
| 6 | Broad and high luminance solar corona caused by extensive scattering | 24 | −2.8 | 0.15 |

**Table 3.2.** *Standard parameters for indicatrix functions and description of standard indicatrix types*

### 3.4. All-weather model for sky luminance distribution – Perez

The CIE standard general sky model is not the only model that can be used for different types of skies. Different intermediate sky conditions as well as conditions of clear and overcast skies can also be described with the Perez all-weather sky model [PER 93]. This model is based on five different parameters, which are related to darkening or brightening of the horizon ($a_p$), luminance gradient near the horizon ($b_p$), relative intensity of the circumsolar region or solar aureole ($c_p$), width of the circumsolar region ($d_p$), and relative backscattered light ($e_p$). Parameters were defined based on more than 16,000 all-sky scans recorded in Berkeley, California, in 1985 and 1986, which covered a wide range of different conditions – from overcast to clear through intermediate skies. This model also uses the CIE gradation function and distorted indicatrix function.

Similar to the previous model, the Perez all-weather sky model is also described with the ratio between luminance of a sky element and zenith luminance, which is defined by the following equation:

$$\frac{L}{L_Z} = \frac{g(\gamma,\chi)}{g\left(\frac{\pi}{2},\frac{\pi}{2}-\gamma_S\right)} \qquad [3.10]$$

where gradation function, $g$, is defined as

$$g(\gamma,\chi) = \left(1 + a_p \cdot \exp\left(\frac{b_p}{\sin\gamma}\right)\right) \cdot \left(1 + c_p \cdot \exp\left(d_p \cdot \chi\right) + e_p \cdot \cos^2\chi\right) \qquad [3.11]$$

In this model, $a_p$, $b_p$, $c_p$, $d_p$, and $e_p$ are the distribution parameters that describe the atmospheric conditions. These parameters depend on sky clearness and sky brightness. Sky clearness and sky brightness are calculated from horizontal diffuse irradiance and normal incident direct irradiance with the help of the following two equations:

$$\varepsilon = \frac{\frac{E_{es}}{E_{ed}} + 1 + 1.041Z_S^3}{1 + 1.041Z_S^3} \qquad [3.12]$$

$$\Delta = \frac{m \cdot E_{ed}}{E_{es0}} \approx \frac{E_{ed}}{E_{es0} \cdot \cos(Z_S)} \qquad [3.13]$$

where:

$\varepsilon$ sky clearness,

$\Delta$ sky brightness,

$E_{ed}$ horizontal diffuse irradiance,

$E_{es}$ normal incident direct irradiance,

$Z_S$ solar zenith angle,

$m$ relative optical air mass.

Relative optical air mass depends on solar altitude, and for its calculation it is recommended to use the following formulation by Kasten and Young [KAS 89]:

$$m = \frac{1}{\sin \gamma_S + 0.50572 \left(\gamma_S + 6.07995^0\right)^{-1.6364}} \quad [3.14]$$

Sky clearness and sky brightness describe two distinct characteristics of the atmosphere. The first characteristic describes the turbidity of the sky and the second the thickness of clouds.

Regarding sky clearness, eight categories of skies are assumed from category 1 for overcast sky to category 8 for clear sky. Boundaries for sky clearness for each of the eight categories are listed in Table 3.3.

| $\varepsilon$ category | | Lower bound | Upper bound |
|---|---|---|---|
| 1 | Overcast | 1.000 | 1.065 |
| 2 | | 1.065 | 1.230 |
| 3 | | 1.230 | 1.500 |
| 4 | | 1.500 | 1.950 |
| 5 | | 1.950 | 2.800 |
| 6 | | 2.800 | 4.500 |
| 7 | | 4.500 | 6.200 |
| 8 | Clear | 6.200 | – |

**Table 3.3.** *Discrete sky clearness categories*

Distribution parameters in equation [3.11] are all calculated using the equation of the same form taking into account the sky clearness and sky brightness together with

the solar zenith angle. As an example, an equation for calculating the coefficient $a_p$ is given as follows:

$$a_p = a_1(\varepsilon) + a_2(\varepsilon) \cdot Z_S + \Delta\left[a_3(\varepsilon) + a_4(\varepsilon) \cdot Z_S\right] \quad [3.15]$$

| Sky clearness interval | | | | | | | | | |
|---|---|---|---|---|---|---|---|---|---|
| $\varepsilon$ | From | 1.000 | 1.065 | 1.230 | 1.500 | 1.950 | 2.800 | 4.500 | 6.200 |
| | To | 1.065 | 1.230 | 1.500 | 1.950 | 2.800 | 4.500 | 6.200 | – |
| Coefficients | | | | | | | | | |
| $a_1$ | | 1.3525 | −1.2219 | −1.1000 | −0.5484 | −0.6000 | −1.0156 | −1.0000 | −1.0500 |
| $a_2$ | | −0.2576 | −0.7730 | −0.2515 | −0.6654 | −0.3566 | −0.3670 | 0.0211 | 0.0289 |
| $a_3$ | | −0.2690 | 1.4148 | 0.8952 | −0.2672 | −2.5000 | 1.0078 | 0.5025 | 0.4260 |
| $a_4$ | | −1.4366 | 1.1016 | 0.0156 | 0.7117 | 2.3250 | 1.4051 | −0.5119 | 0.3590 |
| $b_1$ | | −0.7670 | −0.2054 | 0.2782 | 0.7234 | 0.2937 | 0.2875 | −0.3000 | −0.3250 |
| $b_2$ | | 0.0007 | 0.0367 | −0.1812 | −0.6219 | 0.0496 | −0.5328 | 0.1922 | 0.1156 |
| $b_3$ | | 1.2734 | −3.9128 | −4.5000 | −5.6812 | −5.6812 | −3.8500 | 0.7023 | 0.7781 |
| $b_4$ | | −0.1233 | 0.9156 | 1.1766 | 2.6297 | 1.8415 | 3.3750 | −1.6317 | 0.0025 |
| $c_1$ | | 2.8000 | 6.9750 | 24.7219 | 33.3389 | 21.0000 | 14.0000 | 19.0000 | 31.0625 |
| $c_2$ | | 0.6004 | 0.1774 | −13.0812 | −18.3000 | −4.7656 | −0.9999 | −5.0000 | −14.5000 |
| $c_3$ | | 1.2375 | 6.4477 | −37.7000 | −62.2500 | −21.5906 | −7.1406 | 1.2438 | −46.1148 |
| $c_4$ | | 1.0000 | −0.1239 | 34.8438 | 52.0781 | 7.2492 | 7.5469 | −1.9094 | 55.3750 |
| $d_1$ | | 1.8734 | −1.5798 | −5.0000 | −3.5000 | −3.5000 | −3.4000 | −4.0000 | −7.2312 |
| $d_2$ | | 0.6297 | −0.5081 | 1.5218 | 0.0016 | −0.1554 | −0.1078 | 0.0250 | 0.4050 |
| $d_3$ | | 0.9738 | −1.7812 | 3.9229 | 1.1477 | 1.4062 | −1.0750 | 0.3844 | 13.3500 |
| $d_4$ | | 0.2809 | 0.1080 | −2.6204 | 0.1062 | 0.3988 | 1.5702 | 0.2656 | 0.6234 |
| $e_1$ | | 0.0356 | 0.2624 | −0.0156 | 0.4659 | 0.0032 | −0.0672 | 1.0468 | 1.5000 |
| $e_2$ | | −0.1246 | 0.0672 | 0.1597 | −0.3296 | 0.0766 | 0.4016 | −0.3788 | −0.6426 |
| $e_3$ | | −0.5718 | −0.2190 | 0.4199 | −0.0876 | −0.0656 | 0.3017 | −2.4517 | 1.8564 |
| $e_4$ | | 0.9938 | −0.4285 | −0.5562 | −0.0329 | −0.1294 | −0.4844 | 1.4656 | 0.5636 |

**Table 3.4.** *Model coefficients for the Perez all-weather model*

The terms $a_i(\varepsilon)$ are a discrete function of the parameter $\varepsilon$ represented by eight-term vectors corresponding to each $\varepsilon$ interval. Values of parameters $a_i(\varepsilon)$ are listed in Table 3.4. For the calculation of distribution parameter $b_p$, the parameters $b_i(\varepsilon)$ should be used.

Among all the cases, there are only two exceptions. Those two exceptions are stated for the parameters $c_p$ and $d_p$ in the first $\varepsilon$ interval (1.000–1.065). In this interval, the following two equations should be used for the calculation of $c_p$ and $d_p$:

$$c_p = \exp\left[\left(\Delta\left(c_1 + c_2 \cdot Z_S\right)\right)^{c_3}\right] - c_4 \quad [3.16]$$

$$d_p = \exp\left[\Delta\left(d_1 + d_2 \cdot Z_S\right)\right] + d_3 - \Delta d_4 \quad [3.17]$$

### 3.5. ASRC–CIE model

The ASRC–CIE model was developed by Perez *et al.* [PER 92] who modified Matsuzawa's model to take into account the high turbid intermediate skies. This model is defined as a linear combination of four other sky models: the CIE or Kittler clear sky model, the Gusev turbid clear sky model, the intermediate sky model, and the CIE overcast sky model [PER 90]. The coefficients of linear combination are computed using the sky clearness and the sky brightness factors [PER 92, DUM 03].

For $\varepsilon \leq 1.2$:

$$\frac{L}{L_Z} = (1-a)\left(\frac{L}{L_z}\right)_{\text{CIE}-\text{Overcast}} + a\left(\frac{L}{L_z}\right)_{\text{Intermediate}} \quad [3.18]$$

where $a = \min\left\{1, \max\left[0, \frac{\varepsilon - 1}{0.2}, \frac{\Delta - 0.05}{0.4}\right]\right\}$ [3.19]

For $1.2 < \varepsilon \leq 3.0$:

$$\frac{L}{L_Z} = (1-b)\left(\frac{L}{L_z}\right)_{\text{Intermediate}} + b\left(\frac{L}{L_z}\right)_{\text{Clear}-\text{Gusev}} \quad [3.20]$$

where $b = \frac{\varepsilon - 1.2}{1.8}$ [3.21]

For $3.0 < \varepsilon$:

$$\frac{L}{L_Z} = (1-c)\left(\frac{L}{L_z}\right)_{\text{Clear}-\text{Gusev}} + c\left(\frac{L}{L_z}\right)_{\text{Clear}-\text{Kittler}} \quad [3.22]$$

where $c = \min\left\{1, \frac{\varepsilon - 3}{3}\right\}$ [3.23]

Both the parameters for sky clearness, $\varepsilon$, and sky brightness, $\Delta$, are calculated in the same way as described in the previous section on the Perez all-weather model.

### 3.6. Igawa all-sky model

The Igawa all-sky model is the most recent model and it was introduced in 2004 on the basis of previous models for sky luminance and radiance from Matsuzawa, Igawa, and Nakamura. This model was tested on IDMP data for Tokyo and Fukuoka [IGA 04].

To be able to calculate the sky luminance with the help of this model as well as with some other described models, we need to know at least global irradiance, extraterrestrial direct normal irradiance, and horizontal diffuse irradiance. These values can be obtained from IDMP or any other weather station. Data for the zenith angle of the Sun are also needed for the purpose of calculation. Similar to other models, we have two parameters in this model as well which describe the atmospheric conditions. The first parameter is the so-called clear sky index $K_c$, which is defined by the following equation:

$$K_C = \frac{E_{eg}}{S_{eeg}} \quad [3.24]$$

where:

$K_C$ clear sky index,

$E_{eg}$ global irradiance,

$S_{eeg}$ standard global irradiance.

Standard global irradiance from equation [3.24] is a global irradiance of clear sky with turbidity (TL) of 2.5, and can therefore be defined using the following equation:

$$S_{eeg} = \frac{0.84 \cdot E_{e0}}{m} \cdot \exp(-0.0675 \cdot m) \quad [3.25]$$

where:

$E_{e0}$ extraterrestrial direct normal irradiance,

$m$ relative optical mass.

The relative optical mass depends on solar zenith angle ($Z_s$) and can be calculated using equation [3.14].

The second parameter of the Igawa all-sky model is the cloudless index. The cloudless index is defined with the help of cloud ratio and standard cloud ratio using the following equation:

$$C_{le} = \frac{1 - C_e}{1 - C_{es}} \quad [3.26]$$

where:

$C_{le}$ cloudless index,

$C_e$ cloud ratio,

$C_{es}$ standard cloud ratio.

Cloud ratio is the ratio between the horizontal diffuse irradiance and global irradiance as shown in equation [3.27]. The lower bound values of the cloud ratio appear in the clear sky and depend on the solar altitude.

$$C_e = \frac{E_{ed}}{E_{eg}} \quad [3.27]$$

where:

$E_{ed}$ horizontal diffuse irradiance,

$E_{eg}$ global irradiance.

The second factor in the equation for cloudless index is the standard cloud ratio, which is a cloud ratio with a TL of 2.5 and can be calculated with the help of the following equation:

$$C_{es} = 0.01299 + 0.07698 \cdot m - 0.003857 \cdot m^2 + 0.0001054 \cdot m^3 - 0.000001031 \cdot m^4 \quad [3.28]$$

Using these two parameters – clear sky index ($K_c$) and cloudless index ($C_{le}$) – the sky conditions are defined in such a way that for the calculation of sky luminance distribution, the following equation can be used along with the CIE standard general sky model:

$$L_{a-rel} = \frac{L_\alpha}{L_Z} = \frac{f(\chi) \cdot \varphi(Z)}{f(Z_S) \cdot \varphi(0)} \quad [3.29]$$

with gradation and indicatrix functions defined as

$$\varphi(Z) = 1 + a' \cdot \exp\left(\frac{b'}{\cos Z}\right) \quad [3.30]$$

$$f(\chi) = 1 + c' \cdot \left[\exp(d'\chi) - \exp(d'\frac{\pi}{2})\right] + e' \cdot \cos^2 \chi \quad [3.31]$$

The difference between the CIE standard general sky model and the Igawa all-sky model is in defining the parameters used for the calculation of gradation and indicatrix functions. With the CIE model, the parameters used ($a$, $b$, $c$, $d$, and $e$) are defined in a table and depend on the chosen sky type. Igawa *et al.* [IGA 04] proposed an approximation method for the determination of these coefficients ($a'$, $b'$, $c'$, $d'$, and $e'$), which can be calculated as functions of the sky index ($Si$) using the following equations:

$$a' = \frac{4.5}{1 + 0.15 \cdot \exp(3.4 \cdot Si)} - 1.04$$

$$b' = \frac{-1}{1 + 0.17 \cdot \exp(1.3 \cdot Si)} - 0.05$$

$$c' = 1.77 \cdot (1.22 \cdot Si)^{3.56} \cdot \exp(0.2 \cdot Si) \cdot (2.1 - Si)^{0.8} \quad [3.32]$$

$$d' = \frac{-3.05}{1 + 10.6 \cdot \exp(-3.4 \cdot Si)}$$

$$e' = \frac{0.48}{1 + 245 \cdot \exp(-4.13 \cdot Si)}$$

where:

*Si* sky index

Here, the sky index is defined as the sum of the clear sky index and the root of the cloudless index:

$$Si = K_C + C_{le}^{0.5} \quad [3.33]$$

Sky index *Si* can also be used for defining five basic sky types:

– overcast sky if *Si* is lower than 0.3,

– nearly overcast sky when *Si* is between 0.3 and 0.6,

– intermediate sky for *Si* between 0.6 and 1.5,

– nearly clear sky if *Si* runs from 1.5 to 1.7,

– clear sky if *Si* is more than 1.7.

### 3.7. Absolute luminance

All the above-described sky luminance distribution models define a luminance of an arbitrary sky element in a relative way as a portion of zenith luminance. If we want to calculate the absolute luminance of a sky element or absolute sky luminance distribution, the zenith luminance first needs to be measured or calculated.

Zenith luminance can be calculated in different ways. In 1998, Kittler *et al*. [KIT 98] published the formulation of zenith luminance defined with equation 3.34, which is valid for solar altitude under 700. Typical ratios between diffuse horizontal illuminance ($D_V$) and horizontal extraterrestrial illuminance ($E_v$) and auxiliary parameters are listed in Table 3.5. Other methods can be found in [KIT 12].

$$L_Z = \frac{D_V}{E_V}\left[\frac{B(\cos Z_S)^C}{(\sin Z_S)^D} + E\cos Z_S\right] \quad [3.34]$$

| Sky type | Typical $D_v/E_v$ | B | C | D | E |
|---|---|---|---|---|---|
| 1 | 0.10 | 54.63 | 1.00 | 0.00 | 0.00 |
| 2 | 0.18 | 12.35 | 3.68 | 0.59 | 50.47 |
| 3 | 0.15 | 48.30 | 1.00 | 0.00 | 0.00 |
| 4 | 0.22 | 12.23 | 3.57 | 0.57 | 44.27 |
| 5 | 0.20 | 42.59 | 1.00 | 0.00 | 0.00 |
| 6 | 0.38 | 11.84 | 3.53 | 0.55 | 38.78 |
| 7 | 0.42 | 21.72 | 4.52 | 0.64 | 34.56 |
| 8 | 0.41 | 29.35 | 4.94 | 0.70 | 30.41 |
| 9 | 0.40 | 10.34 | 3.45 | 0.50 | 27.47 |
| 10 | 0.36 | 18.41 | 4.27 | 0.63 | 24.04 |
| 11 | 0.23 | 24.41 | 4.60 | 0.72 | 20.76 |
| 12 | 0.15 | 23.00 | 4.43 | 0.74 | 18.52 |
| 13 | 0.28 | 27.45 | 4.61 | 0.76 | 16.59 |
| 14 | 0.28 | 25.54 | 4.40 | 0.79 | 14.56 |
| 15 | 0.30 | 28.08 | 4.13 | 0.79 | 13.00 |

**Table 3.5.** *Auxiliary parameters for calculating absolute zenith luminance LvZ for standard sky types*

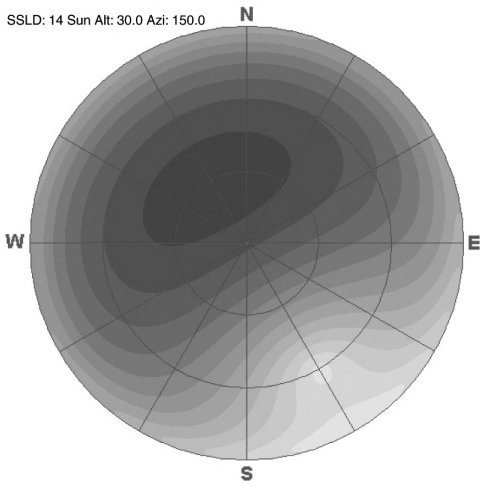


**Figure 3.4.** *Sky luminance distribution created with SunModeller*

### 3.8. Visualization

Realistic visualizations of sky luminance distribution patterns are nowadays easy to create with numerous programs. Some of them are already published as freeware tools on the Internet. The easiest tool to use is a SkyModeller by Roy, an online tool available at http://www.cadplan.com.au/. SkyModeller uses the CIE standard general sky model so that the user needs to choose one of the 15 sky types together with Sun altitude and Sun azimuth.

Another, more sophisticated but still free program tool available on the Internet is HOLIGILM (http://www.holigilm.info), created by Kundracik and Kocifaj. This program also uses CIE standard general sky models for the calculation of sky luminances. The "plus" with this software is that it can be used not only to create realistic sky luminance distributions but also to calculate illuminance in indoor premises, if the premises are lighted with hollow light guides.

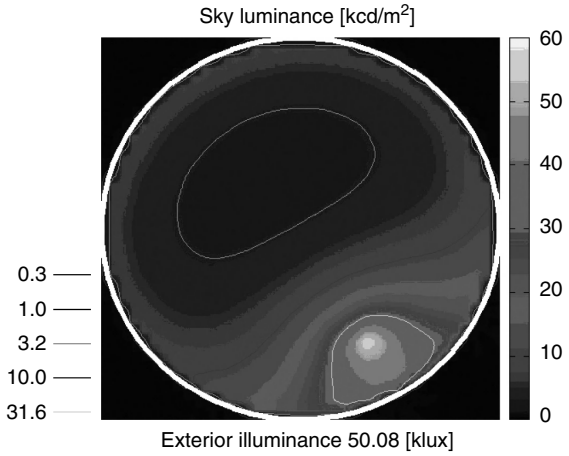


**Figure 3.5.** *Sky luminance distribution created with Holigilm*

Another software tool based on the CIE standard general sky model is Velux Daylight Visualizer, which is the latest version of the software tool being used. The calculations that are made in this program also use formulas from the CIE standard general sky model and 15 different ISO/CIE sky types.

### 3.9. Conclusion

When coming to practical applications, there is always a question about the type of sky model to be used. Unfortunately, the answer is not easy. There are many

elements that influence the choice of the model. Among them are the available data and the task for which the model will probably be used for in the first place. After choosing the sky luminance model, the user also needs to choose the right sky type or the right parameters for the model. The weather changes practically at all locations around the world and so do sky types. The choice would be easier if there were a table with frequencies of occurrences of, e.g. CIE, sky types, for instance, for major world cities. Unfortunately, a table like this does not exist (yet) and so it is the user's responsibility to decide on the model and sky type to be used.

Practical experiences show that each model has its own limitations. For example, the Perez model cannot predict densely overcast skies very well. On the other hand, Kittler's formulation of sky luminance distribution used in the ISO/CIE standardized general sky model covers 15 different sky types from cloudy to clear skies, which can be successfully used to practically model all-sky luminance distribution situations all over the world. Hence, this is one of the major advantages of CIE sky models over other models.

Thus, the authors encourage prospective users to try different models for their application and compare the obtained results with the measurements whenever possible. In this way, the model that will give the most realistic results in given situation can be discovered.

### 3.10. Bibliography

[BOL 35] BOLDYREV N.G., "O raspredeleniyi jarkosti po nebu (About the distribution of luminance on sky)", *Svetotekhnka*, vol. 6, pp. 16–18, 1935.

[CIE 55] CIE – Commission Internationale de l'Eclairage: Natural Daylight, Official recommendation. Compte Rendu CIE 13th Session, 2, part 3.2, 2–4, 1955.

[CIE 73] CIE, Standardization of luminance distribution on clear skies, Publication CIE No. 22, 1973.

[CIE 96] ISO 15469/CIE S003, Spatial distribution of daylight – CIE standard overcast and clear sky, 1996.

[CIE 03] CIE DS 011.1/E:2003 Spatial distribution of daylight – CIE standard general sky, Standard, CIE Central Bureau, Vienna, 2003.

[DUM 03] DUMORTIER, D., VAN ROY F., "Daylighting information throughout Europe from the SATEL-LIGHT and SODA Internet servers", *CIE 25th Conference*, San Diego, vol. 1, D3-4, 2003

[IGA 04] IGAWA N., KOGA Y., MATSUZAWA T., NAKAMURA H., "Models of sky radiance distribution and sky luminance distribution", *Solar Energy*, vol. 77, no. 4, pp. 137–157, 2004.

[KAE 08] KAEHLER K., "Flächenhelligkeit des Himmels und Beleuchtungsstärke in Raumen", *Meteorologische Zeitschrift*, vol. 25, no. 2, pp. 52–57, 1908.

[KAS 89] KASTEN F., YOUNG A.T., "Revised optical air mass tables and approximation formula", *Applied Optics*, vol. 28, no. 22, pp. 4735–4738, 1989.

[KIM 21] KIMBALL H., HAND I.F., "Sky brightness and daylight illumination measurements", *Monthly Weather Review*, vol. 49, no. 9, pp. 481–488, 1921.

[KIT 67] KITTLER R., "Standardisation of the outdoor conditions for the calculation of the daylight factor with clear skies", *Proceedings of the Conference on Sunlight in Buildings*, Bouwcentrum, Rotterdam, pp. 273–286, 1967.

[KIT 98] KITTLER R., DARULA S., PEREZ R., A set of standard skies, characterizing daylight conditions for computer and energy conscious design, American-Slovak grant project, US-SK 92 052, Polygrafia SAV, Bratislava,1998.

[KIT 12] KITTLER R., KOCIFAJ M., DARULA S., *Daylight Science and Daylighting Technology*, Springer, 2012.

[KRA 43] KRAT V.A., "Indikatrisa rasseyaniya sveta v zemnoj atmosfere (Indicatrix of light diffusion in earth atmosphere)", *Astronomical Journal*, vol. 20, pp. 5–6, 1943.

[MOO 42] MOON P., SPENCER D.E., "Illumination from a nonuniform sky", *Illuminating Engineering (N.Y.)*, vol. 37, pp. 707–726, 1942.

[PER 90] PEREZ R., INEICHEN P., SEALS R., MICHALSKY J., STEWART R., "Modeling daylight availability and irradiance components from direct and global irradiance", *Solar Energy*, vol. 44, no. 5, pp. 271–289, 1990.

[PER 92] PEREZ R., MICHALSKY J., SEALS R., "Modelling sky luminance angular distribution for real sky conditions. Expiremental evaluation of existing algorithms", *Journal of Illuminating Engineering Society*, vol. 21, no. 2, pp. 84–92, 1992.

[PER 93] PEREZ R., SEALS R., MICHALSKY J., "All Weather Model for sky luminance distribution – preliminary configuration and validation", *Solar Energy*, vol. 50, no. 3, pp. 234–245, 1993.

[POK 29] POKROWSKI G.I., "Über die Helligkeitsverteilung am Himmel", *Physikalische Zeitschrift*, vol. 30, no. 20, pp. 697–700, 1929.

[SCH 01] SCHRAMM W., "Über die Verteilung des Lichtes in der Atmosphäre", *Schriften d. Naturw.Veriens f. Schl.-Holst*., vol. 12, no. 1, pp. 81–129, 1901.

# Chapter 4

# Satellite Images Applied to Surface Solar Radiation Estimation

## 4.1. The solar resource

*Surface solar irradiance* (SSI) is a measure of solar radiation at the surface of the Earth. More precisely, it is defined as the amount of solar incident energy per unit of time, per unit of area detected on a horizontal surface at ground level. Its unit in the International System is the Watt per square meter (W $m^{-2}$). In August 2010, SSI was identified as an essential climate variable by the Global Climate Observing System, meaning that it is a parameter of key importance for understanding and monitoring the global climate system. In addition to such climatological applications, SSI is of great interest in domains as varied as solar energy, health, architecture, agriculture, and forestry [BLA 11c].

The integration in time of the SSI yields another quantity related to the solar resource, named the *irradiation*. It can be defined as the incident energy flux, i.e. the received energy per area. Its unit in the International System is the Joule per square meter (J $m^{-2}$) though other units such as the Watt-hour per square meter[1] (Wh $m^{-2}$) are widely used. Conversely, from an irradiation data series, the irradiance values may be deduced by convention by dividing by the number of seconds of the period of integration. For example, from daily irradiation values, the daily mean of irradiance is derived by dividing by the number of seconds in a day, including the night period, i.e. 86,400 s. As there is a correspondence between irradiance (solar

---

Chapter written by Bella ESPINAR and Philippe BLANC.

1 The relation between these two units is 1 Wh $m^{-2}$ = 3,600 J $m^{-2}$.

*Solar Energy at Urban Scale* Benoit Beckers

power flux) and irradiation (solar energy flux), it is usual to use the term *radiation* for the sake of conciseness.

The solar resource is the energy source most abundant and the most distributed over the Earth's surface. However, the spatial distribution is not homogeneous either latitudinally or longitudinally on the Earth's surface. Figure 4.1 illustrates this spatial heterogeneity at the worldwide scale. This heterogeneity also exists at a finer scale as discussed later. The spatial distribution is also temporally variable, since it depends on the hour of the day, the day of the year, and on the atmospheric conditions, which are highly variable in time.

Several ways for the exploitation of the solar resource exist. Photovoltaic solar plants directly transform the solar radiation into electricity. Concentrated solar power plants (CSPs) convert solar radiation into heat. Chemical use of the solar energy is also documented in current research, for biomass energy generation, detoxification of water, desalinization of seawater, or generation of hydrogen by hydrolysis. Solar radiation is a very important energy resource and these examples demonstrate the interest in its accurate knowledge, monitoring, and forecast.

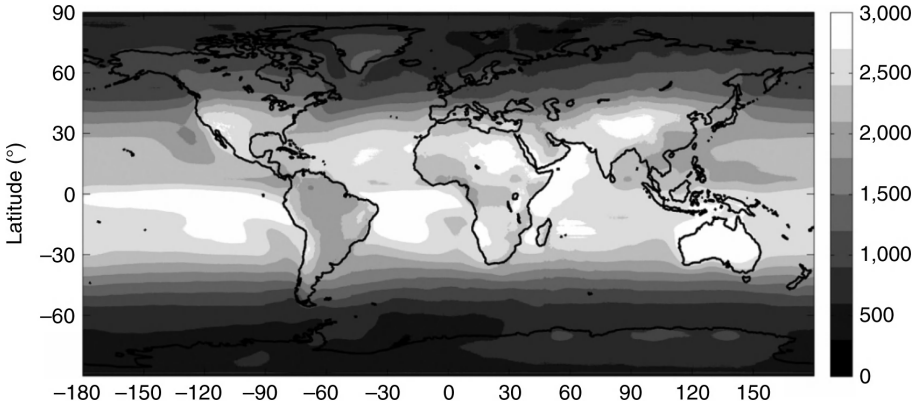


**Figure 4.1.** *Spatial distribution of the annual sum of irradiation, in kWh m$^{-2}$. The figure illustrates the worldwide spatial variability of the solar resource (© MINES ParisTech, 2006)*

The solar radiation emitted by the Sun that reaches the top of the atmosphere has not been attenuated by any process with the exception of the attenuation of the intensity with the square of the distance between the Sun and the Earth. When the solar radiation passes through the atmosphere, several interactions take place (Figure 4.2). A portion is scattered by the molecules and the aerosols of the atmosphere, which causes the *diffuse* component of the incident solar radiation on the Earth's surface; part of this portion is backscattered to space, reflected by clouds

or by the ground. A small portion of the incident solar radiation is absorbed by the components of the atmosphere. Finally, a portion reaches the Earth's surface in the same direction of the original one, i.e. from the Sun, which constitutes the *direct* component of the solar radiation incident on the Earth's surface [WAL 07].

The radiation reaching the ground interacts with the Earth's surface: a part of this radiation is absorbed by the ground, while the remainder is again reflected toward atmosphere and space, throwing up once again the atmosphere and interacting with it once again by reflection, absorption, and scattering processes, on the way up.

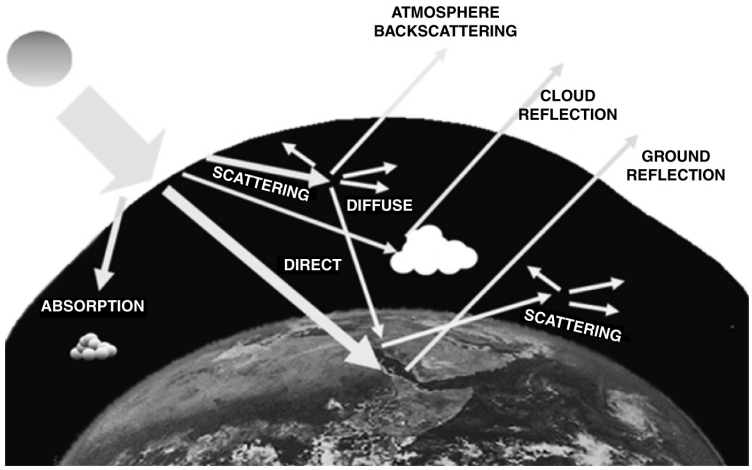


**Figure 4.2.** *Interaction of solar radiation with the atmosphere (Courtesy of J. Polo, 2009)*

SSI incident on a tilted plane, whose orientation is defined by the azimuth $\alpha$ and slope or tilt angle $\beta$, is divided into four components. The irradiance impinging on the tilted plane, coming from the direction of the Sun, is named the *beam-tilted irradiance* (BTI). The irradiance coming from the whole sky except from the Sun's direction is named the *diffuse-tilted irradiance* (DTI). The component reflected by the ground is named the *reflected-tilted irradiance* (RTI). Finally, the sum of these three components compounds the *global-tilted irradiance* (GTI), as:

$$\mathrm{GTI}(\alpha,\beta) = \mathrm{BTI}(\alpha,\beta) + \mathrm{DTI}(\alpha,\beta) + \mathrm{RTI}(\alpha,\beta) \quad [4.1]$$

For a horizontal plane, the *global horizontal irradiance* (GHI) is composed of the *beam horizontal irradiance* (BHI) and the *diffuse horizontal irradiance* (DHI). If the ground is flat, with no obstacle at horizon, there is no reflected component:

$$\mathrm{GHI} = \mathrm{BHI} + \mathrm{DHI} \quad [4.2]$$

## 4.2. Ground measurements of the solar resource

The assessment of solar resource needs continuous and densely distributed observations because solar radiation is very variable both in time and in space. Variations due to the alternation of days and nights or seasonal variability aside, solar radiation is time- and space-dependent due to its interactions with the atmospheric components. The composition and the optical properties of the atmosphere are not constant in time. For example, clouds have a very dynamic evolution and influence the solar radiation.

### 4.2.1. *Ground instruments*

One way to measure the incident solar radiation is setting up dedicated ground stations on the Earth's surface. Various measurements related to SSI can be made: cloud coverage, sunshine duration, GHI, direct or diffuse irradiance, spectral distribution of the irradiance, etc.

Pyranometers measure the GHI when they are exposed to the Sun. For measuring the DHI, the pyranometric sensor must be shaded to prevent the direct component reaching the sensor, but this shading mechanism should hide the minimum of sky outside the small solid angle sustained by the Sun's disk, to receive the maximum diffuse irradiance from the whole sky dome. Figures 4.3 and 4.4 show some examples of pyranometers dedicated to the measurements of GHI and DHI.

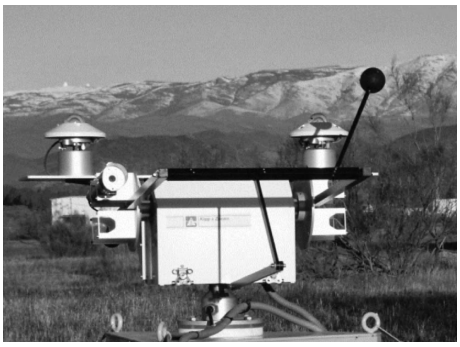

**Figure 4.3.** *Two identical pyranometers, one for measuring GHI (on the left) and the other one shaded by a shadow-ball for measuring DHI (on the right). They are arranged in a sun-tracker to follow the apparent Sun path on the sky (Courtesy of V. Quaschning, 2012 © www.volker-quaschning.de)*

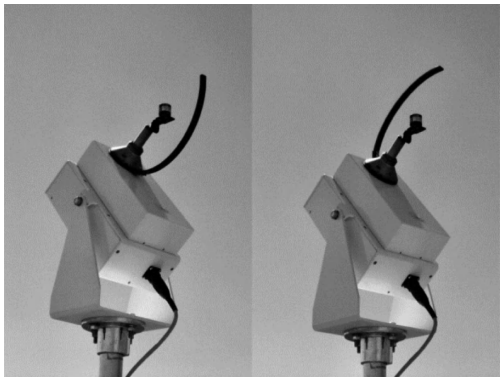

**Figure 4.4.** *Pyranometer with a rotating shadow band. This pyranometer measures GHI while the shadow band is underneath, on the left, and DHI when the shadow band intercepts the beam component, on the right (Courtesy of V. Quaschning, 2012 © www.volker-quaschning.de)*

The instrument used for measuring the beam irradiance is the pyrheliometer. It measures the beam normal irradiance (BNI) as it is always aimed toward the Sun's direction owing to a sun-tracker (Figure 4.5).

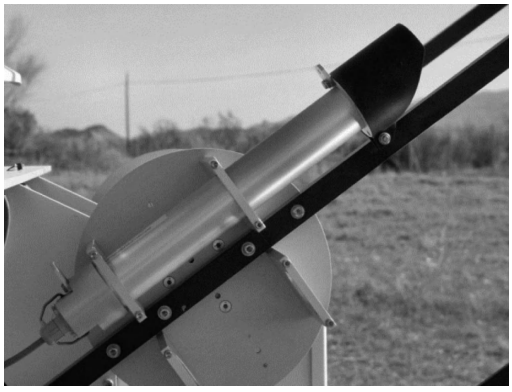

**Figure 4.5.** *The pyrheliometer measures BNI. It is always mounted on a sun-tracker to follow the apparent Sun path in the sky (Courtesy of V. Quaschning, 2012 © www.volker-quaschning.de)*

The instrumentation for measuring the solar radiation on the Earth's surface has been improved along the years, allowing locally accurate measurements. According to Zelenka *et al.* [ZEL 99], the accuracy of hourly SSI average time series from well-maintained ground stations is estimated within the 3–5% range in terms of

relative *root mean square error* (RMSE) [ISO 95]. In this regard, ground stations are currently able to monitor the temporal variation of solar radiation in a proper time resolution.

Well-maintained stations require extensive and constraining procedures for checking the quality of recorded data. Sources of uncertainty in meteorological data are of very different nature. Radiation sensors can be affected by incorrect sensor leveling or shading caused by near building structures or complete or partial shade misalignment in the case of shaded measurements (as for DHI). Other sources that affect all types of measurements are dust, snow, dew, water droplets, bird droppings, an electrical field in the vicinity of cables, mechanical loading on cables and station shutdown, or maintenance mishandling.

Data provided by ground stations must have a known and reasonable quality that guarantees their suitability for scientific research. To control their quality, data are submitted to several checks to detect non-plausible values. Further information about quality control of radiometrical and meteorological measures from ground stations can be found in [ESP 11].

### 4.2.2. *The spatial variability of solar radiation*

Spatial distribution of solar radiation is neither uniform nor homogeneous. Therefore, the geographical representativeness of punctual measures from ground stations is not only dependent on the good maintenance or on the excellence of the measuring devices. The intrinsic variability of the solar radiation is very important. Perez *et al.* [PER 97] and Zelenka *et al.* [ZEL 99] have observed the local variability of the solar radiation using measurements made by well-calibrated ground stations close to each other. They demonstrate that this variability cannot be ignored. Moreover, they found that the variability itself is highly variable from one region to another. Expressing it as the ratio of the variance relative to the mean value over the area, they found typical variability in hourly irradiation of 17% for an area of 10 km in radius. This means that within a 10 × 10 km² area and a given hour, the hourly irradiance measured by a series of similar inter-calibrated sensors would differ with a relative variance equal to 17%. The variability increases as the surface of the area increases. For example, it typically reaches 25% for a radius of 30 km. It decreases as the time integration increases. For example, it is down to 10% for daily values and a radius of 10 km [HOY 10].

In a given location with no ground station, one way to estimate the value of one particular component of solar radiation (GHI, BNI, or DHI) is to apply some existent procedures of interpolation and/or extrapolation of measures registered by the nearest stations.

Several authors [HAY 81, WMO 81, HAY 84, HAY 85, ZEL 92, PER 97] have studied the extrapolation and interpolation inaccuracies due to the spatial variability of SSI discussed earlier, as a function of the distance to the measuring stations. The results are very similar for both cases. The accuracy of the estimation decreases while the distance between the station and the location of interest increases. In terms of relative RSME normalized to the mean value, the inaccuracy for global daily irradiation ranges from 10% to 40% for distances ranging from 16 to 256 km. For the global hourly irradiation, the inaccuracy is worse, with a relative RMSE from 15% to 45% for the same distances. Furthermore, the result is less reliable if topography between both localizations is rather complex, inducing local meteorological and shadowing effects.

Estimating spatial distribution of solar radiation by interpolation/extrapolation techniques is possible, but it must be kept in mind that it leads to large inaccuracies because of the spatial variability. One possibility, to avoid this problem, is the installation of numerous networks including a large number of ground stations, but it is very expensive and, overall, very difficult for maintenance, a non-negligible aspect. It is also important to keep in mind the intrinsic limitation of these techniques because they may be unable to reproduce variability smaller than twice the average distance between stations. Finally, it should be noted that a deficient station, due to lack of maintenance and/or insufficient calibration schedule, might strongly affect the result of a spatial interpolation.

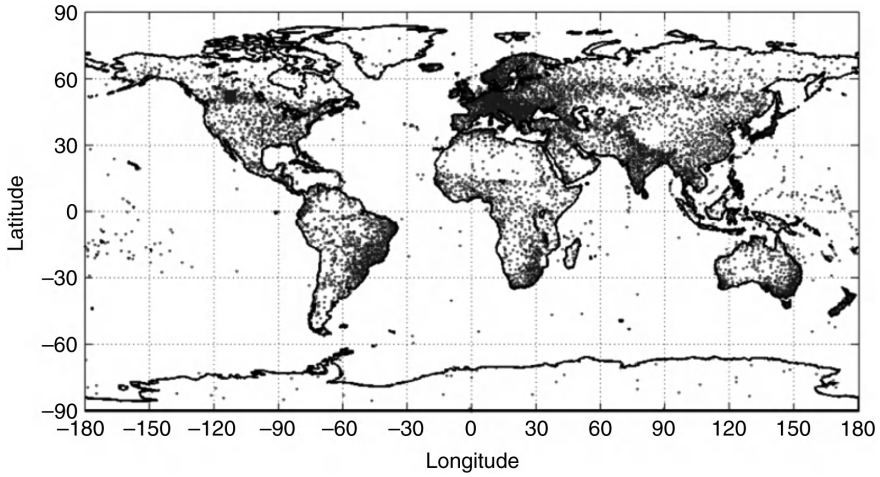


**Figure 4.6.** *Spatial distribution of international networks of meteorological ground stations. The total number of stations is approximately 11,000. The spatial distribution is heterogeneous: much more dense in Europe, more sparse in Asia and America, very dispersed in Africa, and very few in the oceans [WMO 11]*

Therefore, the existent ground stations are insufficient in number. In addition, the geographical distribution of ground stations is heterogeneously distributed in the space (Figure 4.6). There are large areas without any ground station. For comparison, in Western Europe and Northern America, the average distance between stations is approximately 100 km, while in Eastern Europe, it is approximately 500 km and is approximately 1,000 km in Africa [RIG 01]. Over the oceans, the number of stations is very low.

The ground stations are revealed as insufficient to assess, with enough spatial representativity, the spatial variability of the solar resource over large areas.

### 4.3. Satellite images for SSI estimation

In opposition to the spot measurements provided by a ground station are the images from meteorological *geostationary* satellites. These satellites always remain over the same geographical point, following the Earth's rotation. One of the strengths of using such images is the fact that it is possible to scan in an overlapping way, and several times per hour, very large areas, thus capturing the spatial and temporal distribution of the information. In this sense, satellite images represent a source of information of great spatial and temporal density that largely corresponds to the needs for continuous observations of cloud cover evolution and which is not attainable with a network of ground stations.

Satellite images are composed of *digital counts* (DCs), one per pixel and spectral band. DCs are linearly dependent on the energy reflected by the ensemble of atmosphere and the Earth's surface that reaches the satellite sensor. This energy flux is named the *radiance*, *L*. Figure 4.7 is an example of a satellite image from the Meteosat geostationary satellite in the visible channel. The image covers Europe, Africa, the Atlantic Ocean, and part of South America. Radiance increases from black to white. Sea areas are perceived as black zones, while ground is clearly recognizable in gray. Clouds are perceived as white marks. Black sea-areas are under clear sky conditions. Nevertheless, ground gray-areas are also under clear sky conditions. The reason is that radiance received by the satellite sensor from the ground is greater than radiance from the sea even though both were under clear sky conditions. This is because the ground has a Lambertian reflection behavior, while the sea has a specular reflection behavior.

Satellite images are the completion of information in space since their field of view covers large geographical areas. They cover areas between stations, where no actual *in situ* information is available. Satellite images constitute as well the complementary information source for the periods of failure of ground stations.

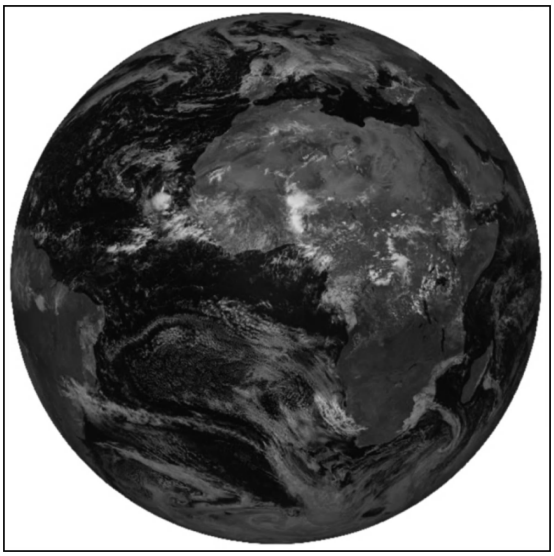

**Figure 4.7.** *Example of a Meteosat image in the visible channel, taken on September 7, 2010, at noon (1200 UTC). Radiance increases from black-to-white. The area scanned by geostationary satellites is approximately one-third of the Earth's surface (© Eumetsat, 2010)*

The aforementioned study carried out by Perez *et al.* [PER 97] and Zelenka *et al.* [ZEL 99] may have another interpretation. They determined the confidence level in the SSI estimation from satellite images at approximately 20%, in terms of RSME, using a simple model available at this time. They proved that there is a threshold distance from the geographical point of interest from which the accuracy of the estimation is better using satellite images than extrapolation techniques applied with data from the nearest ground station. This threshold distance is 50 km for daily GHI and it is reduced as the average time decreases; therefore, for hourly values this threshold is approximately 30 km. The density of ground stations in Europe, one of the greatest in the world, can be set as one station for 100 km since the spatial resolution of a satellite image ranges typically from 3 to 12 km, depending on the latitude (because of the effect of the Earth's curvature). In Figure 4.8, the average RSME obtained after comparing daily measures of GHI between couples of stations in the region of Provence-Alpes-Côte d'Azur, south of France, is shown. Similar trends to those shown in Figure 4.8 are found for other geographical areas, as in North America and Switzerland [ZEL 99].

Therefore, the use of geostationary satellite images for purposes of solar radiation estimation is accepted as a very useful tool as they allow monitoring in an adequate resolution of both the spatial and the temporal variability of the SSI.

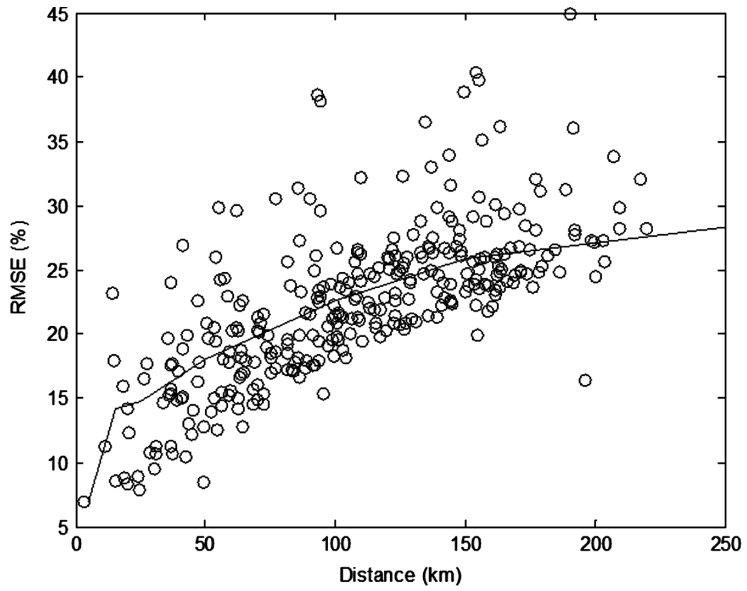


**Figure 4.8.** *In this figure, circles are the average RMSE obtained after comparing the measured daily GHI from a couple of stations in the south of France. The x-axis is the distance between the stations. The solid line is the average of the RMSE for each distance between stations [BLA 11a]. The variability observed on the worldwide scale (Figure 4.1) is also observed in the scale of the kilometers*

It should be noted that there are other types of meteorological satellites apart from geostationary satellites. *Polar* satellites describe circular orbits around the Earth passing over the poles and perpendicularly to the equator plane. They scan in each orbit different areas than from the previous orbit. This fact implies that they scan a given geographic area at the Earth's equator with time laps that range from several hours to several days, depending on the revolution period, the orbit radius of the satellite, and the maneuverability capacity of the spaceborne imaging system. The attainable spatial resolution of these images, which may reach the sub-metric scale, is also in relation to these orbit parameters. For purposes of solar resource assessment, information from a polar satellite may contribute to solar spatial and temporal distribution by the way of data assimilation processes with numeric meteorological models and analysis maps, in conjunction with conventional observations. The Model of Atmospheric Transport and Chemistry (MATCH) [ROB 96, ROB 99] or the European Centre for Medium-Range Weather Forecast (ECMWF) uses information from such type of satellites.

The rough temporal resolution for a given location restrains the use of polar satellites for studying phenomena whose characteristic time of variability is smaller than their revisiting period, like the cloud cover evolution. Therefore, the information from polar satellite images for solar radiation estimation is limited as well. This chapter deals with geostationary satellite images alone, since they capture the temporal and spatial evolution of the state of the atmosphere in a suitable resolution, as discussed earlier.

The generation of satellite images is a complex procedure. The recording of a satellite image requires the combination of a variety of mechanical, optical, and electrical components that are prone to unpredictable and unsystematic performances: a margin of tolerance is permitted regarding the satellite's position; in addition, during the time the image is being scanned, the satellite may roll, pitch, and/or yaw at the same time that the Earth is moving underneath. As a consequence, the raw images are geometrically distorted in an unexpected way. In addition, during the acquisition and its transmission to Earth, reception, and treatment by the data collection system, the signal may be subjected to random disturbances that may degrade radiometrically the quality of the image. Image distortions are usually corrected before their dissemination.

Geometric distortions are the observed deformations from the nominal image due to the aforementioned facts, which induce changes in the perspective of the image. It means that the radiance received for one pixel in one image is not exactly the same radiance than from the same area as in the previous image. Geometric distortions are corrected by means of the calculation of distortion vectors, which allow the resample of the image.

Radiometric distortions result in practice in striping and scan line dropout in the image. They are due to the sensor itself, which may have momentary power losses, calibration failures, and random noise, or also occur the transmission processes. Their correction is done by interpolation of missing pixels or by linear correlations with histograms for every single sensor.

Another aspect to take into account is the computation time cost of a satellite image. The advantages of having a large field of view and high temporal resolution are, in fact, a drawback if the processing time exceeds the normal limit. If the processed information is made available too late, the utility of satellite images becomes insignificant and they would no longer be effective in this regard. Therefore, computational processes in the data collector and dissemination systems have been optimized.

### 4.4. Two different approaches for satellite-based SSI estimation

After the launching of the first meteorological satellites in the 1970s, images from these satellites were applied to different domains, in particular, for SSI estimation. Some examples are provided in [TAR 79], [GAU 80], [PAS 81], [BÉR 84], [MÖS 84], [CAN 86], [GRÜ 86], and [SCH 89].

Satellite-based SSI estimation is carried out, generally, in two stages [OUM 09a]:

– the estimation of SSI under a clear sky ($SSI_{clear}$),

– the aggregation of effects of actual attenuation by the atmospheric components.

This second stage modulates the $SSI_{clear}$ for estimating SSI under all weather conditions (clear, partly cloudy, and cloudy). $SSI_{clear}$ is estimated by *clear sky models*, which constitute a key element in SSI estimation. The uncertainty of the $SSI_{clear}$ estimation has an important impact on the accuracy of SSI estimation results [ESP 09].

First attempt methods were *inverse*, i.e. the inputs are DCs from the satellite images, which are the result from the ensemble of interactions of radiation with the atmosphere and the ground, during the downward and upward paths of the radiation. Inverse methods exploit the fact that radiances that reach the satellite sensor are in relation to the attenuation of the solar radiation.

Another possible approach is *direct* modeling. In this approach, the various optical processes occurring along the path of the light from outer space toward the ground are modeled (effect of Rayleigh scattering, water vapor absorption, etc.) by means of a *radiative transfer model* (RTM).

#### 4.4.1. *SSI clear-sky models*

Clear-sky models are mathematical representations of the sky in the absence of clouds, which is a particular situation of great practical interest. These models include some parameters to describe the state of the atmosphere and its transmissivity conditions.

There exist various models for the calculation of $SSI_{clear}$. See, for example, [BIR 80], [MOL 98], [ESR 00], [RIG 00], [GUE 01], [GEI 02], or the Solar Irradiance Scheme (SOLIS) model by Mueller *et al*. [MUE 04]. The influence of the accuracy of the $SSI_{clear}$ is very important in the SSI estimation results for all weather conditions.

One of the most used clear-sky models is the European Solar Radiation Atlas (ESRA) model [ESR 00], where scattering effects and absorption by the atmospheric gases are gathered by the Linke turbidity factor. This model contemplates the attenuation of the beam component and the increase in the diffuse solar component in actual sky conditions. There are other clear-sky models that respond to other requirements, for example the estimation of the solar spectral distribution. The selection of the clear-sky model depends on the requirements and on the availability of inputs (Linke turbidity factor, aerosol optical thickness, etc.).

### 4.4.2. *The inverse approach*

This first approach is based on the fact that a variation of radiance received by the sensor is in relation to the variation of the cloud coverage over the pixel of interest. These models are named as *inverse models*.

There are two principal facts that are exploited by the inverse models [RAS 87]:

– The transmittances of clouds for solar radiation are highly correlated to their reflectance, i.e. the greater the transmittance, the smaller the reflectance (and therefore, the lower the radiance that reaches the satellite's sensor).

– The upward solar radiation above clouds contains contributions from radiation reflected from the ground underneath.

Generally, inverse models are decomposed into two parts. First, the conversion of radiance received for each pixel in a cloud coverage index and, second, the conversion of the cloud coverage index into SSI.

#### 4.4.2.1. *The calculation of the cloud coverage index*

The inputs are geostationary satellite images whose DCs are related to radiances that are the results of the series of interactions of the solar radiation with the atmosphere and with the ground during the downward and upward paths (Figure 4.9(a)).

In Figure 4.7, it has been seen that, generally, radiance from clouds is greater than radiance from Earth's surface, either sea or ground areas, with the exception of snow-covered areas, which can achieve radiance values greater than those of the clouds. The whiter the clouds are in the image, the thicker the clouds are. The greater the radiance received by the satellite, $L_{sat}$, the lesser the radiance received at the ground level.

$L_{sat}$ takes into account the optical state of the atmosphere and the effect of clouds. For each pixel, $L_{sat}$ is comprised within the minimum value, $L_{sat\text{-}clear}$, and the

maximum, $L_{\text{sat-overcast}}$, which are the values of radiances, respectively, under clear sky and under overcast conditions for each pixel. This radiance may be reformulated in a new parameter, $n$, which is a normalization of $L_{\text{sat}}$ for the whole image. This parameter $n$ is related to the cloud coverage and is named *cloud coverage index*. It ranges from zero, which means clear sky, to one, which means cloudy sky, and is calculated as follows:

$$n = \frac{L_{\text{sat}} - L_{\text{sat-clear}}}{L_{\text{sat-overcast}} - L_{\text{sat-clear}}} \quad [4.3]$$

The cloud coverage index is the result of a comparison between what is observed by the satellite's sensor and what should be observed over this pixel if the skies were clear, without any cloud. In other words, $n$ represents the optical attenuation of solar radiation by the atmosphere.

The cloud coverage index may be computed from reflectance values, instead of using the radiance received by the satellite's sensor. The models of Möser and Raschke [MOS 84] and Martins *et al.* [MAR 07] are examples for the use of radiance. The models of Cano *et al.* [CAN 86], Diabaté *et al.* [DIA 88], Beyer *et al.* [BEY 96], Rigollier *et al.* [RIG 04], Lefèvre *et al.* [LEF 07], and Perez *et al.* [PER 02] are examples of the use of reflectance values instead of radiance. Other well-known inverse models are Heliosat-1 [BEY 96], Heliosat-2 [RIG 04], or Heliosat-3 [MUE 04] that has provided the extensive solar radiation databases HelioClim-1 and HelioClim-3 [BLA 11d] which offer SSI values for any site, at any instant over the large geographical area covered by the Meteosat satellite images, and for a long period of time (from 1985 to 2005, they offer daily SSI values and since 2005, 15 min values).

#### 4.4.2.2. *The calculation of the GHI*

The computation of the irradiance from $n$ may be done in several ways. The basic idea is that the cloud cover index $n$ over a geographical point is related with the GHI incident with this point.

One way to estimate GHI is using the fact that the dynamics of $n$ is in relation to the dynamics of the clearness index, $K_T$, which is defined as the ratio of GHI at ground level to irradiance at the top of atmosphere, $\text{GHI}_{\text{toa}}$.

$$K_T = \frac{\text{GHI}}{\text{GHI}_{\text{toa}}} \quad [4.4]$$

$K_T$ gives the fraction of the depletion of $\text{GHI}_{\text{toa}}$ due to absorption and scattering by gases, water vapor, aerosols, and clouds, and it is a dimensionless quantity. As

well as SSI, $K_T$ may be computed for a given instant or for an hour ($K_{Th}$) or day ($K_{Td}$), etc. [WAL 07].

GHI can be computed from the clearness index $K_T$ according to the following affine relation [CAN 86, DIA 88, GRU 86]:

$$K_T = A\,n + B \qquad [4.5]$$

where the parameters $A$ and $B$ are experimentally determined. Therefore, GHI is computed as

$$\mathrm{GHI} = \mathrm{GHI}_{\mathrm{toa}}\ K_T \qquad [4.6]$$

Another way of GHI estimation is from the transmittance for clear-sky conditions ($T_{\mathrm{clear}}$) and transmittance of clouds ($T_{\mathrm{cloud}}$), retrieved from climatological parameters and the geographical position (Brazil-sr method [MAR 07]).

$$\mathrm{GHI} = \mathrm{GHI}_{\mathrm{toa}}\ \left(T_{\mathrm{clear}}\left(1 - n\right) + T_{\mathrm{cloud}}\ n\right) \qquad [4.7]$$

GHI may also be estimated from the *clear-sky index*, $K_{\mathrm{C}}$. It is defined as the ratio of GHI to irradiance under clear sky ($\mathrm{GHI}_{\mathrm{clear}}$):

$$K_{\mathrm{C}} = \frac{\mathrm{GHI}}{\mathrm{GHI}_{\mathrm{clear}}} \qquad [4.8]$$

Therefore, the estimation of GHI may be done similar to equation [4.6]:

$$\mathrm{GHI} = \mathrm{GHI}_{\mathrm{clear}}\ K_{\mathrm{C}} \qquad [4.9]$$

Several functional dependencies have been presented between $K_{\mathrm{C}}$ and $n$. Beyer *et al.* [BEY 96] proposed the following:

$$K_{\mathrm{C}} = 1 - n \qquad [4.10]$$

while Rigollier *et al.* [RIG 04] presented a piecewise function:

$$K_{\mathrm{C}} = \begin{cases} 1.2 & \text{if } n \le -0.2 \\ 1-n & \text{if } n \in \left]-0.2, 0.8\right] \\ 2.0667 - 3.6667n + 1.6667n^2 & \text{if } n \in \left]0.8, 1.1\right] \\ 0.05 & \text{if } n \ge 1.1 \end{cases} \qquad [4.11]$$

In this last relation, it is taken into account that the $n$ value may be outside of its nominal range from 0 to 1. Negative values of $n$ imply an extremely clear atmosphere. Values >1 may occur for very thick clouds whose reflectance is greater than the estimated $L_{\text{sat-overcast}}$.

### 4.4.3. *The direct approach*

Although SSI databases based on inverse methods are globally judged as satisfactory by their customers, limits are nevertheless reached in terms of capacity to provide advanced description of SSI (e.g. in terms of diffuse and direct decomposition, angular and spectral description of SSI) and/or accurate results. For example, estimations of diffuse and direct components of SSI or spectral decomposition of SSI are only possible by using empirical methods that are established from measurements by ground stations. This raises the problem of the applicability of such empirical methods in some regions that may be atypical compared to the places of the ground stations.

A new advanced approach is based on a *direct* modeling for a satellite-based estimation of SSI (Figure 4.9(b)). In this type, the various optical processes occurring along the path of the solar radiation from the top of atmosphere toward the ground are modeled by the means of an RTM. The required inputs of the RTM describing the optical state of the atmosphere are estimated by spaceborne remote sensing. Operational spaceborne imaging systems such as Meteosat Second Generation, Envisat, and MetOp combined with recent data assimilation techniques into atmospheric modeling offer a favorable context for the design and exploitation of a method based on a direct modeling. This would permit us to deliver advanced, "empirical-free" knowledge on SSI. Notably, they allow the estimation of direct and diffuse SSI components (and more generally, to its angular decomposition) and its spectral distribution.

Several direct models have been already developed ([LI 93], [GEI 08], [DEN 08], or [MUE 09], among others). One option is the simple parameterization for the propagation of solar radiation through the atmosphere, such as the model by Li *et al.* ([LI 93], [HOL 02]). In this model, there is an affine relation between the reflected radiation by the ensemble ground atmosphere and the GHI from radiative transfer simulations. Other direct models are based on abaci, which establish a bijection between the ground irradiance and the atmospheric parameters, for example the model presented by Mueller *et al.* [MUE 09] or the Solar Insolation under Cloudy Conditions from Satellite (SICCS) retrieval model introduced by Deneke *et al.* [DEN 08].

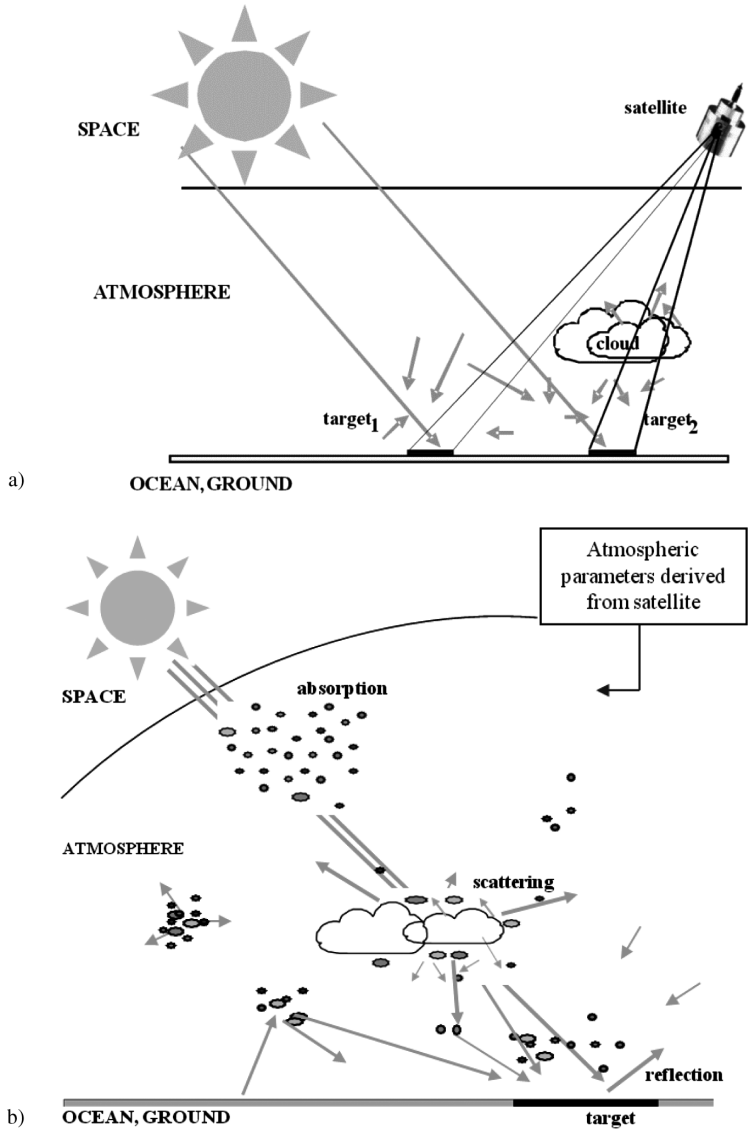


a)

b)

**Figure 4.9.** *Schematic view of the inverse and direct methods for satellite-based estimation of SSI. For the inverse methods (a), inputs are satellite images and a radiance inversion is made to estimate SSI. For the direct methods (b), inputs are atmospheric parameters from spaceborne imaging systems and an RTM is used to estimate SSI (Courtesy of A. Oumbe, 2012 [OUM 09a])*

The Heliosat-4 [MAY 05, OUM 09b] is another direct method for satellite-based SSI estimation. The method is presently under joint development by the DLR (German Aerospace Center) and MINES ParisTech. The RTM code that Heliosat-4 exploits is the libRadtran model that has as input parameters related to time and location (solar zenithal angle, ground spectral albedo, and ground elevation), parameters related to the atmospheric optical state (aerosol optical depth (AOD), the Angstrom coefficient, aerosol type, water vapor content, ozone content, and atmospheric profile), and parameters related to the cloud coverage (cloud optical depth and cloud type).

Heliosat-4 proposes that SSI for all sky conditions can be approximated by the product of the clear-sky SSI ($SSI_{clear}$), a function of the cloud extinction and the ground albedo contribution ($\xi_{cloud/albedo}$) and a function ($f$) for the SSI dependency with respect to the ground elevation, $z$:

$$SSI = SSI_{cls} f(z) \xi_{cloud/albedo} \quad [4.12]$$

The clear-sky model that has been chosen in Heliosat-4 is a combination of libRadtran and the modified Lambert–Beer (MLB) relation proposed in [MUE 04]. It consists of a piecewise MLB with respect to the solar zenithal angle [OUM 11]. It yields very good SSI estimations for both direct and diffuse components, for all wavelengths, and for all solar zenith angles [QU 11].

Finally, for the cloud extinction and the ground albedo contribution to SSI computation, the well-known two-stream and delta-Eddington approximations [PAR 88] have been selected, since the influence on SSI of the cloud geometric parameters (i.e. geometric thickness and vertical position) can be considered negligible. The albedo contribution is calculated as an infinite series of reflection and scattering between the ground and the atmosphere, according to the model proposed by Vermote *et al*. [VER 97].

## 4.5. Accuracy of satellite-based SSI estimations

The usual way of assessing the quality values derived from satellite images is to compare these retrievals to coincident and concomitant pyranometric measurements performed at the ground level. Measurements performed in the global meteorological network, after a quality control test by a trained operator (see section 4.2.1), can be supposed to be of good quality. Therefore, ground measurements that have passed the quality control test are considered as a reference for comparing the satellite retrieval values.

Nevertheless, when the estimated series of solar radiation derived from satellite images are compared to data series registered by ground stations, it should not be expected that both series were the same. That is the reason why a model is necessary to make satellite-derived values fit to the ground measures.

Models in this regard usually deal with the following features. Measures from *in situ* pyranometer and derived from satellite are not physically similar. Pyranometers measure the irradiance while the satellite's sensor records the radiance reflected by the Earth's surface and its atmosphere. The different solid angles in the fields of view for each one of the sensors are also an important matter. Pyranometers receive the irradiance from all over the sky, in a solid angle of $2\pi$, whereas the satellite's sensor receives for each pixel the radiance in a very narrow solid angle. Another aspect is the different spectral response of both instruments, another reason of discordance between satellite-derived data and ground measurements. The pyranometer has a spectral response from 305 to 2,800 nm, while the satellite image has been registered only for narrower spectral bands.

In addition to that, there are some limitations in the comparison. An essential limitation regards the large differences in principles of data series to compare. Ground data series are punctual geometrically and temporally integrated, typically, averaged or sum in hourly values. Satellite-derived data series are, on the contrary, spatially integrated but quasi-instantaneous in time. An assumption of ergodicity, which advocates the equivalence between the temporal and spatial averages, is usually applied. This assumption is correct only if the topography is spatially homogeneous over an area much larger than a pixel, inducing stationary meteorological and orographical conditions. This is generally false when a significant orographic feature is present. Zelenka *et al.* [ZEL 99] have estimated that the ergodicity assumption induces in hourly averaged time series a deviation from 3% to 5% of relative RMSE. Other local effects, such as reflections on the surrounding slopes or the shadows of clouds, may add complexity in comparison.

The intrinsic spatial variability of SSI studied by Perez *et al.* [PER 97] and Zelenka *et al.* [ZEL 99] and explained in section 4.2.2 suggests that within one pixel of geostationary satellite, SSI cannot be considered as homogeneous. This means that the comparison of the satellite retrieval SSI to two ground-based SSI measurements recorded at the same time in two different points within the pixel area may be different. This difference was estimated in the 5–8% range in terms of relative RMSE in hourly averaged time series. The cause of this difference is not in relation to the quality of the satellite-derived SSI value but to the intrinsic spatial SSI variability.

Other effects within a pixel may cause discrepancies between satellite-derived estimates and ground measurements of solar radiation. Indeed, the computation of

the radiometrical variables from satellite images may use a *digital elevation model* (DEM) whose cell size and spatial scales fit that of the pixel. For example, the European Solar Atlas [ESR 00] or the HelioClim-1 database [LEF 07] exploits the DEM TerrainBase [TER 95] whose cell size is 5' of arc angle, i.e. ~10 km at mid-latitude. The size of the cell is even larger for the NASA-SSE database, 1° of arc angle [CHA 04], or for the ISIS database, 280 km [LOH 06]. These sizes are of course too large to describe changes in ground altitude with a sufficient accuracy in areas of steep relief. Figure 4.10 shows an example of changes within a large cell. In this example, a horizontal surface is drawn at the altitude level dictated for a given DEM. It can be seen that the most of the geographical points within the pixel are not at the altitude predicted by the DEM, but sometimes well above (as the marked point) or well below. Very often, changes of 100 m or more can be found between the used altitude and the actual one. Extreme cases achieve more than 1,000 m of difference, and exceptionally, even more.


**Figure 4.10.** *Sample of a cell in a solar radiation database. The horizontal area fenced is at the nominal altitude for this pixel by a given DEM. Nevertheless, the culminant point marked in the figure is well above the nominal altitude for this pixel. Other geographical points are well below*

Wahab *et al.* [WAH 10] report that a difference in altitude of 300 m may induce a relative difference >1% on the monthly mean value of the SSI. This means that change in elevation must also be accounted.

In the neighborhood of relief, irradiance depends on effects of shadows on the sites by surrounding obstacles and not only on changes in altitude alone. Most often, if not always, in operational methods, the contribution by reflection with neighborhood slopes is not accounted for; the calculations of the reflection contributions in SSI are done under the assumption of a flat terrain within the pixel.

An important difficulty in the comparison is the time stamp recorded for each data. The time system for acquisition may be universal time, mean solar time, true solar time, or local time. However, when stored in a database, sometimes there is a conversion from one to another time system, e.g. from local to universal time. There is consequently a change of original values due to a resampling of data series in time. This resampling can be done using various techniques, usually unspecified. In any case, it is not possible to return to the original values and there is an asystematic shift of a fraction of an hour between the two sets of measurements. Due to the time variability of solar radiation, these resampling methods are not equivalent and, therefore, this leads to a difference in the comparison to satellite-derived data series. Moreover, the ground networks do not always follow the existing standard for defining hourly data. This standard is defined by the WMO [WMO 81]: the time assigned to a data corresponds to the end of the measurement period. For example, an hourly data assigned to 11 a.m. has been measured between 10 a.m. and 11 a.m. In several cases, the time associated with a measurement represents the beginning of the period, or the middle of the period, or any instant within the period. Again, the comparison between the two sets requires the resampling of one of the sets at the expense of decay in quality. Of course, this limitation due to the time reference does not hold if one deals with daily, monthly, or yearly averages or sums of solar radiation data.

To summarize, differences between satellite-derived and ground-recorded data are not only due to the performance of the satellite model for fitting ground measures alone. In addition, there are numerous limitations in the comparison due to the intrinsic spatial variability of SSI, the ergodicity assumption, and the accuracy of the measurement instrument itself that introduce differences in the comparison as well.

Finally, it is worth mentioning that ground measurements also may be compared to aggregation of pixels of satellite images, i.e. spatial average of satellite retrievals. Pinker and Laszlo [PIN 91] investigated the effect of the comparison of single pixels to ground data and the comparison of aggregation of pixels instead of single pixels. The result was that under uniform conditions, the comparison outputs were the same as before the resampling. In the heterogeneous case, the results differ significantly in an unpredictable way. It is possible at one time to get better agreement with one aggregation number and at other times better agreement with a different aggregation. The estimated SSI may differ by 9% depending on the aggregation number. Beyer *et al.* [BEY 92] suggested that the local variance might be used as a measure of the spatial heterogeneity and may serve to determine the most appropriate size. The situation is even more complicated due to the sampling in time [BLA 11b].

### 4.6. Use of satellite observations for high-resolution solar radiation estimation

Considering that satellite-based SSI databases are mainly based on geostationary satellites (e.g. Meteosat First and Second Generation), the geographic scale of solar mapping that can be derived is approximately 5 km.

For instance, the Heliosat-2 algorithm [RIG 04], applied to Meteosat Second Generation spinning enhanced visible and infrared imager (SEVIRI) images, is used to update, every 15 min, the solar resource database HelioClim-3. This database covers Europe, Africa, the Mediterranean Basin, the Atlantic Ocean, and part of the Indian Ocean with a spatial resolution of ~5 km (Figure 4.11). More information on the SSI database HelioClim-3 as well as on the HelioClim-1 database (based on Meteosat First Generation) can be found in [BLA 11d].

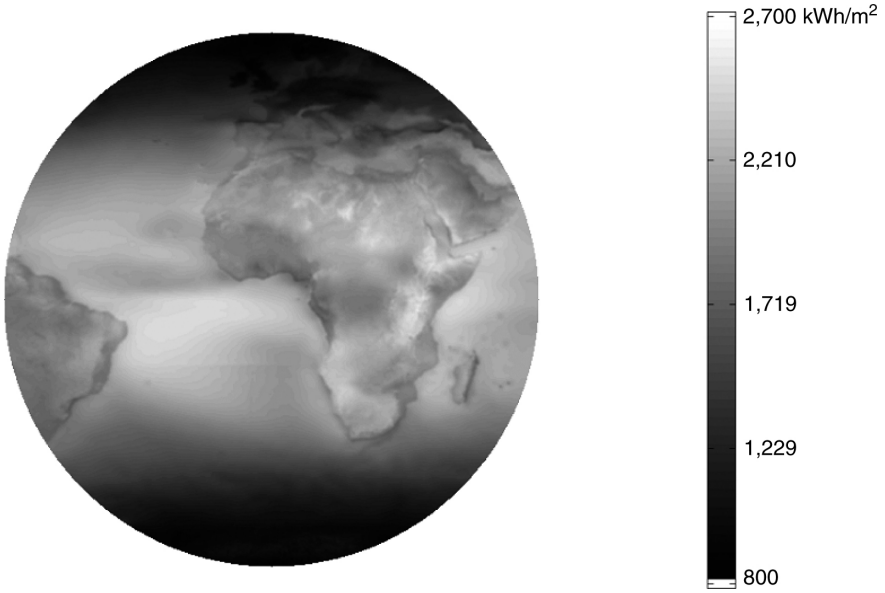


**Figure 4.11.** *Map of average yearly sums of global horizontal irradiation derived from HelioClim-3 database over its field of view (average period: 2004–2010).*


Figure 4.12 illustrates that this geographic scale is suitable for continent or country solar mapping. Nevertheless, customers' feedback notably states that there is a need of spatial resolution improvement for the solar resource assessment to account for spatial variability of the different components of the SSI occurring at finer spatial scales [HOY 10].

In this section is presented an example of use of satellite image retrievals for creating high-resolution solar maps. First, the application of a spatial disaggregation algorithm proposed by Ruiz-Arias *et al.* [RUI 10b] for the improvement of the spatial resolution of solar resource estimation is applied to downscale HelioClim-3 SSI maps for the creation of a 200 m resolution solar atlas in the region of Provence-Alpes-Côte d'Azur (PACA), South of France [BLA 11b]. After that, we discuss which data and solar-processing requirements for solar resource assessment are suitable at the metric or even sub-metric urban scales, taking into account the great gap in spatial resolution with respect to satellite-based SSI databases.

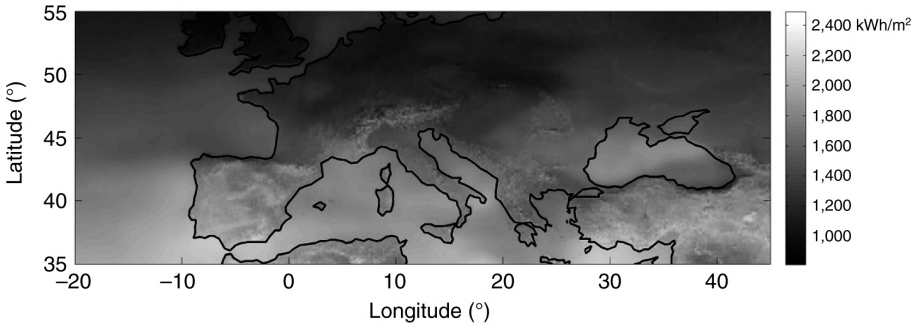


**Figure 4.12.** *European map of average yearly sums of global horizontal irradiation derived from HelioClim-3 (average period: 2004–2010). The spatial resolution of 5 km for the solar resource information is fine enough for studies over large areas such as continents and countries (© MINES Paristech)*

### 4.6.1. *High-resolution solar atlas of Provence-Alpes-Côte d'Azur*

The aim of the high-resolution solar atlas of the French region of PACA is to propose, over this region, 200 m resolution SSI maps for different plane orientations (horizontal, tilted, and normal to the direction of the Sun) for the global, diffuse, and beam components. In terms of temporal resolution, the atlas accounts for the temporal intra- and interannual variations on a monthly basis of the different SSI components.

First, calibration procedures with meteorological ground stations have been established for the daily values of SSI from HelioClim-3, starting from February 2004. The GHI is calibrated thanks to the Météo-France meteorological network (MF stations) comprising approximately 20 meteorological ground stations in PACA.

Daily diffuse and direct horizontal components have been estimated with a transposition model adapted from [RUI 10a], applied to the calibrated daily global horizontal irradiation. This transposition model corresponds to a parametric sigmoid function with empirical parameters. These parameters are locally calibrated thanks

to the three specific ground stations dedicated to the project, named rotating shadow-band pyranometer (RSP) stations, delivering one year of concomitant global and diffuse irradiations on the horizontal plane, measured by a rotating shadow pyranometer (Figure 4.4) [GEU 03].

The downscaling of the 5-km calibrated SSI of HelioClim-3 to the targeted resolution of 200 m has been achieved using the high-resolution DEM named as Shuttle Radar Topography Mission (SRTM) [FAR 07]. This orographic information is exploited at a given geographical location taking into account:

– the variation of the length of the optical path due to the difference between the actual elevation of the geo-location and the elevation considered for SSI computation in HelioClim-3,

– the obstruction effects by the orography on both direct and diffuse components of the SSI.

The following subsections describe more precisely the models that are used to account for these two orographic effects.

#### 4.6.1.1. *Model for the variation of the optical path length*

Wahab *et al.* [WAH 10] proposed a simple model for the estimation of the GHI at the elevation $z$, knowing the one at the elevation $z_0$. This altitude correction model makes use of a clear-sky model and of the clearness index $K_C$ (equation [4.8]). The model is based on the fact that, for elevations $z$ and $z_0$ in the range 0–3 km, the clear-sky index $K_C$ is almost independent of the altitude difference from $z_0$ to $z$:

$$\mathrm{GHI}(z) = K_C \mathrm{GHI}_{\mathrm{clear}}(z) \qquad [4.13]$$

where $\mathrm{GHI}(z)$ is the GHI at the elevation $z$ and $\mathrm{GHI}_{\mathrm{clear}}(z)$ is the GHI at the elevation $z$ in cloud-free condition predicted by the clear-sky model. Therefore, the altitude correction model only concerns the clear-sky irradiance. The empirical model proposed in [WAH 10] is

$$\mathrm{GHI}_{\mathrm{clear}}(z) = \mathrm{GHI}_{\mathrm{toa}}\, \mathrm{e}^{-\tau(z)} \qquad [4.14]$$

where $\mathrm{GHI}_{\mathrm{toa}}$ is the horizontal irradiance at the top of the atmosphere and $\tau$ expresses the optical thickness of the atmosphere:

$$\tau(z) = \tau(z_0) 1.2^{(z_0 - z)} = -\ln\left(\mathrm{GHI}_{\mathrm{clear}}(z_0) / \mathrm{GHI}_{\mathrm{toa}}\right) 1.2^{(z_0 - z)} \qquad [4.15]$$

4.6.1.2. *Model for sky obstruction effects by the orography*

The sky obstruction effects by the surrounding relief, as proposed by Ruiz-Arias *et al.* [RUI 10b], require first the estimation of the local orographic horizon at a given geophysical location (latitude, longitude, and elevation). The local horizon H($\phi$) for a given azimuth $\phi$ is the elevation angle above which the sky is not obstructed by the relief.

The relief is modeled by a DEM that corresponds to elevation data defined on a regular grid in a given geographical reference, e.g. the ellipsoid World Geodetic System, revision of 1984 (WGS 84), or the Universal Transverse Mercator.

Let us consider the local East, North, and Up (ENU) Cartesian coordinate system. This local ENU Cartesian frame is formed from a plane tangent to the Earth's reference ellipsoid, fixed at the local observer. From the local observer, thanks to interpolation, each point $P$ of the DEM along the given azimuth $\phi$ is then defined by its cylinder coordinates ($d_\phi$, $\phi$, $z_\phi$) in the local ENU frame, where $d$ is the radial coordinate. The horizon H($\phi$) for the azimuth $\phi$ is then:

$$\mathrm{H}(\phi) = \max_{d_\phi \in [d_{\min}, d_{\max}]} \arctan\left(\frac{z_\phi}{d_\phi}\right) \qquad [4.16]$$

where $d_{\min}$ and $d_{\max}$ are the minimum and maximum distance, respectively, chosen beforehand. Typically, $d_{\min}$ is set to twice the spatial resolution of the DEM and $d_{\max}$ is set to 50 km. The computation of H($\phi$) is then applied for a regular sampling of azimuth from 0° to 360°, typically for every 1°.

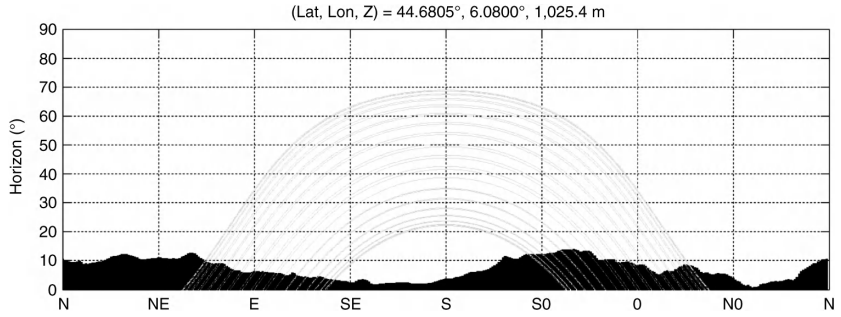


**Figure 4.13.** *Example of horizon (black area) computed from the DEM SRTM at the location (44.6805°N, 6.0800°E). Solid lines are the daily trajectories of the Sun (only three trajectories per month have been depicted, all along the year). The x-axis is the azimuth orientation, beginning from the north. The y-axis is the elevation angle, in degrees*

For the solar atlas of the PACA, the local horizons have been derived from SRTM whose spatial resolution is 3 arcsec (~100 m) and accuracy better than 10 m for 90% of the data [FAR 07]. Figure 4.13 depicts an example of the local horizon (black area) and the different Sun positions (solid lines) along the year. In the first and last hours of the day, the Sun is occulted by the surrounding hills and mountains.

The computation of the orographic effects on the BHI component is straightforward. Indeed, let us consider the BHI derived from HelioClim-3 and $\phi_S$ and $\gamma_S$, respectively, the solar azimuth and elevation angle (the complementary of the zenithal angle). The modified beam irradiance BHI', for a given geophysical location with the local horizon H, is then defined by:

$$\mathrm{BHI}' = \Uparrow_{[\gamma_S > \mathrm{H}(\phi_S)]} \mathrm{BHI} \qquad [4.17]$$

where the operator $\Uparrow_{[\bullet]}$ applied to a condition $C$, noted $\Uparrow_{[C]}$, is a Boolean equal to 1 if the condition $C$ is true, 0 otherwise.

To determine the modified beam tilted irradiance BTI' on a tilted plane whose orientation is defined by the azimuth angle $\alpha$ and its slope $\beta$ of the plane (both expressed in radian), the corresponding cosine of the Sun incidence angle $\theta_I$ has to be considered:

$$\cos\theta_I(\alpha,\beta) = \sin\gamma_S \cos\beta + \sin\beta \cos\gamma_S \cos(\phi_S - \alpha) \qquad [4.18]$$

The modified beam irradiance on the tilted plane is then

$$\mathrm{BTI}' = R_B(\alpha,\beta)\,\mathrm{BHI}'$$
$$\text{where } R_B(\alpha,\beta) = \frac{\cos\theta_I(\alpha,\beta)}{\max(0.02, \sin\gamma_S)} \Uparrow_{[\gamma_S > 0]} \Uparrow_{[\cos\theta_I(\alpha,\beta) > 0]} \qquad [4.19]$$

The computation of the orographic effects on the DHI is more complex since it requires distinguishing the circumsolar $\mathrm{DHI}_{cs}$ and the isotropic $\mathrm{DHI}_{iso}$ diffuse horizontal components. The circumsolar diffuse irradiance corresponds to a fraction of the diffuse irradiance coming from a solid angle centered to the Sun's position with a radial displacement (half-angle) of a few degrees, typically 2.5° up to 3.5°:

$$\begin{aligned} \mathrm{DHI}_{cs} &= F_1 \mathrm{DHI} \\ \mathrm{DHI}_{iso} &= \mathrm{DHI} - \mathrm{DHI}_{cs} \end{aligned} \qquad [4.20]$$

The fraction $F_1$ is defined as the circumsolar brightening coefficient and is determined by an empirical model proposed by Perez *et al.* [PER 90], with precomputed coefficient tables. This model mainly depends on the Sun's zenith angle, the surface and the top of atmosphere BNIs, and the DHI itself. It is to be noted that, in case of completely overcast conditions, (i.e. BHI = 0), $F_1 = 0$.

Considering the circumsolar disk being small enough, the orographic effects on the circumsolar diffuse irradiance are similar than that on the BHI, i.e. the modified $\mathrm{DHI_{cs}}'$ is defined as

$$\mathrm{DHI_{cs}}' = \Uparrow_{[\gamma_S > H(\phi_S)]} \mathrm{DHI_{cs}} \qquad [4.21]$$

The circumsolar diffuse irradiance on the tilted plane is also quite similar to the beam component:

$$\mathrm{DTI}' = R_{cs}(\alpha,\beta)\,\mathrm{DHI}'$$
$$\text{where } R_{cs}(\alpha,\beta) = \frac{\cos\theta_I(\alpha,\beta)}{\max(0.087, \sin\gamma_s)} \Uparrow_{[\gamma_s>0]} \Uparrow_{[\cos\theta_I(\alpha,\beta)>0]} \qquad [4.22]$$

The sky-view factor defined by Dozier and Frew [DOZ 90] and noted $R_{\mathrm{iso}}$ accounts for the effect of the local horizon on the $\mathrm{DHI_{iso}}$, taking also into account the tilted angle with azimuth $\alpha$ and slope $\beta$:

$$\mathrm{DTI_{iso}}' = R_{\mathrm{iso}}(\alpha,\beta)\,\mathrm{DHI_{iso}} \qquad [4.23]$$

Following [DOZ 90],

$$R_{\mathrm{iso}}(\alpha,\beta) = \frac{1}{\pi}\int_{\phi=0}^{2\pi}\int_{\theta=0}^{\pi/2-H(\phi)} F(\theta,\phi,\alpha,\beta)\sin\theta\,\mathrm{d}\theta\,\mathrm{d}\phi \qquad [4.24]$$

where $\theta$ is the solar zenith angle, the operator $(\cdot)_+$ applied to a float $x$ corresponds to $x \Uparrow_{[x>0]}$, and

$$F(\theta,\phi,\alpha,\beta) = \left(\cos\theta\cos\beta + \sin\theta\sin\beta\cos(\phi-\alpha)\right)_+ \qquad [4.25]$$

In case of flat horizon, i.e. $H(\phi) = 0$, we can verify that

$$R_{\mathrm{iso}}(\alpha,\beta) = \frac{1+\cos\beta}{2} \qquad [4.26]$$

In the general case, a straightforward numeric approximation of $R_{\text{iso}}$ by a double Riemann sum is time-consuming. Fortunately, this double integral can be reduced to a single one:

$$R_{iso}(\alpha,\beta)=\frac{\cos\beta}{2\pi}\int_0^{2\pi}\sin^2 Z_+(\phi)\,d\phi + \frac{sin\beta}{2\pi}\int_0^{2\pi}\cos(\phi-\alpha)\left(Z_+(\phi)-\sin Z_+(\phi)\cos Z_+(\phi)\right)d\phi$$

where [4.27]

$$Z_+(\phi)=\min\left(\frac{\pi}{2}-H(\phi),\theta_+(\phi)\right)$$

$$\theta_+(\phi,\alpha,\beta)=\begin{cases}\arctan\left(-\left(\cos(\phi-\alpha)\tan\beta\right)^{-1}\right) & \text{if } \cos(\phi-\alpha)<0\\ \pi/2 & \text{otherwise}\end{cases}$$

It is to be noted that the horizon-brightening coefficient introduced in [PER 90] to account for horizon-to-zenith anisotropy of the diffuse component on a tilted plane is not used in the presented model of orographic effect; apart from the circumsolar diffuse irradiance, the diffuse is assumed isotropic.

The diffuse irradiance coming from reflections by the neighborhood surfaces can be important, depending on the corresponding albedos. Nevertheless, the exact contribution of each facet of the surrounding terrain is very complex to model and to compute, even with simplifying Lambertian reflector assumption. That is the reason why the surround reflective part of the diffuse irradiance is approached as the diffuse irradiance reflected by an infinite horizontal plane of known albedo $\rho$:

$$\text{RTI}'=\rho\left(1-R_{\text{iso}}(\alpha,\beta)\right)\left(\text{BHI}'+\text{DHI}_{cs}'+\left(1-R_{iso}(0,0)\right)\text{DHI}_{\text{iso}}\right) \quad [4.28]$$

The part of the reflective diffuse irradiance coming from the isotropic diffuse horizontal irradiance ($\text{DHI}_{\text{iso}}$) in equation [4.20] is multiplied by the factor $\left(1-R_{iso}(0,0)\right)$, which corresponds to the portion of $\text{DHI}_{\text{iso}}$ obstructed by the surrounding relief.

In [RUI 10b], this orographic correction model related to sky obstruction effects has been assessed for 15-min time series of GHI. For both cloudy and cloud-free conditions, the orographic correction notably improves the mean bias errors (MBEs) that are almost completely removed while the standard deviations remain approximately unchanged. The same results have been observed for the validation of the solar atlas when compared to the MF station in a mountainous region with orographic obstruction effects.

4.6.1.3. *Uncertainty analysis of the solar atlas*

The uncertainty of the monthly sums of global horizontal irradiation provided by the solar atlas has been assessed in two ways:

– The statistical analysis, before and after the calibration procedure, of the residual discrepancies of the estimations with respect to the 20 MF stations. In addition, as all these stations have been used for the calibration, a statistical analysis based on the Leave-one-out cross-validation (LOOCV) approach was also made [ARL 10].

– The statistical analysis, before and after the calibration procedure, of the discrepancies of the estimations with respect the three RSP stations considered as test stations because they have not been used for the calibration.

The statistical measures of the discrepancy of time series comparison are the MBE, the mean absolute error (MAE), the RMSE, and the correlation coefficient (CC). Apart from the last one, these measures are relative to the mean value of the reference time series (MREF) and are expressed in percentages. NDATA corresponds to the number of data that have been used for the comparison.

| | NDATA (months) | MREF (kWh $m^{-2}$) | MBE (%) | MAE (%) | RMSE (%) | CC |
|---|---|---|---|---|---|---|
| Monthly sums of GHI Ref.: MF stations | 1,269 | 132 | −0.2 | 3.1 | 4.3 | 0.996 |
| Monthly sums of GHI Ref.: MF stations Cross-validation LOOCV | 1,267 | 132 | −0.7 | 4.4 | 6.2 | 0.991 |
| Monthly sums of GHI Ref: 3 RSP stations | 38 | 126 | 0.4 | 2.5 | 3.1 | 0.998 |
| Monthly sums of BNI Ref.: 1 MF station and 3 RSP stations | 112 | 156 | 0.9 | 6.3 | 7.9 | 0.977 |

**Table 4.1.** *Results of the statistical analyses for the uncertainty of the monthly sums of GHI and BNI provided by the solar atlas*

Table 4.1 gives the results of these statistical analyses between the monthly sums of GHI provided by the ground stations and the solar atlas, after calibration and correction from orographic effects. The statistical comparisons with the MF stations without and with the LOOCV approach and with the RSP stations are in accordance. The MBE of the estimation of monthly sums of GHI is <1% and its RMSE is close to 5% (i.e. ~7 kWh $m^{-2}$). It is important to note that these values are an average over the region. For mountainous areas, the RMSE is approximately 6% (with almost no bias) whereas for non-mountainous areas, the value is ~3.5%.

Table 4.1 also gives the results of the comparisons of the monthly sums of beam normal irradiation BNI from the solar atlas with the only meteorological station of Météo-France providing BNI measurements (near the city of Carpentras) and the three RSP stations. Although the mean bias error is still <1%, the RMSE for the monthly sums of BNI estimation is approximately 8% (i.e. ~12.5 kWh $m^{-2}$) and is greater than for the GHI.

4.6.1.4. *Dissemination of the solar atlas*

The solar atlas PACA is freely available at www.atlas-solaire.fr. Thanks to Web services (Web Map Services or specific web services), average yearly and monthly sums of global, direct, and diffuse irradiations on horizontal, on normal incidence, and some predefined tilted planes have been built, over the data period from 2004 to 2010.

The availability of this different SSI data at high spatial resolution is an efficient help for studies based on Geographical Information System for ranking and choosing locations for solar power plants and for their prefeasibility and predimensioning studies. The regional organizations and councils, which funded the project, believe that the local atlas represents an efficient promotion tool for alternative electricity generation and for help in decision-making. Another great benefit is that it enables a better prediction of solar resource to control the introduction of renewable energies in the local grid.

Figures 4.14 and 4.15 are two maps from the solar atlas for global horizontal and beam normal irradiations, respectively.

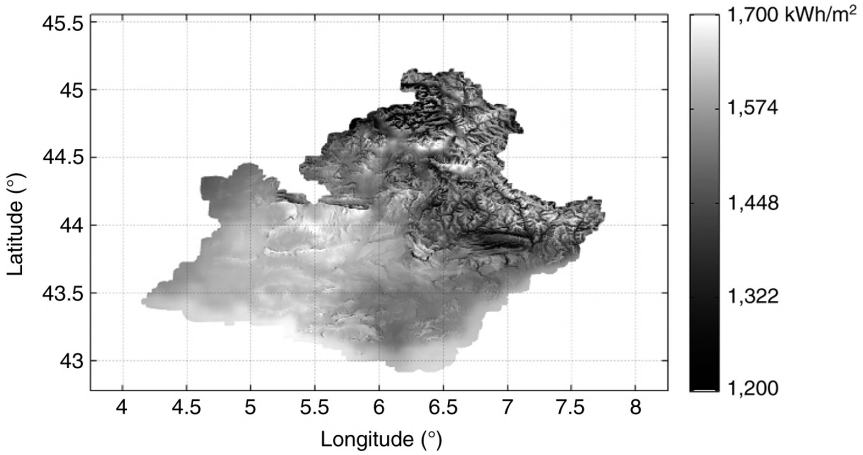


**Figure 4.14.** *Map of average yearly sums of global horizontal irradiation over the PACA region. The period for the average is from 2004 to 2010 [BLA 11a]*

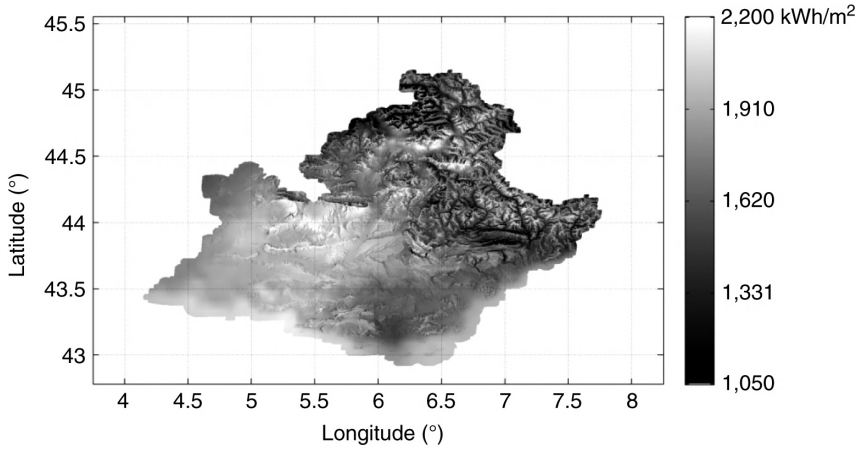


**Figure 4.15.** *Map of average yearly sums of beam normal irradiation over the PACA region. The period for the average is from 2004 to 2010 [BLA 11a]*

### 4.6.2. *Solar resource assessment at urban scale*

Compared to the solar atlas at the hectometric scale, presented in the previous section, solar resource at urban scale implicitly requires a spatial *representativity* of the SSI estimations at the metric or even sub-metric scales. It implies revising the solar modeling and the data used for the SSI retrieval at this urban scale. It also implies defining and discussing the temporal scales at which the estimated SSI is spatially representative.

First, considering, at the urban scale, the multiple non-Lambertian reflection effects of local environment, the variability of the slope to be considered, and the complexity of the shadowing effects in relation to the complexity of the urban geometry (e.g. canyon effect), improvement of solar radiation modeling is required. More precisely, for solar energy purpose, these improvements should be focused on a better modeling of incident radiation on a tilted plane with complex shadow effects on direct and diffuse components.

Derived from [THO 10], the different SSI components impinging at a tilted plane (Figure 4.16) that must be considered at the urban scale are as follows:

– $I_{dir}$: the direct (or beam) irradiance if not obstructed by the neighborhood,

– $I_{refl}$: the reflected irradiance from the neighborhood of the tilted plane,

– $I_{diff}$: the diffuse irradiance non-obstructed by the surround,

– $I_{coup}$: the coupled irradiance because of multiple processes of terrain reflection and atmospheric scattering before reaching the tilted plane.

Each of these SSI components may be highly modified by the complex geometry of the neighborhood (once again by shadow effects, sky obstruction, reflections, and terrain–atmosphere coupling). To use satellite-based SSI retrievals at the urban scale, they should be able to provide accurate estimations of these different SSI components.

According to Robinson and Stone [ROB 04], the isotropic hypothesis for the diffuse irradiance (circumsolar component aside) used for the high-resolution solar atlas previously presented will not have enough resolution to describe the high spatial variability in the complex decomposition of SSI at urban scale. Robinson and Stone [ROB 04] suggest using a sky radiance model of the diffuse component such as the one developed by Perez *et al.* [PER 93].

For this reason, direct methods of satellite-based SSI estimation presented in section 4.4.3 should be more appropriate than the inverse methods. Indeed, the use of RTMs, which include the physical processes interactions between incident photons from the Sun and the atmosphere, enables descriptions and estimations of the different SSI components in a more accurate way and with no empirical adjustments.

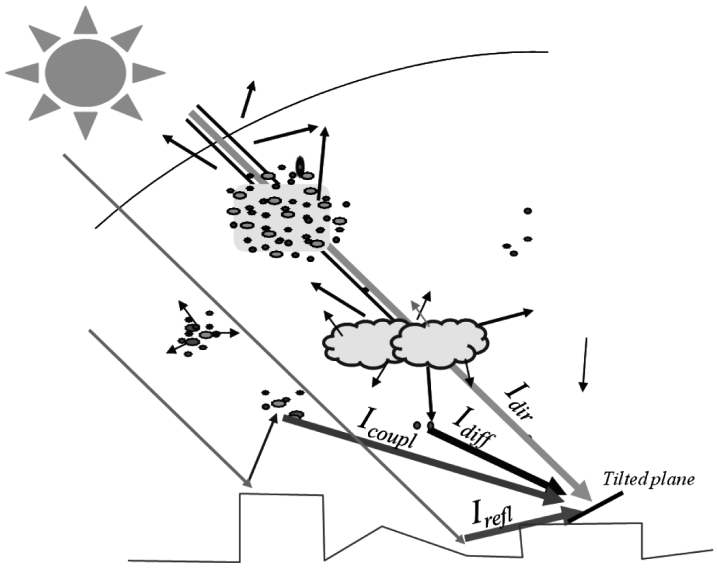


**Figure 4.16.** *SSI components to be considered at the urban scale, based on [THO 10]*

In addition, direct methods are able to provide description of the diffuse component in such an exhaustive way that allows the use of sky radiance model such as the one proposed by Perez *et al.* [PER 93] as well as the estimation of the *spherical albedo* [VER 97] of the atmosphere that is needed for the estimation of the coupled irradiance $I_{coupl}$.

High resolution and accurate DEM is needed. Shadows and thin effects, sky-viewing factors will be computed from this DEM. Roofs and facades of buildings may be suitable for energy production. Their characteristics (usable area, slope, azimuth, etc.) may also be derived from the DEM.

High-resolution sub-metric optical satellites already existing, such as Worldview and Quickbird, or future ones, such as Pleiades, are able to provide metric DEM with a global coverage. The use of metric resolution DEM seems to be sufficient for sky-view factor estimation [BRO 01]. Nevertheless, the estimation of shadow effects or the roof and front characteristics could be very sensitive to even small structures (lift shafts, chimneys, surrounding vegetations, etc.). Very fine and up-to-date three-dimensional (3D) modeling of buildings and surrounding vegetations is then required.

The use of satellite-based metric DEM for 3D building modeling for solar energy purposes needs to be specifically assessed since standard quality DEM assessments, such as exhaustivity, planimetric, and altimetric errors defined, for example by [MAT 04], are not straightforward, relevant, and complete for solar energy at the urban scale.

Another possibility is to resort to high-resolution 3D building databases that are presently becoming available. For example, the French geographic institute IGN provides CARTO3D (http://www.carto3d.fr) products with 3D fine modeling of buildings and infrastructures with a decimetric geometric precision (Figure 4.17). The production of the CARTO3D databases is in progress for 18 cities in France. The CARTO3D products of Marseille, Paris, Nantes, Lille, and Aix-en-Provence are already available. As mentioned above, this type of high-resolution 3D building database has to be assessed specifically for solar energy resource assessment purposes.

There is also a need for better spatial resolution in the definition of the optical state of the atmosphere. As described in section 4.4, the surface solar irradiance can be considered as the product of solar irradiance under clear-sky condition with an extinction function of the atmosphere.

Concerning the data required for the irradiance model under clear-sky condition, current meteorological reanalysis databases, such as the ECMWF reanalysis

program GEMS [GEM 11], provide data only at coarse spatial and temporal resolutions (typically daily or three-hour values at 100 km resolution), which is clearly insufficient.

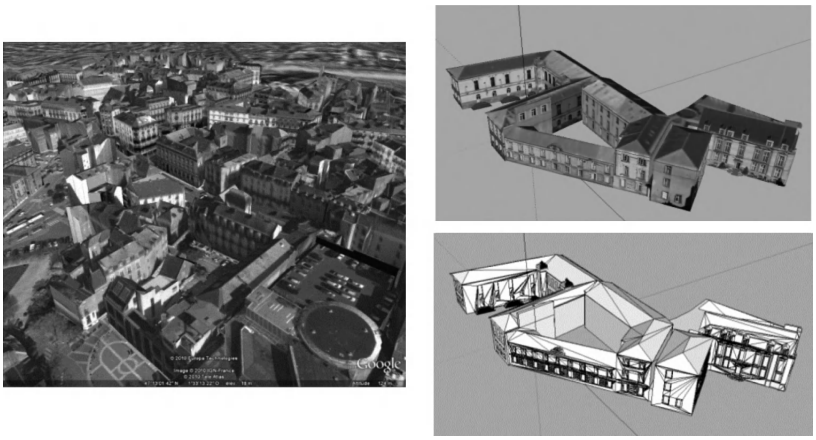

**Figure 4.17.** *Examples of Carto3D© products in Nantes (France): a block (left) and a single building (right) with and without texture (© IGN- Virtuel City – 2011 CARTO3D)*

The aerosol parameters (AOD, Angstrom coefficient, and aerosol types) are very important for SSI retrieval, in particular in regions where cloud-free conditions are predominant. The spatial and temporal variability of these aerosol parameters is very high in urban areas as it is strongly related to pollution by urban or suburban human activities (transports, industries, individual or collective central heating, energy production, etc.). As an example, from a study of variability of the AODs around Manhattan [LIE 03], AOD at 550 nm shows consecutive variations >0.1 with a mean value from 0.3 to 0.4. Typically, a variation of 0.1 on AOD near to 0.3 leads to variations of 9% for the BNI and 2.5% for the GHI. In [THO 10], it is proposed a new AOD retrieval method dedicated to urban areas, by high-resolution visible spaceborne imaging systems in polar orbits, that retrieves AOD from the difference of reflected radiation from sunny areas in relation to the reflected radiation from the alongside shadow area (sunny/shaded transitions). This specific method dedicated to urban areas is based on numeric inversion of two radiative transfer codes: 6S and Amartis v2. It shows promising preliminary results but it is still not operational. Moreover, it enables only very local AOD estimation at specific location (sunny/shaded transitions on homogenous zones) with a very coarse temporal resolution depending on the revisit frequency of the satellites and programmatic constraints.

For the other parameters of the clear-sky model of SSI, such as water vapor and ozone contents or atmospheric profiles, specific sensitivity studies should be done to analyze together both their sensitivity with respect to the SSI retrieval model and their spatial and temporal variability.

These sensitivity analyses should be done specifically for solar energy purposes because spatial and temporal resolution requirements might be different according to the objective to reach. For example, ozone content is essentially important for SSI estimation in the ultraviolet spectral range, while in the visible or broadband range, coarse resolution from meteorological reanalysis databases can be sufficient.

Concerning the extinction function of clouds, knowledge as fine as possible of the cloud coverage is required by the means of exhaustive information of the cloud optical depth or cloud type, for example. These features present extremely high non-stationary spatial and temporal variability, for therein resides the cause of the difficulty. Although the temporal and spatial resolutions of geostationary meteorological satellite images have been greatly improved, they remain technically limited with respect to spatial resolution, which restricts their use at the urban scale. Even the next generation of Meteosat satellites, Meteosat Third Generation (planned for 2017) which will provide a spatial resolution of 1 – 2 km resolution multispectral images, for every 10 min, for the whole field of view by the Full Disk High-Spectral Resolution Imagery mission [EUM 07] remains still too coarse.

Consequently, if the high spatial resolution of the SSI retrieval implicitly required at the urban scale is also required at high temporal resolution (e.g. for monitoring and forecasting solar power plants), complementary solution of permanent high spatial and temporal resolution cloud coverage estimation must be found. A possible solution, which is currently being studied and therefore will not be operative in the near future, is to consider, in addition to geostationary satellite imagery, ground-based cameras with a hemispheric optic named Total Sky Imagers [LON 06]. An example of a total sky imager and corresponding images are displayed in Figure 4.18.

Even more prospective, as shown by Kassianov *et al.* [KAS 05], is the use of a network of total sky imagers to retrieve 3D information of cloud coverage over an extended area. This network would be suitable to urban coverage, by specific stereoscopic and optical flow processes.

Beyond all these very important considerations of spatial and temporal variability and sensitivity of data required for the SSI retrieval on urban areas, a more global analysis should be conducted to determine what timescale is suitable for a given spatial representativity of the SSI estimations. For example, let us consider a direct satellite-based SSI retrieval method with clear-sky condition parameters coming from

a 100 km three-hourly meteorological reanalysis database and cloud parameters from 3 km and 15 min images from Meteosat Second Generation. Solar processing with anisotropic model [PER 90] or an even more sophisticated radiance model [PER 93] of diffuse irradiance that makes use of a high-resolution DEM would provide spatially gridded 15 min time series of SSI. At the finest spatial scale relevant to the urban scale, i.e. the metric or submetric scale, the spatial variability of these SSI estimations is only due to shadow effects. The huge scale gap between this finest spatial scale-up to the coarse resolution of, on the one hand, the cloud coverage and, on the other hand, the clear-sky model, is not covered by any available meteorological information. In other words, the spatial representativity of the SSI estimations at 15 min timescale is roughly null at metric or submetric scale. Consequently, this raises the question of the improvement – or not – of this spatial representativity with temporal aggregation (i.e. temporal upscaling).

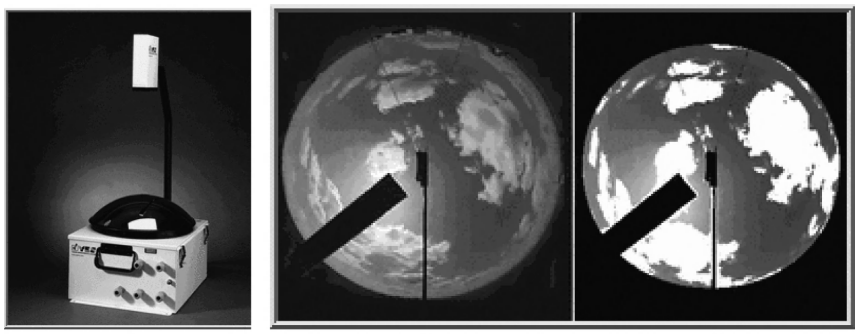


**Figure 4.18.** *(a) Total Sky Imager TSI-880. Examples of sky images provided by the TSI: raw RGB images (b) and processed cloud/clear- sky segmentation (http://www.yesinc.com). (c) Yankee Environmental Systems*

Therefore, the relevancy of the satellite-based SSI estimations at the urban scale depends on the existence and the determination of the suitable temporal scale to reach a given level of spatial representativity of this particular SSI retrieval, taking into account its spatial and temporal resolution.

## 4.7. Bibliography

[ARL 10] ARLOT S., CELISSE A., "A survey of cross-validation procedures for model selection", *Statistics Surveys*, vol. 4, pp. 40–79, 2010.

[BÉR 84] BÉRIOT N., Rapport sur l'évaluation de la ressource énergétique solaire à l'aide de satellites météorologiques, Technical report, World Climate Applications Programme (WCP), pp. 84, 1984.

[BEY 92] BEYER H.G., REISE C., WALD L., "Utilization of satellite data for the assessment of large scale PV grid integration", *Proceedings of 11th Photovoltaic Solar Energy Conference*, Hardwood Academic Publishers, Switzerland, pp. 1309–1312, 1992.

[BEY 96] BEYER H.G., COSTANZO C., HEINEMANN D., "Modifications of the Heliosat procedure for irradiance estimates from satellite images", *Solar Energy*, vol. 56, pp. 207–212, 1996.

[BIR 80] BIRD R., HULDSTROM R., "Direct insolation models", *Transactions on ASME Journal of Solar Energy Engineering*, vol. 103, pp. 182–192, 1980.

[BLA 11a] BLANC P., Atlas du potential solaire photovoltaïque et thermodynamique en région Provence-Alpes-Côte d'Azur, Centre Energétique et Procédés, MINES ParisTech/ *ARMINES,* available at www.atlas-solaire.org, pp. 103, 2011.

[BLA 11b] BLANC P., ESPINAR B., GSCHWIND B., MENARD L., THOMAS C., WALD L., "High spatial resolution solar atlas in Provence-Alpes-Côte d'Azur", *Proceeding of the ISES Solar Word Congress*, *Theme: Resource Assessment*, Kassel (Germany), International Solar Energy Society, pp. 174–182, 2 August–2 September 2011.

[BLA 11c] BLANC P., GSCHWIND B., LEFÈVRE M., MÉNARD L., WALD L., "Satellite-based estimation surface solar irradiance", *SPIE Newsroom,* available at www.spie.org, 2011.

[BLA 11d] BLANC P., GSCHWIND B., LEFÈVRE M., WALD L., "The HelioClim project: surface solar irradiance data for climate applications", *Remote Sensing*, vol. 3, pp. 343–361, 2011.

[BRO 01] BROWN M., GRIMMOND S., RATTI C., "Comparison of methodologies for computing sky view factor in urban environments", *Proceedings of the 2001 International Symposium on Environmental Hydraulics*, pp. 7, 2001.

[CAN 86] CANO D., MONGET J., ALBUISSON M., GUILLARD H., REGAR N., WALD L., "A method for the determination of the global solar radiation from meteorological satellite data", *Solar Energy*, vol. 37, pp. 31–39, 1986.

[CHA 04] CHANDLER W.S., WHITLOCK C.H., STACKHOUSE P.W. Jr., "NASA climatological data for renewable energy assessment", *Journal of Solar Energy Engeneering*, vol. 126, pp. 945–949, 2004.

[DEN 08] DENEKE H., FEIJT A., ROEBELING R., "Estimating surface solar irradiance from Meteosat SEVIRI-derived cloud properties", *Remote Sensing of Environment*, vol. 112, pp. 3131–3141, 2008.

[DIA 88] DIABATÉ L., DEMARCQ H., MICHAUD-REGAS N., WALD L., "Estimating incident solar radiation at the surface from images of the earth transmitted by geostationary satellites: the Heliosat project", *International Journal of Solar Energy*, vol. 5, pp. 261–278, 1988.

[DOZ 90] DOZIER, J., FREW J., "Rapid calculation of terrain parameters for radiation modeling from digital elevation data", *IEEE Transactions on Geoscience and Remote Sensing*, vol. 28, pp. 963–969, 1990.

[ESP 09] ESPINAR B., Radiación solar a partir de imágenes de satélite. Análisis de incertidumbre y ajuste local, PhD Thesis, University of Almería (Spain), pp. 216, 2009.

[ESP 11] ESPINAR B., WALD L., BLANC P., HOYER-KLICK C., SCHROEDTER-HOMSCEIDT M., WANDERER T., Report on the harmonization and qualification of meteorological data, Project ENDORSE, Energy Downstream Service Providing Energy Components for GMES, Grant Agreement No. 262892, available at http://www.endorse-fp7.eu, pp. 81, 2011.

[ESR 00] ESRA, *European Solar Radiation Atlas*, Published for the Commission of the European Communities by Presses de l'Ecole des Mines de Paris, 4th ed., Paris, France, 2000.

[EUM 07] EUMETSAT, MTG mission requirements document, EUM/MTG/SPE/06/0011, Edition v2C, EUMETSAT, Dramstadt, Germany, pp. 146, 2007.

[FAR 07] FARR T.G., ROSEN P.A., CARO E., CRIPPEN R., DUREN R., HENSLEY S., KOBRICK M., PALLER M., RODRIGUEZ E., ROTH L., SEAL D., SHAFFER S., SHIMADA J., UMLAND J., WERNER M., OSKIN M., BURBANK D., ALSDORF D., "The shuttle radar topography mission", *Reviews of Geophysics*, vol. 45, pp. 33, 2007.

[GAU 80] GAUTIER C., DIAK G., MASSE S., "A simple physical model to estimate incident solar radiation at the surface from GOES satellite data", *Journal of Applied Meteorology*, vol. 19, pp. 1005–1012, 1980.

[GEI 02] GEIGER M., DIABATÉ L., MÉNARD L., WALD L., "A web service for controlling the quality of measurements of global solar irradiation", *Solar Energy*, vol. 73, pp. 475–480, 2002.

[GEI 08] GEIGER B., MEUREY C., LAJAS D., FRANCHISTÉGUY L., CARRER D., ROUJEAN J., "Near real-time provision of downwelling shortwave radiation estimates derived from satellite observations", *Meteorological Applications*, vol. 15, pp. 411–420, 2008.

[GEM 11] GEMS PROJECT, A monitoring and forecasting system for atmospheric composition, Final report of the GEMS project, Global Monitoring for Environment and Security, pp. 196, 2011.

[GEU 03] GEUDER N., TRIEB F., SCHILLINGS C., MEYER R., QUASCHNING V., "Comparison of different methods for measuring solar irradiation data", *Proceedings of the 3rd International Conference on Experiences with Automatic Weather Stations*, Torremolinos (Spain), pp. 9, 19–21 February 2003.

[GRÜ 86] GRÜTER W., GUILLARD H., MÖSER W., MONGET J.M., PALZ W., RASCHKE E., REINHARDT R.E., SCHWARZMANN P., WALD L., "Solar radiation data from satellite images", *Solar energy R&D in the European Community, Series F: Solar Radiation Data*, Reidel Publishing Company, vol. 4, 1986.

[GUE 01] GUEYMARD C., "Parameterized transmittance model for direct beam and circumsolar spectral irradiance", *Solar Energy*, vol. 71, pp. 325–346, 2001.

[HAY 81] HAY J.E., "The mesoscale distribution of solar radiation at the earth's surface and the ability of satellites to resolve it", *Proceedings of the First Workshop on Terrestrial Solar Resource Assessment*, Washington D.C., pp. 76–85, 2–5 February 1981.

[HAY 84] HAY J.E., "An assessment of the mesoscale variability of solar radiation at the earth's surface", *Solar Energy*, vol. 32, pp. 425–434, 1984.

[HAY 85] HAY J.E., HANSON K.J., "Evaluating the solar resource: a review of problems resulting from temporal, spatial and angular variations", *Solar Energy*, vol. 34, pp. 151–161, 1985.

[HOL 02] HOLLMANN R., BODAS A., GRATZKI A., DAMMANN K., STUHLMANN R., "The surface shortwave net flux from the scanner for radiation budget (SCARAB)", *Advances in Space Research*, vol. 30, pp. 2363–2369, 2002.

[HOY 10] HOYER-KLICK C., LEFÈVRE M., OUMBE A., SCHROEDTER-HOMSCEIDT M., WALD L., User's guide to the SoDa and SOLEMI services. Towards the solar energy radiation resources MACC-RAD Service, Project MACC, Monitoring Atmosphere Composition & Climate, Sub-project RAD "radiation", Grant Agreement no. 218793, pp. 99, 2010.

[ISO 95] INTERNATIONAL ORGANIZATION FOR STANDARDIZATION (ISO), Guide to the Expression of Uncertainty in Measurement, 1st ed., ISO, Geneva, Switzerland, 1995.

[KAS 05] KASSIANOV E., LONG C.N., CHRISTY J., "Cloud-base-height estimation from paired ground-based hemispherical observations", *Journal of Applied Meteorology*, vol. 44, pp. 1221–1233, 2005.

[LEF 07] LEFÈVRE M., WALD L., DIABATÉ L., "Using reduced data sets ISCCPB2 from the Meteosat satellites to assess surface solar irradiance", *Solar Energy*, vol. 81, pp. 240–253, 2007.

[LI 93] LI Z., LEIGHTON H., CESS R., "Surface net solar radiation estimated from satellite measurements: comparisons with tower observations", *Journal of Climate*, vol. 6, pp. 1764–1772, 1993.

[LIE 03] LIEPERT B., ANDERSON A., EWART N., "Spatial variability of atmospheric transparency in the New York metropolitan area in summer", *Poster presented at American Geophysical Union Fall 2003 Meeting*, 2003.

[LOH 06] LOHMANN S., SCHILLINGS C., MAYER B., MEYER R., "Long-term variability of solar direct and global radiation derived from ISCCP data and comparison with reanalysis data", *Solar Energy*, vol. 80, pp. 1390–1401, 2006.

[LON 06] LONG C., SABBURG J., CALBÓ J., PAGÈS D., "Retrieving cloud characteristics from ground-based daytime color all-sky images", *Journal of Atmospheric and Oceanic Technology*, vol. 23, pp. 633–652, 2006.

[MAR 07] MARTINS F., PEREIRA E., ABREU S., "Satellite-derived solar resource maps for Brazil under SWERA project", *Solar Energy*, vol. 81, pp. 517–528, 2007.

[MAT 04] MATHIEU-MARNI S., BLANC P., ROGNANT L., "Étude sur l'adéquation des futures images du capteur PLEIADES-HR à des thématiques de risques naturels", *Revue Française de Photogrammétrie et de Télédétection*, vol. 174, no. 74, pp. 53–63, 2004.

[MAY 05] MAYER B., KYLLING A., "Technical note: the libRadtran software package for radiative transfer calculations – description and examples of use", *Atmospheric Chemistry and Physics*, vol. 5, pp. 1855–1877, 2005.

[MOL 98] MOLINEAUX B., INEICHEN P., O'NEIL N., "Equivalence of pyrheliometric and monochromatic aerosol optical depths at a single key wavelength", *Applied Optics*, vol. 37, pp. 7008–7018, 1998.

[MÖS 84] MÖSER W., RASCHKE E., "Incident solar radiation over Europe estimated from Meteosat data", *Journal of Applied Meteorology*, vol. 23, pp. 166–170, 1984.

[MUE 04] MUELLER R., DAGESTAD K., INEICHEN P., SCHROEDTER M., CROS S., DUMORTIER D., KUHLEMANN R., OLSETH J., PIERNAVIEJA G., REISE C., WALD L., HEINNEMANN D., "Rethinking satellite based solar irradiance modelling – the SOLIS clear sky module", *Remote Sensing of Environment*, vol. 91, pp. 160–174, 2004.

[MUE 09] MUELLER R., MATSOUKAS C., GRATZKI A., BEHR H., HOLLMANN R., "The CM-SAF operational scheme for the satellite based retrieval of solar surface irradiance – A LUT based eigenvector hybrid approach", *Remote Sensing of Environment*, vol. 113, pp. 1012–1024, 2009.

[OUM 09a] OUMBE A., BLANC P., RANCHIN T., SCHROEDTER-HOMSCEIDT M., WALD L., "A new method for estimating solar energy resource", *Proceedings of the ISRSE 33,* Joint Research Center, Stresa, Italy, pp. 4, 4–9 May 2009.

[OUM 09b] OUMBE A., Exploitation des nouvelles capacités d'observation de la Terre pour évaluer le rayonnement solaire incident au sol, PhD Thesis, MINES ParisTech, pp. 137, 2009.

[OUM 11] OUMBE A., BLANC P., GSCHWIND B., LEFÈVRE M., QU Z., SCHROEDTER-HOMSCEIDT M., WALD L., "Solar irradiance in clear atmosphere: study of parameterisations of change with altitude", *Advances in Science and Research.*, vol. 6, pp. 199–203, 2011.

[PAR 88] PARIS M.V., JUSTUS C.G., "A cloudy-sky radiative transfer model suitable for calibration of satellite sensors", *Remote Sensing of Environment*, vol. 24, pp. 269–285, 1988.

[PAS 81] PASTRE C., "Développement d'une méthode de détermination du rayonnement solaire global à partir des données Meteosat", *La Météorologie*, Societé Météorologique de France, Paris, France, VI$^{e}$ série, N.24, 1981.

[PER 90] PEREZ R., INEICHEN P., SEALS R., MICHALSKY J., STEWART R., "Modelling daylight availability and irradiance components", *Solar Energy*, vol. 44, pp. 271–289, 1990.

[PER 93] PEREZ R., SEALS R., MICHALSKY J., "All-weather model for sky luminance distribution – preliminary configuration and validation", *Solar Energy*, vol. 50, pp. 235–245, 1993.

[PER 97] PEREZ R., SEALS R., ZELENKA A., "Comparing satellite remote sensing and ground network measurements for the production of site/time specific irradiance data", *Solar Energy*, vol. 60, pp. 89–96, 1997.

[PER 02] PEREZ R., INEICHEN P., MOORE K., KMIECIK M., CHAIN C., GEORGE R., VIGNOLA F., "A new operational model for satellite-derived irradiances: description and validation", *Solar Energy*, vol. 73, pp. 307–317, 2002.

[PIN 91] PINKER R.T., LASZLO I., "Effects of spatial sampling of satellite data on derived surface solar irradiance", *Journal of Atmospheric and Oceanic Technology*, vol. 8, pp. 96–107, 1991.

[QU 11] QU Z., BLANC P., LEFÈVRE M., WALD L., OUMBE A., "Study of the MLB parameterisation for change in surface solar irradiance with sun zenith angle in clear sky", *Advances in Sciences and Research*, vol. 6, pp. 233–236, 2011.

[RAS 87] RASCHKE E., GRATZKI A., RIELAND M., "Estimates of global radiation at the ground from the reduced data sets of the international satellite cloud climatology project", *Journal of Climatology,* vol. 7, pp. 205–213, 1987.

[RIG 00] RIGOLLIER C., BAUER O., WALD L., "On the clear sky model of the 4th European Solar Radiation Atlas with respect to the Heliosat method", *Solar Energy*, vol. 68, pp. 33–48, 2000.

[RIG 01] RIGOLLIER C., LEFÈVRE M., WALD, L., Heliosat version 2. Integration and exploitation of networked Solar Radiation Databases for environment monitoring (SoDa Project), Project: Integration and exploitations of networked solar radiation databases for environment monitoring, Contract Number: ST-1999-12245, available at http://www.helioclim.org, pp. 94, 2001.

[RIG 04] RIGOLLIER C., LEFÈVRE M., WALD L., "The method Heliosat-2 for deriving shortwave solar radiation data from satellite images", *Solar Energy*, vol. 77, pp. 159–169, 2004.

[ROB 96] ROBERTSON L., LANGNER J., ENGARDT M., "MATCH – Mesoscale Atmospheric Transport and Chemistry modelling system. Basic transport model description and control experiments with $^{222}$Rn", *Swedish Meteorological and Hydrological Institute Reports Meteorology and Climatology*, vol. 70, pp. 37, 1996.

[ROB 99] ROBERTSON L., LANGNER J., ENGARDT M., "An eulerian limited-area atmospheric transport model", *Journal of Applied Meteorology*, vol. 38, pp. 190–210, 1999.

[ROB 04] ROBINSON D., STONE A., "Solar radiation modelling in the urban context", *Solar Energy*, vol. 77, pp. 295–309, 2004.

[RUI 10a] RUIZ-ARIAS J., ALSAMAMRA H., TOVAR-PESCADOR J., POZO-VAZQUEZ D., "Proposal of a regressive model for the hourly diffuse solar radiation under all sky conditions", *Energy Conversion and Management*, vol. 51, pp. 881–893, 2010.

[RUI 10b] RUIZ-ARIAS J., CEBECAUER T., TOVAR-PESCADOR J., ŠÚRI M., "Spatial disaggregation of satellite-derived irradiance using a high-resolution digital elevation model", *Solar Energy*, vol. 84, pp. 1644–1657, 2010.

[SCH 89] SCHMETZ J., "Toward a surface radiation climatology: retrieval of downward irradiances from satellites", *Atmospheric Research*, vol. 23, pp. 287–321, 1989.

[TAR 79] TARPLEY J., "Estimating incident solar radiation at the surface from geostationary satellite data", *Journal of Applied Meteorology*, vol. 18, pp. 1172–1181, 1979.

[TER 95] TERRAINBASE, *Worldwide Digital Terrain Data*, Documentation Manual, NOAA, National Geophysical Data Center, Boulder, CO, USA, CD-ROM Release 1.0, 1995.

[THO 10] THOMAS, C., Caractérisation des aérosols atmosphériques en milieu urbain par télédétection à très haute résolution spatial, PhD Thesis, University of Toulouse (France), 2010.

[VER 97] VERMOTE E., TANRÉ D., DEUZÉ J., HERMAN M., MORCRETTE J., "Second simulation of the satellite signal in the solar spectrum, 6S: an overview", *IEEE Transactions on Geoscience and Remote Sensing*, vol. 35, pp. 675–686, 1997.

[WAH 10] WAHAB A.M., EL-METWALLY M., HASSAN R., LEFÈVRE M., OUMBE A., WALD L., "Assessing surface solar irradiance in Northern Africa desert climate and its long-term variations from Meteosat images", *International Journal of Remote Sensing*, vol. 3, pp. 261–280, 2010.

[WAL 07] WALD L., "Solar radiation energy (fundamentals)", Chapter 1 in BLANCO J., MALATO S., *Solar Energy Conversion and Photoenergy Systems*, Encyclopedia of Life Support Systems (EOLSS), developed under the Auspices of the UNESCO, Eolss Publishers, Oxford, UK, 2007.

[WMO 81] WMO, Meteorological aspects of the utilization of solar radiation as an energy source, Secretariat of the World Meteorological Organization, WMO-No.557, Geneva (Switzerland), Technical note No. 172, pp. 298, 1981.

[WMO 11] WMO, *Observing Stations and WMO Catalogue of Radiosondes*, World Meteorological Organization, Publication No. 9, vol. A, available at http://www.wmo.int/pages/prog/www/ois/volume-a/vola-home.htm, 28 November 2011.

[ZEL 92] ZELENKA A., CZEPLAK G., D'AGOSTINO V., JOSEFSON W., MAXWELL E., PEREZ R., Techniques for supplementing solar radiation network data, International Energy Agency, Technical report, IEA-SHCP-9D-1, Swiss Meteorological Institute, Zurich, Switzerland, 1992.

[ZEL 99] ZELENKA A., PEREZ R., SEALS R., RENNÉ D., "Effective accuracy of satellite-derived hourly irradiances", *Theoretical and Applied Climatology*, vol. 62, pp. 199–207, 1999.

Chapter 5

# Worldwide Aspects of Solar Radiation Impact

Any thermal state can be modeled as a system subjected to cyclic flows of mass and energy. The Earth is a sphere that is almost smooth, slightly flattened at the poles, and which rotates around the Sun on a slightly elliptical path. This is the largest thermal system that we have to deal with, the one that determines all the other systems such as territory, city, building, machinery, plant, or animal.

## 5.1. Global energy budget at the Earth level

The distance between the Earth and the Sun is about 150 million km (1 AU: astronomical unit) and the radius of the Earth is approximately 6,370 km. The Earth rotates in just less than 24 h (1 day) on it axis, and around the Sun in the ecliptic plane, with a period of about 365.25 days. The axis of the first rotation (which defines the two poles) is tilted 23.5º relative to the normal to the ecliptic plane. This obliquity determines the peculiar tropical latitudes (23.5º with respect to the equator) and the polar circles (23.5º with respect to the poles, and thus 66.5º from the equator).

The surface of the Sun behaves approximately like a blackbody with a temperature of 5,780 K. By Stefan–Boltzmann law, we deduce that a unit area located at the distance of 1 AU, set perpendicular to the sunrays, intercepts a power

Chapter written by Benoit BECKERS.

*Solar Energy at Urban Scale* Benoit Beckers

of 1,367 $Wm^{-2}$. The emitted spectrum has its maximum at 500 nm (wavelength of yellow perceived by the human eye) and is divided almost equally in visible light and near infrared ($\lambda < 4\mu$), with a small amount of ultraviolet.

The solar constant (1,367 $Wm^{-2}$) is equivalent to the average irradiance that can be captured in the vicinity of the Earth. It varies from about 6.9% during the year due to the elliptical shape of the Earth's orbit (1,412 $Wm^{-2}$ in early January to 1,321 $Wm^{-2}$ in July) and very little in the long term. Atmospheric absorption and inclination of the receiving surface relative to the direction of radiation generate significant weakening.

To deduce the average solar illumination of the planet, at the top of the atmosphere, it is sufficient to consider that the Sun sees the Earth as a disk, irradiated at a rate of 1,367 $Wm^{-2}$, but that radiation actually reaches a sphere of the same radius, and thus a four times larger area. The average sunshine is therefore 342 $Wm^{-2}$. It is understood that it is not uniform – the equator receives more than the poles – but this value is used to describe an average annual radiation balance for the entire earth–atmosphere system.

The balance is shown schematically in Figure 5.1. It has changed very little since the early work of [ROT 74] cited in [OKE 87] to the recent evaluations of [KIE 97, TRE 09]. The following results are adapted from the last reference (Appendix 3).

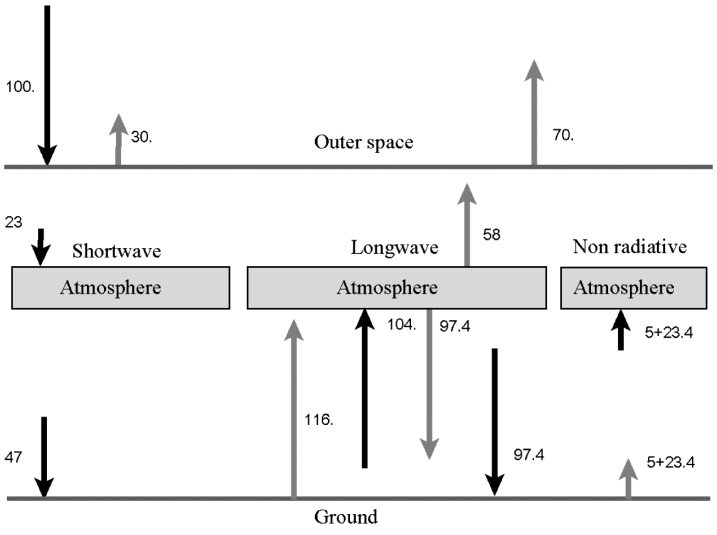


**Figure 5.1.** *Average rate of energy exchanges*

The top of the atmosphere, therefore, receives 342 $Wm^{-2}$. For clarity of reasoning, all flows are expressed as percentages of this value. Over the year, the same amount of energy that comes from the Sun must be lost to space by the earth–atmosphere system (EA). The clouds reflect back about 23% of the incoming flow into space and absorb about 23%, the remaining half reaches the Earth's surface, which reflects about 7% of the flow and absorbs the remaining 47%.

In total, 30% of the flux is reflected and therefore does not take part in the energy balance of the EA system. The atmosphere, which absorbs only a quarter of the flow, can be considered as semitransparent to shortwave solar radiation, and is therefore not heated by it. In contrast, almost half of the flux is absorbed at the surface of the Earth.

The Earth has an average temperature of about 288 K. It therefore emits in longwaves ($\lambda > 4\mu$); for this region of the spectrum, it behaves almost like a blackbody: snow, water, vegetation, or rock have an almost unitary emissivity in the far infrared.

The Earth's surface emits more in the range of longwave (116%) than it receives in the shortwave range above the atmosphere, because it also receives in the longwave emission of the atmosphere; in fact, only a small part of its emission escapes into space, while most of it is absorbed by the atmosphere (104%). The atmosphere radiates into space in longer wavelengths (70%) and to the surface of the Earth (97.4%), with a total of 167.4%.

In total, the EA system is in radiative equilibrium, since the solar irradiation (100%) is equal to the sum of shortwave reflection (30%) and longwave emission of the Earth and atmosphere (70%).

In contrast, the subsystems consisting of the Earth and the atmosphere are not in equilibrium. The Earth's surface receives 47% of the shortwave radiation, but its emission in the longwave is only 18.6% (116% to the atmosphere, from which it receives 97.4% back). On combining all the wavelengths, the Earth has a positive balance of 28.4%.

The atmosphere, however, wins 23% by absorption of clouds and constituents, but loses 51.4% in the longwaves (it absorbs 104% of the terrestrial surface, but emits 97.4 + 58 = 155.4% back to space and to the surface of the Earth). The balance of the atmospheric subsystem is negative: –28.4%.

Convection carries the excess energy from the Earth's surface to the atmosphere in the following proportions: 5% as sensible heat and 23.4% as latent heat. Finally, note that the conduction of heat in the soil is not involved because the net storage of heat in the Earth's surface does not vary over the annual period.

All these data are shown in more detail in Table 5.1 from [TRE 09]. They are reproduced in $Wm^{-2}$ and percentages. Their examination shows that the record is not entirely accurate; there is a slight excess of radiation absorbed by the Earth, which is equal to 0.9 $Wm^{-2}$.

| Trenberth *et al.* | $Wm^{-2}$ | % |
|---|---|---|
| Incoming solar radiation | 341.3 | 100 |
| Reflected solar radiation (a + b) | 101.9 | 30 |
| a) Reflected by clouds and atmosphere | 79 | 23.1 |
| b) Reflected by surface | 23 | 6.75 |
| Absorbed by surface | 161 | 47.2 |
| Absorbed by atmosphere | 78 | 22.9 |
| Thermals (sensible) | 17 | 5 |
| Latent heat | 80 | 23.4 |
| Surface radiation | 396 | 116 |
| Surface radiation to atmosphere | 356 | 104 |
| Surface radiation to sky | 40 | 11.7 |
| Outgoing longwave radiation | 238.5 | 70 |
| Emitted by atmosphere (and clouds) | 169 + 30 | 58.3 |
| Back radiation | 333 | 97.6 |

**Table 5.1.** *Average rate of radiative exchanges*

## 5.2. The distribution of solar radiation on the Earth's surface

Solar radiation reaches the Earth with a variable incidence (angle between the solar ray and the normal to the Earth's surface). This incidence increases as we move away from the Earth, i.e. axis of the Sun by going to the edge of the sphere. Because the axis of rotation of the Earth is tilted with respect to its orbit around the Sun, the Earth–Sun axis moves during the year and its position varies between the two tropics.

The Sun crosses the zenith a few days per year for all points between the tropics. As the Sun moves further away from the equator, the Sun drops over the horizon, and increases the contrast between the summer and the winter. At the poles, there is only 1 day and 1 night that share this throughout the year.

By calculating the irradiance on a horizontal plane at the top of the atmosphere as a function of latitude, we obtain the results summarized in Figure 5.2 [PET 06].

They correspond to the solar constant of 1,367 $Wm^{-2}$. The calculation is based on the actual elliptical orbit of the Earth (see Chapter 10). Note that the average daily irradiance is much greater during the southern summer than during the northern summer. This is because the Earth passes closer to the Sun earlier in the year than at the beginning of July. The irradiance varies inversely as the square of the distance, which leads to a maximum variation of 7% (Figure 5.2).

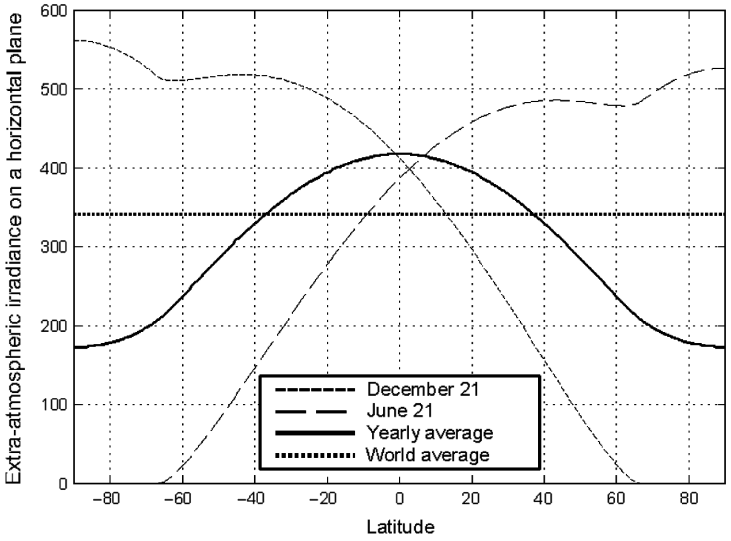


**Figure 5.2.** *Average daily solar irradiance ($Wm^{-2}$) above the atmosphere as a function of latitude during the solstices and on average over the year*

It should be noted that the result in Figure 5.2 is not valid at ground level. This is because, even during a sunny day, the atmosphere produces an attenuation of solar radiation, which depends on the orientation of the solar ray and therefore on the length of its path through the atmosphere [CAM 98].

### 5.2.1. *Consequence of the unequal distribution of sunshine*

The Earth is surrounded by an atmosphere whose composition varies with the altitude. There are several layers. The lowest is called the troposphere. Its thickness is on average equal to 12 km, but it reaches 15–20 km between the tropics and only 7–10 km at the poles [WAU 00, MON 07].

The non-uniform distribution of solar radiation causes atmospheric advection currents that tend to balance important air masses [WAL 06]. Hotter zones near the

equator give rise to significant thermals that reach the limits of the troposphere where the air is pushed toward north or south. Indeed, in the region between the tropics, annual average irradiance at the top of the atmosphere is nearly 30% higher than at 40º latitude and 50% higher than at 50º latitude.

The air mass gradually cools as it moves toward the poles. In the absence of other phenomena, we can imagine an upper flow from the equator to the poles and a return toward the equator in the lower layers of the atmosphere (Hadley cell). This situation is observed on the planet Venus, where there is a single Hadley cell in each hemisphere.

### 5.2.2. *Effect of the Earth's rotation*

Because of the influence of the Earth's rotation, which deflects the atmospheric motions clockwise in the Northern Hemisphere and anticlockwise in the Southern Hemisphere, the movement is more complex and takes place on the basis of the tricellular atmospheric model [WAU 00].

The deviation caused by the Coriolis force can easily be explained. First note that the tangential velocity of a point on the Earth is oriented from west to east. On the equator, it is equal to 40,000 km per 24 h = 1,666 $kmh^{-1}$ or 463 $ms^{-1}$ (faster than the speed of sound: 340 $ms^{-1}$ at sea level). This speed varies with latitude $\alpha$, it is equal to $v_{equator}\ cos\ \alpha$ (at 60º latitude, it is thus equal to half its value on the equator).

In the Northern Hemisphere, the tangential velocity of a point on the Earth therefore decreases as we travel northward. However, the airstream will keep the same speed, implying that the Earth is behind the movement and that air moves eastward (right) in the terrestrial frame. While traveling north–south, the air stream is delayed, since the linear velocity of the soil increases, so the stream deflects westward (right). In the Southern Hemisphere, the phenomenon is reversed.

The terrestrial sphere is subjected to regimes of low pressure at the equator and between parallels 60º north and south. High pressures are present between the parallels 30º and also in the northern and southern poles. Warm air rises in the equatorial low pressure zone, and then it cools as it moves in higher altitudes to the north. It goes down into areas of high pressure located just north of the tropic and returns toward the equator as the trade winds. Except in the equatorial zone, where its effect is not perceptible, the Coriolis force deflects winds clockwise in the Northern Hemisphere and anticlockwise in the Southern Hemisphere. In the Northern Hemisphere, the winds blow from the northeast and head toward southwest.

The atmospheric movement we could observe in a meridian plane is shown schematically in Figure 5.3. It shows the three conventional cells: Hadley, Ferrel, and Polar cell. In the equatorial zone, the movement is fairly stable, but it is not the same in areas closer to the poles, where oscillations are occurring.

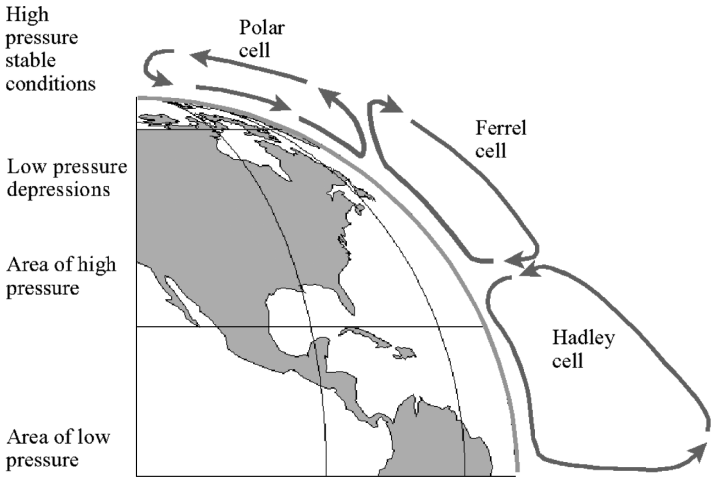


**Figure 5.3.** *Tricellular model of atmospheric circulation*

Movements therefore tend to follow trajectories similar to those shown in Figure 5.4. In this figure, the parallels drawn in dotted lines represent the tropics; those drawn in solid lines correspond to latitudes of ±30º and ±60º.

The local climates depend in first approximation on the latitude. The equator is hot and humid (with the large forests of Amazonia, the Congo, and Indonesia), while the tropics, subject to the rules of the trade winds, are divided between humid climates, where these are found near the sea, and the driest climates in the world. The largest deserts in the world (Sonora, Sahara, Gobi in the Northern Hemisphere; Atacama, Kalahari, and Australia in the Southern Hemisphere) are found around the tropics. Between 30º and 40º latitude, deserts can still be found, but the warm temperate climate of the Mediterranean is also seen.

This pattern of air currents can be explained by the distribution of solar irradiance at ground level as a function of latitude. Indeed, we see that the maximum irradiance occurs in the tropics. This is because cloud cover is always important at the equator (low-pressure area) and is generally low in the tropics (high-pressure areas).

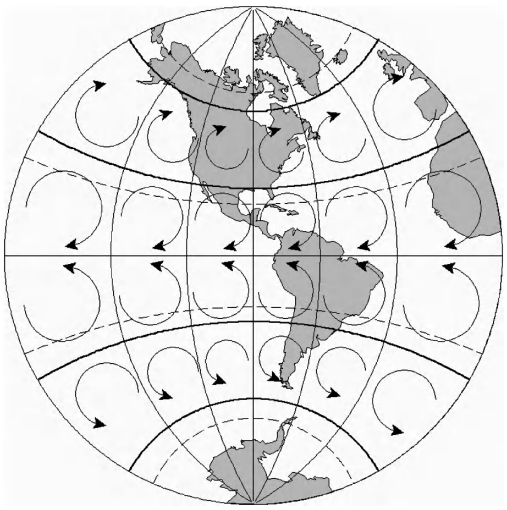

**Figure 5.4.** *Deformation of the streamlines of the atmospheric circulation*

### 5.2.3. *Influence of continental masses*

The climate is also influenced by the proximity of the oceans and the presence of major marine currents. The distribution of land and ocean is very different in both the hemispheres [GOD 09]. This is clearly seen in Figure 5.5. To make the figure readable, we use the equal-area azimuthal projection, also known as Lambert projection, which respects the proportions of areas. This uneven distribution combined with the action of air currents is the cause of ocean currents.

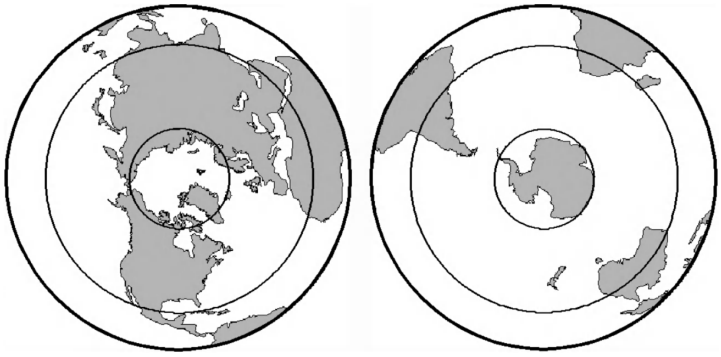

**Figure 5.5.** *Comparison of land and sea areas in both the hemispheres*

The cold-temperate zone starts at around 50º. In the Southern Hemisphere, there is not much land, while the Northern Hemisphere extends to a polar region where the populations are still significant. At the same latitude, Europe is favored by the Gulf Stream circulation, especially compared to the east coast of North America, which suffers the opposite effects (New York, as well as Rome, Barcelona, and Beijing, where it snows regularly in winter, is at 40º north latitude). The Humboldt Current strongly cools down the Pacific off Chile and Peru. The occurrence of cyclical and complex phenomena, like El Niño and La Niña, is just beginning to be incorporated into global climate models. They show how local thermal imbalances can have consequences far away, for example on the monsoon regime in India or on drought in East Africa.

### 5.3. The Sun at different latitudes

To compare the positions of different geographic locations, we perform a Postel projection [SNY 97] (often called azimuthal equidistant). In this projection, the meridians are not deformed, which means that a distance measured along the north–south direction is seen without distortion. Applied as one image to the whole Earth, it appears on the UN flag. Here, the Southern Hemisphere is a superposed on the Northern Hemisphere as a mirror image (Figure 5.6). The equator, the tropics, and the polar circles are drawn in solid lines, while the 40º and 50º parallels are shown as dashed lines.

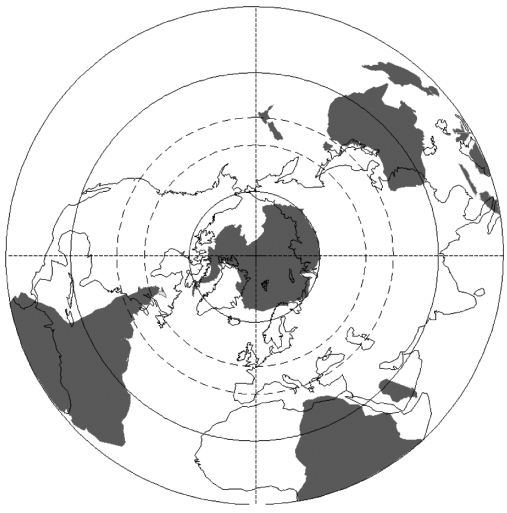

**Figure 5.6.** *Superposition of both hemispheres in a Postel projection*

It is observed that Africa withdraws into itself, and it does not reach the Southern Hemisphere latitudes that Europe covers in the Northern Hemisphere. The southern "cone" of Latin America retreats to Quebec (the two regions share the same time zone), just beyond to the 50th parallel. The Australian continent, like Africa, remains below the 40th parallel.

## 5.4. The solar diagrams

The solar diagram used here is a stereographic projection of the sky vault. The center of the circle represents the zenith, and its circumference the horizon. Solar paths are represented on the simplified circular model of the Earth's orbit (see Chapter 10), and we consider the solar time (the Sun reaches its highest position just at noon).

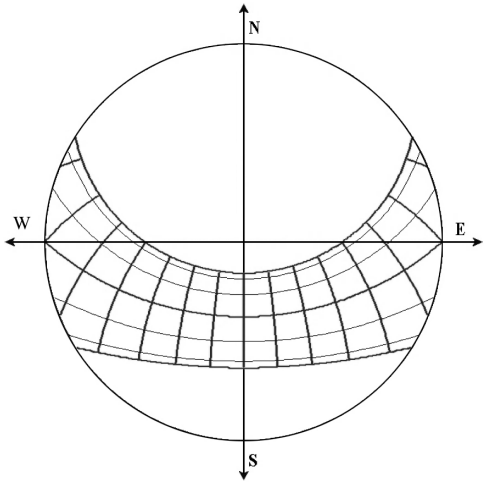


**Figure 5.7.** *Solar diagram in Barcelona* (*41:18:07 N*)

The months are represented by circular arcs centered on the vertical axis. They show the trajectories of the Sun on the 21st day of each month. Three of them appear here in bold: the closer to the center corresponds to the summer solstice (June 21), the second to the equinoxes (March 21 and September 21), the lower is the winter solstice (December 21). The interleaved black lines match two months: they can be read downward (July, August, October, and November) or upward (January, February, April, and May).

The curves of hours (solar hours), orthogonal to those of months, are easily identified if we follow them along the equinox, since the day, wherever we are, lasts

for exactly 12 h. The first curve that intercepts the equinox path at the east corresponds to 6.00 a.m., the middle curve (on the vertical axis) to solar noon, and the last, at the west, to 6.00 p.m.

In Barcelona, at the solstices, the Sun rises at 4.30 a.m. in summer and at 7.30 a.m. in winter. It sets, respectively, at 7.30 p.m. and 4.30 p.m. The amplitude of diurnal variation between the summer and winter is 6 h.

At latitudes close to that of Barcelona, near the 40th parallel, we find Rome, Istanbul, Beijing, Denver, and New York in the Northern Hemisphere, and Melbourne, Wellington, Valdivia, and Bahia Blanca in the Southern Hemisphere.

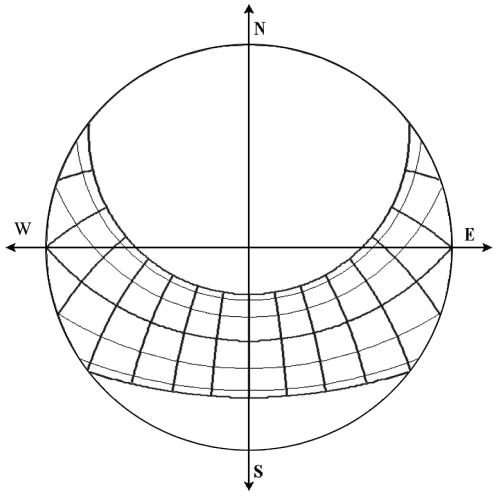


**Figure 5.8.** *Solar diagram in Paris (48° 52′ N)*

In Paris, the days are longer in summer (1 h more) and shorter in winter (1 h less). The amplitude of diurnal variation between the summer and winter is 8 h. Paris, like Barcelona, is located in the temperate climate zone, within which there are already significant variations in the solar path.

At latitudes close to that of Paris, near the 50th parallel, we find in the Northern Hemisphere places such as, Prague, London, Vancouver, and Winnipeg. In the Southern Hemisphere, this parallel intersects Chile and Argentina (up to Santa Cruz) and passes well below Africa.

In the Northern Hemisphere, the Arctic Circle passes right over Iceland. In summer, there is a 24 h day (June 21): from this latitude, we can see the midnight

Sun. Conversely, at the winter solstice, there is a night of 24 h: the dawn is immediately followed by the twilight. The line indicating the Sun path is reduced to a point.

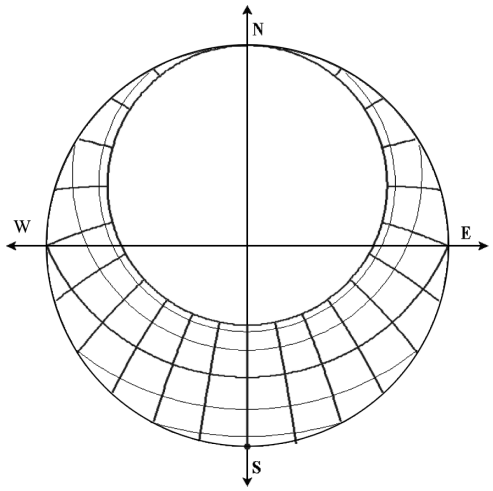


**Figure 5.9.** *Solar diagram on the Arctic polar circle (66.5° N)*

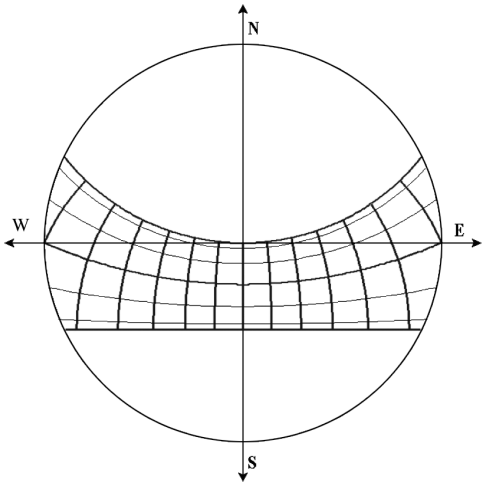


**Figure 5.10.** *Solar diagram on the Tropic of Cancer (23° 30′ N)*

At a point located on the tropic, the Sun shines in the zenith on the day of the summer solstice. Otherwise, at noon, it is always located in the south. Between the

tropics, the Sun passes the zenith twice a year. Hence, the summer solstice is the longest day of the year, but it is not the day when the Sun rises the earliest. In the Northern Hemisphere, around that time, the Sun is north at noon and it is south the rest of the year. In the Southern Hemisphere, the opposite is true.

At latitudes near the tropic, we find in the Northern Hemisphere Mazatlan, Havana, Tamanrasset, Aswan, Canton, and Hong Kong; and Antofagasta, Sao Paulo, and Alice Springs in the Southern Hemisphere.

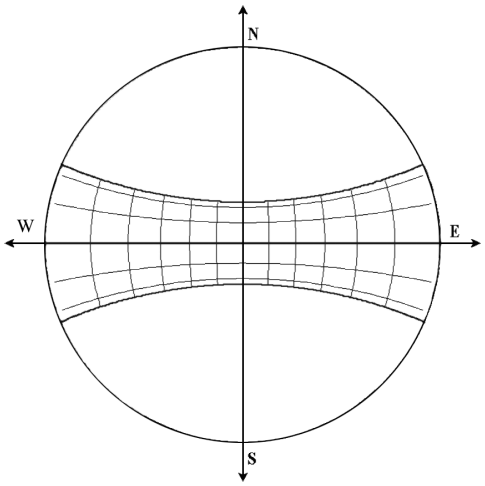


**Figure 5.11.** *Solar diagram on the equator (0°)*

On the equator, the length of days and nights are invariably 12 h. From March 21 to September 21, the Sun is always north, from dawn to dusk. The other half of the year, it is always south. It reaches the zenith at the two equinoxes. At latitudes close to the equator are Quito, Belem, Libreville, Kisangani, Kampala, and Singapore.

## 5.5. Climate and housing

Traditional housing shows very constant properties according to the latitude, because of the necessary adequacy of the resources with respect to the prevailing thermal conditions [ROD 07]. At the equator, where the climate is hot and humid, only ventilation brings comfort. Also, the traditional houses are virtually devoid of walls. The roof is sufficient protection from the almost overhead Sun at noon and from frequent rains. In the humid tropics, it is virtually the same, but we often find that the roofs extend slightly to the south or the north – depending on whether the location is, respectively, in the Northern or Southern Hemisphere – to protect the

windows from the Sun at noon, as it rises lower in the sky in December (Tropic of Cancer) or June (Tropic of Capricorn). Ancient cities were built in the rainforest (by Maya and Khmer civilizations, for example), but they have never resisted the long-term influence of the forest, and they finally had very little influence on modern cities in these regions.

In the dry tropics, and in the Oases or on the shores of the immense deserts, which expand around them, where the climate is dry, with large temperature differences between day and night, the inertia factor brings people relative comfort. The traditional housing, clay or stone, and sometimes half-buried, consist of thick walls, with tiny windows (to protect against scouring winds), topped with roof terraces (little rain), or shaped domes (to increase the contact surface with the sky). The urban structures are welcome because they provide shaded lanes protected from winds, shared walls, and thus further increased inertia. So is it not surprising that the first known cities were built in this climatic zone, in the Fertile Crescent. An important part of humanity still lives in such cities where the houses are built with local materials such as mud bricks, adobe, etc.

The warm temperate climate of the Mediterranean, with its low temperature range throughout the year and its particularly mild temperatures, provides an ideal thermal frame for architecture. The ability to control the building shapes and to use the alternation of shadow and light allows us to take advantage of the winter sunshine and protect from excessive insolation during the summer. It can pretty much help us avoid heating and cooling equipment. The open squares can generate thermal streams (through ventilation) and checkerboard neighborhoods allow the Sun to sweep the streets from morning to night. Classical Greece has left the first evidence of the thought on proportions and the use of shading in architecture and urban planning. The first megacities – Alexandria, Corinth, Rome, and Constantinople – were built in this climate. During the mid-19th Century, the Cerdà plan for the expansion of Barcelona was still classical in style (ideal orientation of streets and facades for sunshine), but its justification comes from modern theories on hygiene.

To the north of the Alps and Pyrenees, the cold temperate climate, with its severe winters, makes heating almost indispensable. Since the late Middle Ages, glazing completed building insulation, while allowing for better solar gain and a greater availability of natural light. From the early 19th Century, in London and Paris, the two major cities of that time, the first effects of the urban heat island (UHI) became noticeable. The relatively mild climate of Western Europe led to the development of large cities on the outskirts of the 60th parallel (St. Petersburg, Stockholm, Oslo), and even beyond. The first oil crisis in 1973 forced the rapid improvement of insulation (double and triple glazing, insulation techniques from the outside, and so on) and the adoption of increasingly restrictive standards.

Initially, European countries, followed by America and Asia, have adopted thermal and environmental regulations that are very specific and depend on their climates and available construction techniques (e.g. by favoring insulation over inertia). Today, the competition between the major suppliers involved at international level (e.g. BREEAM, LEED, and HQE for environmental quality) press on generalizing the meaning of these standards and the underlying calculation methods, adopting them for all climates. To do so would require better control of building physics, especially the effects of the combination of insulation, inertia, ventilation, shading, equipment, and usages (dynamic tools). However, the first difficulty is to properly take into account the urban environment.

In the late 19th Century, the invention of the elevator allowed us to build towers forming extremely dense neighborhoods, with the widespread use of new building materials (glass and steel), first on Manhattan Island, then in other cities of the USA. It is also in Manhattan that we proposed the first regulations limiting the building envelope, including rules to avoid excessive shading of streets and existing buildings [KOO 78]. In the second half of the 20th Century, the neighborhoods of skyscrapers have spread across America, in some European city centers, South East Asia (Hong Kong and Singapore [KOO 95]), and around the whole world. However, the parallel development of the automobile had an adverse effect on the urban sprawl with an uncontrolled development pressure [DUA 10], which is now one of the major problems facing humanity (urban encroachment on agricultural land).

With a population that is now predominantly urban (since 2008 for most of the world, since 2011 in China, see: www.unhabitat.org), it becomes necessary to densify the cities. To establish a regulatory framework that incentivizes and is balanced, it is important to understand the effects of densification on the physics of the city and on the quality of urban environments.

### 5.6. Solar energy at the urban scale

The study of the building environment and of the urban district immediately raises problems of scale. Thus, a few tens of percent of the sky are usually visible from the open space, so that it falls rapidly to a few percent from inside. It may therefore be a factor of ten, or even a one-hundred factor, between the lighting of a street and that of an interior. However, in terms of natural light, nothing is insignificant, because the eye can adapt and perceive very low levels: a sky view factor of 1% may be sufficient to avoid artificial lighting during the day.

In the first part of this book (Chapters 1–4), recent advances in terrestrial and satellite measurements as well as in the definition of sky models have been widely described. However, we know that the uncertainty in the description of the “heaven”

(coming from measurements or models) strongly increases when the view of the sky becomes weaker [TRE 99]. Simulating the illumination of the interiors in a neighborhood from data collected in open space (e.g. a measuring station on a roof) is, therefore, not a simple problem.

By equipping the windows of a building for adequate Sun protection, it is easy to accede to the Sun when it is welcome in winter, and to hide it in summer. It is also necessary that the urban environment makes it possible to place the windows at the right place, with a little view of the sky or at least a clear opposite facade that is able to reflect light. The problem is much more difficult in the streets because the sky is easily visible: the summer Sun is likely to enter the street much easier than the winter Sun. In older cities, this problem was often solved by covering part of the street with arcades or nets filtering the light. It has also been shown that in hot arid climates, compact street canyons improve pedestrian comfort, particularly if they are oriented north–south [ERE 11]. The wider streets arranged for motorized traffic made these remedies quite impossible, and, in most historic cities, older districts provide thermal comfort and lighting, which are now missing in newer neighborhoods.

In temperate climates, a typical modern solution consists of using deciduous trees, as they provide shade in summer and are quite transparent in winter. However, urban vegetation brings a lot of problems, and the overall energy balance is not easy to produce (see Chapter 7). Today, when the wind does not interfere, the energy fluxes are properly simulated. Excellent results are confirmed by the measurements, in relatively simple geometries, such as urban canyon (Chapter 6).

The work carried out by the researchers of Cerma [HÉN 11] corresponds to this trend. Their software simulates the sunshine, evaluates the effects of multiple reflections for shortwave (the classic way consists of solving the radiosity equations), and finally calculates the whole heat exchanges by taking into account the radiative thermal emissions and the temporal evolutions.

These simulations usually involve the optical behavior and the stream [VIN 00] of the air. A delicate point is always the consideration of the boundary conditions. Other non-trivial points are glazing [MIG 02] and concerns of reflective surfaces.

To calibrate the digital mock-ups, it is imperative to compare the measurements. This was done on large-scale models (using containers) [IDC 10] and on districts in cities: Marseille [HÉN 11, MES 05] in the CLU ESCOMPTE project: “Couche Limite Urbaine Expérience sur Site pour COntraindre les Modèles de Pollution atmosphérique et de Transport d’Emissions,” (Urban boundary layer on site experiment to constrain models of Air Pollution and Emissions Transport) and

Toulouse [LAG 12], in the Capitoul experience: (Canopy and Aerosol Particles Interactions in Toulouse Urban Layer). Experimental efforts were undertaken both to increase the knowledge on urban climate and to get sets of observations for the evaluation of numerical models [MES 05, PIG 07].

If the physical model is reliable and if all the constraints of the problem can be formulated, a further step is affordable. It consists of performing shape or topology optimization at the district level [KÄM 09, ROB 11]. The main advantage of this kind of initiative is to generate a lot of valuable information for further design.

Other methods are functioning at the territorial level (a few hundred kilometers). They are using atmospheric models to evaluate the impact of urban buildings on airflow and to evaluate the dispersion of pollutants [MAR 02]. Clappier *et al.* have presented analyses of these phenomena in several cities located in a wide range of geographic zones [TUI 07].

## 5.7. Conclusions and perspectives

In this chapter, it was shown that the astronomical data (surface temperature of the Sun and double-rotation of the Earth), combined with the very general information on the composition of the atmospheric layers and the Earth's surface, are sufficient to explain the main features of the climate prevailing on our planet. A more detailed description must then involve the distribution of emerged land masses, the changes in ocean salinity, and the major air and ocean currents. The continual enrichment of climate models can now state the problem of the interaction between global climate and human activities.

With more than seven billion people being now mostly urban, all the cities and human infrastructures that cover a part of the Earth's surface may no longer be considered negligible. By their mere presence and the activities they generate, our cities thus appear as potential modifiers of climate. Now we probably cannot consider these cities as simple rough surfaces, as we would do with a forest, for instance. The vertical urban dimension, highly variable between cities and within the same city, modifies substantially the different radiative and conductive important parameters: albedo, infrared emission, thermal inertia, not to mention sensitive (winds) and latent (evapotranspiration) energy flows.

Moreover, cities are of interest both for themselves and for the atmosphere they create. They also provide a climatic interface between the buildings themselves and the territory that encloses them. From the perspective of urban policies, new

problems arise. By limiting ourselves to solar energy, we can mention the passive potential (influence of the solar input on the urban environment, and hence on the thermal performance of buildings), the active potential (bearing roofs and facades with thermal and photovoltaic solar panels), the impact of a new building (especially for Sun and sky access of surrounding buildings), the distribution of natural light (comfort, esthetics, but also control of lighting consumption), and not forgetting the participation of radiative exchange in the formation of the UHI.

Being confined, initially, to the study of solar energy and radiative exchanges offers significant advantages. As discussed in the third part of the book, it helps to first develop consistent simulations based on numerical models that are now well understood (radiosity, ray tracing). In fact, most of the works referred to in this chapter were made possible by using software originally designed to study the radiative exchange of daylight throughout the building. These problems being less sensitive to the change of scale (in contrast with the problems of fluid mechanics), it was natural to move from the building to the neighborhood and, due to the progress in computer software and hardware, from the neighborhood to the entire city.

In general, the first results of these works are not yet advanced enough to develop their practical applications across urban policies. However, the ability to better qualify and quantify the different radiative phenomena will enrich our understanding of urban physics in general, and provide a guide for more comprehensive studies that are not yet really feasible today (the study of coupled physical phenomena on 3D urban exhaustive models).

Solar energy has another advantage: it is easy to realize studies in all latitudes. Sun paths and solar radiation on clear days are obviously predictable. Databases now exist to take into account the cloud cover around the world. It is therefore natural to compare cities and projected designs (orientation of solar panels and streets, shape optimization, etc.). This is a very important point, because we find that, in general, the largest studies of urban physics were concentrated in cities of the richest countries, where the experimental means are available, while the urban planning problems focus, meanwhile, on the poorest countries, where urban growth is highest, particularly in the tropical zone.

In general, the exorbitant cost of the long duration measurement campaigns in urban areas and the substantial challenges facing their implementation, require numerical simulation for decision support (quantification) and aided design (optimization). Simulations of solar radiation software offer the first truly universal examples of tools capable of providing local and original solutions for improving energy efficiency and comfort in each of our cities, worldwide.

## 5.8. Bibliography

[CAM 98] CAMPBELL G.S., NORMAN J.M., *An Introduction to Environmental Biophysics*, Springer, New York, 2nd ed., 1998.

[DUA 10] DUANY A., PLATER-ZYBERK E., SPECK J., *Suburban Nation: The Rise of Sprawl and the Decline of the American Dream*, North Pint Press, 10th Anniversary ed., 2010.

[ERE 11] ERELL E., PEARLMUTTER D., WILLIAMSON T., *Urban Microclimate – Designing the Spaces between Buildings*, Earthscan, 2011.

[GOD 09] GODARD A., TABEAUD M., *Les Climats: Mécanismes, Variabilités, Répartition*, Armand Colin, 4th ed., pp. 210, 2009.

[HÉN 11] HÉNON A., MESTAYER P.G., GROLEAU D., VOOGT J., "High resolution thermo-radiative modeling of an urban fragment in Marseilles city center during the UBL-ESCOMPTE campaign", *Building and Environment*, vol. 46, pp. 1747–1764, 2011.

[IDC 10] IDCZAK M., GROLEAU D., MESTAYER P., ROSANT J.-M., SINI J.-F., "An application of the thermo-radiative model SOLENE for the evaluation of street canyon energy balance", *Building and Environment*, vol. 45, pp. 1262–1275, 2010.

[KÄM 09] KÄMPF J.H., On the modelling and optimisation of urban energy fluxes, Doctoral Thesis, Ecole Polytechnique Fédérale de Lausanne, Switzerland, 2009.

[KIE 97] KIEHL J.T., TRENBERTH K.E., "Earth's annual global mean energy budget", *Bulletin of the American Meteorological Society*, vol. 78, no. 2, pp. 197–208, 1997.

[KOO 78] KOOLHAAS R., *Delirious New York: A Retroactive Manifesto for Manhattan*, Oxford University Press, New York, pp. 320, 1978.

[KOO 95] KOOLHAAS R., "Singapore songlines, Portrait of a Potemkin metropolis or thirty years of tabula rasa", in KOOLHAAS R., MAU B. (eds), *S, M, L, XL*, The Monacelli Press, New York, pp. 1008–1089, 1995.

[LAG 12] LAGOUARDE J.P., HÉNON A., IRVINE M., VOOGT J., PIGEON G., MOREAU P., MASSON V., MESTAYER P., "Experimental characterization and modelling of the nighttime directional anisotropy of thermal infrared measurements over an urban area: case study of Toulouse (France)", *Remote Sensing of Environment*, vol. 117, pp. 19–33, 2012.

[MAR 02] MARTILLI A., CLAPPIER A., ROTACH M., "An urban surface exchange parameterization for Mesoscale models", *Boundary-Layer Meteorology*, vol. 104, pp. 261–304, 2002.

[MES 05] MESTAYER P.G. *et al.*, "The Urban Boundary-Layer Field Campaign in Marseille (UBLCLU-Escompte) set-up and first results", *Boundary-Layer Meteorology*, vol. 114, pp. 315–365, 2005.

[MIG 02] MIGUET F., GROLEAU D., "A daylight simulation tool for urban and architectural spaces – application to transmitted direct and diffuse light through glazing", *Building and Environment*, vol. 37, pp. 833–843, 2002.

[MON 07] MONTEITH J.L., UNSWORTH M.H., *Principles of Environmental Physics*, Elsevier, 3rd ed., 2007.

[OKE 87] OKE T.R., *Boundary Layer Climates*, Methuen & Co, New York, 2nd ed., 1987.

[PET 06] PETTY G.W., *A First Course in Atmospheric Radiation*, Sundog Publishing, 2nd ed., pp. 456, 2006.

[PIG 07] PIGEON G., Les échanges surface-atmosphère en zone urbaine – Projets clu-escompte et Capitoul, Doctoral Thesis, Université Paul Sabatier, Toulouse III, 2007.

[ROB 11] ROBINSON D., *Computer Modelling for Sustainable Urban Design. Physical Principles, Methods & Applications*, Earthscan, London, pp. 320, 2011.

[ROD 07] RODRÍQUEZ DE SANTIAGO D., El juego de las geometrías bajo el sol, Master Thesis, Fundación UPC, Barcelona, 2007.

[ROT 74] ROTTY R.M., MITCHELL J.M., "Man's energy and the world's climate", *67th Annual Meeting American Institute of Chemical Engineers*, Washington, D, 1974.

[SNY 97] SNYDER J.P., *Flattening the Earth: Two Thousand Years of Map Projections*, University of Chicago Press, 1997.

[TRE 99] TREGENZA P.R., "Standard skies for maritime climates", *Lighting Research and Technology*, vol. 31, no. 3, pp. 97–106, 1999.

[TRE 09] TRENBERTH K.E., FASULLO J.T., KIEHL J., "Earth's global energy budget", *Bulletin of the American Meteorological Society*, vol. 90, pp. 311–323, 2009.

[TUI 07] TUIA D., OSSÉS DE EICKER M., ZAH R., OSSES M., ZARATE E., CLAPPIER A., "Evaluation of a simplified top-down model for the spatial assessment of hot traffic emissions in mid-sized cities", *Atmospheric Environment*, vol. 41, pp. 3658–3671, 2007.

[VIN 00] VINET J., Contribution à la modélisation thermo-aéraulique du microclimat urbain. Caractérisation de l'impact de l'eau et de la végétation sur les conditions de confort en espaces extérieurs, Doctoral Thesis, Ecole Centrale de Nantes and Nantes University, France, pp. 245, 2000.

[WAL 06] WALLACE J.M., HOBBS P.V., *Atmospheric Science An Introductory Survey*, Elsevier, 2nd ed., 2006.

[WAU 00] WAUGH D., *Geography: An Integrated Approach*, Nelson Thornes, Gloucester, UK, 2000.

# Chapter 6

# Local Energy Balance

## 6.1. Introduction

With their large artificial surfaces, and under some special meteorologic conditions, towns are able to significantly transform the characteristics of the atmosphere with which they are in contact with. They give rise to a special behavior of the atmospheric boundary layer whose characteristics are different from those of the surrounding rural zones with regard to their temperatures, water vapor content, and so on [HEI 79, LAN 81, OKE 87a]. Urban climate specialists distinguish several atmospheric layers in and over a city:

(i) between the soil and the average roof level they identify the urban canopy layer (UCL), which can be highly fragmented by the alignment of the buildings and is not necessarily a continuous layer. In this case, its air volumes are disconnected with each other and confined into urban "canyons" in which they can interact only at the crossroads. UCL is also the most influenced atmospheric layer since it is in close contact with the urban objects at its base (like roads) and laterally (the facades); and

(ii) between the average roof level to a level of altitude (sometimes several hundreds of meters high), the urban boundary layer (UBL) is more or less influenced by the roofs and by the air crossing the top of the underlying UCL. The behavior of these two layers is very different across the rural zones and especially during sunny days with weak winds. Under these weather conditions they give rise to special phenomena like the urban heat island (in the UCL) during the night [ARN 03] and the formation of an urban plume (in the UBL) downwind of the city [RAI 07].

---

Chapter written by Pierre KASTENDEUCH.

*Solar Energy at Urban Scale* Benoit Beckers

Because of the great influence exerted by the ground on the lower atmospheric levels, the numeric weather models working from meso- to microclimate scales must take into account the ground atmosphere transfers. This is of great importance because it greatly improves the numeric weather prediction of local phenomena like mountain breezes [KAS 00] and in terms of temperature, vapor pressure, etc. [PIT 03, ARN 03]. However, to be able to properly simulate the soil–biosphere–atmosphere interactions, the models must resolve the energy and the water balance equations for the various types of objects that make up the ground (towns, lakes, vegetated areas, etc.).

The energy balance is a principle that is based on the conservation of energy, and it is a physical concept according to which energy cannot be created or destroyed, but only be modified into different forms. This principle can be translated into a mathematical form by a very simple equation called the energy balance equation:

$$\text{Change in Body Stores} = \text{Energy in} - \text{Energy out} \qquad [6.1]$$

The change in internal energy of a body must be equal to the difference between its intake and output. The simplicity of this equation is deceiving because energy can take a number of different forms (e.g. kinetic energy, thermal energy, electromagnetic energy, etc.), can be transformed from one form into another, and can be transferred through different ways (e.g. sound, heat, radiation, etc.). Nevertheless, some physical processes can be eliminated or neglected in some cases because they are not of interest or because they carry a very small amount of energy. From the point of view of weather modeling, several energy transfers must absolutely be taken into account: latent heat flux (evapotranspiration or condensation), ground heat flux (conduction), sensible heat flux (convection), and radiation.

## 6.2. Soil–vegetation–atmosphere transfer model

The terms of the energy balance equation must be evaluated for different types of objects that can be found in the UCL. From a numerical point of view, it is the task of the soil–vegetation–atmosphere transfer model, which is a special program also commonly called “surface scheme”. This program is implemented as a subroutine into the atmospheric weather models where its main role is to reproduce the interactions between the ground and the atmosphere in terms of friction, heat, and moisture fluxes [MAS 00, MIN 10, SEL 86]. In surface schemes implemented in mesoscale atmospheric models running on rather large simulation domains (dozens to hundreds of kilometers) (see [DUP 06, KUS 01, MAS 00]), the ground is generally described by its topography (altitudes), by the way of indices (e.g. the H/W ratio for urban areas), the land use (percentages of water, vegetation, etc.), characteristic dimensions (e.g. mean height of the roofs and trees), and its physical

properties (thermal conductivity, etc.). The algorithms implemented in this kind of surface scheme take advantage of this situation because some of them can be simplified or parameterized (especially the radiative transfers that occur in the urban canyons).

However, when the simulation domain becomes very small and when the horizontal resolution increases (to investigate the characteristics of flow field or pollutant dispersion inside urban street canyons or around the buildings, for example), microscale atmospheric models are employed [EHR 00, LET 08, XIE 08]. This kind of simulation model is particularly useful in architecture, urban planning, or for pollution studies (see [WAL 02]). At these resolutions, the ground must be depicted with more details and the objects are explicitly introduced and described with their real physical appearance [DEL 04, MIL 97, ROB 06]. This is the reason for the complexity of the associated surface schemes. The relative positions of the objects completely modify the radiative energy they can receive from their surroundings. The radiative exchanges must be explicitly resolved [KAS 06, KAS 09].

The idea is then to couple a surface scheme that is able to work with the real geometry of a city with a mesoscale model, which can run on a sufficiently large simulation domain to simulate the UBL. In the following sections, the procedure to simulate the energy balance in an urban environment is explained for such a surface scheme. The text is illustrated with the results of a simulation performed for an urban district of Strasbourg (France). To demonstrate the ability of the scheme to simulate the energy transfers, the results are compared to the measurements taken from an experimental campaign [NAJ 04].

### 6.3. Physiographic data and boundary conditions

The quality of the energy balance equation terms will not only greatly depend on the physical equations included in the surface scheme, but also, to a lesser extent, on the "physiographic" data describing the simulation domain. It can be expected that working with real geometry improves the results. However, it is important to obtain the geometric information necessary to build up the simulation domain. Until the previous years, this information was not easily available at the scale of an entire urban area. Hopefully, nowadays, most of the towns possess their own three-dimensional archives and hence obtaining data has become easier (Figure 6.1). In these databases, the contours and the height of the buildings are generally available and sometimes more details such as the windows on the facades, the slopes of the roofs (flat or inclined), and the location of the lawns can be found. To preserve reasonable memory management and computation time, this information must be selected and reduced according to the scientific objectives of the simulation before

being introduced in the surface scheme. The available information is organized as a four-level hierarchic structure: (i) because the surface scheme is designed to work in coordination with a mesoscale atmospheric model in which the atmosphere is divided into quadrilateral boxes, the UCL is also divided into boxes of the same horizontal dimensions; (ii) each UCL box contains numerical objects (representing buildings, soil, etc.); (iii) each object is made up of a collection of planar polygons (facades, roofs, lawns, and roads); and (iv) at the finest level, the polygons are divided into small triangular meshes for which the energy balance equation is solved (the greater the number of meshes, the better will be the results and the longer will be the computation time).

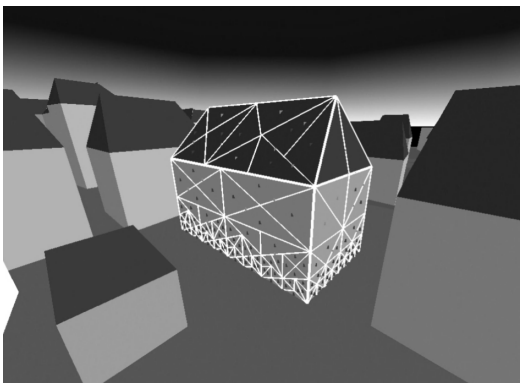

**Figure 6.1.** *An example of urban simulation domain for the use in a surface scheme that is able to take the real geometry into account. The breaking down of the objects into meshes is shown for a building*

To properly compute the energy balance of several kinds of elements, the objects are allocated to a small number of main types (terrain, building, water, etc.). This allows us to control the behavior of each object by a special set of equations according to its type (e.g. the thermal conductivity of the terrain can change according to its water content, but is constant for a building). To come closest to the reality, the polygons (roofs and facades) can be made with multiple layers of different materials. Of course, the thickness and the physical properties of these materials must be prescribed (e.g. density and thermal conductivity). As it is possible to precisely find all the physiographic data for small simulation domains, it can be more difficult to obtain data for large simulation domains that contain various types of structures (as for a district, or even a town). At these scales, assumptions (empirical generalization) must be made.

Once the simulation proceeds, it is necessary to impose the conditions that prevail at the boundaries of the surface scheme. They consist of several forcing

variables whose values must be known at each time step. The most important of these are the atmospheric and radiative constraints that prevail just over the roof level (Figure 6.2). The atmospheric forcing variables consist of the classic air temperature, wind speed, relative humidity, and so on; the radiative forcing variables consist of the horizontal atmospheric infrared radiation, the direct solar radiation (perpendicular to the sunbeam), and the horizontal diffuse solar radiation. As the UCL is divided into boxes, the boundary conditions must be prescribed at the top of each box. This information can be obtained in two ways: (i) from a weather model (when the surface scheme runs in association with such a model); and (ii) from measurements (when the surface scheme runs in stand-alone mode). When the boundary conditions are prescribed, the task of the surface scheme is to compute the state of the atmosphere and the radiative and energy exchanges into and out of the top of the UCL (i.e. the sensible heat flux).

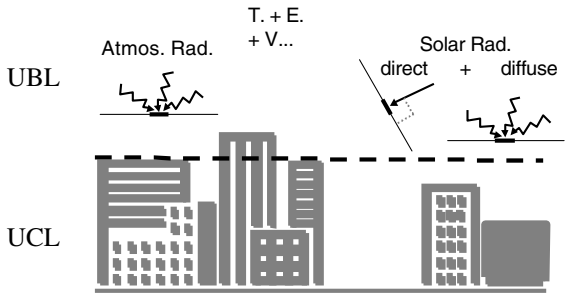


**Figure 6.2.** *Limit between the urban canopy layer (UCL) and the urban boundary layer (UBL). The radiative and atmospheric constraints necessary to conduct a simulation are given at the bottom of the UBL: infrared horizontal atmospheric radiation (atmos. rad., $Wm^{-2}$), direct solar radiation at right angle from the Sun beam (solar rad. direct, $Wm^{-2}$), horizontal diffuse solar radiation (solar rad. diffuse, $Wm^{-2}$), and all the atmospheric conditions, like air temperature (T, K), specific humidity (E, $kgm^{-3}$), wind speed (V, $ms^{-1}$). The state of the atmosphere in the UCL is computed by the surface scheme*

Electromagnetic radiation (EMR) is the first mode of energy transfer that must be solved. From a meteorological point of view, EMR comes from the Sun (essentially as visible light) or from the ground and the atmosphere (as infrared). First of all, the solar radiation received by the meshes is computed.

## 6.4. Solar radiation transfers

Solar radiation is the total of three components: the solar direct, diffuse atmospheric, and the "back reflection" from the ground. Despite their similar origin (the Sun), these three components are very different in the manner the light travels toward the objects and hence must be processed separately. The direct solar radiation

is the amount of energy an object receives from the rays of sunlight traveling in the atmosphere in a straight line (without interaction with the atmospheric constituents). The diffuse solar radiations are the rays of sunlight that have been scattered during their travel by the atmospheric components. Back reflections are the rays that are reflected by the objects on the ground before reaching other objects.

The relative position of the objects must be taken into account to compute the direct solar radiation. This is because a sunbeam can be blocked by obstacles before it can reach a mesh (Figure 6.3). This mechanism produces shadows that considerably modify the local energy balance. As we are working with a real environment, it is not possible to parameterize such an effect (the position of the objects varies from mesh to mesh). A special test is necessary for this kind of situation to evaluate if obstacles are present along the path of the beams [MOL 97]. If no obstacle is detected, the amount of direct radiation received on a mesh is computed according to the incidence angle of the sunbeams (the position of the Sun in the sky must be known). This test can easily take into account the transparencies.

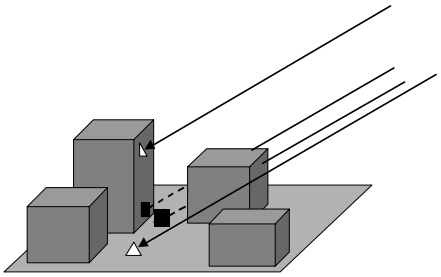

**Figure 6.3.** *Sunbeams intercepted by obstacles*

As a result of the atmospheric scattering, the entire sky seems to "emit" some light toward the ground. However, a comprehensive examination of this phenomena shows that the overall distribution of diffuse solar radiation over the sky varies (i.e. some parts of the sky contribute more to this mechanism than others). For example, under clear sky conditions (Figure 6.4), the quantity of diffuse radiation coming from directions situated near the Sun disk is more important than the quantity coming from the other directions [TEM 77]. This effect is called anisotropy. Anisotropy can be neglected for horizontal surfaces, but not for tilted surfaces. It will lead to big differences in the amount of diffuse energy they receive, based on their relative angle from the current Sun position. In towns, this effect cannot be neglected on the vertical facades. It is the reason why this solar component is simulated with an algorithm that considers the sky as an anisotropic source of diffuse radiation [BRU 93, NOO 08]. Another difficulty is that the distribution of diffuse radiation over the sky also varies according to the actual sky conditions

(cloud cover and atmospheric turbidity). These problems are solved with a statistic model of sky luminance distribution [PER 93]. A radiative sky model is obtained that is able to estimate the contribution of each part of the sky according to the position of the Sun and the different possible atmospheric weather types. Finally, the amount of solar diffuse radiation a mesh can receive is computed by integrating the radiative contribution of all the visible sky sectors (a test is required to evaluate the visibility between the sky sectors and the mesh).

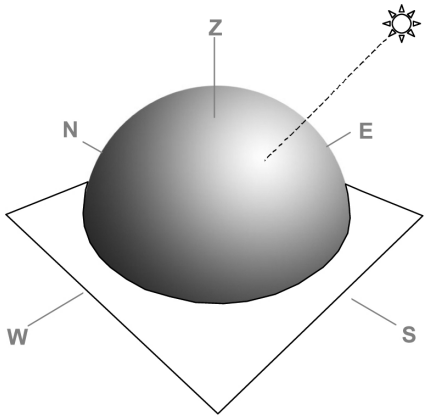


**Figure 6.4.** *Distribution of the solar diffuse radiation over the sky dome during clear sky conditions. Parts of the sky located near the Sun (white colors) contribute more to the diffuse radiation than the parts located near the horizon (dark colors)*

Solar radiation that reaches the ground is not entirely absorbed by the objects. Some of it is reflected toward the sky (definitively lost) and some toward the other objects (which is referred as back reflection). Back reflection can only be effective for non-flat terrain or on terrain with artificial or natural obstacles (like buildings or trees). The contribution of this reflected radiation can be of special importance in a complex environment, where it represents an additional source of energy for the objects. After multiple reflections, the solar radiation can be trapped into the urban canyon rather than allowing it to escape [AID 82, HAR 04, KON 01, TER 80]. The amount of radiation an object is able to reflect will greatly depend on a physical property called spectral reflectivity (its value varies according to the wavelength). After reflection, the solar radiation can be of two types: (i) diffuse (isotropic) for rough surfaces (typically a brick wall); and (ii) specular (anisotropic) for smooth surfaces (e.g. a mirror). By chance, most of the objects that can be found in a town are rough and they reflect the light with equal radiance in all directions (according to the Lambert's cosine law). However, a problem remains: the exact amount of solar energy reflected by a facet depends not only on the diffuse and direct radiation it receives from the Sun, but also on the back reflection it receives from the other

objects around it (Figure 6.5). Therefore, multiple inter-reflections can occur between the objects, and the radiation received on one object affects the radiation received on the other objects by virtue of reflection. Special algorithms can be used to solve this circular problem (e.g. path tracing or radiosity) [CHA 98, CLI 05]. The computation time of all these reflections is very high, and this is the sequence where the code wastes the most time.

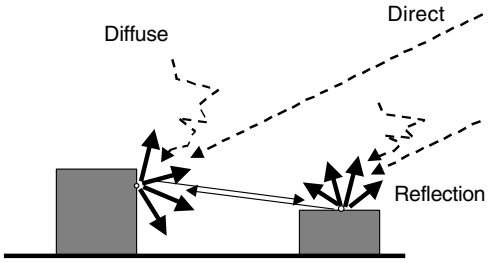


**Figure 6.5.** *Exchange of solar radiation between the objects and back reflection*

The three algorithms described earlier to simulate the solar direct, diffuse, and reflection can be validated for a real urban environment in which the radiative sensors were installed during an experimental campaign [NAJ 04]. The simulation scene inserted in the surface scheme reproduces the real geometry of the urban canyon in a three-dimensional form (Figure 6.6(b)), but with some simplification. To compare the results of the simulation and the measurements, we introduce fictitious devices in the simulation domain at the exact place the sensors were installed during the experiment [KAS 09]. As the simulation is done in a stand-alone mode, the forcing atmospheric variables necessary for the algorithms at the bottom of the UBL are obtained from measurements. The time step is of 15 min. The simulated solar radiation is validated (Figure 6.7) with the measurements obtained by a horizontal albedometer placed at half height (11.7 m) of the canyon. This device is a combination of two pyranometers: one facing upward and the other downward. The simulation seems to be in good agreement with the measurements for the two sensors of the device. The obstruction by the buildings is well reproduced for the upper pyranometer during the morning (until 8 UTC) and the afternoon (from 16 UTC). The sensor receives only diffuse and back-reflected radiation during these moments. During the time the sensor is directly illuminated by the Sun, the level of radiation increases sharply, up to 810 $Wm^{-2}$. The lower sensor receives only the reflected radiation from the objects that are located at the bottom of the canyon. The maximum amount of energy reaches only 83 $Wm^{-2}$ around mid-day. This figure clearly demonstrates the ability of the algorithms implemented in the surface scheme to reproduce faithfully the solar radiation transfers for a complex environment and at high spatial and temporal resolution.

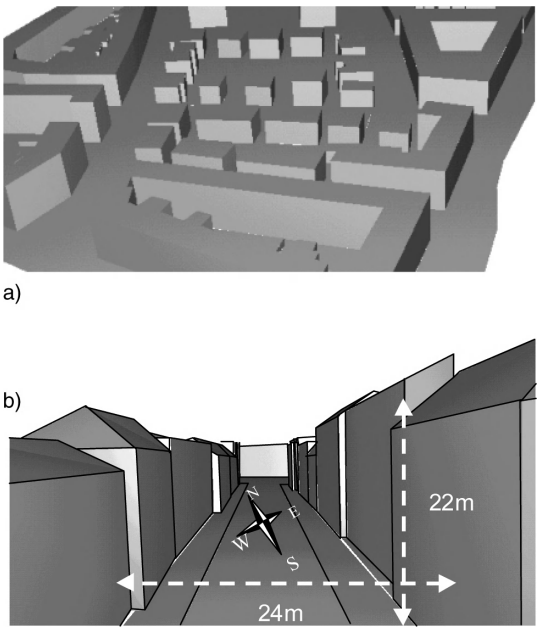


**Figure 6.6.** *The simulation domain: (a) an urban district of Strasbourg (France); (b) a view of the urban canyon in which the experimental devices were installed (two vegetated bands of grass can be seen at the bottom of the buildings, on both sides of the road). The characteristic dimension (height and width) of the canyon are also given*

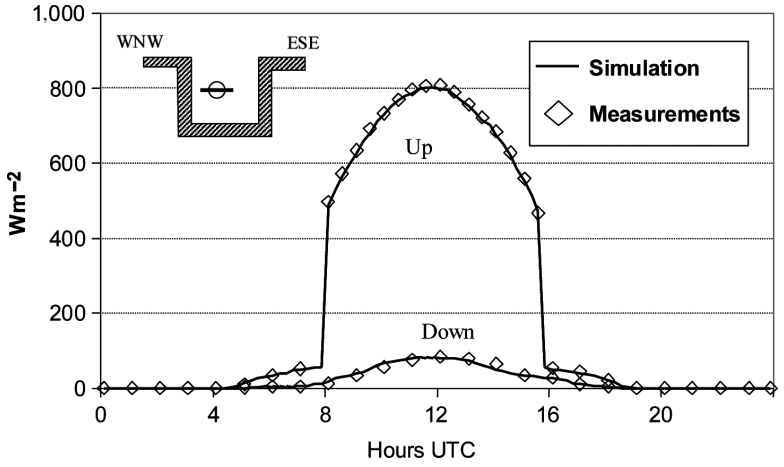


**Figure 6.7.** *Simulated and measured global radiation received on the two sides of an horizontal albedometer placed at half height of the urban canyon (11.7 m over the street) on August 15, 2002*

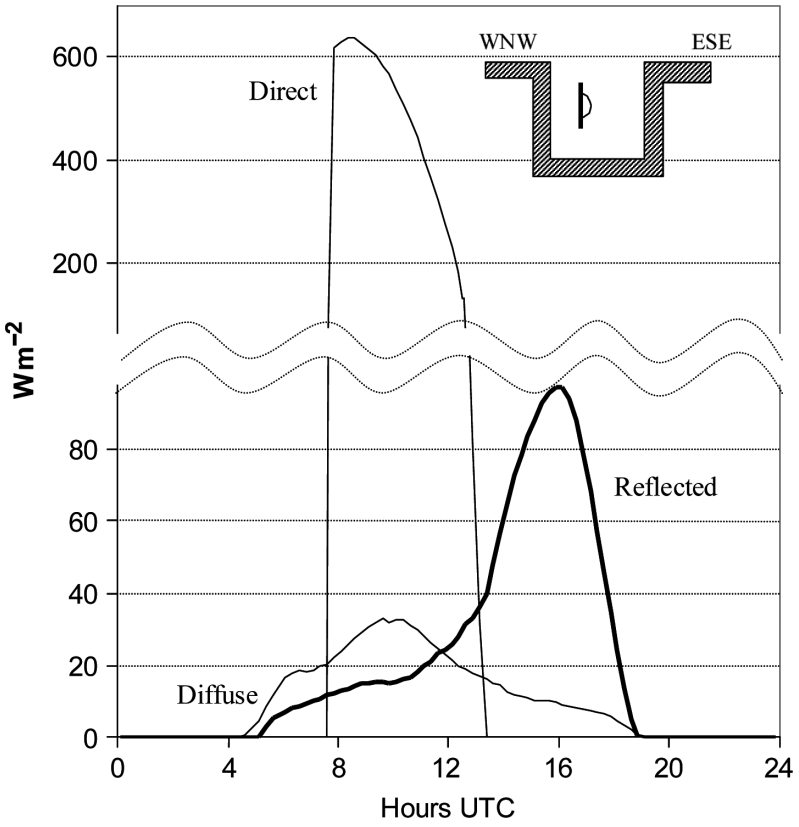


**Figure 6.8.** *Simulated components of the solar radiation for a fictitious vertical device facing the ESE direction (the median part of the figure is suppressed for convenience) on August 15, 2002*

The great advantage of the numeric simulation (compared with the measurements) is that each component of the solar radiation can be precisely quantified. Such decomposition is shown for a vertical device located in the simulation domain at nearly the middle of the canyon and facing the east–south–east (ESE) direction (Figure 6.8). The radiation is maximal by the direct solar radiation between 8 UTC and 13 UTC (when no obstruction occurs). The secondary contribution (about 100 $Wm^{-2}$) is due to the solar radiation reflected from the surrounding structures. The amount of energy reflected varies greatly during the day in coordination with the course of the Sun. The maximum radiation is recorded during the afternoon (around 16 UTC), when the Sun is able to efficiently illuminate the wall located in front of the sensor. The third component (the diffuse radiation) contributes the least (maximum 33 $Wm^{-2}$). This is because the device cannot really

face the sky during most parts of the day. This component reflects the influence of the anisotropic effect of the diffuse algorithm. The amount of diffuse radiation received by the device varies asymmetrically during the day. The values are stronger when the Sun is in front of the device during the morning, than when it is in its back during the afternoon (this will not be the case with an isotropic algorithm).

### 6.5. Infrared radiation transfers

In addition to the fact that the atmosphere or the terrestrial objects are able to reflect, transmit, or scatter the solar radiation, they must also be considered as emitters of some EMR. This occurs for longer wavelengths than for the solar radiation, and especially infrared (IR). The atmosphere and the terrestrial objects can be considered as perfect IR emitters or diffusers – the IR transfers are governed by the Lambert's cosine law. If we consider the atmospheric IR first, there appears to be a great difference between the atmospheric IR radiation and solar diffuse radiation; the sky is seen here as a homogeneous source of IR. This simplifies the algorithm considerably, and there is no need to use a distribution model as earlier. By using this assumption, the atmospheric IR received by a mesh only depends on the well-known "sky view factor" [GRI 01, JOH 84, OKE 81]. The sky view factor (*svf*) is a coefficient proportional to the unobstructed percentage of sky, that a mesh is able to observe. In other words, the *svf* is also proportional to the ratio of IR received by a mesh to the IR emitted by the sky. The value obtained for the *svf* of a mesh depends only on the way the obstacles are placed in the surroundings and it does not change with time (it can be computed once at the beginning of the simulation). Of course, in a town, *svf* will vary enormously between the flat roofs (values near 1) and the bottom of the vertical walls (values near 0).

The IR emitted from the ground is one of the most important ways through which the objects lose their energy. The amount of IR an object is able to emit depends on the Stefan–Boltzmann law for gray bodies [EDM 68]. Its estimation is not really a problem provided that the correct values of surface temperature and emissivity are known. Emissivity is the relative ability of a surface to emit energy by radiation. This physical property varies according to the material and with time (as for a soil according to its water content, for example), but it can sometimes be considered as constant over the time (as for artificial materials). The knowledge of the surface temperature remains a problem (as explained in the next section). When the amount of IR radiation is known, some part of it will be emitted towards the sky (definitely lost) and the remaining part towards other objects. A tremendous amount of IR can be exchanged between the objects in this way.

When IR reaches the ground, it is not entirely absorbed. Some of the rays can be reflected toward the sky (definitively lost) and some toward other objects (this phenomena is referred to as back reflection). Now, the question is to obtain the IR reflectivity ($\rho$). If transmission of IR is not possible and if Kirchhoff's law of thermal radiation is applied (it assumes that IR emissivity ($\varepsilon$) equals the IR absorptivity ($\alpha$)), then the IR reflectivity can easily be found from emissivity ($\rho = 1 - \alpha = 1 - \varepsilon$). As multiple reflections (inter-reflection) can also occur between the objects, this circular problem is solved with the same techniques as for inter-reflections in the solar wavelengths.

To validate the IR algorithms, it is possible to compare the simulation results with the measurements of two horizontal pyrgeometers placed at the middle of the canyon (Figure 6.9), one facing upward and the other downward. The device exposed to the ground observes only the objects of relatively high temperatures. As a consequence, it logically records the highest IR values (511 $Wm^{-2}$). The IR amplitude is about 110 $Wm^{-2}$ along the day and the temporal kinetic clearly follows the warming and the cooling of the canyon's bottom. The things are slightly different for the upward device. It receives a bigger proportion of atmospheric IR than of terrestrial IR and, as a consequence, its temporal kinetic softens and it records lower energy (390 $Wm^{-2}$).

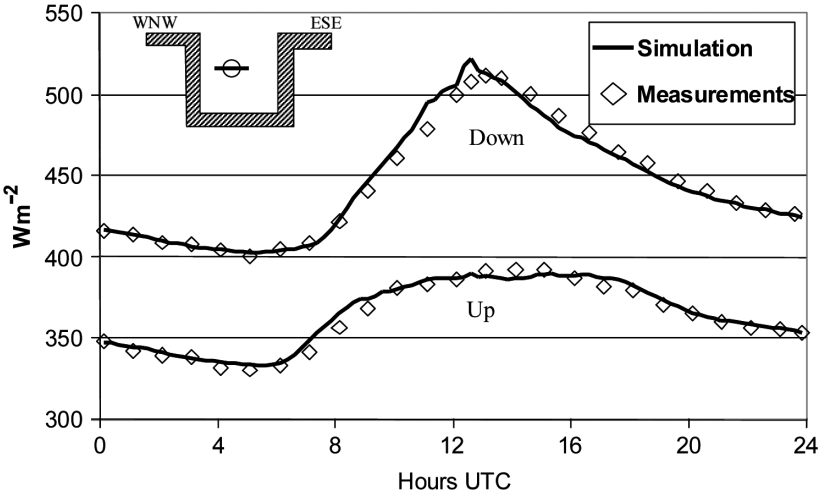


**Figure 6.9.** *Infrared radiation of two horizontal pyrgeometers placed at half height of the urban canyon on August 15, 2002. The upper side is exposed to the sky (top) and the lower side is exposed to the ground (bottom)*

The simulation of IR is globally more delicate than the simulation of solar radiation, and especially when terrestrial IR is involved. In fact, this component depends closely on the calculation of the surface temperature, which reflects the thermal state of the objects. This state is determined by all the energy transfers (radiative, thermal conduction, sensible, and latent heat) between the objects and their environment. For this reason, all the errors that are incorporated on the calculation of these fluxes influences the quality of the simulated surface temperature and therefore of the terrestrial IR. However, as can be seen on Figure 6.9, the differences between the simulation and the observation remain acceptable. They do not exceed 10 $Wm^{-2}$ for the upper device and 16 $Wm^{-2}$ for the lower device.

## 6.6. Other heat fluxes

As mentioned earlier during the discussion of surface temperature, the three heat fluxes – thermal conduction, sensible, and latent heat – have to be computed for the process to complete.

The ground heat flux (thermal conduction) is the transfer of heat into the objects from a zone of high temperature to a zone of low temperature. This transfer plays a fundamental role in urban climatology. The ground stores a part of the incident radiative energy during the day and sends it deep downward (it warms up), during the night, it clears a part of the heat toward the surface (it cools down). This is one of the key mechanisms at the origin of the urban heat island [GRI 99, OKE 87b, OKE 88]. The profile of temperatures within the objects must be known to obtain the ground heat flux and the heat equation is applied to predict this distribution [CAR 59]. For an isotropic and homogeneous medium this equation is:

$$\frac{\partial T}{\partial \tau} = \alpha \frac{\partial^2 T}{\partial x^2} \qquad [6.2]$$

where the rate of change of temperature at a point over time (the left term) is equal to the flux balance over space (the right term), $T$ (K) represents the soil temperature, $x$ (m) the distance between the layers, $\tau$ (s) the time, and $\alpha$ ($m^2s^{-1}$) the thermal diffusivity. It can be difficult to solve this partial differential equation because heat conduction propagates in the material in the three directions of space. For our simple application, the one-dimensional form is used (the lateral transfers of heat between the meshes are ignored). The equation is solved by applying a finite difference method [DAV 03] to compute the temperatures of the objects at different levels. However, a more complex form of equation [6.2] must be used because of the

presence of a non-homogenous medium: the objects can be composed with several layers of different materials with different thicknesses. To obtain results as realistic as possible, it is also necessary to specify the boundary conditions of the temperatures, and especially at the deepest material layer. Different solutions are employed depending on the type of object (e.g. river, terrain, and building). For a soil, the last temperature level can be kept constant with time for a sufficiently deep soil column. However, for a building, the room temperature can evolve with time (hence the need of indoor air-conditioning systems [BAD 03]). This evolution can be obtained with specialized building simulation models [CLA 07] or with parameterizations. A special form of the heat equation [STU 88] is applied to obtain the surface temperature. It takes into account the strong external constraints – net radiation (RN), latent heat flux (Le), and sensible heat flux (S) – that are exerted on the surface, and the corresponding equation is given as:

$$\frac{\partial T}{\partial \tau} \cdot \frac{\rho \cdot c \cdot dx}{2} = G + Rn + Le + S \qquad [6.3]$$

This equation states that the variation of temperature in the first-half soil level must be equal to the sum of the surface heat fluxes. An example of computed temperatures is given for a wall facing ESE (Figure 6.10). The surface temperature reacts sharply when the sunbeams strike the wall during the morning. The thermal wave propagates progressively into the wall.

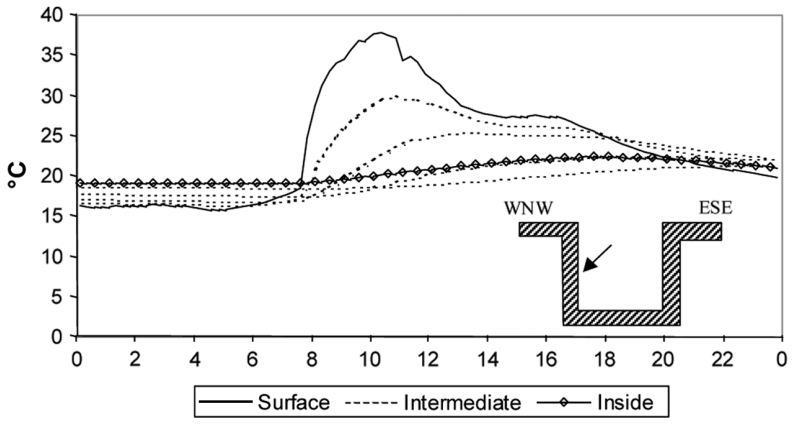


**Figure 6.10.** *Evolution of simulated temperatures for an ESE facing wall on August 14 from outside (surface) to inside. Hours are UTC*

Once the temperature profile is obtained, the ground heat flux ($G$, $Wm^{-2}$) is computed between the surface and the first internal level according to the Fourier's law:

$$G = k\frac{\partial T}{\partial x} \qquad [6.4]$$

where $k$ is the thermal conductivity of the material ($W\ m^{-1}K^{-1}$).

Sensible heat is the heat energy transferred between the surface and air when there is a temperature difference between them [NIC 82]. It can be approximated with the following basic formula:

$$S = \rho \cdot c_p \cdot h \cdot U \cdot \left(T_s - T_a\right) \qquad [6.5]$$

The sensible heat flux ($S$, $Wm^{-2}$) is calculated with the atmospheric density ($\rho$, $kgm^{-3}$), the specific heat of air at constant pressure ($c_p$ $Jkg^{-1}K^{-1}$), an aerodynamic transfer coefficient for heat ($h$, dimensionless), the wind speed ($U$, $ms^{-1}$), and the difference in temperature between the surface ($T_s$, K) and the air ($T_a$, K). If the mesh is located on a roof, $T_a$ is taken into the lower UBL; if it is located in the UCL, $T_a$ is taken into the urban canyon. In principle, the value of the heat transfer coefficient ($h$) depends on the vertical mixing (stability) of the atmosphere [ALS 02, BEL 91, LOU 79, STU 88].

Despite scarcity of natural surfaces in towns, it is not possible to neglect evapotranspiration [PIC 04, ROB 06]. Sometimes bare soil, water, and vegetated zones like parks, lawns, and even trees can be of some importance. The latent heat flux (i.e. the heat flux associated with evapotranspiration) can be obtained by several methods [BRU 81, MON 81]. We use an equation of the following form:

$$Le = \rho \cdot \lambda \cdot h \cdot U \cdot \left(Q_g - Q_a\right) \qquad [6.6]$$

where the latent heat flux ($Le$, $Wm^{-2}$) is proportional to the specific humidity difference between the ground ($Q_g$, $kgm^{-3}$) and the air ($Q_a$, $kgm^{-3}$). $\rho$, $h$, and $U$ have the same significance as in equation [6.5] and $\lambda$ is the latent heat of vaporization ($Jkg^{-1}$). Here too, the specific humidity of the air ($Q_a$) is taken at different places (UBL or UCL), if necessary. Of course, the water balance of the soil must be taken into account for inputs and outputs of water in the soil column [DRI 86, NOI 89, NOI 96].

The simulated sensible and latent heat fluxes can be validated with sensors installed at the top of the urban canyon (just at the level of the roofs). The sensible

heat flux is measured by the combination of a sonic anemometer and a thermocouple; the latent heat flux is measured with a krypton hygrometer. The simulation results are compared with the measurements for a period of several days as shown in Figure 6.11. All the fluxes are averaged over a period of 1.5 h to eliminate the deviation of the turbulent velocities about the mean [STU 88]. The comparison between the two sets of data is not easy, because it is well known that they are submitted to a spatial representativeness problem due to the wind; the heat flux measured by the sensor is not necessarily the local heat flux and the source areas can change with the wind (there is a "footprint" problem). Ideally, to make sure that the local heat fluxes are measured, the measurement must be done over flat zones, low winds, and short distances from the surfaces. Another problem is that at the top of the canyon, the sensors can sometimes be influenced by advection from the UBL. Despite these remarks, the two simulated fluxes are of the same order of magnitude as those of the measured fluxes.

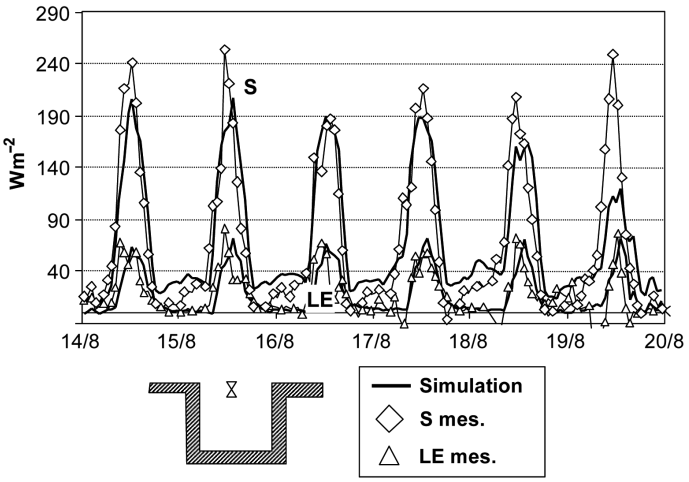


**Figure 6.11.** *Heat fluxes at a canyon top of Strasbourg city for the period between August 14 and August 19, 2002. The fluxes are averaged over a 1.5 h period*

## 6.7. Conclusions

The high-computation complexity of the surfaces in a town is a challenge for the surface schemes, whose primary objective is to simulate the heat and radiative fluxes of the energy balance equation. At a very high resolution (microscale), it becomes necessary to work with the real geometry of the objects, and this can actually be done as the information is available. However, it can lead to several problems: (i) it can be difficult to correctly apply the thermophysical properties of each object for large urban simulation domains; (ii) specialized algorithms must be

used to simulate the radiative fluxes and they increase the computational time; and (iii) the interfacing with the atmospheric models must be carefully examined. Paradoxically, the algorithms of radiative energy transfers are those where the errors are minimum (and especially for the solar wavelength), while the other heat flux algorithms (sensible, latent, and ground heat fluxes) are more imprecise. This is due to the fact that they depend on a number of variables (like the soil water content) that are themselves difficult to obtain. Despite these difficulties, the present knowledge about the energy transfers is able to provide rather good results at local scales. These techniques can be very useful to improve the microscale applications designed for decision makers, developers, and people involved in the well-being of society [PIC 04, ROB 06].

## 6.8. Bibliography

[AID 82] AIDA M., "Urban albedo as a function of the urban structure – a model experiment (Part I)", *Boundary-Layer Meteorology*, vol. 23, pp. 405–413, 1982.

[ALS 02] AL-SANEA S.A., "Thermal performance of building roof elements", *Building and Environment*, vol. 37, no. 7, pp. 665–675, 2002.

[ARN 03] ARNFIELD A.J., "Two decades of urban climate research: a review of turbulence, exchanges of energy and water, and the urban heat island", *International Journal of Climatology*, vol. 23, pp. 1–26, 2003.

[BAD 03] BADESCU V., SICRE B., "Renewable energy for passive house heating: II. Model", *Energy and Buildings*, vol. 35, pp. 1085–1096, 2003.

[BEL 91] BELJAARS A.C.M., HOLTSLAG A.A.M., "On flux parameterization over land surfaces for atmospheric models", *Journal of Applied Meteorology*, vol. 30, pp. 327–341, 1991.

[BRU 93] BRUNGER A.P., HOOPER F.C., "Anisotropic sky radiance model based on narrow field of view measurements of shortwave radiance", *Solar Energy*, vol. 51, pp. 53–64, 1993.

[BRU 81] BRUTSAERT W.H., *Evaporation into the Atmosphere: Theory, History and Applications*, D. Reidel Publ. Co., pp. 340, 1981.

[CAR 59] CARSLAW H.S., JAEGER J.C., *Conduction of Heat in Solids*, 2nd ed., Oxford University Press, Oxford, pp. 520, 1959.

[CHA 98] CHANG C.C., SHIH Z.C., "An accuracy enhancement algorithm for hierarchical radiosity", *Computer Graphics*, vol. 22, pp. 225–232, 1998.

[CLA 07] CLARKE J.A., KELLY N.J., TANG D., "A review of ESP-r's flexible solution approach and its application to prospective technical domain developments", *Advances in Building Energy Research*, vol. 1, no. 1, pp. 227–247, 2007.

[CLI 05] CLINE D., TALBOT J., EGBERT P., "Energy redistribution path tracing", *ACM Transactions on Graphics*, vol. 24, no. 3, pp. 1186–1195, 2005.

[DAV 03] DAVIES M.G., "A rationale for nodal placement for heat flow calculations in walls", *Building and Environment*, vol. 38, pp. 247–260, 2003.

[DEL 04] DE LA FLOR F.S., DOMÍNGUEZ S.A., "Modelling microclimate in urban environments and assessing its influence on the performance of surrounding buildings", *Energy and Buildings*, vol. 36, no. 5, pp. 403–413, 2004.

[DRI 86] DRIESSEN P.M., "The water balance of soil", in VAN KEULEN H., WOLF J. (eds), *Modelling of Agricultural Production: Weather, Soils and Crops*, PUDOC, Wageningen, The Netherlands, pp. 76–116, 1986.

[DUP 06] DUPONT S., MESTAYER P., "Parameterization of the urban energy budget with the submesoscale soil model", *Journal of Applied Meteorology and Climatology*, vol. 45, pp. 1744–1765, 2006.

[EDM 68] EDMONDS I.R., "Stephan–Boltzmann law in the laboratory", *American Journal of Physics*, vol. 36, no. 9, pp. 845–846, 1968.

[EHR 00] EHRHARD J., KHATIB I.A., WINKLER C., KUNZ R., MOUSSIOPOULOS N., ERNST G., "The microscale model MIMO: development and assessment", *Journal of Wind Engineering and Industrial Aerodynamics*, vol. 85, pp. 163–176, 2000.

[GRI 99] GRIMMOND C.S.B., OKE T.R., "Heat storage in urban areas", *Journal of Applied Meteorology*, vol. 38, pp. 922–940, 1999.

[GRI 01] GRIMMOND C.S.B., POTTER S.K., ZUTTER H.N., SOUCH C., "Evaluation and application of automated methods for estimating sky view factors in urban areas", *International Journal of Climatology*, vol. 21, pp. 903–913, 2001.

[HAR 04] HARMAN I.N., BEST M.J., BELCHER S.E., "Radiative exchange in an urban street canyon", *Boundary-Layer Meteorology*, vol. 110, pp. 301–316, 2004.

[HEI 79] HEINO R., "Urban effect on climatic elements in Finland", *Geophysica*, vol. 15, pp. 171–188, 1979.

[JOH 84] JOHNSON G.T., WATSON I.D., "The determination of view-factors in urban canyons", *Journal of Applied Climate and Meteorology*, vol. 23, pp. 329–335, 1984.

[KAS 00] KASTENDEUCH P.P., LACARRERE P., NAJJAR G., NOILHAN J., GASSMANN F., PAUL P., "Mesoscale simulations of thermodynamic fluxes over complex terrain", *International Journal of Climatology*, vol. 20, pp. 1249–1264, 2000.

[KAS 06] KASTENDEUCH P.P., NAJJAR G., RINGENBACH N., "Modélisation du bilan radiatif et d'énergie d'un canyon urbain à Strasbourg", *Climatologie*, vol. 3, pp. 25–42, 2006.

[KAS 09] KASTENDEUCH P.P., NAJJAR G., "Simulation of radiative transfers in urbanised areas", *Solar Energy*, vol. 83, pp. 333–341, 2009.

[KON 01] KONDO A., UENO M., KAGA A., YAMAGUCHI K., "The influence of urban canopy configuration on urban albedo", *Boundary-Layer Meteorology*, vol. 100, pp. 225–242, 2001.

[KUS 01] KUSAKA H., KONDO H., KIKEGAWA Y., KIMURA F., "A simple single-layer urban canopy model for atmospheric models: comparison with multi-layer and SLAB models", *Boundary-Layer Meteorology*, vol. 101, pp. 329–358, 2001.

[LAN 81] LANDSBERG H.E., *The Urban Climate*, International Geophysics Series, vol. 28, pp. 275, 1981.

[LET 08] LETZEL M.O., KRANE M., RAASCH S., "High resolution urban large-eddy simulation studies from street canyon to neighbourhood scale", *Atmospheric Environment*, vol. 42, no. 38, pp. 8770–8784, 2008.

[LOU 79] LOUIS J., "A parametric model of vertical eddy fluxes in the atmosphere", *Boundary-Layer Meteorology*, vol. 17, pp. 187–202, 1979.

[MAS 00] MASSON V., "A physically-based scheme for the urban energy budget in atmospheric models", *Boundary-Layer Meteorology*, vol. 94, pp. 357–397, 2000.

[MIL 97] MILLS G., "The radiative effects of building groups on single structures", *Energy and Buildings*, vol. 25, pp. 51–61, 1997.

[MIN 10] MINVIELLE M., CASSOU C., TERRAY L., BOURDALLE-BADIE R., "A statistical-dynamical scheme for ocean downscaling in the Atlantic. Part II: methodology, validation and application to high resolution ocean models", *Climate Dynamics*, vol. 3–4, pp. 401–417, 2010.

[MOL 97] MOLLER T., TRUMBORE B., "Fast, minimum storage ray-triangle intersection", *Journal on Graphic Tools*, vol. 2, no. 1, pp. 21–28, 1997.

[MON 81] MONTEITH J.L., "Evaporation and surface temperature", *Quarterly Journal Royal Meteorological Society*, vol. 107, pp. 1–27, 1981.

[NAJ 04] NAJJAR G., KASTENDEUCH P.P., STOLL M.P., COLIN J.R., NERRY F., RINGENBACH N., BERNARD J., DE HATTEN A., LUHAHE R., VIVILLE D., "Le projet Reclus, Télédétection, rayonnement et bilan d'énergie en climatologie urbaine à Strasbourg", *La Météorologie*, vol. 46, pp. 44–50, 2004.

[NIC 82] NICHOLLS S., SMITH F.B., "On the definition of the flux of sensible heat", *Boundary Layer Meteorology*, vol. 24, pp. 121–127, 1982.

[NOI 89] NOILHAN J., PLANTON S., "A simple parameterization of land surface processes for meteorological models", *Monthly Weather Review*, vol. 117, pp. 536–549, 1989.

[NOI 96] NOILHAN J., MAHFOUF J.F., "The ISBA land surface parameterization scheme", *Global and Planetary Change*, vol. 13, pp. 145–159, 1996.

[NOO 08] NOORIAN A.M., MORADI I., KAMALI G.A., "Evaluation of 12 models to estimate hourly diffuse irradiation on inclined surfaces", *Renewable Energy*, vol. 33, pp. 1406–1412, 2008.

[OKE 81] OKE T.R., "Canyon geometry and the nocturnal urban heat island: comparison of scale model and field observations", *Journal of Climatology*, vol. 1, pp. 237–254, 1981.

[OKE 87a] OKE T.R., *Boundary Layer Climates*, 2nd ed., Methuen, London and New York, 435 p., 1987.

[OKE 87b] OKE T.R., CLEUGH H.A., "Urban heat storage derived as energy balance residuals", *Boundary-Layer Meteorology*, vol. 39, pp. 233–246, 1987.

[OKE 88] OKE T.R., "The urban energy balance", *Progress in Physical Geography*, vol. 12, pp. 471–508, 1988.

[PER 93] PEREZ R., SEALS R., MICHALSKY J., "An all-weather model for sky luminance distribution – preliminary configuration and validation", *Solar Energy*, vol. 50, no. 3, pp. 235–245, 1993.

[PIC 04] PICOT X., "Thermal comfort in urban spaces: impact of vegetation growth case study: Piazza della Scienza, Milan, Italy", *Energy and Buildings*, vol. 36, pp. 329–334, 2004.

[PIT 03] PITMAN A.J., "The evolution of, and revolution in, land surface schemes designed for climate models", *International Journal of Climatology*, vol. 23, pp. 479–510, 2003.

[RAI 07] RAIL A., *Urban Thermal Plumes: Their Possible Impact on Climate Change*, 1st ed., Kastell Books, Sudbury, pp. 29, 2007.

[ROB 06] ROBITU M., MUSY M., INARD C., GROLEAU D., "Modeling the influence of vegetation and water pond on urban microclimate", *Solar Energy*, vol. 80, pp. 435–447, 2006.

[SEL 86] SELLERS P.J., MINTZ Y., SUD Y.C., DALCHER A., "A simple biosphere model (SiB) for use within general circulation models", *Journal of Atmospheric Science*, vol. 43, pp. 505–531, 1986.

[STU 88] STULL R.B., *An Introduction to Boundary Layer Meteorology*, Kluwer Academic Publishers, pp. 666, 1988.

[TEM 77] TEMPS R.C., COULSON K.L., "Solar radiation incident upon slopes of different orientations", *Solar Energy*, vol. 19, pp. 179–184, 1977.

[TER 80] TERJUNG W., O' ROURKE P., "Influence of physical structures on urban energy budgets", *Boundary-Layer Meteorology*, vol. 19, pp. 421–439, 1980.

[WAL 02] WALTON A., CHENG A.Y.S., YEUNG W.C., "Large-eddy simulation of pollution dispersion in an urban street canyon-Part I: comparison with field data", *Atmospheric Environment*, vol. 36, pp. 3601–3613, 2002.

[XIE 08] XIE Z.T., COCEAL O., CASTRO I.P., "Large-eddy simulation of flows over random urban-like obstacles", *Boundary-Layer Meteorology*, vol. 129, no. 1, pp. 1–23, 2008.

# Chapter 7

# Evapotranspiration

Trees, green roofs, water ponds, greenswards, and sustainable urban drainage systems (SUDSs) are solutions that are being used by city planners to respond to the climate challenge. Indeed, their physical behavior is favorable to mitigate the urban heat island (UHI) effect. Even if it can be admitted that the more a city is green, the less it suffers from the UHI, it is very difficult to have an objective assessment of the presence of vegetation in a city and the related impact on urban climate.

Some experimental campaigns have demonstrated and quantified the effect of a cool island with respect to the size of parks and the arrangement of vegetation [CAO 10, TAK 09]. These experimental studies can be carried out because we dispose of a reference that is used to measure the effect of the park: the temperatures are compared to those measured in surrounding built-up areas.

To characterize the overall effect of vegetation, at city scale, there is no reference value and the measures do not give the specific effect of vegetation, separated from the other effects due to the presence of water, urban form, activities, etc. The only way to evaluate the impact of vegetation in different specific contexts is the physical modeling of phenomena and, thereafter, the simulation of different cases. In the literature, we can find comparisons of the urban climate due to different land usage scenarios from the more vegetated to the more artificial, as those carried by Velasquez-Lozada *et al.* [VEL 06]. They proceed to study microclimatic simulations, using numerical models and then compare the results with the others.

One of the multiple interests of natural urban surfaces lies in their capacity to dissipate energy by the way of evaporation (soil) and transpiration (plants) or

Chapter written by Marjorie MUSY.

*Solar Energy at Urban Scale* Benoit Beckers

evapotranspiration (we later include the phenomena in the term “evapotranspiration”) when both phenomena occur. This feature is mainly interesting in the case of a hot climate or during summer. However, this capacity is not permanently mobilized and mobilizable. Indeed, evapotranspiration requires energy to convert and water to vaporize: a dry soil will not evaporate, no more than a dry green roof. They will also be more efficient in a dry climate than in a humid one. Moreover, the effect also depends on plant species.

Much research has been carried out to characterize the thermal parameters (albedo, emissivity, conductibility, etc.) of different urban materials. Plants have essentially been characterized by agricultural researchers and for agricultural purposes, that is, in open-field or forest-canopy conditions. The growing conditions of the plants in cities are quite different: trees are often planted in isolation from other plants, in heterogeneous environments, under the shade of buildings and exposed to air pollution. Moreover, they are subjected to particular treatments and pruning. With respect to soil too, they are in competition with obstacles that are barriers to the growth of their roots or to flow of water. The global characteristics of vegetation, as optical ones, are highly dependent on the form and the arrangement of the foliage, which are obviously dependent on the growing conditions of the plants.

## 7.1. Physical bases

Irrespective of the considered surface (homogeneous or not, smooth or rough) and the analysis scale, the energy budget equation can be written as

$$Rn - L_eE - H - S = 0 \qquad [7.1]$$

where

– $Rn$ is the net radiation;

– $S$ is the energy flux conducted in the layer of material (ground or wall);

– $H$ is sensible heat flux;

– $L_eE$ is the latent heat flux.

This equation, in which the energy absorption by photosynthesis is neglected, clearly shows the balance between heat fluxes related to each phenomenon.

When detailing each term, we can highlight the characteristics of the surface and those of the surrounding that are involved in the balance equation (Table 7.1).

| Heat flux | Variable of the surface | Surface intrinsic characteristics | Characteristics of the surrounding |
|---|---|---|---|
| Radiation: longwave | Surface temperature, $T_s$ (K) | Emissivity, $\varepsilon_s$ (−) | Emissivity, $\varepsilon_i$ (−)<br>Surface temperature, $T_i$ (K)<br>View factor from the considered surface to surrounding ones, $F_{si}$ (−) |
| Radiation: shortwave | | Reflection, $\alpha_s$ (−)<br>Transmission, $\tau_s$ (−)<br>Absorption, $a_s$ (−) | Geographical location<br>Solar view (masks)<br>Optical characteristics of surrounding surfaces<br>View factor from the considered surface to surrounding ones, $F_{si}$ (−) |
| Sensible | Surface temperature, $T_s$ (K) | Roughness (m) | Surrounding air temperature, $T_a$ (K)<br>Wind velocity near the surface, $V$ ($m \cdot s^{-1}$) |
| Conductive | Surface temperature, $T_s$ (K) | Thermal conductivity, $\lambda$ ($W \cdot m^{-1} \cdot K^{-1}$)<br>Specific heat at constant pressure, $C_p$ ($J \cdot kg^{-1} \cdot K^{-1}$)<br>Density $\rho$ ($kg \cdot m^{-3}$)<br>(characteristics of the inner layers of the surface) | Temperature of the internal face of the wall or into the ground, $T_{s\_int}$ or $T_{ground}$ (K) |
| Evapotranspiration | Specific humidity surface, $q_s(T_s)$ ($kg \cdot kg^{-1}$) | Boundary layer resistance, $r_b$ ($s \cdot m^{-1}$)<br>Case of vegetation:<br>Leaf area density $LAD$ ($m^2 \cdot m^{-3}$)<br>Stomatal resistance $r_{sto}$ ($s \cdot m^{-1}$) | Surrounding air specific humidity, $q_a$<br>Air temperature ($T_a$) |

**Table 7.1.** *Characteristics and variables interfering in surface balance equation*

– *Rn* includes the net shortwave radiation flux (incoming flux minus the reflected one) and the net longwave radiation flux. The only intrinsic parameter modifying the net shortwave flux is the absorption coefficient ($a_s$), which in case of an opaque surface is complementary to the albedo ($\alpha_s$) of the surface.

The surrounding modifies this flux by acting as a mask or reflecting energy. The longwave flux depends on two intrinsic parameters of the surface: its temperature ($T_s$) and its surface emissivity ($\varepsilon_s$). This flux also depends on the temperature and emissivity of the surrounding surfaces (including the sky) and the way the considered surface is subjected to them.

– $H$ varies according to the surface temperature ($T_s$), the near-surface air temperature, and a convection coefficient that depends on airflow velocity just near the surface. The roughness of the surface can then be an intrinsic parameter to account for.

– $S$ also depends on the surface temperature ($T_s$). The nature of material and more precisely its thermal conductivity ($\lambda$), specific heat at constant pressure ($C_p$), and density ($\rho$) regulate this flux. The boundary condition of conductive flux is either the temperature into the ground or this on the inner face when the considered surface is a building wall.

– $L_eE$ depends on the difference between the surface moisture content ($q_s$) and the specific humidity of the near-surface air ($q_a$). It is regulated by a boundary layer resistance ($r_b$). When the surface is covered with vegetation, the stomatal resistance of plants ($r_{sto}$) and the leaf area density (LAD) intervene.

A key variable is present in almost all the terms: the temperature of the surface to which the balance equation is applied.

Referring to the daily cycle of the energy balance for a grass-covered surface shown by Brutsaert [BRU 82], we can observe that the latent heat of vaporization is following the variation of net radiation during daytime and that latent heat flux and the sensible one nearly compensate the net radiation. When evaporation is not possible, the radiation flux leads to greater surface temperatures, and to more transfer of heat to the air by convection, more transfer by longwave radiation, and more transfer to the ground by conduction.

By understanding this equilibrium, we can analyze the difference in the behavior of different kinds of surfaces in a city.

## 7.2. Related interest of different types of evapotranspirating surfaces

### 7.2.1. *Bare soil*

Compared to a pavement, a bare soil is porous, permeable, and for that reason contains more water. Evaporation contributes in the reduction of the surface temperature. Latent heat flux that results from evaporation directly depends on water diffusion in the material and air moisture. Herb *et al.* obtained surface

temperatures from bare soils that lie between those for pavements and plant-covered surfaces [HER 08]. Indeed, the evaporative surface is larger than in the pavement case but much smaller than in the plant-covered one.

Takebayahi and Moriyama compare the quantity of evaporation from the green surface and bare soil, in Kobe, Japan [TAK 07]. The results show that the evaporation varies throughout the day and the seasons, depending on the climatic condition and water availability in the soil. They found that the quantity of evaporation from the bare soil surface can be larger or smaller than that from the green surface. Indeed, the lawn can either moderate the influence of the atmosphere on evaporation, or contribute to increasing it.

### 7.2.2. *Grass-covered areas*

Grass-covered areas have been studied either in the context of parks or compared to mineral surfaces. Grass surface temperature can be measured, but its effect on air temperature is more difficult to access. Armson and Ennos have compared the temperatures of small test plots, composed of grass and concrete in Manchester, in full Sun or under tree shade [ARM 11]. Over two summers (2009/2010), they showed that grass lowered surface temperatures to below air temperature, even in full Sun. Ca *et al.*, who have done some field measurements in Tama New Town, a city to the west of Tokyo, identified temperatures above a grass field park that are lower by 2°C than those measured above the asphalt and on the concrete surfaces of a commercial parking area. However, in another context, Nichol concludes that there were no significant cooling effects observed for grassy surfaces [CA 98, NIC 96].

Takebayahi and Moriyama have studied the urban heat island mitigation effect of conversion from asphalt-covered parking areas to grass-covered ones [TAK 09]. They used observation (in Kobe City Center, Japan) and calculation, evaluating the mean surface temperature in a parking lot from a thermal image captured by an infrared camera and deducing the sensible heat flux in each parking space by applying the surface heat budget. They conclude that there is a tendency for the mean surface temperature of a parking space to decrease with an increase in the green coverage ratio. They also assert that this decrease varies strongly depending on the other materials used in addition to grass (concrete, water-stoning concrete, wood, etc.). In comparison with an asphalt surface, they obtained a sensible heat flux reduced by ~100–150 $W \cdot m^{-2}$ during the day and 50 $W \cdot m^{-2}$ during the night. As a result, the air temperature reduction due to the grass-covered parking areas is calculated to be about 0.1°C.

The effect on air temperature is barely perceptible but the effect on comfort is verified using mean radiant temperature (MRT) because of the lower temperature of grass-covered surfaces.

### 7.2.3. *Green roofs*

The operation of a green roof differs from that of a planted area by different boundary temperature conditions in the soil and different water transfer conditions.

Green roofs have been studied from the building energy saving point of view. For example, Santamouris *et al.* have studied a green roof system installed in a nursery school building in Athens (Greece) [SAN 07]. They highlighted a significant reduction in the usage of conventional air-conditioning equipment during the summer. However, they observed such an impact on the heating load during winter that they consider it as insignificant.

One of the conclusions of these studies is that the energy-saving effect of green roofs depends on several parameters including the climate (effect on energy demand and water availability), the location and situation related to other buildings (effect on convection and solar interception), and the variety of vegetation (effect on evapotranspiration).

To study the influence of this type of surface on the urban climate, we are interested in the distribution of the fluxes involved in the heat balance. Feng *et al.* have analyzed the energy balance of extensive green roofs [FEN 10]. Their experimental results allow them to demonstrate that during a typical summers day, when the soil is wet, solar radiation accounted for 99.1% of the total heat gain while the convection contribution is 0.9%. However, 58.4% of this energy is dissipated by the evapotranspiration of the plants–soil system, 30.9% by the net longwave radiation to the atmosphere, and 9.5% by the net photosynthesis of plants. Effectively this means that it results in only 1.2% of this energy being stored by plants and soil, and then transferred into the rooms of the upper floor. In other words, in these conditions, the absorbed solar energy is almost completely stopped by the green roof.

Takebayahi and Moriyama have observed the surface temperature, net radiation, water content ratio, and other variables on a green roof and a high reflection one to assess their UHI mitigation performance [TAK 07]. Their results give less extreme repartitions but agree with a low sensible heat flux because of high dissipation of radiation by evapotranspiration in the green roof case while in the case of high reflective roof, the sensible flux is low because of a low net radiation flux.

### 7.2.4. *Green walls*

Green walls not only have some similarities with green roofs, but also differences. From a thermal point of view, green walls have three effects on climate:

Radiative effects: the leaves not only provide protection from the Sun for the wall during the day but also prevent the cooling by blocking longwave radiation during the night. Because of their physiology, the leaves absorb a significant amount of solar radiation without raising their temperature through transpiration. Finally, the presence of a moist substrate can also cause a passive cooling by evaporation.

Conductive effects: the vegetation and its growing medium can insulate the wall and modify its inertia.

Convective effects: the plants limit the airflow velocity near the wall and for that reason, the energy exchanges due to convection is also reduced.

These effects have different weights depending on the technique used to build the facade. Green walls are often categorized into three families:

– green facades made up of climbing plants growing on supporting structures placed at a distance from the wall;

– green facades made up of climbing plants growing directly on a wall;

– living walls made up of plants and their growing medium.

In the two first systems, the plants are rooted in the ground. A living wall is often made up of modular panels containing a substratum and an irrigation system. While the first kind of facade has only radiative effects, the second combines convective and radiative effects, and the third has the three effects. Facades covered with climbing plants or growing on a medium close to the wall differ from the vegetation used as a distant shading device because of the presence of a layer of air in the canopy, the temperature of which differs from the outside temperature.

The physical phenomena that occur in living facades differ from those of green roofs due to their vertical arrangement that induces gravitational effects in the water distribution in the substrate. This is one of the conclusions drawn by Cheng *et al.* [CHE 10]. Due to this distribution, and due to an access to lighting that varies vertically (especially in dense urban areas), growth of plants and evapotranspiration fluxes can vary all over the facade (Figure 7.1).

Until recently, studies of the climatic impact of these types of walls were quite rare. As for green roofs, they have mainly been studied for their impacts on thermal-building behavior [IP 10, PÉR 11].

Pérez *et al.* have studied and monitored a double-skin green facade (first family) in a Mediterranean Continental climate [PÉR 11]. They find building surface temperatures that can be 15.2°C higher on areas without shade than on areas partially covered by vegetation. In the intermediate space, they find that the temperature and relative humidity of air were different from those measured in the

air surrounding the building. During the period with leaves, the temperature is lower and the relative humidity is higher and it is the contrary during the period without leaves. This tendency can be reduced by wind effect and depends on the permeability to air of the system.

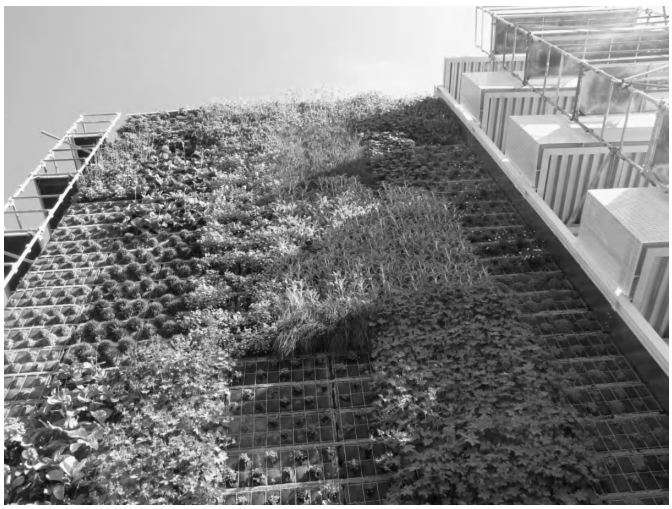

**Figure 7.1.** *Living wall in Nantes (France) with different varieties of plants, and a heterogeneous shading effect*

By way of simulations, Alexandri *et al.* have studied the effect of green facades (second family) in different climates [ALA 08]. They showed that there is an important potential of lowering urban temperatures when covering the buildings with vegetation. In very hot and dry climates, the effect of vegetation on urban temperatures can be very high. For example, they find for Riyadh (Saudi Arabia), temperatures inside the canyon decreasing up to 11.3°C with a daytime average decrease of 9.1°C. In the humid climate of Hong Kong (China), when walls and roofs are covered with vegetation, they obtained a temperature decrease reaching up to 8.4°C. According to the authors, the effect of vegetation primarily depends on the amount of vegetation and temperature decrease is higher in narrow canyon streets.

### 7.2.5. *Trees*

The contribution of trees to the mitigation of the urban heat island is also partly demonstrated. Several phenomena are involved in this action: advection, evaporation, windshield effect, and radiative effect (solar mask and shortwave and

longwave exchanges). The relative weight of each of them depends on many local parameters of climate and plant, acting in various combinations at any given particular moment.

According to McPherson, in most circumstances, the impact of trees on air temperature is less efficient than the effect of surfaces' shading because the cool air produced in the tree crown is dissipated in the airflow [PHE 94]. However, the concentration of trees and other green surfaces creates a cool island effect that can be transported by advection to the surroundings. Hamada and Ohta, as Spronken and Oke have shown, that during the day, the cool park effect is established through a combination of shading and evaporation in which evaporating effect is not negligible [HAM 10, SPR 98].

Because they limit their gaseous exchanges with the atmosphere to reduce their water loss, trees that can resist drought stress allow conservation of water and are well adapted to urban conditions where they often have to grow in a surrounding of artificial soil. These kind of trees do not transpire when the thermal stress is too severe so that their effect on urban climate is limited to an indirect effect due to shading [PHE 94].

When there is no limitation of water availability, Kjelgren and Montague compared transpiration of several tree species over vegetated and paved surfaces and showed that the evapotranspiration also depends on soil [KJE 98]. The response of trees to an increase in energy load due to the higher soil temperature varies with species. Indeed, stomata of many woody plants close when the leaf-to-air vapor pressure difference reaches a threshold level. This closure reduces the water loss but increases leaves' temperature. However, in the absence of or below this threshold level, the higher the soil temperature is, the more the tree will transpire because it receives more longwave radiation from the soil. Therefore, a tree planted above stuff is likely to transpire less than the same tree planted above asphalt.

Thanks to this ability to transpire, trees can keep the temperature of their leaves in a range close to the air temperature. Leuzinger *et al.* have reported the tree crown temperature of 10 tree species frequently planted in central European cities [LEU 10]. They showed that at an ambient temperature of 25°C, tree crown temperature ranges from 24°C to 29°C. Note that water was measured at 18°C, street at 37°C, and roofs up to 45°C. Trees' temperature depends on their location (street, park, etc.) and their species. They find that coniferous species do not vary in temperature with location, keeping their foliage temperature very close to air temperature. They also remark that the larger leaves generally correspond to higher temperatures. The measure of stomatal conductance validates that the measured temperature differences were not due to water status of trees (water deficit might induce higher leaf temperatures). The authors argue that the higher crown temperatures of trees located in streets are due to higher energy load resulting from the environment that are the reflection of solar radiation and the longwave radiation due to higher surface temperatures in the

street (37°C). This is consistent with the previously cited work of Kjelgren and Montague [KJE 98]. To extrapolate their results for higher temperature conditions (summer heat waves), using properties of the different species, they calculate the leaf temperature when air temperature arises above 40°C. Given their assumptions, for the studied species, they predict a leaf-to-air temperature difference ranging from 2°C to 5°C with a stomatal downregulation to 50% and from 4°C to 10°C at more drastic stomatal downregulation to 20%. These values have to be compared to a range of −1°C to 4°C obtained during the experimental campaign (25°C). All these measures and calculations have been done with low wind velocity (2 m $s^{-1}$). In case of higher wind velocity, these leaf-to-air temperature differences would decrease because of convective heat exchanges.

In this range of temperature, tree crowns constitute cool radiative and convective surfaces. It is the reason why, from the point of view of comfort of the city dweller, foliage temperature of urban trees is of particular interest.

The windshield effect of trees modifies the balance equation because the decrease in wind airflow velocity in the near region of surfaces reduces heat transfer by convection. This effect could be a benefit in winter (less heat loss from buildings) but, in summer, it reduces the heat extraction from warm surfaces.

However, the effects of urban growing conditions on tree growth and, in turn, on their cooling performance need to be investigated. Indeed, the models used to evaluate the impact of greening strategies lie on tree forms and leaf area densities that are provided for trees that have grown in "normal" conditions. Rahman *et al.* have studied the growth and leaf physiology of a commonly planted urban tree: *Pyrus calleryana* "Chanticleer" [RAH 11]. This study has been carried out on streets in Manchester (United Kingdom) where the trees have been growing for 5−6 years under contrasting growth conditions: in pavement, in grass verges, and in Amsterdam soil. The results show that trees in Amsterdam soil have grown almost twice as fast as those in pavements. The authors conclude that the difference is related to the lower degree of soil compaction, and hence lower shear strength. Leaf physiological parameters such as stomatal conductance, leaf water potential, and foliar nutrient status have also been compared and they find that trees grown in Amsterdam soil also have better performance. This results in the evapotranspirational cooling performance of trees grown in Amsterdam soil being up to 7 kW, five times higher than those of trees grown in pavements.

### 7.2.6. *Parks*

Potchter *et al.* have conducted a research in the city of Tel Aviv (Israel) during the summer in three urban parks with various amounts of green and forested areas [POT 06]. They find that the differences in air temperature during the day between the built-up area and the urban park containing mature trees with a wide canopy

reached 3.5°C, whereas urban parks covered with grass were sometimes warmer and more humid than the built-up area during the day. Sugawara *et al.* have conducted studies over one year in Sinjyuku-Gyoen, one of the largest parks in Tokyo (Japan) [SUG 06]. They find that the average temperature difference between the built-up area and the park from 09:00 to15:00 was about 1°C.

These studies and others are presented by Bowler *et al.* who have produced a large literature review of many studies about the climatic effect of greening interventions [BOW 10]. They show that green areas have an effect on urban climate that varies and it is difficult to transpose the results from one a park to another, from an urban form to another, and from one climate to another.

## 7.3. From microscale to city scale: the modeling approaches

Initially, most of the models dedicated to urban climate simulation took into account the built environment alone. Then, they included a description of the effects of vegetation. Physical laws reflecting these effects are quite well known, but translating them into models requires defining a way of representing a set of branches (in the case of timber) and leaves that are of various shapes, thin and semitransparent. The approximations are of the same order than those made when representing buildings details: the representation of the leaves is carried out only if their form or arrangement is a parameter of the study.

The geometry of plants is complex. It combines geometries of numerous different organs, varies in time (during the day or seasonally), and from one species to another. Because of this complexity and plasticity, modeling plants' geometry is a multidisciplinary research topic for researchers from ecophysiological modeling to computer graphics.

Boudon presents various existing types of representation and generative systems of plant models [BOU 04]. He identifies two categories of approaches for modeling plants' geometry: the global approaches, which consider a plant as a whole and represents it by an envelope, and the modular one, where a plant is represented by all the geometric models of its components. With the idea to organize plant models in different levels of details to adapt the complexity of the representation or for a better understanding of plant growth, he defines a general multiscale geometric model of plant architecture.

### 7.3.1. *Microscale*

Geometric modeling of plants is particularly studied not only in the field of 3D digital imaging, for visualization software for architecture, landscape, but also for video games, animation, etc. before being used in scientific models.

The models developed by the laboratory AMAP of CIRAD are particularly used to study the distribution of active radiation for photosynthesis in plant covers and its influence on the development of new leaves [SIL 08, SIN 98]. In the software PlantGL, several methods are provided to create plant architectures from field measurements or from procedural algorithms. Because they are found to be particularly useful in plant design and simulation, special attention has been paid to the definition and use of branching system envelops [PRA 09].

**Figure 7.2.** *Trees and asphalt just behind the Agbar (J. Nouvel) tower in Barcelona (Spain)*

One of the most studied physical problems is the distribution of radiation within the canopy. It influences a large number of physiological functions (photosynthesis, transpiration, stomatal aperture, etc.), and particularly photomorphogenesis, which is involved in the dynamics of development of plant geometry. At this scale, the plants can be represented geometrically with details (leaves and wood). However, the geometrical modeling of vegetated surfaces is complicated by the extreme variability that can be encountered in the species. Moreover, the effort needed for this precise modeling has to be compared with the approximation done, e.g. when neglecting the leaves' mobility due to wind. With regard to urban issues, a detailed representation of the vegetation has applications primarily for the characterization and comparison of vegetal devices (shadow of a climbing plant, etc.). These characterizations answer questions related to plants' growth, their role in climate, or their effect on comfort or energy consumption. Is it possible for us to have a detailed representation for the whole system?

At a very detailed scale, to study the thermal behavior of plants, we can go down to the thermal budget of a leaf or a branch. Hummel *et al.* proposed a thermal model based on a geometrical representation of a tree divided in cylindrical components to which different material properties can be assigned [HUM 91]. The thermal model is then built by linking models representing the thermal behavior of these components. This kind of model can be used to assess plants' temperature, but transpiration being a crucial phenomenon, it is necessary to model the soil–plant–atmosphere continuum to take into account water flux through this hydraulic system.

Another example is that of the radiation simulation models. Starting from a detailed geometric model, SOLENE and DART allow calculating the radiative exchanges within the plant crop or between the leaves and the built-up environment [GAS 08, GRO 03]. Using SOLENE, Malys *et al.* have represented the leaves within a green wall to study the impact of the different characteristics of the leaves and their arrangement onto the reflection and transmission of shortwave radiation [MAL 10]. These characteristics are then parameterized and integrated for simulations at district scale, scale at which leaves' representation is not realizable (Figure 7.3).

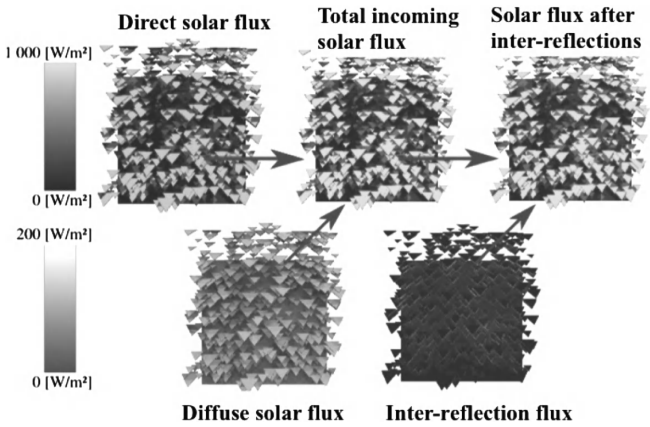


**Figure 7.3.** *Calculation of solar fluxes on the leaves of a green wall. Simulations made for a wall oriented to the west, on 6th of June at 14:00, in Nantes (France) – Adapted from [MAL 10]*

Other applications are related to the understanding of coupled phenomena that occur within plants and to interactions between vegetation and the built-up environment. These interactions are still to be explored, but adequate numerical studies should be carried out to complete and better understand the experimental ones that have already highlighted that physiological behavior and effect on microclimate of plants differs with the context in which they were planted.

### 7.3.2. *District scale*

At district scale, vegetation has been introduced in models differently owing to the different applications under study: comfort, microclimate, remote sensing analysis, etc. We distinguish two families of models that represent the radiation phenomena: radiation models and microclimatic ones. In both approaches, vegetation is modeled as a surface or a volume to which mean characteristics are attributed.

With regard to the modeling technique used to calculate radiation transfers, the trees can be modeled either as the outer layer of their crown (and if necessary those of their trunk), like in SOLENE, or as a semitransparent volume for shortwave radiation like in DART [GAS 08, ROB 06]. These surfaces and volumes can be divided to accommodate different foliage characteristics (e.g. variation of LAD with altitude). This simplification does not allow representing the inter-reflections that occur between the leaves; the phenomenon is taken into account by global characteristics. In DART, the progressive absorption of solar radiation is directly handled by the discrete ordinate method, the vegetation volumes being turbid cells. In SOLENE, decay curves are used to evaluate the energy that is transmitted through the foliage. The models that are able to represent specular reflections as DART can have more complex energy distribution in tree foliage, taking into account, e.g. the distribution of leaves' orientation [GAS 96]. Vegetation is often considered impervious to longwave radiation. In Figure 7.4, radiative exchanges between a tree and its environment are illustrated, as modeled by Robitu *et al.* [ROB 06].

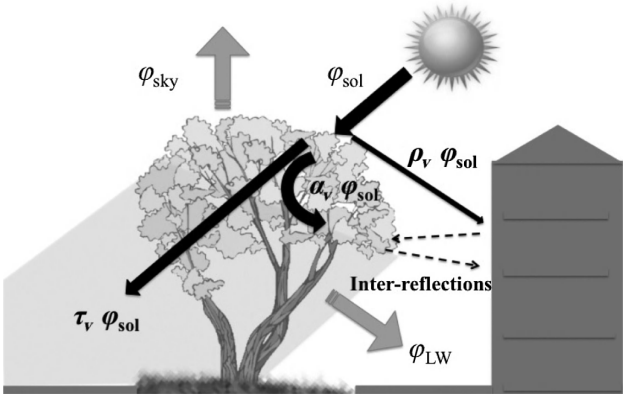


**Figure 7.4.** *Schematic representation of radiative exchanges of a tree*

In these models, either the foliage temperature is approximated as being equal to the air temperature or it is calculated writing a global (or local) balance equation considering the different fluxes exchanged by the tree with its environment.

In atmospheric models, like envi-met (http://www.envi-met.com/), vegetation is modeled as a porous element offering resistance to the airflow; this drag force is taken into account in momentum equations to air volumes that contain a part of the tree foliage. In the heat balance equation, sources and sinks are applied to account for radiative absorption and latent flux dissipation. Therefore, the calculated temperature is the one of the air–foliage mix. In the coupled option retained by the SOLENE developers, the atmospheric model is outsourced. A vegetation volume is modeled as a surface in SOLENE and as a volume in the CFD model [ROB 06]. Radiation net flux is calculated over the tree crown surface and affected to contiguous cells in the CFD code. Latent flux is calculated in each tree cell. The heat balance equation results in a mix foliage–air temperature that is used by SOLENE as the surface temperature of the tree (seen as its enveloping surface).

### 7.3.3. *City scale*

At city scale, the plants are not represented geometrically (building neither). Some modelers have chosen to neglect the latent heat flux resulting from vegetation evapotranspiration, only considering the characteristics of highly built-up environments.

The two kinds of models that take into account vegetation at this scale are radiative models for remote sensing analysis and climatic models. In the first one, vegetation is represented as surfaces that are visible from sky to which optical characteristics are attributed. In climatic models that make possible simulation at city scale, two approaches are explored. The more sophisticated one allows taking into account interactions between vegetation and built-up surfaces as shadowing effects and absorption of radiation by vegetation [LEE 08]. In intermediate approaches, latent heat flux from natural surfaces and vegetation are added in the surface heat balance equation proportionally to the quantity of these surfaces, but vegetation does not directly modify the other fluxes.

To define some guidelines for modeling, an international research action has been initiated [GRI 10, GRI 11]. The purpose was to identify in “classes” the most successful approaches to represent exchanges between an urban canopy and atmosphere, and the physical processes that should not be neglected in the physical modeling. Several conclusions were drawn based on two sets of experimental data and 33 models. Among them, one is of particular interest for us: the comparison shows that the modeling of the effects of vegetation and natural surfaces improves the results of the model, even if it is present in small proportion. However, it appears that the latent heat flux is the less well-modeled component of the energy balance. This may be due to poor knowledge of the soil–water content, and to the use of rural vegetation models.

It should be noted that even if the models were able to correctly represent the physical phenomena associated with the presence of vegetation, the description of the quantity and distribution of vegetation across the city remains a problem. It is therefore necessary to develop acquisition methods such as remote sensing that allow for providing input data to these models [KAS 10].

## 7.4. Conclusions

To understand the issues of mitigation and climate adaptation in urban environments, the inclusion of vegetation is required. When considering vegetation, we quickly realize that the problem is multiscale, multiphysical, and varies over time.

The extensive bibliography of recent years shows that the scientific community has begun to address the understanding and the modeling of the role of vegetation in the urban context. This remains a relatively new field of research in which much remains to be done. Moreover, the development of new knowledge in this field requires the involvement of several disciplines: agronomy, hydrology, thermal sciences, climatology, etc. Their approaches are converging toward models that are more and more adapted to assess the impact of vegetation on urban climate phenomena. It remains to provide them with information tailored to the assumptions on which the models are based.

## 7.5. Bibliography

[ALA 08] ALAXANDRI E., JONES P., "Temperature decreases in an urban canyon due to green walls and green roofs in diverse climates", *Building and Environment*, vol. 43, no. 4, pp. 480–493, 2008.

[ARM 11] ARMSON D., ENNOS A.R., "The effect of trees and grass on surface water runoff and the surface and globe temperatures in urban areas", *Communication to Ecocity World Summit*, Montréal, Canada, pp. 22–26, August 2011.

[BOU 04] BOUDON F., Représentation géométrique multi-échelles de l'architecture des plantes, PhD Thesis, Montpellier University, France, 2004.

[BOW 10] BOWLER D.E., BUYUNG-ALI L., KNIGHT T.M., PULLIN A.S., "Urban greening to cool towns and cities: a systematic review of the empirical evidence", *Landscape and Urban Planning*, vol. 97, no. 3, pp. 147–155, 2010.

[BRU 82] BRUSTAERT W., *Evaporation into the Atmosphere: Theory, History and Applications*, Springer, 1982.

[CA 98] CA V.T., ASAEDA T., ABU E.M., "Reductions in air conditioning energy caused by a nearby park", *Energy and Buildings*, vol. 29, no. 1, pp. 83–92, 1998.

[CAO 10] CAO X., ONISHI A., CHEN J., IMURA H., "Quantifying the cool island intensity of urban parks using ASTER and IKONOS data", *Landscape and Urban Planning*, vol. 96, no. 4, pp. 224–231, 2010.

[CHE 10] CHENG C.Y., CHEUNG K.K.S., CHU L.M., "Thermal performance of a vegetated cladding system on facade walls", *Building and Environment*, vol. 45, no. 8, pp. 1779–1787, 2010.

[FEN 10] FENG C., MENG Q., ZHANG Y., "Theoretical and experimental analysis of the energy balance of extensive green roofs", *Energy and Buildings*, vol. 42, no. 6, pp. 959–965, 2010.

[GAS 96] GASTELLU-ETCHEGORRY J.-P., ZAGOLSKI F., ROMIER J., "A simple anisotropic reflectance model for homogeneous multilayer canopies", *International Journal of Remote Sensing*, vol. 20, no. 14, pp. 2761–2785, 1996.

[GAS 08] GASTELLU-ETCHEGORRY J.-P., AUDA Y., MARTIN E., BRUT A., DEMARZ V., GRAU E., HUBIO J., BENECH N., Suere C., SOLIGNAC P.-A., GROUSSOUS A., BELOT A., HENRY P., BERNAT V., PRECHEUR G., "Dart: Modèle physique 3D d'images de télédétection et de bilan radiatif du paysage urbain et naturel", *Revue Télédétection*, vol. 8, no. 3, pp. 159–167, 2008.

[GRI 10] GRIMMOND C.S.B., BLACKETT M., BEST M.J., BARLOW J., BAIK J.-J., BELCHER S.E., BOHNENSTENGEL S.I., CALMET I., CHEN F., DANDOU A., FORTUNIAK K., GOUVEA M.L., HAMDI R., HENDRY M., KAWAI T., KAWAMOTO Y., KONDO H., KRAYENHOFF E.S., LEE S.-H., LORIDAN T., MARTILLI A., MASSON V., MIAO S., OLESON K., PIGEON G., PORSON A., RYU Y.-H., SALAMANCA F., SHASHUA-BAR L., STEENEVELD G.-J., TOMBROU M., VOOGT J., YOUNG D., ZHANG N., "The international urban energy balance models comparison project: first results from phase 1", *Journal of Applied Meteorology and Climatology*, vol. 49, no. 6, pp. 1268–1292, 2010.

[GRI 11] GRIMMOND C.S.B., BLACKETT M., BEST M.J., BAIK J.J., BELCHER S.E., BERINGER J., BOHNENSTENGEL S.I., CALMET I., CHEN F., COUTTS A., DANDOU A., FORTUNIAK K., GOUVEA M.L., HAMDI R., HENDRY M., KANDA M., KAWAI T., KAWAMOTO Y., KONDO H., KRAYENHOFF E.S., LEE S.-H., LORIDAN T., MARTILLI A., MASSON V., MIAO S., OLESON K., OOKA R., PIGEON G., PORSON A., RYU Y.H., SALAMANCA F., STEENEVELD G.J., TOMBROU M., VOOGT J., YOUNG D., ZHANG N., "Initial results from phase 2 of the international urban energy balance model comparison", *International Journal of Climatology*, vol. 31, no. 2, pp. 244–272, 2011.

[GRO 03] GROLEAU D., FRAGNAUD F., ROSANT J.M., "Simulation of the radiative behavior of an urban quarter of Marseille with the Solene model", in *ICUC5*, *Fifth International Conference on Urban Climate*, Lodz, 2003.

[HAM 10] HAMADA S., OHTA T., "Seasonal variations in the cooling effect of urban green areas on surrounding urban areas", *Urban Forestry and Urban Greening*, vol. 9, pp. 15–24, 2010.

[HER 08] HERB W.R., JANKE B., MOHSENI O., STEFAN H.G., "Ground surface temperature simulation for different land covers", *Journal of Hydrology*, vol. 356, nos. 3–4, pp. 327–343, 2008.

[HUM 91] HUMMEL J., JONES J., LONGTIN D., PAUL N., Development of a 3-D tree thermal response model for energy budget and scene simulation study, Scientific report no. 8, SPARTA Inc and Phillips Laboratory, Air force systems command, p. 48, 1991. Consulted from: http://handle.dtic.mil/100.2/ADA240693, 3/9/2012.

[IP 10] IP K., LAM M., MILLER A., "Shading performance of a vertical deciduous climbing plant canopy", *Building and Environment*, vol. 45, no. 1, pp. 81–88, 2010.

[KAS 10] KASSOUK Z., LAUNEAU P., ROY R., MESTAYER P., ROUAUD J.-M., GIRAUD M., *Urban Mapping Using Hyperspectral Hyspex Images over Nantes City*, *France*, IASIM-10, Dublin, 18–19 November 2010.

[KJE 98] KJELGREN R., MONTAGUE T., "Urban tree transpiration over turf and asphalt surfaces", *Atmospheric Environment*, vol. 32, no. 1, pp. 35–41, 1998.

[LEE 08] LEE S.H., PARK S.U., "A vegetated urban canopy model for meteorological and environmental modeling", *Boundary-Layer Meteorology*, vol. 126, no. 1, pp. 73–102, 2008.

[LEU 10] LEUZINGER S., VOGT R., KÖRNER C., "Tree surface temperature in an urban environment", *Agricultural and Forest Meteorology*, vol. 150, pp. 56–62, 2010.

[MAL 10] MALYS L., MUSY M., Évaluation des Caractéristiques Radiatives Solaires des Couvertures Végétales de Façades, IBPSA France, Morêt-sur-Loing, pp. 9–10, November 2010.

[NIC 96] NICHOL J.E., "High-resolution surface temperature patterns related to urban morphology in a tropical city: a satellite-based study", *Journal of Applied Meteorology*, vol. 35, no. 1, pp. 135–146, 1996.

[PÉR 11] PÉREZ G., RINCÓN L., VILA A., GONZÁLEZ J.M., CABEZA L.F., "Behaviour of green facades in mediterranean continental climate", *Energy Conversion and Management*, vol. 52, no. 4, pp. 1861–1867, 2011.

[PHE 94] MCPHERSON E.G., "Cooling urban heat islands with sustainable landscapes", *The Ecological City, Preserving and Restoring Urban Biodiversity*, PLATT R.H., ROWNTREE R.A., MUICK P.C. (eds), University of Massachusetts Press, Boston, MA, pp. 151–171, 1994. Consulted from http://gis.fs.fed.us/psw/programs/uesd/uep/products/cufr_82_EM94_59.PDF, 3/9/2012.

[POT 06] POTCHTER O., COHEN P., BITAN A., "Climatic behavior of various urban parks during hot and humid summer in the mediterranean city of Tel Aviv, Israel", *International Journal of Climatology*, vol. 26, no. 12, pp. 1695–1711, 2006.

[PRA 09] PRADAL C., BOUDON F., NOUGUIER C., CHOPARD J., GODIN C., "Plant GL: a python-based geometric library for 3D plant modelling at different scales", *Graphical Models*, vol. 71, no. 1, pp. 1–21, 2009.

[RAH 11] RAHMAN A., SMITH J.G., STRINGER P., ENNOS A.R., "Effect of rooting conditions on the growth and cooling ability of *Pyrus calleryana*", *Urban Forestry and Urban Greening*, vol. 10, pp. 185–192, 2011.

[ROB 06] ROBITU M., MUSY M., INARD C., GROLEAU D., "Modeling the influence of vegetation and water pond on urban microclimate", *Solar Energy*, vol. 80, no. 4, pp. 435–447, 2006.

[SAN 07] SANTAMOURIS M., PAVLOU C., DOUKAS P., MIHALAKAKOU G., SYNNEFA A., HATZIBIROS A., PATARGIAS P., "Investigating and analysing the energy and environmental performance of an experimental green roof system installed in a nursery school building in Athens, Greece", *Energy*, vol. 32, pp. 1781–1788, 2007.

[SIL 08] DA SILVA D., BOUDON F., GODIN C., SINOQUET H., "Multiscale framework for modeling and analyzing light interception by trees", *Multiscale Modeling and Simulation*, vol. 7, no. 2, pp. 910–933, 2008.

[SIN 98] SINOQUET H., THANISAWANYANGKURA S., MABROUK H., KASEMSAP P., "Characterization of the light environment in canopies using 3D digitising and image processing", *Annals of Botany*, vol. 82, pp. 203–212, 1998.

[SPR 98] SPRONKEN-SMITH R.A., OKE T.R., "The thermal regime of urban parks in two cities with different summer climates", *International Journal of Remote Sensing*, vol. 19, no. 11, pp. 2085–2104, 1998.

[SUG 06] SUGAWARA H., NARITA K., MIKAMI T., HONJO T., ISHII K., "Cool island intensity in a large urban green: seasonal variation and relationship to atmospheric conditions", *Tenki*, vol. 53, no. 5, pp. 3–14, 2006.

[TAK 07] TAKEBAYASHI H., MORIYAMA M., "Surface heat budget on green roof and high reflection roof for mitigation of urban heat island", *Building and Environment*, vol. 42, no. 8, pp. 2971–2979, 2007.

[TAK 09] TAKEBAYASHI H., MORIYAMA M., "Study on the urban heat island mitigation effect achieved by converting to grass-covered parking", *Solar Energy*, vol. 83, no. 8, pp. 1211–1223, 2009.

[VEL 06] VELASQUEZ-LOZADA A., GONZALES J.E., WINTER A., "Urban heat island effect analysis for San Juan, Puerto Rico", *Atmospheric Environment*, vol. 40, pp. 1731–1741, 2006.

Chapter 8

# Multiscale Daylight Modeling for Urban Environments

## 8.1. Introduction

Daylight in buildings is the natural illumination experienced by the occupants of any man-made construction with openings to the outside. The quantity and quality of daylight in buildings is continually varying due to the natural changes in the Sun and sky conditions from one moment to the next. In urban settings, the dynamics of daylight illumination are amplified by the vertical extent of buildings and the density of the built form. Traditional schema for evaluating daylight in the built environment consider only one or perhaps a few "snapshot" conditions, e.g. a single overcast sky, or a sequence of shadow patterns for selected hours. This chapter describes the application of a technique called climate-based daylight modeling (CBDM) across various urban scales – from office spaces to large-scale city models. CBDM is the prediction of various radiant or luminous quantities (e.g. irradiance, illuminance, radiance, and luminance) using Sun and sky conditions that are derived from standard meteorological datasets. CBDM delivers predictions of absolute quantities (e.g. illuminance) that are dependent on both the locale (i.e. geographically specific climate data are used) and the building orientation (i.e. the illumination effect of the Sun and non-overcast sky conditions are included), in addition to the building's composition and configuration. The examples described in the chapter include theoretical studies and two "live" projects.

---

Chapter written by John MARDALJEVIC and George M. JANES.

*Solar Energy at Urban Scale* Benoit Beckers

## 8.2. Background

### 8.2.1. *Climate and microclimate*

"Microclimate" is a commonly used term, but just as is the case with the word "climate", the meaning is multifarious and therefore lacks precision. The dictionary definition of climate is given as:

> *Climate – the meteorological conditions, including temperature, precipitation, and wind, that characteristically prevail in a particular region.*

As is evident from the definition, climate is not characterized by one specific measurable quantity. Rather, it is taken to be a combination of several physical quantities. Temperature, perhaps, is what first springs to mind when one thinks of climate. The phrase "historical temperature record" is generally used to refer to the time from which reasonably reliable records exist, i.e. data founded on actual observations taken with accurate thermometers. This is generally considered to be from about 1850 – earlier records exist, but coverage and instrument standardization were poorer. Note that atmospheric pressure has been accurately recorded over a similarly long period. However, its primary purpose was to gain an understanding of the dynamics of weather systems, i.e. forecasting. Rainfall is relatively easy to measure, as is wind speed and wind direction. Solar radiation – the principal driver of the Earth's weather system – is, however, difficult to measure. The amount of solar radiation resulting from the sky and the Sun at any one instant is characterized by a quantity called the global horizontal irradiance. This is a measure of the energy density incident on a horizontal surface and it has units of Watts per square meter (W $m^{-2}$). Note that the orientation of the surface is important. A horizontal surface is specified in the definition of global (horizontal) irradiance because it receives radiation from the entire hemisphere of sky. Radiation from the sky is called diffuse because it originates from all directions above the horizon. Cloudy skies without Sun produce mainly diffuse radiation (i.e. producing soft shadows). On clear days, however, the Sun is often the dominant source of radiation, resulting in sharp, high-contrast shadows. To distinguish between radiation originating from the sky and the Sun, it is necessary to measure the components separately. The sky component is called the diffuse horizontal irradiation. This can be measured in the same way as global horizontal irradiation with the addition of a "shadow band" to block any (direct) solar radiation. The direct solar radiation is usually characterized by measurements of direct normal irradiance. To achieve this, the measuring instrument must track the movement of the Sun to ensure that it is always pointing at the solar disk.

Microclimate is commonly taken to be that which occurs in any "local zone" where the climate differs from what is generally prevailing. Microclimates exist across a vast range of scales, a crevice in a rock, a walled garden, a sheltered meadow, etc. In each

case, one or more components of the climate differ from what would otherwise be the case. For example, a walled garden would allow access to the Sun from the south, while sheltering plants from wind and the full sky hemisphere which can have very low radiative temperatures on clear nights. The ancient Persians, masters of passive design, used the principle in reverse to create ice by having the wall cast a shadow across a canal running in an east-west direction. This ensured that any ice that formed due to the low air temperature and radiative cooling at night would not be melted by the Sun [RAE 08]. The solar microclimate therefore is that which happens when the exposure due to radiation from the Sun and sky differs from what would otherwise occur. In practice, this means that any surface which is not simply horizontal-planar has its own solar microclimate. The nature of the solar microclimate will depend on the shapes of the surfaces and their surroundings; the reflective, absorptive, and emissive properties of the surfaces; and the quantity and character of the radiation from the Sun and sky that "illuminates" the scene.

Irradiance is a radiometric quantity which is equal to the incident total radiant energy (W $m^{-2}$). Illuminance is the visible part and it has units of lumens per square meter or lux. The illuminance is equivalent to the irradiance where the power at each wavelength is weighted according to the luminosity function, a standardized model of human visual brightness perception. In this chapter, the examples given show either radiometric (e.g. irradiance) or visible (e.g. illuminance) units depending on the application. It should be noted, however, that the radiation model used in the simulations does not account for the emission and/or reradiation of longwave radiation. While the output of the daylight sources is specified in radiometric units, the reflection models used in the simulation are characterized primarily in terms of visible radiation, e.g. 0.2 or 20% reflectivity for typical ground surfaces. This is a reasonable approximation to employ for many scenarios; however, the reader needs to be aware of this limitation when extrapolating to other situations where the quantity and character of the thermal radiation is a key consideration.

### 8.2.2. *The urban solar microclimate*

The interaction between buildings and light from the Sun and sky is the defining characteristic of the urban environment. The urban form, in particular its vertical extent, serves to amplify the dynamic character of daylight through the casting and progression of shadows by tall buildings. Planners and architects have long appreciated, at least qualitatively, that the perception of the urban environment is directly related to the prevailing daylight conditions, or as it is often called, the "urban solar microclimate" (USM). Characteristic features of urban environments are the large gradients in solar access over small spatial scales. A few stories below an office or apartment perceived as benefiting from daylight may be one that is quite shaded.

Until recently, daylight in buildings was thought of primarily in terms of its amenity value. Toward the end of 1990s, the daylighting of buildings began to attract greater attention for a number of reasons. The two most important drivers were:

1) the widespread belief that the potential to save energy through effective daylighting was greatly underexploited;

2) the availability of data suggesting that daylight exposure has many positive, productivity, health, and well-being outcomes for the occupants.

The first of these concerns originated in the 1970s following the energy crisis, and culminated with the widely accepted need to reduce carbon emissions from buildings to minimize the anticipated degree of anthropogenic climate change. This in turn led in the 1990s to the formulation of guides and recommendations to encourage the design and construction of low-energy buildings and also for the retrofit of existing buildings. More recently, it is envisaged that buildings could become net producers of energy where there is the potential to deploy electricity generating facades, i.e. building-integrated photovoltaic (or BIPV) panels [DTI 00].

### 8.2.3. *The USM and human experience*

People will inevitably form judgments about their immediate environment, be it the workplace, home, or a public area. Commonly perceived notions of the local solar microclimate might include the following considerations/appreciations:

– In terms of overall perception, is the space “bright and open” or “gloomy and dark” – this could apply equally to inside and outside spaces.

– Is there direct exposure to sunlight, and if so when and for how long?

– Availability of daylight – how “much” of the sky is visible? Is there a greater “view” of sky in some directions than others?

The primary concern in the daylighting of buildings has generally been to provide illumination for task, e.g. 500 lux on the horizontal work plane. However, in the last few decades, there has been a gradual increase in awareness of the non-visual effects of daylight/light perceived by the eye [ANN 06]. It is well known that occupants almost without exception will prefer a workstation with a view of the outdoor environment to a windowless office [BEL 76]. A view to the outside indicates of course the presence of daylight, although the relation between view and daylight provision is not straightforward being dependent on many factors. Might there be productivity and well-being benefits in providing occupants with well – daylit spaces? In addition to subjective preferences for daylit spaces, it is now firmly established that light has measurable biochemical effects on the human body, in particular with respect to maintaining a healthy sleep–wake cycle. Could the quality and nature of the internal

daylit environment have a significant effect on the health of the human body, which can be proved through the measurement of, say, hormone levels? Evidence is suggestive of links between daylight exposure and both health and productivity.

The USM, therefore, has considerations that now extend far beyond the notions of "solar access" that were common in architectural circles a few decades ago.

### 8.2.4. *The USM in guidelines and recommendations*

Efforts to systematize the various perceptions of the USM into a schema that can be applied to the evaluation of building designs or urban plans have not resulted in a consensus view: solar access means different things to different people. Two very different analysis techniques are commonly employed in an attempt to make some measure of solar access in urban environments. One of these is based on shadow patterns cast by the Sun at various times of the year, e.g. on the summer solstice. For this, a sequence of images are produced using either scale models with a heliodon or by computer simulation. This approach is essentially qualitative: the brightness of the Sun plays no part and the light from the sky is not considered. The other method is based on the illumination provided by a single (i.e. unchanging) standard overcast sky without Sun. The brightness of the standard overcast sky increases gradually with altitude from the horizon to the zenith, but it does not vary with azimuth. In other words, the illumination received at any surface will not change if the building model is rotated about the vertical axis. Although quantitative, the second approach is highly idealized because only one sky condition is considered – no account whatsoever is made of the Sun or non-overcast skies. It may be that both methods are employed together. However, it is not at all clear how, in an analysis, it is possible to weigh one (or more) shadow pattern(s) against a measure of the illumination from a (sunless) overcast sky.

Where attempts have been made to recommend (usually) minimum levels of solar access, the definitions vary and are largely incompatible. For example, in San Jose (USA) solar access is defined as the unobstructed availability of direct sunlight at solar noon on December 21, the winter solstice, whereas in Boulder (Colorado, USA) an ordinance was enacted to guarantee unobstructed sunlight availability between 10.00 a.m. and 2.00 p.m. on December 21. These could be tested using the shadow pattern technique. Other definitions make a less specific measure of solar access, e.g. the Solar Envelope [KNO 85].

The current situation with the evaluation of solar access has arisen because the fundamentals of the two most commonly used approaches have changed a little over the past 50 years. Indeed, they are now part of the mental landscape of the majority of practitioners and researchers, be they planners, architects, or engineers. Computer modeling may be preferred nowadays over scale models to generate shadow patterns

and predict illuminance under standard overcast sky conditions. This, however, gives only the illusion of progress because the fundamental limitations are an intrinsic part of the methodology, not the means by which it is carried out.

The reality of our everyday experience of the daylit luminous environment differs markedly from what the two most commonly used assessment methods can tell us. Light from the Sun and the sky (overcast, clear, etc.), both directly and indirectly, illuminates the urban environment. And, of course, the Sun and the sky act together to provide illumination. Direct sunlight accounts, overall, for about half of the available daylight energy. The remainder comes from the sky and is usually referred to as diffuse light. Of the diffuse (sky) light, less than half of that, depending on locale, is due to conditions that approximate standard overcast. It is evident therefore that the shadow casting and overcast sky methods, either independently or together, provide only a very limited insight into solar access. To advance our perception of solar access, indeed to make some measure of it that is closer to our experience of the daylit environment, we need to first examine the underlying meteorological conditions.

### 8.2.5. *"Real" climate*

The quantity and character of light from the Sun and sky are subject to regular daily and seasonal patterns of variation together with irregular events governed by local meteorological conditions. An illustration of the dynamic nature of sky and Sun conditions is given in Figure 8.1. Hourly values of diffuse horizontal illuminance and direct normal illuminance over a period of a full year are shown as (tiny) shaded rectangles arranged in a 365 (days of the year) by 24 (hours of the day) matrix. The diffuse horizontal illuminance is the visible part of the energy from the sky that is incident on an unobstructed horizontal surface. The direct normal illuminance is the visible part of the energy from the Sun and circumsolar region incident on a surface that is normal to the direction of the Sun. The shading in Figure 8.1 represents the magnitude of the illuminance with zero values shaded light gray. Presented in this way, it is easy to appreciate both the prevailing patterns in either quantity and their short-term variability. Most obvious are the daily/seasonal patterns for both illuminances: short periods of daylight in the winter months, longer in summer. The hour-by-hour variation in the direct normal illuminance is clearly visible, though it is also present to a lesser degree in the diffuse horizontal illuminance (i.e. from the sky). Of course, both diffuse and direct illuminance will, in reality, vary over periods shorter than an hour. The hourly datasets, however, are the most generally available and they do exhibit much of the variation in conditions that might be expected, e.g. in the absolute magnitudes of the two quantities, the occurring Sun positions, etc. Furthermore, these standard datasets provide definitive yardstick quantities for modeling purposes.

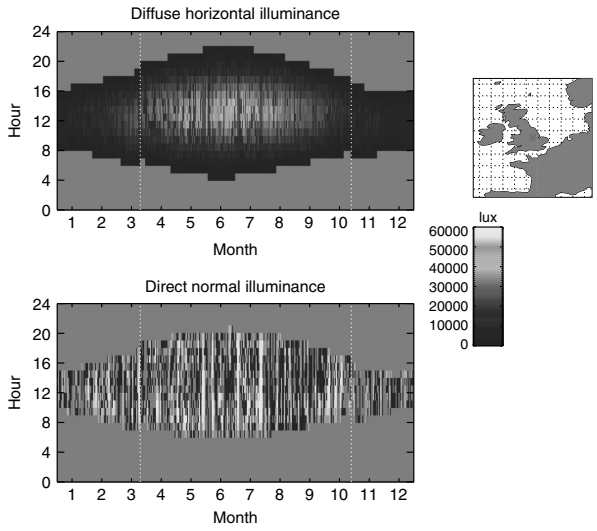


**Figure 8.1.** *Illuminance data from a standardized climate file for Nottingham, UK*

It is a relatively straightforward matter to generate sky and Sun conditions from, respectively, the diffuse horizontal and the direct normal irradiance quantities [MAR 08]. It is understood that it is impossible to recreate an actually occurring instantaneous sky brightness pattern from a measurement of diffuse horizontal irradiance because a real sky may often exhibit unique brightness configurations resulting from cloud patterns. However, it is possible to achieve reasonable approximations to actually occurring conditions using theoretical sky models that generate idealized sky brightness patterns from the basic irradiance quantities found in climate datasets. The general character of the sky brightness pattern (e.g. overcast, intermediate, or clear) can be inferred from the relative values in the diffuse horizontal and the direct normal irradiances, and the Sun's position is calculated from the "time-stamp".

### 8.2.6. *Climate-based daylight modeling*

The theoretical models and the basic meteorological data (i.e. standardized weather files) exist to generate hour-by-hour descriptions for the sky and Sun that are representative of the actually occurring conditions for the majority of locales in the developed world. CBDM is the prediction of various radiant or luminous quantities (e.g. irradiance, illuminance, radiance, and luminance) using Sun and sky conditions that are derived from these standardized annual meteorological datasets. Climate-based modeling delivers predictions of absolute quantities (e.g. illuminance)

that are dependent on both the locale (i.e. geographically specific climate data are used) and the fenestration orientation (i.e. accounting for solar position and variable sky conditions), in addition to the space's geometry and material properties.

The term CDBM does not yet have a formally accepted definition – it was first coined by Mardaljevic in the title of a paper given at the 2006 CIBSE National Conference [MAR 06a]. However, it is generally taken to mean any evaluation that is founded on the totality (i.e. Sun and sky components) of time series daylight data appropriate to the locale over the course of a full year. In practice, this means Sun and sky parameters found in, or derived from, the standard meteorological data files which contain 8,760 hourly values for a full year. Given the self-evident nature of the seasonal pattern in sunlight availability, a function of both the Sun position and the seasonal patterns of cloudiness, an evaluation period of 12 months is needed to capture all of the naturally occurring variation in conditions that is represented in the climate dataset. It is also possible to use real-time monitored weather for a given time period, if calibration to actual monitored conditions within a space is desired. Standardized climate datasets are derived from the prevailing conditions measured at the site over a period of years, and they are structured to represent both the averages and the range in variation that typically occurs. Standard climate data for a large number of locales across the world are freely available for download from several Websites. One of the most comprehensive repositories is that compiled for use with the EnergyPlus thermal simulation program [CRA 01]. This contains freely available climate data for over 1,200 locations worldwide.

There are a number of possible ways to use CBDM [MAR 00a, MAR 06b, NAB 06, REI 00, REI 06]. The two principal analysis methods are cumulative and time-series. A cumulative analysis is the prediction of some aggregate measure of daylight (e.g. total annual illuminance) founded on the cumulative luminance effect of (hourly) sky and the Sun conditions derived from the climate dataset. It is usually determined over a period of a full year, or on a seasonal or monthly basis, i.e. predicting a cumulative measure for each season or month in turn. Evaluating cumulative measures for periods shorter than one month is not recommended since the output will tend to be more revealing of the unique pattern in the climate dataset than of "typical" conditions for that period. Time-series analysis involves predicting instantaneous measures (e.g. illuminance) based on each of the hourly (or subhourly) values in the annual climate dataset. These predictions are used to evaluate, e.g. the overall daylighting potential of the building, the occurrence of excessive illuminances, or luminances, as inputs to behavioral models for light switching and/or blinds usage, and the potential of daylight responsive lighting controls to reduce building energy usage. Thus, a daylight performance metric would need to be based on a time series of instantaneously occurring daylight illuminances since these cannot be reliably inferred from cumulative values [MAR 09]. As noted, evaluations should span an entire year. CDBM can be used in both cumulative and time-series modes to help evaluate and understand the USM, examples for which are given in the following sections.

All the examples shown in this chapter were created using a CBDM tool founded on the *Radiance* lighting simulation system [WAR 98]. The CBDM software (created by Mardaljevic) is a gradually evolving suite of tools for investigating a wide range of daylighting applications, including non-visual effects [MAR 11]. Some of the CBDM modalities described in this chapter are now available in end-user tools such as DAYSIM[1]. As noted in section 8.2.1, the radiation model used in *Radiance* does not account for the exchange of longwave radiation.

## 8.3. Visualizing the urban solar microclimate

It is proposed that the total annual illuminance (or irradiance) incident on a surface should be used as the basis for visualizing the "USM". As noted above, any cumulative period shorter than a full year will not be representative of the overall prevailing conditions for that locale. A cumulative measure (illuminance or irradiance) over a full year provides a relatively unambiguous basis for the USM. And, since standardized climate data are used, the results offer a "yardstick" for comparison purposes.

### 8.3.1. *The San Francisco 3D model*

One of the first complex scenes to be irradiation mapped was a 3D model of the financial district in San Francisco [MAR 00b]. At the time (2001), this was one of the more complex 3D city models available on the Web. A rendering of the model with the removal of texture-mapped surfaces is shown in Figure 8.2. For this rendering, the model was illuminated by three light sources – effectively, three "suns" – to better show detail in the geometry than would be the case with a single light source.

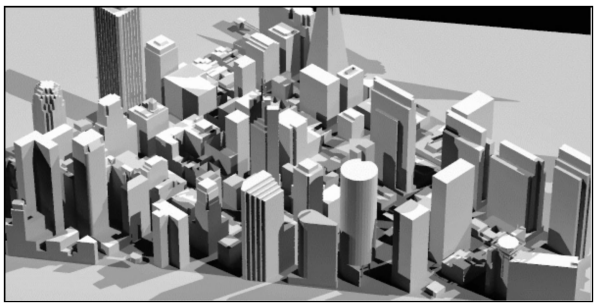

**Figure 8.2.** *3D model of San Francisco*

Five views showing the total annual irradiation (TAI) incident on the surfaces of the San Francisco city model are given in Figure 8.3. The central image shows the TAI

1 http://daysim.com/

as viewed from directly above an area in the center of the model. The magnitude of the predicted TAI is shown using false-color – the legend indicates the range used for the mapping, i.e. 200 kWh $m^{-2}$ to 1,400 kWh $m^{-2}$. The surrounding images show the views from the four mid-compass directions, northeast, southeast, etc. Most readily apparent is the difference in the TAI between the two views from the north and those from the south. On closer inspection, the large gradients in TAI across many of the building facades become evident.

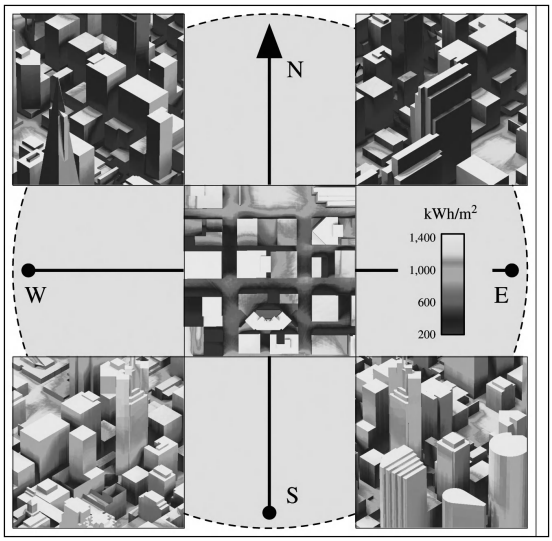


**Figure 8.3.** *Five views of the San Francisco 3D model showing the predicted TAI*

These images are first and foremost representations of quantitative data – the result of exacting computations. Their significance, however, can be readily appreciated by non-engineers – planners and architects quickly understand the significance of the data. This is in large part because the approach is view-based. Each 600 by 600 pixel image is comparable to a visualization of the annual total of hourly data collected by 360,000 irradiance meters arranged over the building facades, ground, etc. Therein lies one of the key advantages of an image-based approach over a points-based calculation: the new technique makes visible, literally, the solar microclimate in complex urban settings. If desired, the individual pixel values can be read interactively on-screen.

The San Francisco city model was chosen because it was, at the time, one of the most detailed 3D models freely available on the Web. The climate dataset (TMY) for San Francisco was downloaded from the Renewable Resource Data Center in the United States. Hourly Sun and sky conditions for San Francisco were derived from

the meteorological data and used in the simulations. An unexpected feature of using San Francisco was that the TAI on unshaded east-facing surfaces was predicted to be a little lower than on unshaded west-facing surfaces. At first, this was puzzling because weather files for other locations did not show this effect. Further investigation revealed that this is, in fact, a consequence of the San Francisco morning fog. The fog occurs so regularly throughout the year that its effect is present in the weather file: irradiation from the Sun in the morning (in the east) is slightly attenuated compared to irradiation in the afternoon (in the west) when the fog has usually lifted. It is noteworthy that this subtle aspect of the locale should be discernible in the visualizations of the solar access. The use of the San Francisco model was also important to demonstrate the inherent scaleability of the approach: to have a real-world application, there should not be practical limits on the complexity of the 3D model used in the simulation. The approach shown here can be equally applied to small-scale architectural features as to large-scale city models.

### 8.3.2. *Harvesting solar energy*

Of the renewable technologies that have been proposed to reduce the carbon emissions associated with the energy consumption of buildings, *in situ* generation of electricity by photovoltaics (PVs) is considered one of the most promising [IEA 98]. PVs devices at present are based on silicon in various formulations. New materials and novel approaches to PV fabrication are under vigorous investigation. Whatever the type of the PV module, the potential for exploitation of BIPV installations depends primarily on the available solar irradiation. A report by the UK Department of Trade and Industry gave details of 16 typical BIPV projects [DTI 00]. For these demonstration projects – completed, planned, or speculative – shading issues were largely avoided by choosing open sites with minimal nearby obstructions. In the medium-to-long-term planning however, BIPV in dense urban environments will need to be considered since this is where the majority of the energy use takes place. The wider adoption of BIPV will depend on sound demonstrations of its economic viability. Foremost in the evaluation of PV economics is the calculation of the available solar energy. Images of TAI allow rapid identification of candidate facade and roof areas where the total received solar energy is sufficient to warrant consideration as a site for BIPV. The performance of a BIPV installation can be degraded by transient shading effects which are not revealed in images showing cumulative totals. Therefore, detailed analysis of these effects using a time series might be required once a candidate site has been identified.

Another, rather more speculative, technology that has been proposed to harvest solar energy in urban environments is the growth of algae to produce biofuels. The key rate-limiting "external" factor for algal growth is the availability of the photosynthetically active component of daylight. In the urban environment, the

degree and occurrence of daylight availability results from the complex interaction of the built form and the irradiation microclimate. Maximum, sustainable yield of biomass from algae photobioreactors (PBRs) would depend on the optical design being tailored to the available light field [UGW 08]. Thus, the optical design of the PBRs at small scales would need to be optimized with respect to the large-scale urban irradiation microclimate and the surface type used. This is another potential application for multiscale irradiation mapping: to determine the quantity and distribution of photosynthetically active radiation across all relevant scales from the centimeter dimensions of the transparent tubes of an algae reactor to large-scale 3D city environments.

### 8.3.3. *A strategic evaluation of urban solar potential*

Whatever the nature of a solar technology intended for urban settings, the economic rationale for its wide-scale deployment will depend on an assessment of both the total available facade area and the solar potential since the effectiveness of these technologies is critically dependent on the magnitude of the received TAI. How this might be achieved in practice is as follows. The building facade area, graded for TAI, was determined for the entirety of the 3D model shown in Figure 8.2. To gain further insight into this quantity, a 2D grading was used: the facade area was sorted into bands of TAI and height above ground. The results are shown in Table 8.1. The total area for vertical and slightly sloping facades was determined to be $1.18 \times 10^6$ m$^2$. The target area was set to include the entire model (to remove the need for incremental steps) and five views similar to those shown in Figure 8.3 were generated. The irradiation map for one view is given in Figure 8.4, with one of the height ranges shaded green for illustration.

The *Radiance* software on which the CBDM system is founded uses a backwards ray-tracing method to transport light. Compared to, say, radiosity, ray-tracing in *Radiance* places few, if any, limitations on either material properties (for both transmission and reflection) or scene complexity. However, a consequence of the ray-tracing approach is that the solution for global illumination is not "coupled" to the scene geometry. In other words, the full solution is obtained only for those surfaces that are visible in the image. Thus, for a survey of the 3D model to be comprehensive, multiple views from several vantage points must be taken to ensure that most of the building surfaces are visible in at least one of the images – hence, the high-up viewpoint for the image shown in Figure 8.4. Using tools that are part of the standard *Radiance* release, it is possible, for every pixel point in an image, to determine the following:

– the solid angle subtended by the pixel;

– the surface normal at the point where the ray intersects the model;

– the world (i.e. $x, y, z$) coordinates of the point of intersection.

From these data, it is then a straightforward matter to determine the (building) surface area associated with each pixel – for which, of course, there is a prediction of total annual irradiance. Then, in summing – and grading – the building surfaces over the five images, it is necessary to avoid the multiple counting of building surfaces since they are usually visible in more than one image. For most vertical surfaces, the azimuth of the surface normal is a sufficient discriminator to avoid multiple counting. The method, therefore, provides an estimate of TAI-graded surface area rather than an exact solution. Tests have shown, however, that for many typical geometries, the approach delivers results of more than acceptable accuracy. Furthermore, data on this scale and resolution would be otherwise unobtainable with such relative ease.

| | Total annual irradiation (Wh $m^{-2}$) | | | |
|---|---|---|---|---|
| Height range (m) | 4E5 to 6E5 | 6E5 to 8E5 | 8E5 to 1E6 | >1E6 |
| 3 – 25 | 1.04E+05 | 4.96E+04 | 3.73E+04 | 1.92E+04 |
| 25 – 50 | 1.03E+05 | 7.68E+04 | 4.78E+04 | 1.66E+04 |
| 50 – 75 | 6.96E+04 | 9.08E+04 | 5.71E+04 | 1.68E+04 |
| 75 – 100 | 3.54E+04 | 6.91E+04 | 6.31E+04 | 1.64E+04 |
| 100 – 125 | 1.85E+04 | 3.86E+04 | 4.94E+04 | 1.84E+04 |
| 125 – 150 | 7.47E+03 | 2.51E+04 | 3.52E+04 | 2.17E+04 |
| 150 – 175 | 6.44E+03 | 1.44E+04 | 2.11E+04 | 1.74E+04 |
| 175 – 200 | 2.68E+03 | 3.82E+03 | 6.80E+03 | 4.08E+03 |
| >200 m | 2.13E+03 | 3.36E+03 | 7.01E+03 | 3.17E+03 |

**Table 8.1.** *Facade area ($m^2$) graded for total annual irradiation and height above ground level for the San Francisco model (see Figure 8.4)*

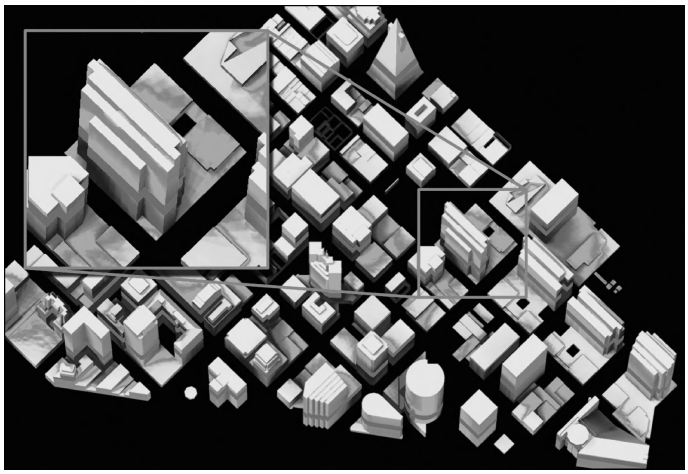

**Figure 8.4.** *Strategic evaluation of solar potential for the San Francisco 3D model*

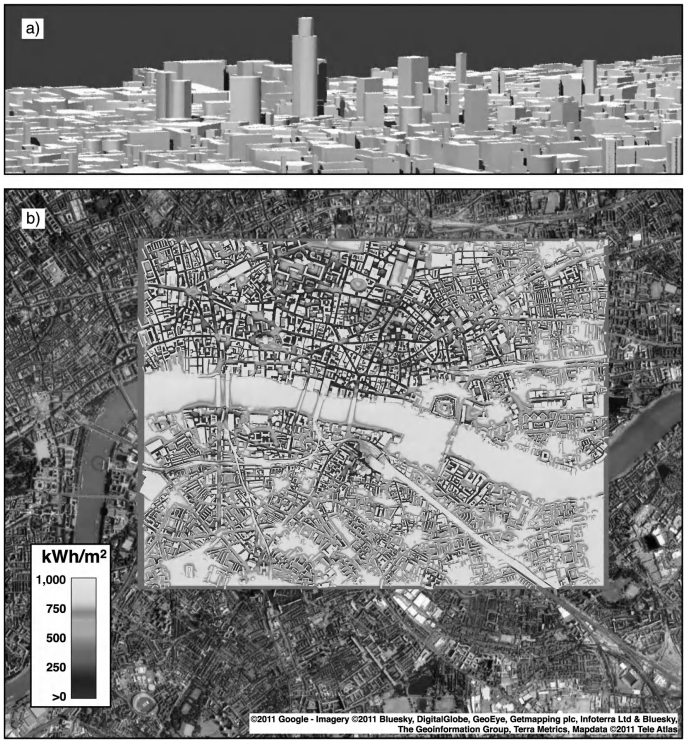


**Figure 8.5.** *Map showing the predicted TAI for central London overlaid on an aerial photograph*

### 8.3.4. *Irradiation mapping of "virtual London"*

The 3D model of "virtual London" shown in Figure 8.5(a) (without textures) comprised approximately 340,000 polygons. As can been seen in the rendering, the buildings are mostly flat-topped. For the determination of TAI received at the ground, having flat-topped rather than pitched roofs should not greatly influence the outcome. The image below the rendering shows a prediction of TAI – as "seen" from above – across an area approximately 12 km$^2$ (3 km $\times$ 4 km), Figure 8.5(b). The irradiation map is superposed on a satellite image of a wider area. The reflectance of the building surfaces was set to 0.2. The TAI received for an unobstructed horizontal surface is approximately 1,000 kWh m$^{-2}$ (shaded in light gray). The irradiation map dramatically reveals the effect of urban texture – the greater the building density, the lower the cumulative irradiation that reaches the ground. In the "canyons" between tall buildings, the TAI is of the order of 50 kWh m$^{-2}$ or less (shaded in dark gray).

Government agencies have responded to calls from various quarters to promote "green" spaces in cities. The amenity aspects of green spaces are usually foremost in these discussions; however, there are now recognized positive health and well-being aspects too [MAA 06]. In dense urban environments, the key consideration is the availability of daylight to support plant growth and survival. Plant species for shaded "green" areas should be selected on the basis of the predicted levels of the photosynthetic component of TAI. Here, perhaps, knowledge of the seasonal components would be helpful too. Assessments of the available area and prevailing illumination for planting could be carried out at a city-wide scale using images such as the irradiation map shown in Figure 8.5(b). Instead of TAI, the legend could be shown in units of photosynthetic active radiation [ALA 99], or, more simply, something that relates to everyday notions of overall shade, e.g. a "half" or "quarter" shade. To help planners, the irradiation map images could be incorporated as a layer in a geographic information system (GIS) [MAR 03].

The low cumulative irradiances predicted at ground levels are an indication of the potential for the "urban texture" to "trap" radiation and so add to the urban heat island (UHI) effect [DAV 08]. The irradiation map therefore may have some role as a proxy for radiation trapping if it can be shown that there is a robust relation between the cumulative irradiation at ground level and the radiation absorbed by (largely vertical) building surfaces.

## 8.4. The ASL building: a solar access study

This section describes a solar access study carried out for a building in New York (USA) where a proposed development has the potential to significantly reduce the daylight availability for the existing building. The building at risk of daylight injury from the proposed development is the historic Art Students League. The evaluation proved to be a landmark study – we believe that it is the first example in any city where the legal agreement covering the development of a site incorporates measures of daylight availability founded on CBDM.

### 8.4.1. *Density and zoning in New York City*

Density in New York City is governed by the New York City Zoning Resolution, which primarily uses the concept of floor area ratios (FARs) to regulate building size. In much of Manhattan, maximum building height is not directly regulated, but the amount of floor area allowed is limited to a ratio of zoning floor area to lot area[2]. The maximum FAR for a new residential building in Manhattan in its highest density

2 Zoning floor area is similar to building floor area, but does not include cellars, pipe chases, mechanical spaces, certain accessory parking, and some other typically small areas of buildings.

district is 12 FAR with standard density bonuses (or 12 ft of building area for every one foot of lot area). For commercial buildings, the maximum is 18 FAR with all standard bonuses.

Yet, very large buildings have recently been built legally under the New York City Zoning Resolution that obviously appear to have FARs much larger than the maxima allowed under the Zoning Resolution. In most of these cases, these large buildings are allowed because the Zoning Resolution also allows something known as a Zoning Lot Merger (ZLM). A ZLM is a legal agreement between separate land owners which merges adjacent tax lots so that they are considered as a single larger lot for the purposes of zoning[3]. This mechanism allows owners of buildings that are smaller than what the underlying zoning allows to sell their unused floor area to adjacent developers while still owning and operating their building. ZLMs allow developers to build very large buildings that would not be allowed under zoning if the maximum FAR was calculated only on the property owned by the developer. A ZLM is commonly referred to as selling "air-rights", but is actually more than just a transaction involving floor area, as all other zoning rules apply to this larger lot including lot coverage, building spacing, and legal windows. Therefore, for example, a building on a merged zoning lot may be able to have windows allowing legally habitable rooms on a lot line.

### 8.4.2. *The Art Students League building*

The Art Students League (ASL) of New York is housed in a four-storey brick and limestone building on West 57th Street in Midtown Manhattan. The building is both historically and architecturally notable and has been designated a New York City Landmark, which means that no changes to the structure that are visible from the street would be allowed without the approval of the New York City Landmarks Commission. The institution has educated many notable artists and remains a magnet for talent from around the world. This talent was educated, in part, in two artist studios that occupy the top floor of the building. These artist studios have no artificial lights and are lit by north-facing skylights.

A new development was proposed on the lot adjacent to the ASL by the Extell Development Corporation, which is the developer of some of Manhattan's largest new buildings. A very tall building on the site would have largely clear views of Central Park, the southern boundary of which is just two blocks to the north. Views of Central Park are considered a desirable amenity for luxury residential units and the taller the building, the more the units would have views of the Park, which provided incentive for Extell to merge lots with the ASL. Both lots are split between the C5-1 and C5-3 zoning districts. C5-3 is one of the highest density districts in Manhattan, with FARs

3 The mechanism is described in section 12-10 of the New York City Zoning Resolution [DCP 11].

up to 18 with density bonuses. The C5-1 district is high in density with a maximum FAR of 10. The existing ASL building is 33,979 $ft^2$ (3,156 $m^2$), and its lot is 15,062 $ft^2$ (1,399 $m^2$) which meant that it had 154,296 $ft^2$ (14,334 $m^2$) of unused floor area that it could sell to Extell for use in the building planned adjacent to it. Further, a merger with the ASL would allow the proposed building to have legal windows along the lot line[4]. Finally, if the ASL merged lots with Extell, it would mean that other lots to the east of it on the same block could be merged with the Extell lot providing the proposed building even more floor area.

If the ASL sold the development rights and a large building was constructed so close to the skylights, the amount and quality of daylight to the artist studios could be degraded. Before any final decision could be taken regarding the sale of the floor area to Extell, the ASL needed to know how much its skylights could be affected, how building design would impact the light the skylights received, and finally, if the amount of diminution was large, what kind of remedy, if any, would be available.

### 8.4.3. *Quantifying the potential daylight injury*

The challenges for the evaluation of potential injury were as follows:

1) to determine some meaningful measure of the reduction in daylight levels caused by the proposed building;

2) to quantify the sensitivity of the injury to various design alternatives;

3) to determine the limits of mitigation that can be reasonably expected.

The standard evaluation methods that were initially offered to the clients by a US-based practitioner were deemed either inappropriate or could not address fully their concerns. For example, the skylights are north facing and receive hardly any direct Sun, so the offered shadow pattern study was fairly pointless. Even if that had not been the case, the shadow pattern method offers only qualitative indicators of likely impact. The daylight factor approach was rejected because the client already appreciated how the character of illumination in the ASL studios depends on various sky conditions, including the potential for reflected sunlight from nearby buildings – aspects of natural illumination that the daylight factor approach cannot address.

The solution offered to the client was an assessment of the daylight injury in terms of realistic measures of illumination determined using New York climate data. Total annual illumination is a measure of all the visible daylight energy incident on a surface over a period of a full year. In everyday terms, this is equivalent to the cumulative measure of illumination recorded by a light meter left at a fixed position on a building

4 This expression refers to windows that can make a legally habitable room.

for a full year. The potential daylight injury to the studios would be determined by predicting the total annual illuminance incident on the skylights for the existing situation and with the proposed building in place. For the client, the significance of these measures was readily understood since a decrease in incident illumination at these skylights translates directly into reduced daylight provision for the studios.

**Figure 8.6.** *Art Students League building (right) with adjacent lot*

Standard climate datasets contain hourly values for various irradiation and illumination quantities (section 8.2.5). From these, it is possible to derive hourly varying sky and Sun conditions for use in lighting simulations. Equally, it is possible to synthesize cumulative luminance "maps" for arbitrary periods (e.g. annual and monthly) that contain the aggregated luminance effect of all the unique hourly sky and the Sun configurations. Separate luminance maps for the annual cumulative Sun and the annual cumulative sky were synthesized from the standard climate TMY2 dataset for New York City (WBAN# 94728).

A highly detailed 3D model of the ASL and surrounding buildings was employed in the simulations. Renderings of the 3D model showing both the existing situation and with the proposed development are given in Figure 8.7. The two skylights – the only sources of daylight for the studios – are enclosed by the dashed-line ovals. Note that the skylights are not of the same size. The cumulative luminance maps were used to determine the sky and Sun components of total annual illumination (TAIL) incident on the skylights of the ASL. The simulations were carried out for the existing arrangement of buildings and with the proposed tower in place (Figure 8.7). Simulations with the proposed tower in place were carried out with the

tower reflectivity set first to zero and then 50%. The zero reflectance case determines the diminution of TAIL with the tower acting purely as an obstruction. For the 50% reflectance case, the tower acts both as an obstruction and a reflector of light from the Sun and the sky, including multiple reflections from other buildings. A reflectance of 50% is the highest that can be expected for an exposed vertical facade. The effect of intermediate reflectivity values for the proposed tower can then be determined from a simple interpolation of the results for the zero and 50% reflectivity cases. A summary of the results is presented in Figure 8.8. In addition to the mean TAIL for each skylight marked on the images, the inset value shows the area-weighted mean TAIL for the two skylights.

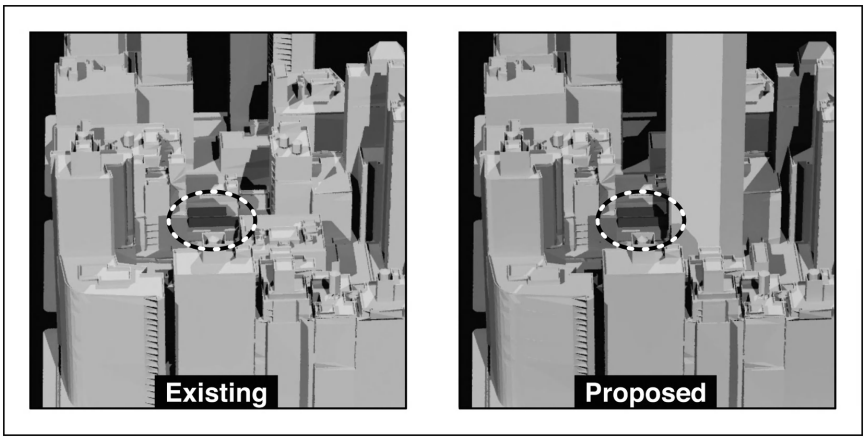


**Figure 8.7.** *Existing and proposed arrangement of buildings – skylights marked in dark gray and ringed*

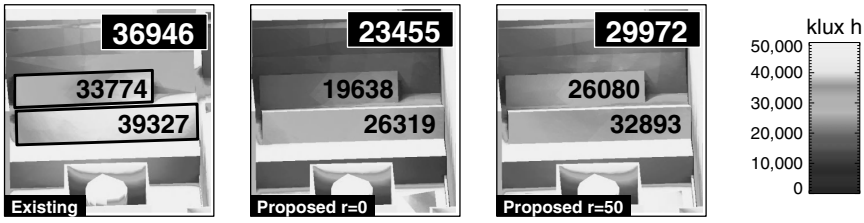


**Figure 8.8.** *Total annual illumination incident at the skylights for the existing and proposed cases*

The area-weighted mean TAILs were 36,946 klux-h for the existing scenario, 23,455 klux-h with a tower of zero reflectance, and 29,972 klux-h for a tower with 50% reflectance. The results are summarized in Table 8.2. The simulations showed that

the building as planned had a potential to significantly impact the quantity of natural light that reached the skylights of the artist studios. The simulations also showed that the impacts on the skylights could be mitigated through both building design and materials.

| Case | Predicted TAIL (klux-h) | Change in TAIL (%) |
|---|---|---|
| Existing | 36,946 | |
| Proposed 0% refl. | 23,455 | −36.5 |
| Proposed 50% refl. | 29,972 | −18.9 |

**Table 8.2.** *Predicted change in total annual illuminance (TAIL) caused by the proposed building*

### 8.4.4. *Outcomes and implications*

The information from the simulations discussed in this chapter was used in at least two ways. First, and most importantly, they showed the ASL management that there was a real risk to the quantity and quality of the light reaching their artist studios. In other words, unlike most Zoning Lot Mergers where the seller has little risk of impairing their property, the ASL faced a very real risk of a diminution of an important asset. Knowing these risks, the ASL was more informed during negotiations with Extell regarding the Zoning Lot Merger. Second, the simulations helped to guide the legal agreement for the Zoning Lot Merger that came out of the negotiations. Extell has agreed to attempt to minimize the impact that their building will have on the skylights to the greatest degree possible, provided the developer is still able to use all the floor area he has acquired. Extell has further agreed to provide the ASL plans for the proposed building early in the design process so that the ASL can evaluate the buildings impact and suggest ways an alternate building design could mitigate impacts. The developer has reserved the right to build a building that may seriously impair the light received by the skylights, but this would require a one-time payment of $10,000,000 to the ASL for damages.

While not entirely novel – some of the same techniques were applied in the New York Times' (NYT) evaluation (see section 8.5) – the nature of this study was certainly unusual for New York City. Codified in the city's environmental reviews are requirements for shadow studies, but except in very limited circumstances, proposed projects are not required to study impacts on daylight, on either public or private property. This is ironic considering that one of the major reasons for the adoption of the nation's first zoning ordinance, the 1916 New York City Zoning Resolution, was because very large buildings (such as the famous 31-storey Equitable Building) were built with no setback from the sidewalk and created very dark streets. The darkness these buildings created was only partly related to the shadows they cast, of course, and have much more to do with the area of sky that is visible from the street. The

New York City Zoning Resolution recognizes that the sky is important in creating light and attractive streets, and requires in many zoning districts sky exposure planes to ensure that light reaches the street below. Indeed, the Mid-town Special District adopted in 1982 includes a performance-based sky exposure system based on the Waldram diagram that helps to shape the building form to maximize sky exposure from street level. Nevertheless, despite these relatively innovative regulations to increase the exposure to sky that are already part of New York City's laws, developers are never required to measure their proposed project's impact on light.

The ASL study helps to show both how simple and how important it can be to study the impact of a proposed building on neighboring buildings and at the street/sidewalk level, and that simulation can be used to inform design and minimize impacts. Considering the state of the current practice, the time may be coming when instead of simply following a predetermined sky exposure plane that may or may not impact light reaching the street, a designer can demonstrate how a proposed building will actually diminish light levels at the street. Such concepts should not be revolutionary, yet, when they regard regulations that are slow to change, they often are.

The ASL study also has implications for the United Kingdom where the almost century-old "rights to light" schema devised by Waldram [HAR 07] for the determination of daylight injury has recently been critiqued in a number of papers [CHY 04, CHY 05, CHY 09, DEF 07]. The measure of daylight used in the Waldram method is direct sky illumination under a uniform sky (without Sun). It is now believed that this measure has little correspondence to commonly perceived notions of daylight sufficiency. Furthermore, the measure is largely irrelevant for the purpose of, say, determining the injury (i.e. degraded performance) of some solar-dependent building technology, e.g. BIPV. Indeed, for PVs a decrease in total annual illuminance (or alternatively, irradiance) has direct correspondence to the degradation in performance caused by the introduced overshadowing. Thus, the analysis described for the ASL building could, with minimal adjustment, quantify the reduced output of a BIPV array, and so provide a basis for financial compensation to indemnify the owner for the reduced performance of the system. BIPV installations are costed on a performance lifetime of 20 years or more, during which time it is quite probable that an unforeseen building development could be proposed that overshadows the BIPV array to some degree. As yet, there is no technical–legal framework to assess the degree of injury. CBDM, however, using standardized climate files, is well suited to provide the technical basis for any legal procedure(s).

The financial injury due to overshadowing on a BIPV array is a relatively straightforward quantity to estimate. Putting a price on injury due to reduced solar access at a window, however, is considerably more problematic because, unlike electricity, units of daylight (e.g. the lux-hour) do not have a tangible monetary value. In part, this is because effective daylighting for buildings needs artificial lighting

controls that respond to varying levels of daylight illumination. Field trials in San Francisco have shown that daylight responsive lighting control systems can "bring about sustainable reductions 30% to 41% in electrical energy for an outermost row of lights in a perimeter zone, and 16% to 22% for the second row of lights" [RUB 98]. The field trials should be repeated for other settings and locales. However, it is clear that there is considerable potential to reduce electricity demand for lighting. Thus, it should be possible to place a monetary value on daylight. However, solar gain and the resulting cooling should also figure in the estimation of overall energy consumption. It may be that additional overshadowing could reduce the energy consumption of the "injured" building if the reduction in cooling exceeds the increase in electric lighting consumption. These interactions are complex; however, it is conceivable that the irradiation mapping technique could be expanded to include some representation of the energy flows across the building perimeter. Then it would be possible to carry out fairly detailed energy modeling of the facade and perimeter zone of the building using only the building envelope and a "virtual construct" for the internal spaces. Sometimes, so much solar radiation is reflected from buildings using mirrored glass that the heat-load on adjacent buildings is increased [AND 03]. These and similar effects could in principle be predicted using the irradiation mapping mode of CBDM.

## 8.5. Daylighting the New York Times building

The NYT building is a 52-storey tower on the east side of Eighth Avenue between 40th and 41st Streets in the borough of Manhattan. The building, which houses *The New York Times* newspaper, was announced at the end of 2001, construction started in 2003, and it was completed in 2007. Daylight simulations were used to support decisions later in the design process during the construction phase of the building, rather than for early schematic design or meriting green building status.

The NYT building features an automated shading system where a motorized roller blind is deployed incrementally according to some sensor input, e.g. measured daylight level. This shading system features in the facade design throughout the majority of the 52 floors of the building [LEE 05]. The design goals for the shading system were to:

– maximize natural light;

– maximize occupant connectivity with the outdoors, i.e. external views;

– intercept sunlight penetration so as to avoid direct solar radiation on the occupants;

– maintain a glare-free environment;

– to provide occupant manual override capability.

The overall intent was to keep the shades up as much of the time as possible without causing thermal or visual discomfort. Thermal comfort is assured by solar tracking and the geometry of the external Sun screens. Visual comfort is attained by managing the luminance on the window wall so that it does not exceed certain threshold values. A manual override system was specified because previous post-occupancy evaluations of automated shade systems indicated that occupants were likely to complain if a manual override was not provided. Although a formal post-occupancy evaluation of the NYT building has yet to be carried out, anecdotal evidence from informal surveys indicates a high level of user satisfaction with the daylighting systems. Furthermore, effective daylighting has significantly reduced the energy consumed for artificial lighting. The NYT building's daylighting system provides a degree of modulation for the shading (they are deployed by increments) and has greatly reduced the need for user interventions. Good daylighting alone is unlikely to save energy unless it is part of an integrated design scheme. The typical lighting power densities (LPDs) for consumed electricity in office spaces range from about 12 to 20 W $m^{-2}$, with those at the lower end considered "good practice". However, it is possible to achieve LPDs significantly lower than the good practice value – without recourse to emerging technologies such as light-emitting diodes – using only good quality low-energy fluorescent lights. This was successfully demonstrated in the NYT building which has an LPD of only 4.26 W $m^{-2}$. The simulations that were carried out in support of the design and calibration of daylighting systems of the NYT's building are described in the following sections.

### 8.5.1. *3D model for NYT's building and surroundings*

Extensive *Radiance* simulations were used to assist the building owner and manufacturers in making informed decisions on the design and control of an automated roller shade and electric lighting control system for the NYT headquarters in the pre- and post-bid phases of the project [LEE 05]. A prior monitored field study in a full-scale mockup answered initial questions concerning technical feasibility and performance benefits of automated control. Simulations enabled extension of the monitored field study to the final building in its complex urban context. The 3D model created for the NYT's building was highly detailed since the daylighting properties of the spaces in the tower are dependent on both the small-scale facade structures (e.g. the ceramic bars) and of course also on the properties of the space (e.g. desk layout and partition height). The detail achieved can be seen in the "close-up" image of the NYT's tower in Figure 8.9. The office detail was generated and "inserted" into the building envelope model at the appropriate floor level for the daylighting simulations. The facade detail for the levels above and below the floor was also added since these could affect the ingress of daylight to the space. Note that realistic finishes were applied to all internal and facade surfaces for the NYT office model, e.g. desktops, furniture and floor (see $\times 100$ rendering). The 3D model for the tower with office detail for one floor comprised about 200,000 polygons.

The NYT tower was set in a 3D model of Manhattan of extent approximately 3 km by 2 km. This surrounding context comprised nearly 300,000 polygons. Thus, the tower and context model in total comprised nearly half a million polygons (Figure 8.9). Most of the context building surfaces were given a default diffuse reflectance of 0.2, which is typical for many buildings. However, certain context buildings near to the NYT tower were assigned more specific reflective properties, including part specular, based on observations of the building. One of the key daylighting parameters to be investigated was visual comfort for the building occupants. Thus, the luminance of the view to the outside – which may include reflections from surrounding buildings – needed to be accurately captured in the simulations.

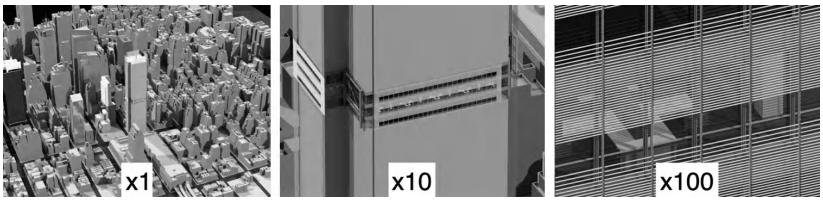


**Figure 8.9.** *Renderings of the NYT building and surrounding context – three views showing effective magnifications of ×1, ×10, and ×100*

### 8.5.2. *The spatiotemporal dynamics of sunlight exposure*

Daylight simulations were used for a variety of purposes, from understanding the effects of urban shadow on shade usage to assisting with precalibration of photosensor sensitivity in a complex daylit interior environment. Time-lapsed images enabled stakeholders (building owner and manufacturers) to visualize the daylit environment of the final building in its urban context with automated shade control and assess how well visual comfort (direct Sun, surface luminance, etc.), daylight quality (illuminance level and distribution), and view were to be addressed by the system at different orientations and locations within the building.

The spatiotemporal dynamics of direct Sun illumination were investigated using a combination of spatial and temporal exposure maps. The spatial exposure map shows the cumulative number of hours of Sun exposure assuming clear-sky conditions throughout the year. Sun exposure maps of the principal building facades reveal the transition from heavily obstructed through moderate to low/zero obstruction, and so helped to guide the designers in the selection of shade material and zoning of the control system for the automated roller shades.

The spatial exposure map for the south facade of the NYT tower is shown in Figure 8.10. The exposure in number of hours is shown using color. The

accompanying temporal exposure maps are for two selected points on the building facade and show the propensity for Sun exposure throughout the year at a time-step of 15 min. The presentation is similar to that used for the climate data given in Figure 8.1, only now the time-step is shorter. In the temporal map, color is used to reveal the angle between the facade surface normal and the Sun vector. For example, angles of 80° or more are grazing incidence and will have little penetration into the building, whereas angles around 10° or less indicate when the Sun vector is almost normal to the facade, i.e. the Sun is "shining" almost face-on and will penetrate deeply into the space. The south facade has an orientation that is a little west of south, hence the exposure (and penetration) is greater in the afternoon. Note that there is no correction for daylight savings in the temporal maps. Times when the Sun is below the horizon (i.e. during night) are shaded white, when it is above the horizon but "behind" the facade the shade is gray, and when the Sun is obstructed by surrounding geometry the shade is black. The temporal maps for points on the 6th and 26th floors of the tower readily show how the propensity for solar exposure varies throughout the year (Figure 8.10). On floor 26 between the hours of about 13 h and 16 h during winter, the Sun shines almost face-on to the south facade. This presents the greatest risk for visual discomfort for persons on that floor occupying the south perimeter. For floor 6 however, the angle between the Sun vector and the facade surface normal is rarely less than 40°, and then only for short periods lasting 15–30 min around 15 h during winter. The "spike" of color in the temporal map surrounded by black suggests that low winter Sun is only very occasionally not obstructed by surrounding buildings.

### 8.5.3. *Balancing daylight provision and visual comfort*

A good provision of daylight is now considered to be highly desirable in terms of building occupants' well-being and productivity [ANC 06, BEG 97]. Daylight, however, can cause visual discomfort by inducing glare and veiling reflections. Efforts to control glare often result in the loss of predicted daylight benefit as occupants deploy blinds, etc., which may remain closed long after the glare condition has diminished. Annualized, climate-based daylight simulations were conducted to more thoroughly assess comfort conditions and availability of view for the NYT occupants.

In the CIBSE Lighting Guide LG7, glare is defined as a "Condition of vision in which there is discomfort or a reduction in the ability to see details or objects, caused by an unsuitable distribution or range of luminance, or to extreme contrasts" [LG7 05]. There are two types of glare: disability glare, where stray light reaching the eye results in a reduction in visibility and visual performance, and discomfort glare, which leads to users' discomfort, often with less immediately noticeable effects such as headaches or posture-related aches after work. Glare can be caused by direct sunlight through a window or by the luminance differences between bright areas such as windows with

bright sky views and the darker task area. Furthermore, veiling reflections on reflective surfaces such as computer screens can affect visual comfort at workstations facing away from the window.

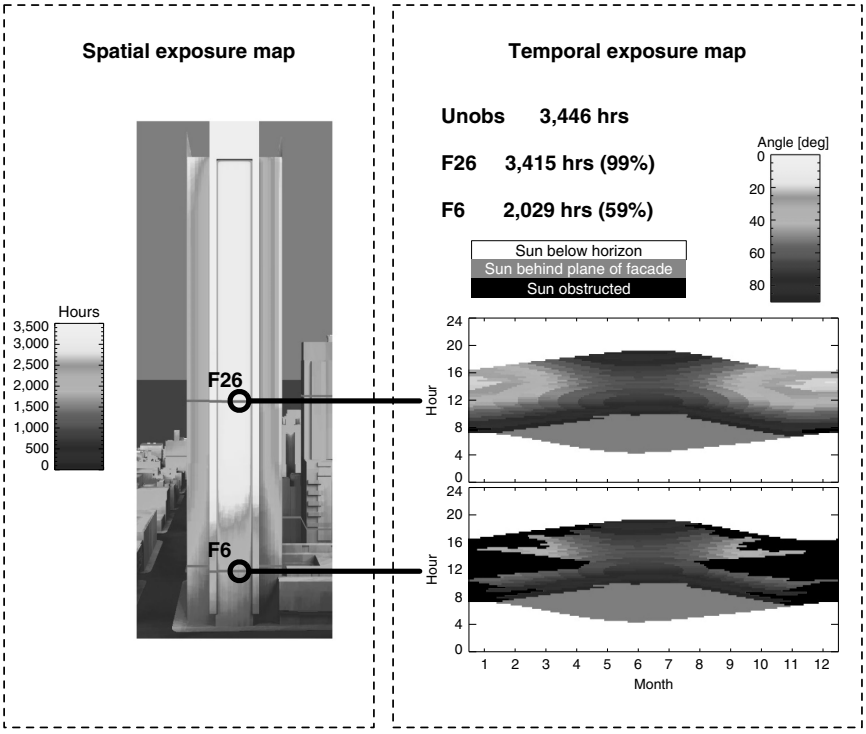


**Figure 8.10.** *Spatial and temporal exposure maps for the NYT building*

While there are accepted, albeit imperfect, models for the potential glare effect of (fixed output) luminaires, it is recognized that glare from daylight sources is poorly understood [OST 05]. The first daylight glare formulations were extrapolations from studies of discomfort glare due to artificial lighting [CHA 82]. The light sources used in those studies subtended relatively small solid angles from the viewpoint of the subject, and the luminance conditions (source and environment) were very different from typical daylit offices. In short, those extrapolations proved to be inadequate for the purpose of determining discomfort glare from daylight.

For the NYT study, the project team made preliminary overtures to derive a visual comfort-based metric similar to the thermal comfort percent people dissatisfied (PPD) metric. In the United States, mechanical engineers have long relied on the metrics defined in the ASHRAE Standard 55 [ASH 04] to determine whether mechanical system designs will provide thermal environmental conditions acceptable to a majority

of the occupants within the space. The predictive model is based on hundreds of field and laboratory studies that correlate physical measures to subjective response. Calculations are done for critical design conditions, i.e. for the 1% or 3% peak condition, e.g. for high levels of solar radiation that are exceeded for only 1% or 3% of the year. For more innovative designs (naturally ventilated, hybrid ventilation schemes, or large amounts of glazing), more detailed calculations are conducted: e.g. spatial distribution or temporal computations of PPD.

Conversely, predictive models for visual comfort are based on very few, limited field studies and, consequently, there are no standards or requirements in place to ensure provision of visual comfort with daylighting designs: the occupant is simply expected to lower the shade. With the increased interest in daylighting and with the use of innovative systems, the need for robust predictive models for discomfort glare, in particular, is acute and was needed particularly for the NYT analysis. A simplified measure was used to evaluate comfort conditions based on a limited field study [CLE 06] and on calculations derived from a combination of comfort metrics (luminance ratios, daylight glare index, etc.). The resulting measure was the number of annual hours when the mean window luminance exceeded 2,000 cd $m^{-2}$. This measure helped to determine the trade-offs between the number of hours of glare discomfort versus access to view and daylight. Calculations were made with the occupants' seated field of view located in a worst-case position close to the window in a direction normal to the window (Figure 8.11).

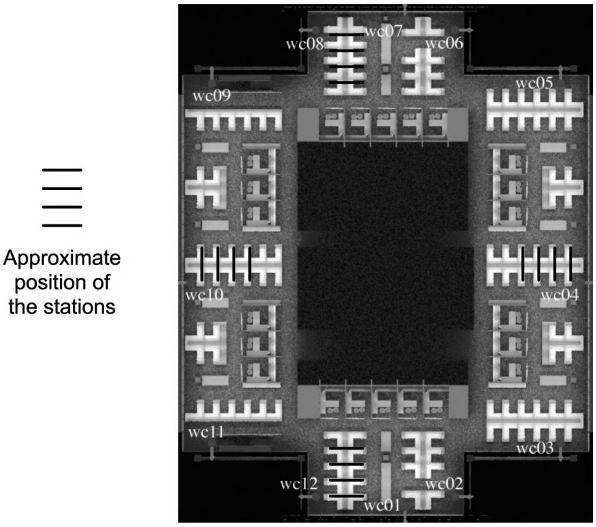


**Figure 8.11.** *Simulated plan view showing the position and view direction for the 12 "window commissioning" viewpoints, i.e. wc01 to wc12*

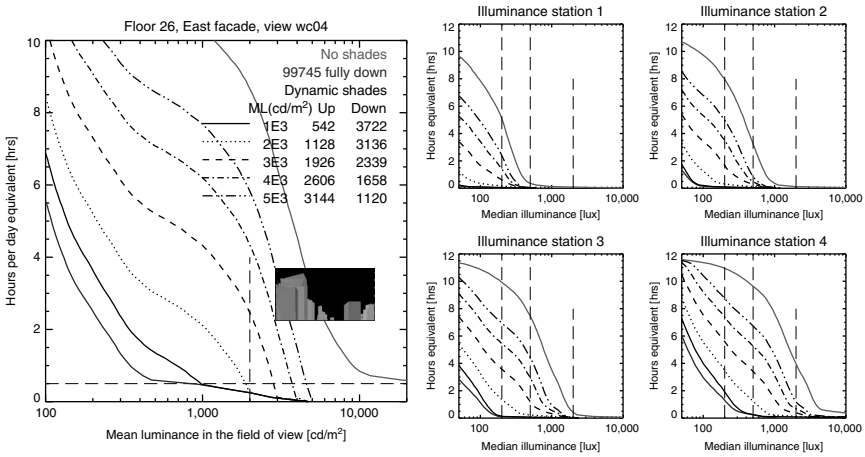


**Figure 8.12.** *Annualized profiles for field-of-view luminance (floor 26, wc04) and illuminance at the workstation*

Example outputs for the view position wc04 (i.e. east-facing) are shown in Figure 8.12. The large plot shows the annual occurrence of predicted mean field-of-view luminance (expressed as hours per day equivalent) for various shade control conditions. The shade control limits were "No shades" and shades "fully down". The number code (e.g. "99745") refers to a particular shade material – the analysis was carried out for a number of different shade fabrics. The in-between cases determined the occurrence of mean field-of-view luminance for various control conditions, e.g. blinds were lowered whenever the mean field-of-view luminance exceeded $1 \times 10^3$cd m$^{-2}$, $2 \times 10^3$cd m$^{-2}$, and so on up to $5 \times 10^3$cd m$^{-2}$. At the time of the study, there was a "rough" consensus that a mean luminance of 2,000 cd m$^{-2}$ can serve as a proxy for visual comfort. From the large plot in Figure 8.12, it can be seen that (for view wc04) this condition is exceeded on average approximately 8 h per day with the shades fully up (i.e. "no shades") and for less than approximately 30 min per day with the shades fully down (for material 99745). The small inset rendering shows the simulated view of the sky (black) and neighboring buildings. The illuminance profiles show the annual occurrence of illuminance at the work plane (also expressed as hours per day equivalent) for the various shade control conditions. For example, with the shades fully down throughout the year, an illuminance of 200 lux is achieved on average only for about 1 h per day at station 4 (nearest the window) and hardly at all for the other stations. Conversely, with the shades always up, 200 lux is achieved on average for 11 h per day (station 4) and approximately 5 h per day at station 1 (farthest from the window). The illuminance profiles for the various shade control conditions can be read from the individual plots.

The simulations carried out for the NYT study were used to inform and support the decisions taken by the design team rather than to demonstrate, say, compliance with any current or proposed daylighting metric. It remains to be seen how the recently proposed climate-based metrics will influence the nature and practice of building design and evaluation [MAR 09].

## 8.6. Summary

The notion of "solar architecture" has existed since the dawn of architecture itself. In 400 BC, Socrates is believed to have considered solar design principles in house construction [BUT 80]. Until recently, the availability of daylight in buildings was thought of largely in terms of task illuminance and the potential to reduce energy for artificial lighting. In the last decade, we discovered that the non-visual effects of light received by the eye can have significant influences on long-term health, well-being, and productivity. Furthermore, the imperative to save energy has led to speculation that future buildings could become "harvesters" of energy. All of these factors must lead us to a wider and more rigorous consideration of daylight in the urban setting – in terms of availability to building occupants; the building itself; and also, the public spaces between buildings. The examples given in this chapter show how important it is to accommodate in the simulations building detail across a range of scales, e.g. from shading bars on the facade to the massing of surrounding buildings. Multi-scale CBDM is one of the tools that can help us to understand the complex daylit environment that exists in dense urban environments, giving us the means to maximize the potential benefits of natural light for both buildings and people.

## 8.7. Acknowledgments

Simon Gibson (Department of Computer Science, University of Manchester, UK) carried out the conversion of the VRML models to *Radiance* format. The San Francisco VRML model was created by Planet 9 Studios, San Francisco, USA. The 3D image of "virtual London" was supplied by Infoterra (UK). Eleanor Lee (Lawrence Berkeley National Laboratory, Berkeley, USA) provided material for the section on the New York Times building.

## 8.8. Bibliography

[ALA 99] ALADOS I., ALADOS-ARBOLEDAS L., "Direct and diffuse photosynthetically active radiation: measurements and modelling", *Agricultural and Forest Meteorology*, vol. 93, no. 1, pp. 27–38, 1999.

[ANC 06] ANCA D.G., JENIFER A.V., "Occupant preferences and satisfaction with the luminous environment and control systems in daylit offices: a literature review", *Energy and Buildings*, vol. 38, no. 7, pp. 728–742, 2006.

[AND 03] ANDER G.D., *Daylighting Performance and Design*, John Wiley & Sons, 2003.

[ANN 06] ANN R.W., "Considerations for lighting in the built environment: non-visual effects of light", *Energy and Buildings*, vol. 38, no. 7, pp. 721–727, 2006.

[ASH 04] ASHRAE, Standard 55: Thermal Environmental Conditions for Human Occupancy, American Society of Heating, Refrigerating and Air-Conditioning Engineers, Inc., Atlanta, 2004.

[BEG 97] BEGEMANN S.H.A., VAN DEN BELD G.J., TENNER A.D., "Daylight, artificial light and people in an office environment, overview of visual and biological responses", *International Journal of Industrial Ergonomics*, vol. 20, no. 3, pp. 231–239, 1997.

[BEL 76] BELINDA L.C., "Review of the psychological reaction to windows", *Lighting Research and Technology*, vol. 8, no. 2, pp. 80–88, 1976.

[BUT 80] BUTTI K., PERLIN J., *A Golden Thread: 2500 Years of Solar Architecture and Technology*, Van Nostrand Reinhold, 1980.

[CHA 82] CHAUVEL P., COLLINS J.B., DOGNIAUX R., LONGMORE J., "Glare from windows: current views of the problem", *Lighting Research and Technology*, vol. 14, no. 1, pp. 31–46, 1982.

[CHY 04] CHYNOWETH P., "Progressing the rights to light debate – part 1: a review of current practice", *Structural Survey*, vol. 22, no. 3, pp. 131–137, 2004.

[CHY 05] CHYNOWETH P., "Progressing the rights to light debate: part 2: the grumble point revisited", *Structural Survey*, vol. 23, no. 4, pp. 251–264, 2005.

[CHY 09] CHYNOWETH P., "Progressing the rights to light debate: part 3: judicial attitudes to current practice", *Structural Survey*, vol. 27, no. 1, pp. 7–19, 2009.

[CLE 06] CLEAR R.D., INKAROJRIT V., LEE E.S., "Subject responses to electrochromic windows", *Energy and Buildings*, vol. 38, no. 7, pp. 758–779, 2006.

[CRA 01] CRAWLEY D.B., LAWRIE L.K., WINKELMANN F.C., BUHL W.F., HUANG Y.J., PEDERSEN C.O., STRAND R.K., LIESEN R.J., FISHER D.E., WITTE M.J., GLAZER J., "EnergyPlus: creating a new-generation building energy simulation program", *Energy and Buildings*, vol. 33, no. 4, pp. 319–331, 2001.

[DAV 08] DAVIES M., STEADMAN P., ORESZCZYN T., "Strategies for the modification of the urban climate and the consequent impact on building energy use", *Energy Policy*, vol. 36, no. 12, pp. 4548–4551, 2008.

[DCP 11] DEPARTMENT OF CITY PLANNING, Zoning Resolution, the City of New York, http://www.nyc.gov/html/dcp/html/zone/zonetext.shtml, 2011.

[DEF 07] DEFOE P., FRAME I., "Was Waldram wrong?", *Structural Survey*, vol. 25, no. 2, pp. 98–116, 2007.

[DTI 00] DTI, Photovoltaics in buildings: BIPV projects programme – strategy document 1998–2002, Technical report, Department of Trade and Industry, UK, 2000.

[HAR 07] HARRIS L., *Anstey's Rights of Light and How to Deal with Them*, 4th ed., RICS Books, London, 2007.

[IEA 98] IEA, Photovoltaic power systems programme – strategy document 1998–2002, Technical report, International Energy Agency, 1998.

[KNO 85] KNOWLES R., *Sun, Rhythm, Form*, MIT Press, 1985.

[LEE 05] LEE E.S., SELKOWITZ S.E., HUGHES G.D., CLEAR R.D., WARD G., MARDALJEVIC J., LAI J., INANICI M.N., INKAROJRIT V., Daylighting the New York Times headquarters building, Lawrence Berkeley National Laboratory. Final report LBNL-57602, 2005.

[LG7 05] LG7 CIBSE/SLL, *Lighting Guide 7: Office Lighting*, Chartered Institution of Building Services Engineers, London, 2005.

[MAR 00a] MARDALJEVIC J., "Simulation of annual daylighting profiles for internal illuminance", *Lighting Research and Technology*, vol. 32, no. 3, pp. 111–118, 2000.

[MAR 00b] MARDALJEVIC J., RYLATT M., "An image-based analysis of solar radiation for urban settings", *PLEA – Passive and Low Energy Architecture*, Cambridge, UK, pp. 442–447, 2000.

[MAR 03] MARDALJEVIC J., RYLATT M., "Irradiation mapping of complex urban environments: an image-based approach", *Energy and Buildings*, vol. 35, no. 1, pp. 27–35, 2003.

[MAR 06a] MARDALJEVIC J., "Examples of climate-based daylight modelling", *CIBSE National Conference 2006: Engineering the Future*, Oval Cricket Ground, London, UK, 21–22 March 2006.

[MAR 06b] MARDALJEVIC J., "Time to see the light", *Building Services Journal*, pp. 59–62, September 2006.

[MAR 08] MARDALJEVIC J., "Sky model blends for predicting internal illuminance: a comparison founded on the BRE-IDMP dataset", *Journal of Building Performance Simulation*, vol. 1, no. 3, pp. 163–173, 2008.

[MAR 09] MARDALJEVIC J., HESCHONG L., LEE E., "Daylight metrics and energy savings", *Lighting Research and Technology*, vol. 41, no. 3, pp. 261–283, 2009.

[MAR 11] MARDALJEVIC J., ANDERSEN M., ROY N., CHRISTOFFERSEN J., "Daylighting metrics for residential building", *CIE 27th Session*, Sun City, South Africa, 2011.

[MAA 06] MAAS J., VERHEIJ R.A., GROENEWEGEN P.P., DE VRIES S., SPREEUWENBERG P., "Green space, urbanity, and health: how strong is the relation?", *Journal of Epidemiology and Community Health*, vol. 60, no. 7, pp. 587–592, 2006.

[NAB 06] NABIL A., MARDALJEVIC J., "Useful daylight illuminances: a replacement for daylight factors", *Energy and Buildings*, vol. 38, no. 7, pp. 905–913, 2006.

[OST 05] OSTERHAUS W.K.E., "Discomfort glare assessment and prevention for daylight applications in office environments", *Solar Energy*, vol. 79, no. 2, pp. 140–158, 2005.

[RAE 08] RAEL R., *Earth Architecture*, Princeton Architectural Press, 2008.

[REI 00] REINHART C.F., HERKEL S., "The simulation of annual daylight illuminance distributions – a state-of-the-art comparison of six RADIANCE-based methods", *Energy and Buildings*, vol. 32, no. 2, pp. 167–187, 2000.

[REI 06] REINHART C.F., MARDALJEVIC J., ROGERS Z., "Dynamic daylight performance metrics for sustainable building design", *Leukos*, vol. 3, no. 1, pp. 7–31, 2006.

[RUB 98] RUBINSTEIN F., JENNINGS J., AVERY D., BLANC S., "Preliminary results from an advanced lighting controls testbed", *IESNA Annual Conference*, San Antonio, Texas, 1998.

[UGW 08] UGWU C.U., AOYAGI H., UCHIYAMA H., "Photobioreactors for mass cultivation of algae", *Bioresource Technology*, vol. 99, no. 10, pp. 4021–4028, 2008.

[WAR 98] WARD LARSON G., SHAKESPEARE R., *Rendering with Radiance: The Art and Science of Lighting Visualization*, Morgan Kaufmann, San Francisco, 1998.

# Chapter 9

# Geometrical Models of the City

## 9.1. Introduction

Modeling cities, and urban spaces in general (e.g. buildings, neighborhoods, towns, states, etc.), is a daring task for computer graphics, computer vision, and visualization. Cities and urban spaces are an intricate collection of man-made structures arranged into buildings, parcels, blocks, and streets distributed over a terrain. Dense urban environments are particularly difficult to model because they are very complex, large, and widespread, spanning from a few to hundreds of square kilometers. Traditionally, modeling cities has been a rather manual task that consumes significant amounts of resources. With the growing requirements of quantity and quality in urban content, there is an imperative need for alternative solutions that allow for fast, semi-automatic urban modeling.

In addition to city-scale solar energy applications, enabling such large-scale city modeling would be beneficial to numerous other highly sought-after applications including the following:

*Urban planning and simulation*: Visualizing and predicting the future effect of adopting urban policies and population changes that affect cities and countries; showing the potential effect of social, economic, and climatological aspects on urban development; providing road planners with visualization tools; and allowing architects to see the results of using common buildings blocks.

*Emergency response*: Creating models to train emergency response personnel in current and speculative urban layouts, including planning evacuation routes for

Chapter written by Daniel ALIAGA.

*Solar Energy at Urban Scale* Benoit Beckers

various catastrophes, and suggesting emergency deployments of communication networks, resources, policing, and large-scale military deployments.

*Mapping and visualization*: Providing maps and navigation services; using incomplete information to generate plausible models of urban locations (e.g. partial data obtained from aerial views of enemy territory); correlating urban and architectural styles with changes over time.

Research in modeling cities and urban spaces can be divided into areas of *geometrical modeling* and *behavioral modeling*. The first area overlaps significantly with computer graphics and computer vision (see [PAR 01]). The focus is on algorithms that produce intricate geometry quickly from a compact set of specifications and on algorithms that create geometry from aerial and terrestrial images, LIDAR, and other sensor modalities. The goal of behavioral modeling is understanding the underlying socioeconomic processes occurring within an urban space [BAT 07] and is intended to assist decision-making on urban policies in current and future urban areas (see [ALK 08, WAD 02]). In this section, we focus on geometrical modeling.

### 9.1.1. *Modeling challenges*

There are two significant challenges for geometric modeling of cities and urban spaces: (i) the acquisition of sufficient information on the underlying large real-world city environment; and (ii) the support of compact and succinct editing of the underlying three-dimensional (3D) model. Some applications seek exact physical replicas of the city (e.g. navigation), while other applications can tolerate geometric approximations but they should be able to efficiently make speculative and extensive changes to run the desired simulations under new conditions (e.g. urban planning and simulation).

The huge data explosion due to the rapid growth of geographical information systems (GIS) and geo-registered aerial imagery is greatly facilitating the first challenge. The Internet (e.g. Google Maps, MapQuest, LiveEarth, Google Earth, etc.) has provided public and widespread access to a very large number of top-down and oblique aerial images of many countries, in addition to publicly available GIS data (e.g. www.openstreetmap.org). Previously, although such information was available, at a smaller scale, it was not provided to the public. Today, the resolution and coverage of such data are rapidly improving. For example, very soon the raw data for the USA will easily reach and exceed peta-byte size image databases (e.g. the USA's 10 M $km^2$ at 6-inch/pixel resolution already amounts to peta-byte size databases). Furthermore, a huge amount of ground-level imagery also exists that is being captured by Google, Microsoft, Navtec, and other companies and by private

citizens (e.g. tourists). This last source of data has already fomented research to produce animations and 3D reconstructions of distant urban locations using large photo collections extracted from the Web (see [FRA 10, GOE 07]) (e.g. 100,000+ pictures can be found in a single popular location).

### 9.1.2. *State-of-the-art*

There is a very large body of research tackling the problem of geometrical modeling and reconstruction of cities and urban spaces. Broadly, we can divide approaches into the following three groups:

*Reconstruction*: These methods focus mostly on automatic algorithms to reconstruct the geometry of existing urban spaces. The input is primary aerial and ground-level images, laser and LIDAR scans as well [NAN 10]. Traditionally, this approach has been pursued by the disciplines of computer vision and photogrammetry and remote sensing. The focus is primarily on reconstruction and not on providing a structured model and/or one suitable for model editing. Musialski *et al.* [MUS 12] provide a survey of urban reconstruction methods.

*Interactive modeling*: These approaches often use human input and guidance to create 3D urban models. Highly manual methods have been the predominant strategy – Yin *et al.* [YIN 09] provide a summary of recent interactive drawing-based methods, including the ones based on computer-aided design methods. Another direction within this group is interactive photogrammetric methods, such as those derived from the facade system [DEB 96], which found its way into commercial products (e.g. Canoma). More recently, several image-based modeling and rendering systems bypass explicit geometric reconstruction and directly synthesize novel photorealistic images of urban areas from previously acquired imagery.

*Procedural modeling*: This group of methods exploits the observation that city and urban spaces exhibit a significant degree of repetition on a global scale and individuality at a local scale. This structured redundancy can be captured using procedural modeling. Procedural methods have the advantage of exhibiting a high degree of detail amplification, e.g. from only a small number of parameters significant details can be synthetically generated. Even though a small change in the parameter values can cause massive changes in the resulting model, promising results have been shown in several restricted domains.

In the remaining part of this chapter, we focus on procedural modeling methods, both forward modeling techniques and inverse modeling strategies.

## 9.2. Forward procedural modeling

We describe several approaches of forward procedural modeling. The commencement of procedural modeling stems from the study of both plants and architecture. We divide the modeling methodologies based on the scene content, but in general focus on urban spaces.

### 9.2.1. *Plants and architecture*

Several fundamental methodologies for procedural plant and architecture modeling have been proposed. For example, grammar-based systems have been used to model trees and other plants. The authors Prusinkiewicz and Lindenmayer [PRU 90] proposed L-systems for procedurally modeling the plants. Later works in this regard improved the expressivity of these methods in a variety of directions (see [MEC 96, PRU94]).

In architecture, several approaches have been presented that exploit and represent repetition using patterns and grammars. In particular, Stiny [STI 75] proposed the notion of using a shape grammar to construct and analyze architectural spaces. Alexander [ALE 77] defined desirable patterns for configuring entire urban spaces. Other works have focused on implementing procedural methods for selected and well-known architectural styles (e.g. Le Corbusier-style buildings [HAL 08]). Marshall [MAR 04] summarizes a variety of styles and street patterns in a form suitable for procedural modeling.

Recently, some works have combined plant modeling with architectural structures. For example, Wissen Hayek *et al.* [WIS 10] encoded design guidelines for urban green spaces into shape grammar rules and produced plausible 3D urban models. Benes *et al.* [BEN 09] provide an interactive, intuitive, and efficient modeling process for virtual plants and plant ecosystems that respond to surrounding shape and geometry cues. Vegetation can be made to interactively grow, in a plausible way, around existing architectural and geometrical structures, thus populating a model with vegetation. In a follow-on work, Benes *et al.* [BEN 11] extended the scale to entire cities and supported managed and unmanaged growth of a simple ecosystem over an entire city. This work enabled the exploration of city designs and vegetation management rules for obtaining a desired outcome.

### 9.2.2. *Buildings and cities*

Several works have focused their attention on the procedural modeling of structures varying from individual buildings and entire cities (Figure 9.1). Parish and

Mueller's [PAR 01] seminal work on city modeling describes an entire system that models streets using an L-system, divides the space in between streets into parcels, and populates the parcels with simple building models, altogether yielding a pioneering approach to rapid city model creation.

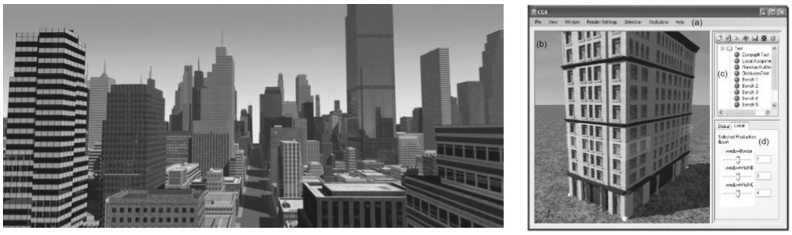

a) b)

**Figure 9.1.** *Procedural modeling: (a) Example city rendering [PAR 01]; (b) Graphical interface for procedural building editing [LIP 08]*

Subsequent work has centered on improving several aspects of the aforementioned pipeline. Wonka *et al.* [WON 03] and Mueller *et al.* [MUE 06] proposed split-grammar-based procedural methods to construct detailed building models. Lipp *et al.* [LIP 08] introduced the notion of interactive grammar editing, thus avoiding having to explicitly write grammar rules using a text editor. These algorithms have worked their way into CityEngine, a commercially available software platform for building-scale and city-scale procedural modeling (http://www.esri.com/software/cityengine).

### 9.2.3. *Streets and parcels*

Another aspect of city modeling that has received particular attention is the modeling of an interconnected set of streets and the parcels interior to it (Figure 9.2). This modeling task is mostly carried out in two dimensions, though the underlying terrain can of course be of varying height. Hertzmann *et al.* [HER 01] proposed an image editing scheme that enables synthesizing new aerial views of cities but no underlying structure is generated or known – it is purely an image processing method.

Later works have included the use of vector-type data to generate explicit, and editable, road networks and parcel geometries [GAL 10]. Aliaga *et al.* [ALI 08a] use a stochastic and by-example methodology to reproduce existing, or generate new, road networks. The works also include an algorithm to generate plausible parcel geometries. Aliaga *et al.* [ALI 08b] and Lipp *et al.* [LIP 11] provide additional tools to edit the existing road and parcel layouts. Chen *et al.* [CHE 08] use a different

strategy of exploiting the visual similarity between flow/tensor fields and road networks. Their modeling pipeline consists of tensor field modeling and street graph generation to yield, under user control, plausible and editable street networks.

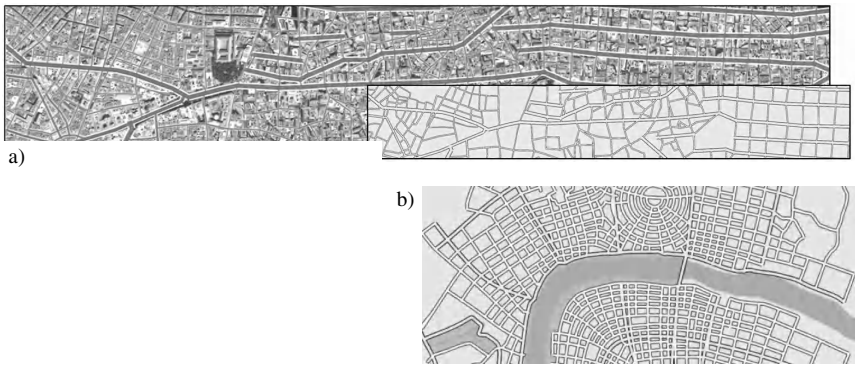


**Figure 9.2.** *Procedural streets: (a) Example-based design yielding both synthetic street networks and plausible imagery [ALI 08a]; (b) Design of complex street networks using tensor fields [CHE 08]*

Recently, Vanegas *et al.* [VAN 12] focus on providing a comprehensive and fully interactive approach for subdividing blocks into parcels, a task that has been largely ignored in previous computer graphics systems potentially resulting in unrealistic and implausible results. The approach performs a partitioning of the interior of city blocks using user-specified subdivision attributes and style parameters. Moreover, the method is both robust and persistent in the sense of being able to map individual parcels from before an edit operation to after an edit operation – a critical task for interactive editing of city models.

## 9.3. Inverse procedural modeling

A more recent, and alternative, form of procedural modeling reverses the computational direction to yield an "inverse modeling" framework. While procedural modeling has its clear advantages, it may often be the case that (i) the procedural model is known but the parameter values that yield a desired outcome are not, or (ii) neither the procedural model nor the parameter values are known. The former case is arguably simpler and occurs when the underlying structure is well understood and can be modeled, but the parameter values for a particular instance are not available. The latter occurs when a geometric model can be observed (by pictures or by laser scanning), but the underlying procedural model is not known – having knowledge of the procedural model would then enable the same powerful and succinct editing ability of forward procedural modeling.

### 9.3.1. *Inverse parameter estimation*

Several inverse procedural modeling papers have described a set of assumed building and facade structural priors and focus on estimating the parameter values for a particular instantiation (Figure 9.3). In the following, we describe several exemplary works at the building and at the facade levels.

For buildings, Aliaga *et al.* [ALI 07] propose a general grammar-based structure for an arbitrary building. The building is assumed to have a unique ground floor, followed by several intermediate floors, and a unique top floor. Each floor is further divided into facades, windows, and doors. Given a new building model reconstructed using an interactive photogrammetry, for example, its components (e.g. windows, doors, floors, and facades) are labeled by the user. The system then determines the parameter values for a particular instantiation of the general building grammar. The user can then interactively, and automatically, apply the grammar to any new building structure resulting in a building of similar "style" as the original building. Vanegas *et al.* [VAN 10] later extended this methodology to a fully automatic methodology that can be used for buildings observed in oblique-angle aerial views and belonging to the so-called Manhattan World (i.e. there is a predominance of three mutually orthogonal directions in the building) [COU 99].

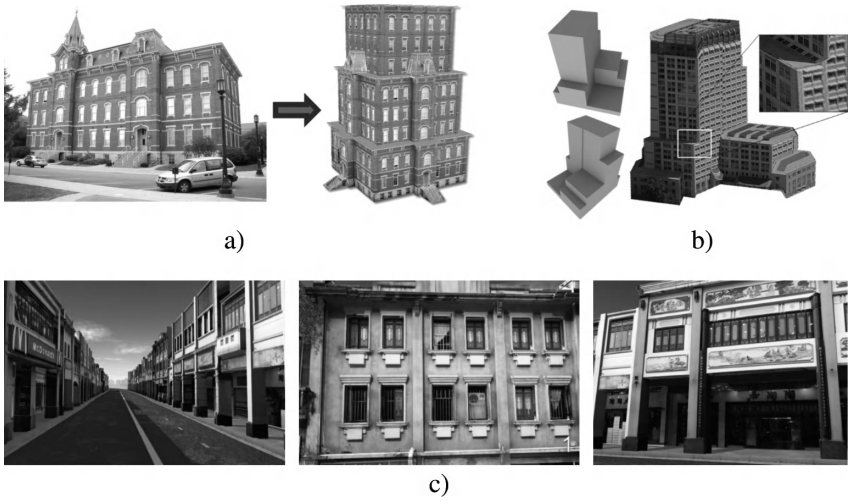


**Figure 9.3.** *Inverse parameter estimation: (a) From images, a semi-automatic method enables creating similar style buildings [ALI 07]; (b) Also from images, an automatic method reconstructs Manhattan-world buildings robustly; (c) Xiao et al. [XIA 08] exploit recursive subdivision and symmetries to reconstruct street-level facades*

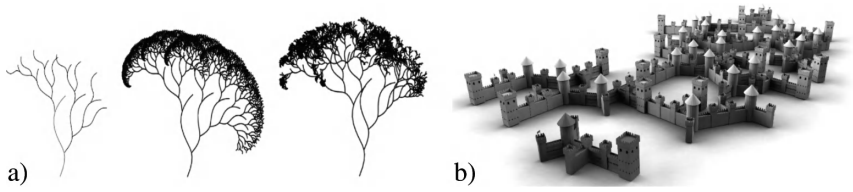


**Figure 9.4.** *Inverse procedure estimation: (a) From 2D vector data,* Stava *et al. [STA 10] discover the underlying L-system grammar rules, which then permit altering the model; (b) From 3D geometry, Bokeloh et al. [BOK 10] exploit symmetry assumptions to discover hidden relationships between geometric elements to enable producing new but similar style models*

For facades, Mueller *et al.* [MUE 07] use the idea of splitting rules to infer the procedural structure of a facade from a single orthographic image as input. The general structure of the facade is assumed to follow a predetermined heuristic and the method finds important symmetry information. Global optimization is used as well to find adequate splitting lines to define rows and columns within the facade. Then, a library of detailed shape grammar rules are used to obtain the final model. Xiao *et al.* [XIA 08] propose a similar facade method that decomposes a photograph of a facade using top–down recursive subdivision, followed by a bottom–up merging with the detection of architectural bilateral symmetry and repetitive patterns. Teboul *et al.* [TEB 10] use an assumed procedural shape prior (i.e. style) and a random exploration of the grammar space to optimize the sequence of derivation rules toward a best semantic-geometric interpretation of the observations. In later work, they apply machine learning techniques to refine the inference process for a focused style (i.e. the Parisian Haussmannian architecture) [SIM 10, TEB 11].

### 9.3.2. *Inverse procedure and parameter estimation*

The general task of discovering both the procedural rule set and the parameter values is a significant and exciting challenge. Several works have focused on exploiting a small set of fundamental assumptions that can be made for a particular domain. In the following, we list some exemplary works from a variety of research perspectives (Figure 9.4).

Stava *et al.* [STA 10] focused on recovering the L-system that represents a given arbitrary 2D scene. The input scene is assumed to consist of a set of atomic elements, such as curves, polygons, or polylines. Similarities and position/ orientation symmetries between the atomic elements are discovered by using dual spaces. The discovered structure is then coded as L-system rules, including branching and hierarchies. The extracted procedural model can then be used to alter, symmetrize [MIT 07], or substitute parts of the original input.

A later work is that of Bokeloh *et al.* [BOK 10], which extends inverse modeling to 3D meshes of urban structures. The authors exploit symmetry and look for repetitive occurrences of object parts, ultimately extracting a plausible shape grammar for the model. The grammar can then be used to generate altered versions of the input 3D model.

From a very different perspective, Beirão *et al.* [BEI 05, BEI 11] describe a "city induction" process where from geospatial data and design principles a suitable set of urban design patterns is inducted. The result is a grammar for generating plausible models of an urban space.

## 9.4. Simulation-based modeling

Another approach to geometrical city modeling is to integrate urban simulation with geometric generation (Figure 9.5). Few systems have proposed initial solutions to this promising direction. An early work is that of Honda *et al.* [HON 04], which generates virtual cities that vary dynamically over time. Their approach focuses on a method of relocating buildings suitable to residents' time-varying activities. More recently, Weber *et al.* [WEB 09] present a geometric simulation of a city over time (e.g. up to 25 years). Their interactive simulator focuses on urban growth without feedback (e.g. a change in height of the building does not modify the distribution of population and jobs).

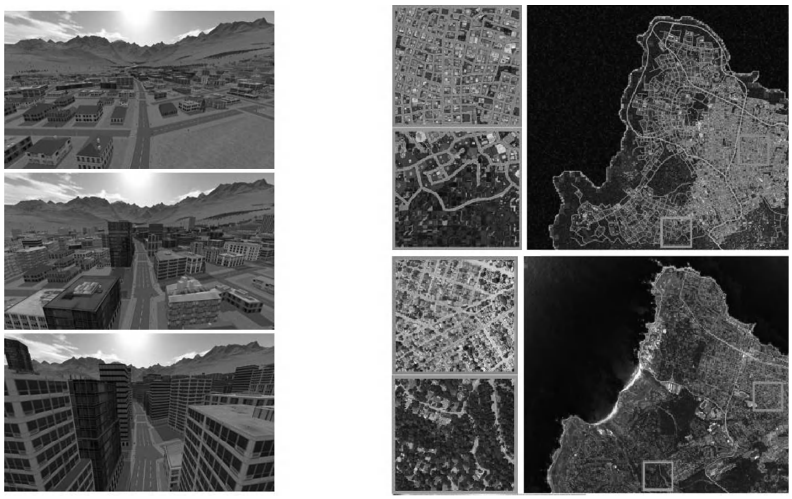

a) b)

**Figure 9.5.** *Simulation-based modeling: (a) A geometrical simulation evolves a 3D city model over time [WEB 09]; (b) A behavioral-geometrical simulation builds a detailed plausible 3D model (top) that qualitatively approximates a real city (bottom) [VAN 09b]*

Vanegas *et al.* [VAN 09a, VAN 09b] develop a system to create city models that builds off of the well-known UrbanSim simulation platform [WAD 02]. In Vanegas *et al.* [VAN 09a], the output of a previous urban simulation is used to generate a plausible 2D urban layout. In Vanegas *et al.* [VAN 09b], their system creates 3D urban models from scratch and then simulates the interdependency of several aspects of a city, thus enabling fast design of very realistic city models, shown for regions spanning over 200 $km^2$. Their proposed design process uses an iterative dynamical system for reaching equilibrium: a state where the demands of behavioral modeling match those of geometrical modeling. 3D models are generated in a few seconds and conform to both plausible urban behavior and plausible urban geometry. The framework includes an interactive agent-based behavioral modeling system as well as adaptive geometry generation algorithms.

## 9.5. Example systems

The aforementioned methods for the geometric modeling of cities and urban spaces have been used in a variety of prototypical systems:

*Urban vision*: Open source software system for visualizing alternative land use and transportation scenarios at scales ranging from large metropolitan areas to individual neighborhoods. The motivation behind this system is to fill the gap between the outputs of existing land use and transportation models and the automatic generation of 3D urban models and visualizations.

*Urban ecosystem*: A system that uses a biologically inspired simulation and procedural system for integrating plants into the interactive design process of future 3D city models [BEN 11].

*Urban weather*: This decision support tool enables exploring and understanding the link between urban land use planning policies and urban weather – in particular thunderstorms, heavy rainfall, and temperature changes.

## 9.6. Bibliography

[ALE 77] ALEXANDER C., ISHIKAWA S., SILVERSTEIN M.A., *Pattern Language: Towns, Buildings, Construction*, Cess Center for Environment, 1977.

[ALI 07] ALIAGA D., ROSEN P., BEKINS D., "Style grammars for interactive visualization of architecture", *IEEE Transactions on Visualization and Computer Graphics*, vol. 13, no. 4, pp. 786–797, 2007.

[ALI 08a] ALIAGA D.G., VANEGAS C.A., BENES B., "Interactive example-based urban layout synthesis", *ACM Transactions on Graphics*, vol. 27, no. 5, 2008.

[ALI 08b] ALIAGA D., BENES B., VANEGAS C., ANDRYSCO N., "Interactive reconfiguration of urban layouts", *IEEE Computer Graphics and Applications*, vol. 28, no. 3, pp. 38–47, 2008.

[ALI 08c] ALIAGA D., VANEGAS C., MING L., NIYOGI D., "Visualization-based decision tool for urban meteorological modeling", *Environment and Planning B*, submitted, 2012.

[ALK 08] ALKHEDER S., WANG J., SHAN J., "Fuzzy inference guided cellular automata urban-growth modeling using multi-temporal satellite images", *International Journal of Geographical Information Science*, vol. 22, nos. 11–12, pp. 1271–1293, 2008.

[BAT 07] BATTY M., *Cities and Complexity: Understanding Cities with Cellular Automata, Agent-based Models, and Fractals*, MIT Press, Cambridge, MA, 2007.

[BEI 05] BEIRÃO J.N., DUARTE J.P., "Urban grammars: towards flexible urban design", *Proceedings of the 23rd Conference on Education in Computer Aided Architectural Design in Europe (eCAADe)*, 2005.

[BEI 11] BEIRÃO J.N., NOURIAN P., MASHHOODI B., "Parametric urban design: an interactive sketching system for shaping neighborhoods", *Proceedings of 29th Conference on Education in Computer Aided Architectural Design in Europe,* eCAADe, pp. 225–234, September 2011.

[BEN 09] BENES B., ANDRYSCO N., STAVA O., "Interactive modeling of virtual ecosystems", *Proceedings of Eurographics Workshop on Natural Phenomena*, pp. 9–16, 2009.

[BEN 11] BENES B., ABDUL M., JARVIS P., ALIAGA D., VANEGAS C., "Interactive ecosystem design", *Proceedings of ACM Symposium on Interactive 3D Graphics and Games*, pp. 8, 2011.

[BOK 10] BOKELOH M., WAND M., SEIDEL H.P., "A connection between partial symmetry and inverse procedural modeling", *ACM Transactions on Graphics*, vol. 29, no. 4, 2010.

[CHE 08] CHEN G., ESCH G., WONKA P., MUELLER P., ZHANG E., "Interactive procedural street modeling", *ACM Transactions on Graphics*, vol. 27, no. 3, 2008.

[COU 99] COUGHLAN J.M., YUILLE A.L., "Manhattan world: compass direction from a single image by Bayesian inference", *Proceedings of IEEE International Conference on Computer Vision*, pp. 941–947, 1999.

[DEB 96] DEBEVEC P., TAYLOR C.J., MALIK J., "Modeling and rendering architecture from photographs", *Proceedings of ACM SIGGRAPH*, pp. 11–20, August 1996.

[FRA 10] FRAHM J.M., GEORGEL P., GALLUP D., JOHNSON T., RAGURAM R., WU C., JEN Y.H., DUNN E., CLIPP B., LAZEBNIK S., POLLEFEYS M., "Building Rome on a cloudless day", *Proceedings of European Conference on Computer Vision*, 2010.

[GAL 10] GALIN E., PEYTAVIE A., MARECHAL N., GUERIN E., "Procedural generation of roads", *Computer Graphics Forum (Proceedings of Eurographics)*, vol. 29, no. 2, pp. 429–438, 2010.

[GOE 07] GOESELE M., SNAVELY N., CURLESS B., HOPPE H., SEITZ S., "Multi-view stereo for community photo collections", *Proceedings of International Conference on Computer Vision*, 2007.

[HAL 08] HALATSCH J., KUNZE A., SCHMITT G., "Using shape grammars for master planning", *Proceedings of Design Computing and Cognition*, pp. 655–673, 2008.

[HER 01] HERTZMANN A., JACOBS C., OLIVER N., CURLESS B., SALESIN D., "Image analogies", *Proceedings of ACM SIGGRAPH*, 2001.

[HON 04] HONDA M., MIZUNO K., FUKUI Y., NISHIHARA S., "Generating autonomous time-varying virtual cities", *Proceedings of International Conference on Cyberworlds*, pp. 45–52, 2004.

[LIP 08] LIPP M., WONKA P., WIMMER M., "Interactive visual editing of grammars for procedural architecture", *ACM Transactions on Graphics*, vol. 27, no. 3, 2008.

[LIP 11] LIPP M., SCHERZER D., WONKA P., WIMMER M., "Interactive modeling of city layouts using layers of procedural content", *Computer Graphics Forum (Eurographics)*, vol. 30, no. 2, pp. 345–354, 2011.

[MAR 04] MARSHALL S., *Streets and Patterns*, Routledge, pp. 336, 2004.

[MEC 96] MECH R., PRUSINKIEWICZ P., "Visual models of plants interacting with their environment", *Proceedings of ACMSIGGRAPH*, pp. 397–410, 1996.

[MIT 07] MITRA N., GUIBAS L., PAULY M., "Symmetrization", *ACM Transactions on Graphics*, vol. 26, no. 3, pp. 63, 2007.

[MUE 06] MUELLER P., WONKA P., HAEGLER S., ULMER A., VAN GOOL L., "Procedural modeling of buildings", *ACM Transactions on Graphics*, vol. 25, no. 3, pp. 614–623, 2006.

[MUE 07] MUELLER P., ZENG G., WONKA P., VAN GOOL L., "Image-based procedural modeling of facades", *ACM Transactions on Graphics*, vol. 26, no. 3, pp. 85, 2007.

[MUS 12] MUSIALSKI P., WONKA P., ALIAGA D., WIMMER M., VAN GOOL L., PURGATHOFER W., "A survey of urban reconstruction", *State of the Art Report (STAR)*, *Proceedings of Eurographics*, 2012.

[NAN 10] NAN L., SHARF A., ZHANG H., COHEN-OR D., CHEN B., "Smartboxes for interactive urban reconstruction", *ACM Transactions on Graphics*, vol. 29, no. 4, 2010.

[PAR 01] PARISH Y.I., MUELLER P., "Procedural modeling of cities", *Proceedings of ACM SIGGRAPH*, pp. 301–308, 2001.

[PRU 90] PRUSINKIEWICZ P., LINDENMAYER A., *The Algorithmic Beauty of Plants*, Springer-Verlag, New York, 1990.

[PRU 94] PRUSINKIEWICZ P., JAMES M., MECH R., "Synthetic topiary", *Proceedings of ACM SIGGRAPH*, pp. 351–358, 1994.

[SIM 10] SIMON L., TEBOUL O., KOUTSOURAKIS P., PARAGIOS N., "Random exploration of the procedural space for single-view 3D modeling of buildings", *International Journal on Computer Vision (Special Issue on Image Grammars)*, vol. 93, no. 2, pp. 253–271, 2010.

[STA 10] STAVA O., BENES B., MECH R., ALIAGA D., KRISTOF P., "Inverse procedural modeling by automatic generation of L-systems", *Computer Graphics Forum (Eurographics)*, vol. 29, no. 2, pp. 665–674, 2010.

[STI 75] STINY G., *Pictorial and Formal Aspects of Shape and Shape Grammars*, Birkhauser Verlag, 1975.

[TEB 10] TEBOUL O., SIMON L., KOUTSOURAKIS P., PARAGIOS N., "Segmentation of building facades using procedural shape prior", *Proceedings of IEEE Conference on Computer Vision and Pattern Recognition*, 2010.

[TEB 11] TEBOUL O., KOKKINOS I., SIMON L., KOUTSOURAKIS P., PARAGIOS N., "Shape grammar parsing via reinforcement learning", *Proceedings of IEEE Conference on Computer Vision and Pattern Recognition*, 2011.

[VAN 09a] VANEGAS C.A., ALIAGA D., BENES B., WADDELL P., "Visualization of simulated urban spaces: inferring parameterized generation of streets, parcels, and aerial imagery", *IEEE Transactions on Visualization and Computer Graphics,* vol. 15, no. 3, pp. 424–435, 2009.

[VAN 09b] VANEGAS C., ALIAGA D., BENES B., WADDELL P., "Interactive designing and editing of urban spaces using geometric and behavioral modeling", *ACM Transactions on Graphics*, vol. 28, no. 5, 2009.

[VAN 10] VANEGAS C., ALIAGA D., BENES B., "Building reconstruction using Manhattan-world Grammars", *Proceedings of IEEE Conference on Computer Vision and Pattern Recognition*, pp. 358–365, 2010.

[VAN 12] VANEGAS C., KELLY T., WEBER B., HALATSCH J., ALIAGA D., MÜLLER P., "Procedural generation of parcels in urban modeling", *Computer Graphics Forum (Proceedings Eurographics)*, 2012.

[WAD 02] WADDELL, P., "Urbanism: modeling urban development for land use, transportation and environmental planning", *Journal of the American Planning Association*, vol. 68, no. 3, pp. 297–314, 2002.

[WEB 09] WEBER B., MUELLER P., WONKA P., GROSS M., "Interactive geometric simulation of 4D cities", *Computer Graphics Forum (Eurographics)*, vol. 28, no. 2, pp. 481–492, 2009.

[WIS 10] WISSEN HAYEK U., NEUENSCHWANDER N., HALATSCH J., GRÊT-REGAMEY A., "Procedural modeling of urban green space pattern designs taking into account ecological parameters", *Proceedings of the 28th Conference on Education in Computer Aided Architectural Design*, eCAADe, Europe, 2010.

[WON 03] WONKA P., WIMMER M., SILLION F., RIBARSKY W., "Instant architecture", *ACM Transactions on Graphics*, vol. 22, no. 3, pp. 669–677, 2003.

[XIA 08] XIAO J., FANG T., TAN P., ZHAO P., OFEK E., QUAN L., "Image-based academic modeling", *ACM Transactions on Graphics*, vol. 27, no. 5, 2008.

[YIN 09] YIN X., WONKA P., RAZDAN A., "Generating 3D building models from architectural drawings: a survey", *IEEE Computer Graphics and Applications*, vol. 29, no. 1, pp. 20–30, 2009.

# Chapter 10

# Radiative Simulation Methods

## 10.1. Introduction

A building's thermal engineers have developed methods to simulate all of the heat flow in a model consisting of the interior volume of a building, limited by different kinds of walls usually with windows. This model includes various equipments and reflects the activities of people. One difficulty is that urban buildings have strong interactions (conduction between adjacent buildings, radiation from nearby buildings, sky and the Sun's obstruction, and perturbation of convective flow between buildings even quite far apart from the other). Many researchers are now trying to model a full city block, which may include buildings of very different styles and epochs. They hope to reach the district level in the near future, or even the entire city.

However, two problems make this task almost intractable. First, it is necessary to collect a huge amount of information and organize it for calculation. Second, the customer of such simulation, which is no longer the architect, but the city planner, does not have knowledge of what is going on inside the buildings.

The proposed approach starts from the urban scene, that is to say, what can be seen from the street, including a few deductions on the interiors and their use, from outward appearance, cadastral map, and data services generally available in the city or state offices (e.g. differentiation between homes, offices, and shops).

---

Chapter written by Pierre BECKERS and Benoit BECKERS.

*Solar Energy at Urban Scale* Benoit Beckers

The city is not considered as a collection of buildings, but as a specific entity whose main parameters are the topology of streets and squares, the width and height of buildings, and the slopes of roofs. The constructions are reduced to a shell composed of roofs, facades, and possibly windows, each surface being provided with semantics (color, surface emissivity, wall thickness, and possible presence of single or double-glazing).

The general idea is to introduce first the terrestrial and solar geometries, recalling the interest of the preferred tool of azimuthal projections. Then, the solar gain is discussed by focusing on an open sector (without obstacle). This quantifies the ideal solar radiation. The next step is to present the radiosity method, including, of course, the consideration of obstacles. Urban geometric models capable of handling large scenes were specifically addressed in the previous chapter written by D. Aliaga; these are based on behavioral [VAN 09] and procedural [BES 11] approaches for automatic generation of levels of detail (LOD) of building models. Once the shortwave radiative interactions were computed, the problem of coupled heating inside the whole city is solved with the same techniques as in the aerospace domain. They are presented in the next chapter written by T. van Eekelen.

## 10.2. Geometry

### 10.2.1. *The geometric model*

The geometric model includes the description of the town placed on the terrain and the surrounding topography. This model can significantly alter the size of the visible sky portion of the cities built in the valleys. At great distance, the topographic surface is simply represented by its skyline. Figure 10.1 shows the polar diagram of the sky at some point in the Chamonix valley [COL 08]. In this mountain valley, the skyline rises to almost 30° in certain directions. As shown in this example, the topographic configuration of a city may require taking into account these masks.

To build the geometrical model of the city, the most accessible information is the definition of the building envelope. It is visible from the street or in an aerial view. This envelope is partially reduced to a set of plane patches, sometimes as large as full facades. The curve-shaped buildings can be approximated by polygons and in more complex situations by Delaunay triangular meshes [GEO 98]. In the early stages of the simulation, the surface model that does not require specifying the thickness of the walls is good enough. The inclusion of windows can be achieved at different levels: in some simulations, they may be omitted, in others they have only to hide part of the wall. At the highest level, they are fully defined with their offset from the facade. The windows are entities belonging to the geometric patches.

The patches are divided into meshes regardless of the possible presence of windows. Each element is characterized by the name of the patch to which it belongs. The windows are other components of the patch. When they are involved in the simulation, they have priority over the underlying mesh. The whole mesh is the calculation model. In the limiting case of the coarsest grid, each patch can be considered as an element of the calculation model.

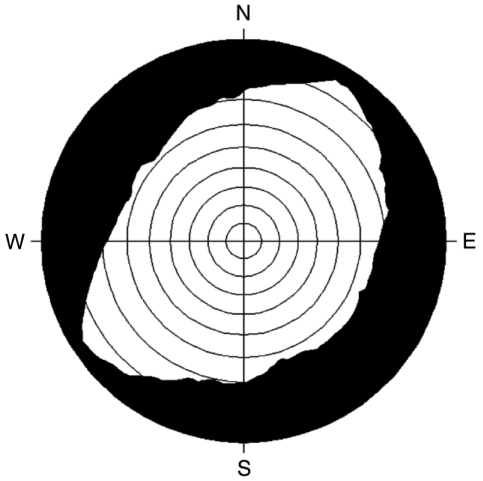


**Figure 10.1.** *Skylines in Chamonix (France) – circles are 10° spaced*

The definition, at a higher level, of rectangular boxes that include buildings, alone or in groups, contributes significantly to improve the performances in the detection of visible parts. With these three levels: boxes, patches, and meshes, a further structuring of data by identifying buildings, streets, and neighborhoods is very useful to control the simulations and perform operations like copy and move.

### 10.2.2. *Solar geometry: calculating the Sun's position*

To describe the relative positions of the Sun and the Earth, both bodies can stand for the point of view. Since the goal here is to have the Sun's position from a point located on Earth, it is more convenient to adopt a geocentric point of view.

The parameters needed to define an orbit are called orbital elements. In celestial mechanics, they are generally introduced through the classic problem of the two bodies, one body moving relative to the other on a Kepler orbit. There are several ways to describe an orbit, but one of the most familiar is based on six parameters: the

eccentricity, the semimajor axis, the inclination, the longitude of the ascending node, the periapsis argument, and the mean anomaly (a variable able to represent the time).

The *eccentricity* describes the flattening from a circle to an ellipse; it varies between zero and one. The *semimajor axis* is the average between the *periapsis* (point closest to the center of attraction) and *apoapsis* (farthest point from the center of attraction). In the study of the apparent motion of the Sun around the Earth, the orbital plane is the *ecliptic plane*, and the two points are called *perihelion* and *aphelion*. These parameters describe the shape of the ellipse.

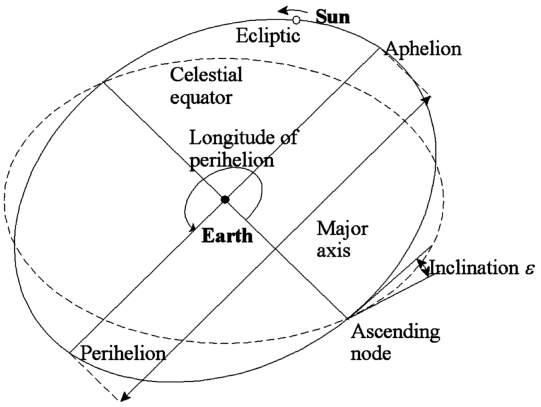


**Figure 10.2.** *Kepler parameters*

Two elements describe the orientation of the orbital plane. The *inclination* is the angle between the orbital plane and a horizontal reference plane; in this case, the angle between the ecliptic plane and the terrestrial equatorial plane. The *longitude of the ascending node* measures the angle between the intersection of these two planes and a defined direction in the reference plane. As the ellipse intersects the reference plane at two points, the ascending node corresponds to the crossing in the direction of the top of the reference plane (in the case of the solar system, the *vernal equinox*, which marks the transition from southern hemisphere to northern hemisphere). The vernal equinox occurs in March.

The *periapsis argument* gives the orientation of the ellipse in its plane. This angle is measured from the ascending node to the radius connecting the center of attraction to the perihelion.

The *mean anomaly* or time defines the position of the body in its orbit at any given time. It sets out an angle of practical use as it varies linearly with time, but it

does not correspond to an actual angular position. It must therefore be converted into the *true anomaly*, which itself represents the angle between the radius that describes the position of the body and that describes the periapsis. The three angles, inclination, longitude of the ascending node, and argument of periapsis, can also be viewed as the *Euler angles* defining the orientation of the orbit relative to the reference system.

The Sun's position relative to a point on the Earth's surface is the result of the yearly movement due to the *Earth's revolution* and is described by the six Kepler parameters and the *Earth's rotation*, with periodicity equal to 1 day or 24 h.

The calculation of the Sun's position is completed in two steps: first, the Earth will be assimilated to a material point without rotation, and then, a local reference frame rotating with the Earth will be used.

10.2.2.1. *Earth's revolution*

In the two bodies' theory of Kepler, the relative motion is described by an ellipse on which one of the two bodies is moving, while the other lies at the focus of the ellipse. However, as the eccentricity of the orbit is very small, it is simpler to assimilate the Sun's trajectory to a circular orbit in the ecliptic plane inclined at an angle $\varepsilon = 23.44383° = 0.409172$ rad relative to the Earth's equatorial plane.

The *declination* $\delta$ denotes the angular height of the Sun relative to the equatorial plane. The *longitude of the Sun* $L$ is a function of the day number of the calendar year (for January 1, $D = 1$). It corresponds to the angular position measured on the circular orbit from the vernal point where the Sun is assumed to pass on March 21 ($D = 81$):

$$L = 2\pi \frac{(D - 81)}{365.25} \qquad [10.1]$$

The Sun's position in the ecliptic plane is then expressed in Cartesian coordinates:

$$x = \cos L \; ; \; y = \sin L \; ; \; z = 0 \qquad [10.2]$$

A rotation of angle $\varepsilon$ gives the coordinates in the equatorial plane:

$$\begin{bmatrix} x_{eq} \\ y_{eq} \\ z_{eq} \end{bmatrix} = \begin{bmatrix} 1 & 0 & 0 \\ 0 & \cos\varepsilon & -\sin\varepsilon \\ 0 & \sin\varepsilon & \cos\varepsilon \end{bmatrix} \begin{bmatrix} x \\ y \\ z \end{bmatrix} = \begin{bmatrix} \cos L \\ \sin L \cos\varepsilon \\ \sin L \sin\varepsilon \end{bmatrix} \qquad [10.3]$$

The declination $\delta$ and the *right ascension* $\varphi_{RA}$, which is the angle measured on the equator from the ascending node, figure the spherical coordinates similar to longitude and latitude used to identify points on the Earth. They are calculated either in terms of equatorial coordinates or in terms of the angles $L$ and $\varepsilon$:

$$\begin{aligned} \tan(\varphi_{RA}) &= y_{eq} / x_{eq} = \tan L \cos \varepsilon \\ \sin \delta &= z_{eq} = \sin L \sin \varepsilon \end{aligned} \qquad [10.4]$$

Summing up, the Sun's position is given by its longitude [10.1] in the ecliptic plane or coordinates [10.4] in the equatorial plane.

Actually, the Earth moves on an elliptical orbit of low eccentricity, $e$ = 0.016710219, slightly higher than those of the planets Venus and Mercury that have more circular orbits. The Sun's position has to be computed at any given time with respect to the orbital period and the time of perihelion passage.

The anomalies are angles that can situate an object on an elliptical trajectory. The first angle to consider is the mean anomaly $M$. It allows locating the Sun in the time scale. Above, we called this quantity longitude $L$ when measured from the vernal equinox, while the mean anomaly is measured from the perihelion. This is the angle that would be measured on a clock graduated over a year by placing the origin at perihelion. Two other anomalies are used: the *eccentric anomaly* $E$ when the position vector starts from the center of the conic and the *true anomaly* $v$ when it starts from the focus. Kepler's equation allows computing the eccentric anomaly from the mean anomaly:

$$M = \left(E - e \sin E\right) \qquad [10.5]$$

This equation is trivial if the goal is to calculate $M$ from $E$, but it has no explicit solution when it is intended to calculate $E$ from $M$. However, a numerical solution can be developed without difficulty, using, for example, an iterative method of Newton. We can then calculate the position of the Sun in its orbit as a function of the true anomaly.

$$\cos v = \frac{(\cos E - e)}{(1 - e \cos E)}; \quad \sin v = \frac{\sqrt{1 - e^2} \sin E}{(1 - e \cos E)} \qquad [10.6]$$

Adding the longitude of perihelion $\omega$ (more or less equal to 283°) to the true anomaly $v$, gives, as in the formula [10.1], the Sun's longitude:

$$L = \omega + v \qquad [10.7]$$

The equations [10.2]–[10.4] again allow computing the Cartesian coordinates in the equatorial plane or the right ascension $\varphi_{RA}$ and the declination $\delta$.

The problem can also be solved more accurately by calculating the position of the Earth from astronomical data where the evolution over time is taken into account.

| | | |
|---|---|---|
| Reference day | $d$ | $= JD - 2451543.5$ |
| Eccentricity | $e$ | $= 0.016709 - 1.151\ 10^{-9}\ d$ |
| Longitude of perihelion (degrees) | $\omega$ | $= 282.9404 + 4.70935\ 10^{-5}\ d$ |
| Mean anomaly (degrees) | $M$ | $= 356.0470 + 0.9856002585\ d$ |
| Obliquity of the ecliptic (degrees) | $\varepsilon$ | $= 23.4393 - 3.563\ 10^{-7}\ d$ |

**Table 10.1.** *Astronomical data as functions of the Julian day*

In these corrections, the days are counted from January 1, 2000, which is the Julian day *J2000* = 2,451,545. The value of the Julian day *JD* can be obtained from many Web sites. For example, January 1, 2012 corresponds to *JD* = 2455927.5; it follows that, on this date, *d* = 4,384. The above table contains the astronomical data of January 1, 2000 with a first-order correction. The quality of the data determines the precision of the results deduced from the simple procedure described above in formulas [10.5] – [10.7]. This approach is similar to many other procedures in this regard [MÜL 95].

10.2.2.2. *Earth's rotation*

From now on, let us consider the Earth as a rotating body. The variables are the time zone and the longitude. Greenwich mean time (GMT) is obtained by adding the mean anomaly *M*, which gives the solar time, to the longitude of perihelion $\omega$.

$$t_{Greenwich} = \omega + M \qquad [10.8]$$

The local sidereal time is calculated by adding to GMT the zone time *t* and the longitude $\varphi$ of the studied point, counted positively eastward and expressed in hours.

$$t_{sideral} = t_{Greenwich} + t_{zone} + \varphi \qquad [10.9]$$

The hour angle (HA) indicates the Sun's direction. It is equal to the difference between sidereal time and the right ascension [10.4]. All angular quantities are expressed in hours.

$$\varphi_{HA} = t_{sideral} - \varphi_{RA} \qquad [10.10]$$

In the equatorial plane, the Sun's position is:

$$\begin{aligned} x_{sun} &= \cos\varphi_{HA}\cos\delta \\ y_{sun} &= \sin\varphi_{HA}\cos\delta \\ z_{sun} &= \sin\delta \end{aligned} \qquad [10.11]$$

It only remains to express this position in the local coordinates defined with reference to the local horizontal plane, defined by the south direction ($x$-axis), the east direction ($y$-axis), and its normal pointing toward the local zenith. The angle $\alpha$ is the latitude.

$$\begin{bmatrix} x_L \\ y_L \\ z_L \end{bmatrix} = \begin{bmatrix} \sin\alpha & 0 & -\cos\alpha \\ 0 & 1 & 0 \\ \cos\alpha & 0 & \sin\alpha \end{bmatrix} \begin{bmatrix} x_{sun} \\ y_{sun} \\ z_{sun} \end{bmatrix} = \begin{bmatrix} \sin\alpha\cos\varphi_{HA}\cos\delta - \cos\alpha\sin\delta \\ \sin\varphi_{HA}\cos\delta \\ \cos\alpha\cos\varphi_{HA}\cos\delta + \sin\alpha\sin\delta \end{bmatrix} \qquad [10.12]$$

We now deduce the azimuth $\zeta$ (angle measured from the north) and the zenith angle $\psi$ (angular distance measured from the vertical; it is the complement of the Sun's height).

$$\begin{aligned} \zeta &= \arctan(y_L / x_L) + \pi \\ \pi/2 - \psi &= \arcsin z_L \end{aligned} \qquad [10.13]$$

This concludes the calculation of the Sun's position for a point located at coordinates $\varphi$, $\alpha$ (longitude, latitude), at the time $t$.

10.2.2.3. *Sun's azimuth and zenith angle*

As shown in [10.13], at latitude $\alpha$, the zenith angle $\psi$ of the solar ray is given by:

$$\cos\psi = \sin\alpha\sin\delta + \cos\alpha\cos\delta\cos\varphi_{HA} \qquad [10.14]$$

Every day, the minimum value of the zenith angle is obtained at solar noon (when $\varphi_{HA} = 0$).

$$\psi = \alpha - \delta \qquad [10.15]$$

The day length measured in hours for a geometric sunset (no atmospheric refraction) is given by:

$$h_S = \frac{24}{\pi}\arccos\left(-\tan\alpha\tan\delta\right) \qquad [10.16]$$

The Sun's azimuth $\zeta$ depends on its declination $\delta$ calculated by [10.4], and its zenith distance $\psi$, [10.14], itself a function of time and latitude $\alpha$:

$$\cos\varsigma = \frac{-\left(\sin\delta - \cos\psi \sin\alpha\right)}{\cos\alpha \sin\psi} \qquad [10.17]$$

The azimuth is measured with respect to south, increasing in the counter-clockwise direction (so 90° is east).

### 10.2.3. *Geometric description of the environment of a point*

The basic problem when computing radiative exchanges is the determination of the visibility of the elements of the scene. To analyze what is happening around a point, the spherical projection is perfect because, by definition, we can calculate the projections of all points in space with the exception of the center of the sphere. The spherical projection is reduced to the projection of a hemisphere when the point of interest is located on a surface. The base of the hemisphere is then the tangent plane.

The shortcoming of the spherical projection is that it is not a developable surface. A second projection on the plane is needed. This is the problem that the cartographers faced to represent the world map.

#### 10.2.3.1. *Contribution of cartography*

The experience of geographers is useful to establish the classification of spherical projections. Among the representations they have imagined, we note azimuthal projections in which one hemisphere (more rarely the whole sphere) is represented in polar coordinates. A first image of the sphere is obtained by simple orthographic projection on the plane (Figure 10.3). This is a very familiar image because it corresponds to the pictures of planets taken at great distances.

In the gnomonic projection, the projection center is located at the center of the sphere. The large circles are projected as straight lines; the circles parallel to the projection plane are projected as circles and the other circles as conic sections. In the case of the Earth, when the projection plane is parallel to the equator, the parallels are projected as concentric circles. The projections of meridians and parallels are orthogonal lines. The negative aspect of this projection is to introduce very large deformations when approaching the base of the hemisphere (Figure 10.4).

In the stereographic projection (Figures 10.3 and 10.4), the center is located on the sphere at the farthest point of the radius perpendicular to the plane of projection

(see Table 10.2). Stereographic projection of an arc drawn on the sphere is an arc or a straight line segment. In addition, the angle between two curves drawn on the sphere is reproduced without deformation. It is the property of conformity. This projection is probably the best suitable for the representation of a hemisphere.

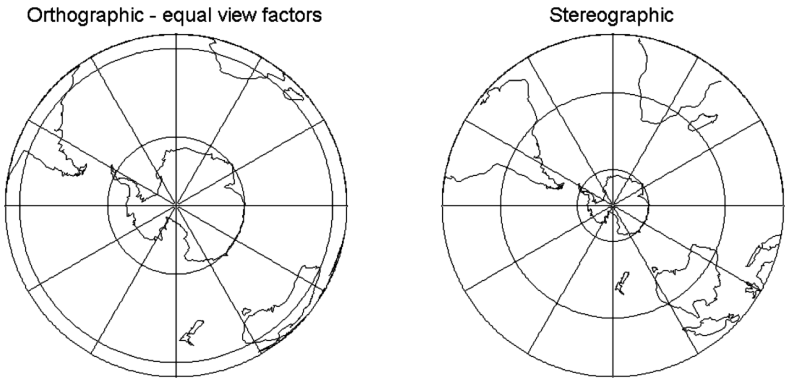


**Figure 10.3.** *Comparison of two azimuthal projections of the southern hemisphere*

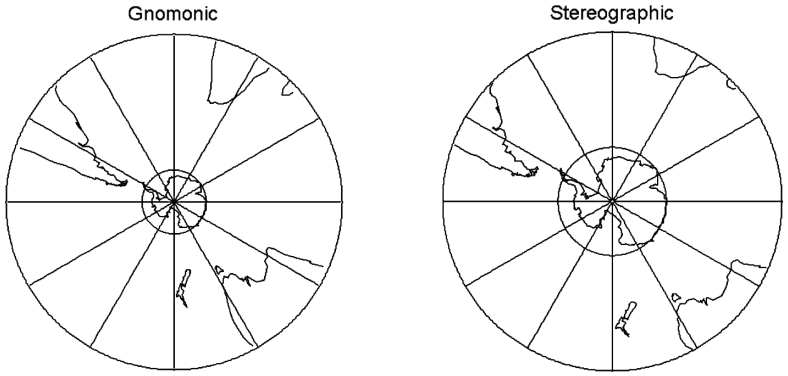


**Figure 10.4.** *Comparison of two azimuthal projections of the southern hemisphere beyond the tropics*

There are also a variety of methods where the projection of a point is not constructed by projecting a straight beam. One of the most widespread, called "plate carrée", is built by plotting latitudes and longitudes on a rectangular graph. By plotting these coordinates on a polar diagram, it gives the "Postel projection" (Figure 10.5). Both methods can easily represent the whole sphere, but the poles are

represented by two lines in the “plate carrée”, while in the Postel projection, one pole is represented by a circle. The distortions are very strong in areas close to one or both poles.

The Lambert or equal-area projection (Figure 10.5) is constructed similar to the Postel projection, but the radial distance is adjusted so that the area of each disk is the same as that of the spherical cap it represents. In this projection, the full spherical surface is represented by a disk whose radius is equal to the diameter of the sphere.

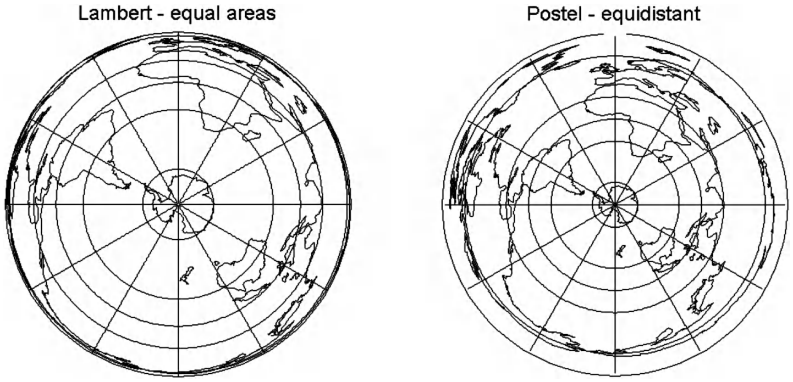


**Figure 10.5.** *Comparison of two azimuthal projections of the world map centered on the South Pole*

These data are presented in Table 10.2 where it should be noted that the colatitude $\theta$ is the angular distance defining the extension of a spherical cap centered on the pole of the hemisphere. The second column gives the radius of the disk image of the shell. The last column gives the ratio of the circumferences of the parallel limiting the spherical cap and of its projection.

| Colatitude $\theta$ | | |
|---|---|---|
| Projection | Disk radius | Circumference ratio |
| Orthogonal | $\sin \theta$ | 1 |
| Gnomonic | $\mathrm{tg}\ \theta$ | $\cos \theta$ |
| Stereographic | $2\ \mathrm{tg}\ (\theta/2)$ | $(1 + \cos \theta)/2$ |
| Lambert equivalent | $2 \sin (\theta/2)$ | $\cos (\theta/2)$ |
| Postel | $\theta$ | $(\sin \theta)/\theta$ |

**Table 10.2.** *Geometrical properties of the azimuthal projections*

Figure 10.6 shows the results of the table. The gnomonic projection is not able to represent the area near the equator where the colatitude is equal to $\pi/2$. Among the three linear projections (gnomonic, stereographic, and orthogonal), the stereographic is most likely to give a satisfactory representation of the areas near the equator. The main characteristics of azimuthal projections are summarized Table 10.3.

| | | |
|---|---|---|
| The orthogonal | projection respects | view factors |
| The gnomonic | | shape of orthodromies |
| The stereographic | | angles |
| The Lambert equivalent | | areas |
| The Postel | | distances from central point |

**Table 10.3.** *Principal characteristics of the azimuthal projections*

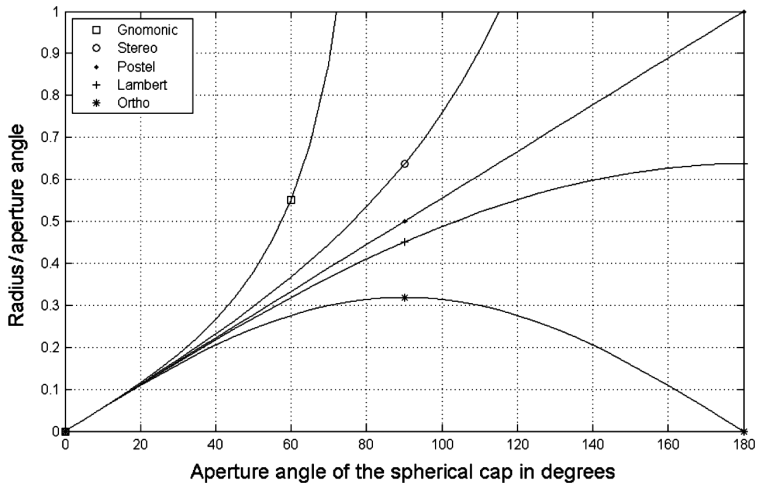


**Figure 10.6.** *Radial distortions of azimuthal projections of the sphere*

10.2.3.2. *Urban geometry, stereography, and isochronous graph*

Periods of sunshine are clearly seen in a stereographic projection, which superimposes the solar paths, and the buildings projections. For the sake of clarity, here, the trajectories are calculated using solar simplified formula [10.1].

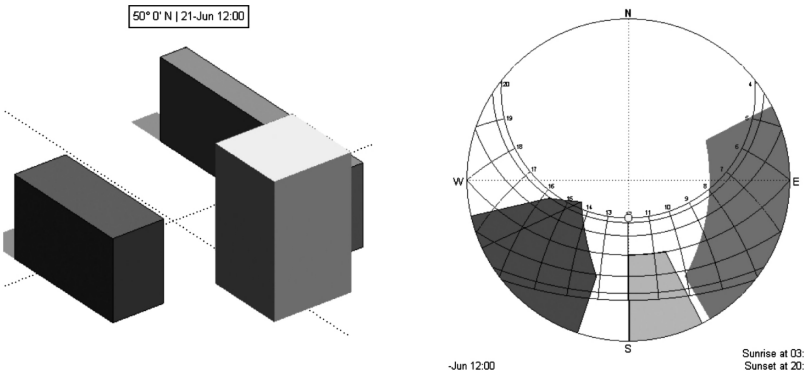


**Figure 10.7.** *3D view and stereographic projection*

This projection, however, has two drawbacks. The first is to represent the double time scale in a distorted way. The second is to superimpose the two periods between the solstices. The solution proceeds as follows. First, the area of the stereography beneath the solar trajectories is separated.

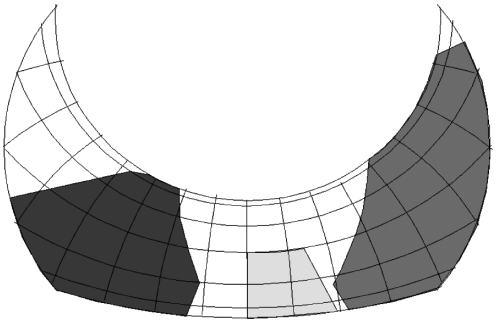

**Figure 10.8.** *Selection of the area corresponding to solar trajectories*

Second, it is redrawn, keeping the two time scales proportional. This is shown in Figure 10.9.

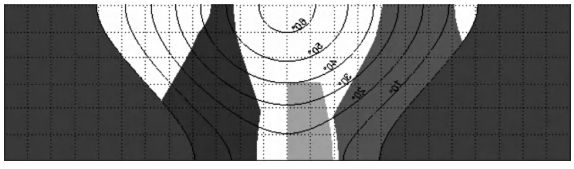

**Figure 10.9.** *Transformation making the proportionality of two time scales*

Finally, to avoid overlapping of the two periods of the year, the chart is split by symmetry and, in addition, the time axis is inverted to get a reading from left to right.

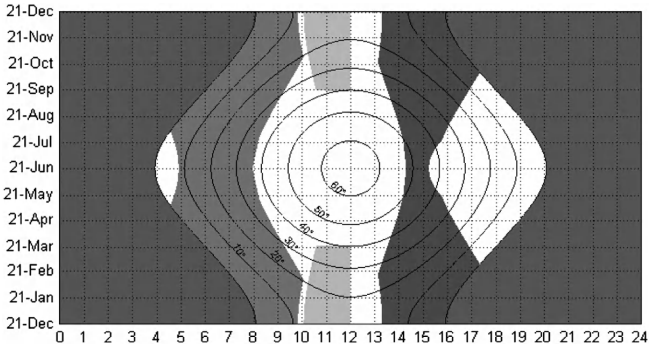


**Figure 10.10.** *Isochronous*

This representation is more interesting than the representation in Figure 10.7. Indeed, the days and the year are seen proportionally, respectively, on the horizontal and the vertical axes. As the two time scales are linear, we gave it the name of isochronous [BEC 07].

All azimuthal projections contain the same information but each projection with its own deformation. For the simulation, we can stay with one of these methods [BEC 11a]. However, in the framework of design, when assessing behavior of the model, it is preferable to choose the best projection able to raise a particular property. The remarkable property of the isochronous is its capability to show the sunshine hours throughout the year.

## 10.3. Loading

Solar radiation reaches the Earth's surface after passing through the atmospheric layer. It comes in different forms: direct, diffuse, reflected by the environment, or other elements of the scene. Other phenomena contribute, for example, the effects of physical and chemical reactions that take place in the atmosphere and the phenomena induced by vegetation.

### 10.3.1. *Radiation sources: Sun and sky*

The Sun's position is characterized only by one direction. In the absence of a barrier, solar irradiance is easily calculated according to the angle of sunrays with

the receiving surface and the intensity of radiation, which depends only on the angular height of the Sun. This is the phenomenon of atmospheric attenuation considered below in the case of a clear sky.

### 10.3.2. *Irradiance on differently oriented planes*

#### 10.3.2.1. *Direct radiation on a plane always facing the Sun*

The irradiance of solar radiation on a surface perpendicular to the solar ray is designated, outside the atmosphere, by the variable $S_{p0}$ ($S_{p0}$ = 1,367 $Wm^{-2}$) and on the Earth's surface by the variable $S_{pb}$. Both quantities are measured in $Wm^{-2}$. They are linked by the atmospheric transmittance, a dimensionless number whose value is between 0.65 and 0.75, according to [CAM 98, LIU 60]:

$$S_{pb} = S_{p0}\ \tau^{m} \qquad [10.18]$$

The optical air mass $m$ is a measurement made at sea level on the length of the path traveled through the atmosphere by light rays from a celestial body. It is expressed as a multiple of the length of the path corresponding to a light source placed at the zenith.

According to the Glossary of Meteorology published by the American Meteorological Society (AMS) [LIS 51], for zenith distances [10.14] up to about 70°, it is approximately equal to the secant of the angle defining the zenith distance of the given celestial body. For a more accurate calculation, the refraction of the light beam must be taken into account [KRI 98, WIT 97].

To obtain a representative value at high altitude, these parameters must be multiplied by the ratio of the actual atmospheric pressure $p_a$ and the pressure at sea level $p_0$:

$$m_0 = \sec\psi\ ;\ \ m = m_0 p_a / p_0 \qquad [10.19]$$

Atmospheric pressure $p_a$ is calculated based on the altitude $h$ expressed in meters:

$$p_a / p_0 = e^{-\frac{h}{8{,}200}} \qquad [10.20]$$

At sea level, the pressure is $p_0$ = 101,325 Pa (1.013 bars). The standard temperature is 288° K. In the troposphere, which extends approximately from 0 to 11 km, temperature decreases linearly from about 6.5 K/km.

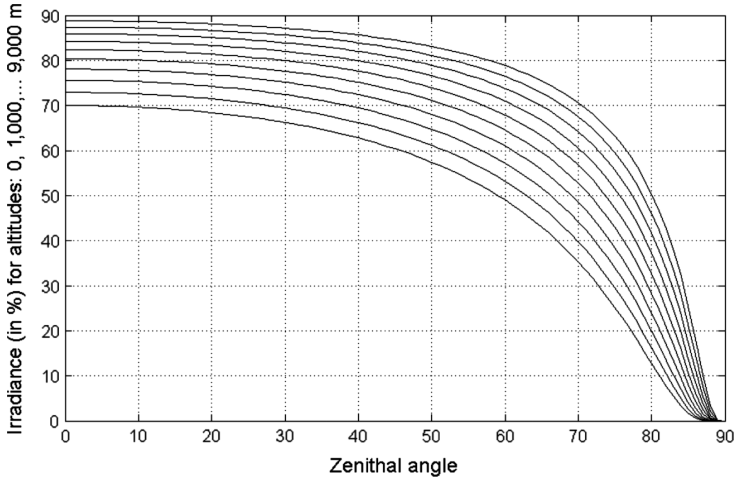


**Figure 10.11.** *Direct irradiance on a surface perpendicular to the sunray ($\tau = 0.7$)*

In this formulation, the number $m$ goes to infinity when the sunrays become horizontal. Whatever the value (by definition, <1) of the transmittance, the direct irradiance tends to zero as the Sun sets on the horizon. A transmittance equal to 1 corresponds to a perfectly transparent medium.

Between 0 and 4,000 m (Figure 10.11), the irradiance in the vertical direction increases by 15%. For larger zenith angles, the effect of altitude is greater (Table 10.4).

| Date | Zenith angle at noon | % at 0 m | % at 4,000 m | Ratio 4,000 m/0 m(%) |
|---|---|---|---|---|
| June 21 | 26.5° | 67.13 | 78.29 | 116 |
| December 21 | 73.5° | 28.48 | 46.25 | 162 |

**Table 10.4.** *Change in irradiance with elevation to a point at 50° north*

In summer, when the Sun is higher, the increased radiation with elevation is almost the same as for the zenith ray: 16%. However, in winter, it is 62%, but at that time, the Sun rises only at about 16.5° above the horizon.

The direct irradiation computed on an arbitrary plane is, by definition, less than the just calculated irradiation. It decreases in proportion to the cosine of the angle $\beta$ between the ray and the normal to the receiver. Assuming a uniform sky, the diffuse radiation on the same receiver must be multiplied by the sky view factor equal to $(1 + \cos\beta)/2$. In principle, we must also take into account the albedo of the environment, unless the receiver is horizontal and the sky is not hidden. Neglecting

albedo is equivalent to considering that the surface viewed from the receptor is black. A comprehensive study of these situations was carried out by Duffie and Beckmann [DUF 06].

10.3.2.2. *Horizontal plane*

On a horizontal surface, the direct irradiance (beam irradiance) is designated by the variable $S_b$, the diffuse, $S_d$, and the total, $S_t$.

$$\begin{aligned} S_b = S_{pb}\cos\psi &= \tau^m S_{p0}\cos\psi \\ S_d &= 0.3\,(1-\tau^m) S_{p0}\cos\psi \\ S_t &= \left(0.3\,(1-\tau^m)+\tau^m\right) S_{p0}\cos\psi \end{aligned} \qquad [10.21]$$

The formulas [10.14] and [10.21] allow calculating the irradiance anytime and anywhere on the globe. Figure 10.12 shows the change at noon as a function of the latitude, three times of the year: solstices and equinox. Since the declination of the Sun at the equinoxes and solstices, 0 and ±23.45°, is known [10.15], this calculation does not require the solution of the equation of time.

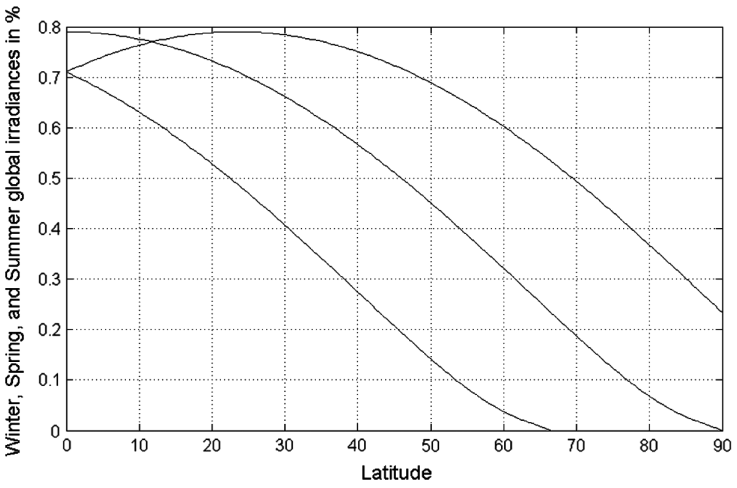


**Figure 10.12.** *Global irradiance at noon in the northern hemisphere with bottom-up the winter solstice, the equinoxes, and the summer solstice*

These calculations provide the total direct irradiance in the absence of obstacles. In more complex scenes, the determination of the shadows requires many operations. A local mesh refinement is often necessary to establish more precisely the contours of the shadows.

10.3.2.3. *Computation of energy*

The integration of irradiance over a period of time, i.e. a day [10.16], allows following the evolution of the energy received. According to the disciplines or habits, energy is expressed in Joules (MJ most often) or kh (1 kh = 3.6 MJ). For energy, the same indices are used, with letter *J* instead of *S*.

$$J_{pb} = \int_{t_1}^{t_2} S_{pb}\, dt \qquad [10.22]$$

These calculations give a first idea of the spatial and temporal distributions of energy from solar irradiance, e.g. in the city of Compiègne (49°24′ N) at the solstices and equinoxes. The extra-atmospheric irradiance is assumed equal to 1,367 $Wm^{-2}$, and the atmospheric transmittance $\tau = 0.7$. Calculations are carried out for the year 2010. The variable *h* indicates the day length [10.16]. Between summer and winter, the ratio of received energy is greater than 5 for a panel always oriented in the direction of the Sun ($J_{pb}$), and is equal to 9 for a horizontal panel ($J_b$), while the daylight period varies only by a factor of 2.

| | Day length (*h*) | $J_{p0} = 1{,}367 \times h$ | $J_{pb}$ | $J_b$ | $J_d$ | $J_t$ |
|---|---|---|---|---|---|---|
| March 21 | 11.98 | 16,376 | 6,255 | 3,219 | 1,065 | 4,284 |
| June 21 | 16.05 | 21,943 | 10,015 | 6,854 | 1,546 | 8,400 |
| September 21 | 12.17 | 16,632 | 6,460 | 3,397 | 1,090 | 4,487 |
| December 21 | 7.95 | 10,867 | 1,811 | 455 | 493 | 948 |

**Table 10.5.** *Solar energy ($Whm^{-2}$) received in Compiègne 49°24′ N*

At the summer solstice, for a panel facing the Sun, energy ($J_{pb}$) is increasing up to the highest latitudes, while for the horizontal panel it ($J_t$) reaches a maximum at latitude 40° N (more precisely, 36°42′ N, i.e. Malaga, Algiers, Mersin). The maximum occurs with different positions: (30° N) for the direct radiation ($J_b$) and (65° N) for the diffuse radiation ($J_d$).

The calculation of energy over periods in excess of a day makes sense only if we take into account the meteorological data. For most available sky models, it is difficult to define the parameters. An interesting idea is to use cumulative skies, which unfortunately lose the temporal evolution but can be performed in only one calculation [COM 04, ROB 11]. When a sky model is available (often, an analytical model [PER 93]), it can be discretized, e.g. using the 145 Tregenza cells [TRE 87].

| Latitude (degrees) | Day length ($h$) | $J_{p0} = 1{,}367 \times h$ | $J_{pb}$ | $J_b$ | $J_d$ | $J_t$ |
|---|---|---|---|---|---|---|
| 0 | 12 | 16,404 | 7,915 | 5,597 | 1,196 | 6,792 |
| 10 | 12.58 | 17,203 | 8,540 | 6,360 | 1,271 | 7,631 |
| 20 | 13.21 | 18,059 | 9,045 | 6,884 | 1,339 | 8,223 |
| 30 | 13.93 | 19,046 | 9,448 | **7,141** | 1,404 | 8,545 |
| 40 | 14.84 | 20,292 | 9,768 | 7,120 | 1,472 | **8,592** |
| 50 | 16.15 | 22,075 | 10,030 | 6,829 | 1,551 | 8,380 |
| 60 | 18.49 | 25,275 | 10,299 | 6,305 | 1,670 | 7,975 |
| 65 | 21.12 | 28,871 | **10,502** | 5,984 | **1,775** | 7,759 |

**Table 10.6.** *Solar energy received on the summer solstice – June 21 – northern hemisphere*

Databases provide the values of direct, diffuse, and total radiations for a large number of places. From there, it can be inferred for sky models. Another way is, while keeping the sky uniform, to use statistical data to adjust the direct illumination to the collected data and to introduce the diffuse contribution in proportion to the sky factor. Different questions arise: how were the databases created, what is their relevance, which kind of uncertainties do they involve, and what is their influence on simulations. Another problem comes from the periodicity of measurements, which has a direct impact on the liability of the simulations. Most databases provide results every hour (8,760 points per year), but for some simulations, e.g. solar awnings, it is not enough. The question is then to interpolate the data. As a final point, an additional problem is the data cleaning, often required because the raw measurements are incorrect [CRA 01].

## 10.4. Computation model

The solution of radiative exchange problems is based on either ray tracing methods [WAR 94] and their many variants, either on radiosity methods. The former are widely used in rendering while the latter were initially introduced in heat transfer problems [GEB 61].

Radiosity methods have the advantage of addressing the problem of radiative exchange for the entire scene. They involve two steps:

1) Calculation of the view factors;

2) Solution of the radiosity equations.

There is a clear separation between the pure geometrical step and the radiative calculations. The positive consequence is that the setting of the radiative problem is completely independent and can be modified retrospectively and inexpensively.

As the black bodies spectra of around 6,000 K (Sun) and 300 K (land, air) are separated, it is possible to decouple the corresponding radiations. If we accept the assumption of diffuse reflection essentially, it can be considered that each surface is characterized by a single parameter: the reflection coefficient (plus, possibly, the transparency of glazes).

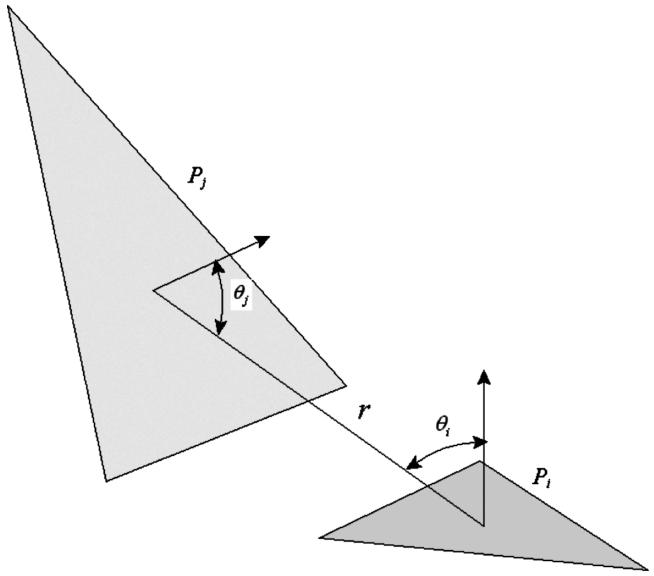


**Figure 10.13.** *View factor definition scheme*

### 10.4.1. *Radiosity equations*

Radiosity equations express the balance of radiative exchanges between all possible pairs of elements of the scene, assuming diffuse reflections (Figure 10.13).

$$\begin{pmatrix} B_1 \\ B_2 \\ \vdots \\ B_n \end{pmatrix} = \begin{pmatrix} E_1 \\ E_2 \\ \vdots \\ E_n \end{pmatrix} + \begin{pmatrix} \rho_1 F_{11} & \rho_1 F_{12} & \cdots & \rho_1 F_{1n} \\ \rho_2 F_{21} & \rho_2 F_{22} & & \vdots \\ \vdots & & & \vdots \\ \rho_n F_{n1} & \cdots & \cdots & \rho_n F_{nn} \end{pmatrix} \begin{pmatrix} B_1 \\ B_2 \\ \vdots \\ B_n \end{pmatrix} \qquad [10.23]$$

In the above system, the components of the matrix consist of the reflection coefficients $\rho_i$ and the view factors $F_{ij}$, also known as form factors. The view factor is a purely geometrical variable, but its definition relies on energy concepts: $F_{ij}$ is the proportion of the total power leaving $P_i$, which is received by $P_j$. It, therefore, links

two patches: $P_i$ and $P_j$. The radiosities $B_i$ and the exitances[1] $E_i$ are measured in $Wm^{-2}$, while the view factors are dimensionless. $V$ is the visibility function, equal to 1 if the item is visible and 0 if not.

$$F_{ij} = \frac{1}{P_i} \int_{P_i} \int_{P_j} \frac{\cos\theta_i \cos\theta_j}{\pi r^2} V(x,y)\, dP_j dP_i \; ; \; x \in P_i \; ; \; y \in P_j \qquad [10.24]$$

### 10.4.2. *View factors*

The view factor consists of a double integral, which can be calculated analytically in a few very specific situations. This topic has been analyzed in detail by Howell [HOW 10], who has compiled a catalog of known analytical solutions.

#### 10.4.2.1. *Properties of the view factor*

The system of linear equations [10.23] works with the unknown radiosity $B_i$ gathered in the vector $B$ and the second member of exitances $E_i$, in the vector $E$. It is written in a more compact form by introducing the radiosity matrix $R$.

$$RB = E \; ; \; R_{ij} = \delta_{ij} - \rho_i F_{ij} \qquad [10.25]$$

The view factor of a plane patch toward itself is equal to zero. Consequently, in a closed cavity, the sum of the view factors of the elements surrounding a plane patch is equal to 1. This is the *closure property*.

$$\sum_{j=1}^{n} F_{ij} = 1 \; ; \quad i = 1,n \qquad [10.26]$$

This property is verified by a simple inspection of the view factors matrix: the sum of the terms of each row must be equal to 1. It can also be done by solving the system of equations. Indeed, if all the reflection coefficients are identical, all the walls have the same properties, and if the second member is composed of exitances all equal to 1, then all the radiosities are identical:

$$E_i = 1 \; ; \quad i = 1,n \;\; \rightarrow \;\; B_i = \frac{1}{1-\rho} \; ; \quad i = 1,n \qquad [10.27]$$

The discrepancies with respect to [10.27] are reflecting the closure defaults of the view factors.

---

1 The Commission internationale de l'éclairage recommends the name *exitance* instead of *energetic emittance*.

Considering the symmetry of the integral [10.24], we deduce also the *property of reciprocity*. If *Ai* and *Aj* are the areas of the elements *i* and *j*, we obtain:

$$A_i F_{ij} = A_j F_{ji} \; ; \; F_{ji} = F_{ij} \;\; A_i / A_j \qquad [10.28]$$

This property means that, for example, if $A_i$ is a disk and $A_j$ is the hemisphere above it, $F_{ij} = 1$ according to the closure condition [10.26]. Moreover, because the area of the hemisphere is twice that of the base disk, by [10.28], $F_{ji} = 1/2$. This means that the disk can only see the dome; meanwhile, the dome sees partly the disk and partly itself.

Like the previous property, this property can be verified by a simple inspection of the view factors matrix. Note that if all elements have the same area (a condition seldom met), the matrix of view factors is symmetric.

The property of reciprocity can also be verified by solving the equations of importance. Denoting by $A$ the vector (single column matrix) whose components are the areas of the elements, since radiosities are constant in each element, the power dissipated by the walls of the scene is calculated simply by the product:

$$p = B^T A = (R^{-1}E)^T A = E^T (R^{-1})^T A = E^T X \qquad [10.29]$$

The vector $X$ defines the importance; it is the solution of the system of equations:

$$R^T X = A \qquad [10.30]$$

This system of equations where the coefficient matrix is the transpose of [10.25] is the adjoint of the radiosity equations. These are the equations of importance. The quantities $A$ and $X$ are areas measured in $m^2$. Writing [10.30] explicitly:

$$\sum_{i=1}^{n} X_i R_{ij} = A_j \qquad [10.31]$$

Assuming that all the reflection coefficients are equal:

$$\sum_{i=1}^{n} X_i \left( \delta_{ij} - \rho F_{ij} \right) = A_j \qquad [10.32]$$

Hence:

$$X_j - \rho \sum_{i=1}^{n} X_i F_{ij} = A_j \;\; \rightarrow \;\; \frac{X_j}{A_j} - \rho \sum_{i=1}^{n} X_i \frac{F_{ij}}{A_j} = 1 \qquad [10.33]$$

In addition, taking into account the reciprocity equation [10.28]:

$$\frac{X_j}{A_j} - \rho \sum_{i=1}^{n} X_i \frac{F_{ji}}{A_i} = 1 \qquad [10.34]$$

This equation is verified by the solution:

$$\frac{X_i}{A_i} = \frac{1}{1-\rho} \; ; \; i = 1, ..., n \qquad [10.35]$$

If all the reflection coefficients are equal, the importances per areas are too. The discrepancies between the actual solution of [10.30] and the result [10.35] show evidence of the deficiencies caused by the failure of the reciprocity equations.

According to [10.29], the power can be calculated in two ways:

$$p = B^T A = E^T X \qquad [10.36]$$

Let $w$ be the power emitted by all sources.

$$w = E^T A \qquad [10.37]$$

*If all the reflection coefficients are equal and if the room is closed*, a simple physical reasoning [BEC 11b] allows us to deduce the exact theoretical power developed by the system:

$$p_{exact} = \frac{w}{1-\rho} = \frac{E^T A}{1-\rho} \qquad [10.38]$$

Power [10.38] is an input of the problem: it depends on exitances and areas, which are respectively the second members of the radiosity and importance equations. The denominator depends only on the unique reflectance of the elements.

The solution of the radiosity equations gives the same result if the view factors are calculated exactly. However, since it is usually not possible in three dimensions (3D), the comparison of the radiosity solution and the result [10.38] gives a useful indication of the error in calculating the view factors. We deduce the accuracy of the radiated power calculated from the radiosity or importance:

$$\frac{p}{p_{exact}} = \frac{(1-\rho)}{E^T A} B^T A = \frac{(1-\rho)}{E^T A} E^T X \qquad [10.39]$$

10.4.2.2. *View factors algebra*

Reciprocity law [10.28] provides a simple way to calculate half of the view factors. There is also an obvious rule of addition: if an element sees two or more patches, the view factor of this group of patches is equal to the sum of the view factors of the individual patches.

$$F_{i-(j\cup k)} = F_{i-j} + F_{i-k} \qquad [10.40]$$

Combining this result and the law of reciprocity:

$$\left(A_j + A_k\right) F_{(j\cup k)-i} = A_i F_{i-(j\cup k)} \qquad [10.41]$$

By [10.28] and [10.40], the view factor for the union of two elements to one-third is equal to the weighted average for the two elements to the third:

$$F_{(j\cup k)-i} = \frac{A_j F_{j-i} + A_k F_{k-i}}{A_j + A_k} \qquad [10.42]$$

In the presence of two meshes with known view factors for all elements, the above formulas allow us to calculate easily the view factors for the two meshes. The numerical integration methods, such as Gauss integration rule, are based on the same concepts of addition and average.

10.4.2.3. *Point to area view factor*

Except for very special 3D configurations, it is not possible to calculate the view factors accurately. We must, therefore, turn to numerical methods. One approach is to calculate in two steps. First, we calculate the "differential view factor", "point view factor", or "point to area view factor", which is the inner core of expression [10.24]. Then, we integrate this quantity on the concerned element.

The view factor of an element $A_j$ seen from the point $X_i$ belonging to the element $A_i$ is given by:

$$\begin{aligned} F_{dA_i - A_j} &= \int_{y\in A_j} \frac{\cos\theta_i \cos\theta_j}{\pi r^2} V(x,y)\, dy \\ &= \frac{1}{\pi} \int_{\Omega_{X_i - A_j}} \cos\theta_i \; V(x,y) d\omega \; ; x \in dA_i \end{aligned} \qquad [10.43]$$

For a polygonal surface *P, Q, R*… [LAM 60], the following formula is exact if there are no obstacles:

$$F_{dS-j} = \frac{1}{2\pi} \sum_{j} n.g_j \qquad [10.44]$$

The vector *n* is normal to the surface supporting *dS*, for which we calculate the view factor (Figure 10.14). The vectors *gj* are the normal to the faces of the pyramid: *SPQ*, etc. Their modules are equal to the angles at the top *S* of the pyramid: *α, β*.

The other way to calculate the view factor takes place in two steps. The element is projected onto the hemisphere defined by a point on the surface. Then, it is projected orthogonally on the plane tangent to the surface. This projection is related to the area of the base of the hemisphere. This interpretation of the view factor is known as the "Nusselt analogy" [NUS 28]. The calculation method is, in principle, easy to implement. Using an appropriate scaling, it is also possible to perform the computation of the areas on the stereographic projection instead of the orthogonal projection, with the advantage that the projections of spherical polygons are triangles whose edges are straight lines or circular arcs [BEC 11a].

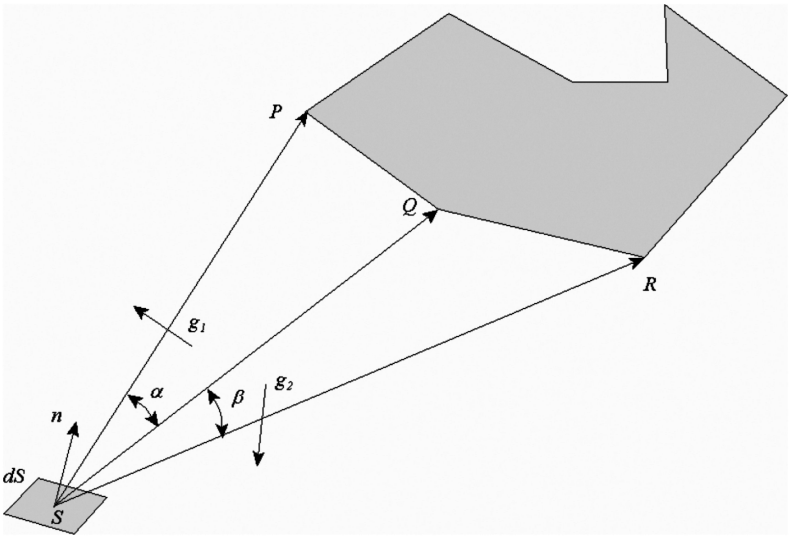


**Figure 10.14.** *Point to area view factor*

### 10.4.3. *Digital processing of the view factor*

Many publications in the field of numerical analysis of continuous media indicate that the most effective method to calculate the view factors from area to area is to perform numerical integration over the differential view factors. This technique consists of evaluating the integrand in a number of points. Then, it is sufficient to calculate the weighted average by assigning *a priori* defined weights for each of the integration points.

$$\int f(x)dx \simeq \sum f(x_i)w_i \qquad [10.45]$$

One of the most popular integration schemes is that of Gauss, presented in Table 10.7, in 1D, but it is also used in the case of quadrilaterals, in the frame of the isoparametric elements technique. In this case, the same pattern is used in both directions of the rectangle defined in intrinsic coordinates. There are also schemes well adapted to triangular elements [ZIE 71].

| Number of points | Positions $x_i$ in interval [0 1] | Weight |
|---|---|---|
| 1 | 0.5 | 1 |
| 2 | $0.5 \pm \sqrt{3}/6$ | 0.5 |
| 3 | $0.5,\ 0.5 \pm \sqrt{3/20}$ | 4/9, 5/18, 5/18 |
| 4 | $0.5 \pm 1/70\sqrt{525 - 70\sqrt{30}}$<br>$0.5 \pm 1/70\sqrt{525 + 70\sqrt{30}}$ | $1/4 + \sqrt{30}/72;\ 1/4 + \sqrt{30}/72$<br>$1/4 - \sqrt{30}/72;\ 1/4 - \sqrt{30}/72$ |

**Table 10.7.** *Positions and weights of Gauss integration points*

To calculate the point to area view factor, the obstacle detection is the same as in ray tracing methods. In practice, it is sufficient to test the visibility of some points of the target. It has been observed that for not too coarse meshes, it is sufficient to test the center of gravity of the target. The quality test of the computed view factors can be done using the method proposed in section 10.4.2.1 or the formula [10.35].

Instead of examining all the elements of the scene, we can also trace a ray in an "arbitrary" direction and see what item is reached. Each time an item is reached, its account number is increased by one. At the end of the process, the account numbers of the items are divided by the number of rays that have reached a target. In this way, the sum of the view factors is automatically equal to one and the closure condition is therefore satisfied.

We are talking about deterministic shoot if the directions are predefined and random shoot (Monte Carlo) if the directions are specified randomly. These directions can be evenly distributed over the hemisphere. This is not the best solution, because this technique focuses on directions close to the horizontal line and therefore to low view factors. It is better to create equal-area cells in the circle constituting the orthogonal projection of the hemisphere (importance sampling). This means that two elements of the scene that receive the same number of rays actually have the same view factor. The only problem is the definition of equal-area cells. This can be done without great difficulty and under different types of criteria [BEC 12]. In this method, as in the following, the closure condition is automatically satisfied.

The choice of tracing directions can be arbitrary on the hemisphere or within equal-area cells spread uniformly throughout the hemisphere. In this case, it is called stratified sampling. In the latter two methods, it is necessary to specify the number of shots to be made. The first question is whether to send more rays than elements within the field of view. Even if this introduces a loss of accuracy and perhaps some visible elements are not reached, the system still conserves a correct behavior.

### 10.4.4. *Characteristics of the discrete model: the mesh and its control*

The accuracy of the solution of the radiosity equation is influenced in part by the accuracy of the calculation of the view factors and in part by the quality of the mesh. As noted above, the first point can be controlled with the equations of importance. The calculation of factors for two neighboring elements, which is quite difficult to achieve [BAU 89], can also be used to compare test methods.

Used only for the radiative exchange, the surface mesh does not need to be congruent (a mesh is said to be congruent if the contact between two neighboring elements is carried out only between nodes or faces or sides); all quantities involved in the calculation can be assumed to be constant per element. The mesh is, however, difficult to handle and requires some experience of the discretization process.

The calculations made in the area of realistic rendering have shown that the size of the mesh in areas of high light transition, like the limit of shadows, strongly influences the quality of the image. However, tests carried out in 2D have confirmed that the energy response is not very sensitive to the mesh as long as the loading is correctly applied (it could be justified on a similar principle to that of Saint Venant, used in strength of materials methods). We also verified that the balance achieved at the patch level is good enough, even for relatively coarse meshes.

These observations agree well with the practice of thermal engineers who use nodal methods [PLA 98] in which they focus the attention on heat flow balance.

However, it is mandatory to comply properly with the laws of conservation, which led us to carefully calculate the view factors.

## 10.5. Transient thermal coupled problem

The shortwave radiative exchanges limited to diffuse reflections could only be calculated based on radiosity. The more complete treatment, including the transient heat transfer in solids and the possible inclusion of the atmosphere, requires more sophisticated methods. We start from the classical equation of heat conduction in a solid:

$$div\left[k\ grad\ T\right]+Q=\gamma c\frac{\partial T}{\partial t} \qquad [10.46]$$

$Q$ is the heat density ($Wm^{-3}$), $T$ is the temperature measured in degrees Kelvin, $k$ is the thermal conductivity ($Wm^{-1}K^{-1}$), $t$ is the time, $c$ is the specific heat ($Jkg^{-1}K^{-1}$), and $\gamma$ is the density ($kgm^{-3}$). The variable associated with the temperature is the heat flux linked to the temperature gradient by Fourier's law:

$$q=-k\ gradT \qquad [10.47]$$

To discretize these equations, the most used technology is the *nodal method* [MEY 99], used for instance in *Esarad* [PLA 98] and *Thermica*[2]. This technique also known as "*Lumped Parameter Method*" offers a number of advantages among which we note that it highlights the thermal balance and heat flux. The fundamental assumption of the method is the use of isothermal nodes arranged in a network where they are connected by resistances and capacitances (electrical analogy). Its main drawback is that it requires a step of idealization from the geometrical definition of the model (Computer Aided Design-CAD step) and the definition of the calculation model. For small models, it can be very useful, because it gives a summary of the exchanges. However, it offers only a coarse representation of the temperature distributions.

An alternative is the finite elements method [FRA 65, LEW 96, ZIE 71], originally developed in mechanical and civil engineering. In this method, the domain is covered with a congruent mesh. In each element, the field is replaced by a polynomial approximation respecting the discretized field continuity conditions required through the interfaces (borders with neighboring elements). The border area consists of a boundary layer through which the exchanges occur with the fluid (here, the atmosphere). Through this boundary radiative exchange also occurs with the outside or with other elements of the scene.

2 http://www.astrium.eads.net/fr/equipements/thermica-engineering-tool.html

In the thermal problem, the temperature field is discretized, so that the result of the simulation is a temperature map "painted" on the skin of the solid.

The boundary conditions consist of Dirichlet or essential conditions where the temperature $T$ is imposed, natural or Neumann conditions where the heat flux is imposed, and Robin conditions that are a weighed combination of Dirichlet and Neumann boundary conditions. These three zones cannot overlap and their union should be the total boundary.

The loads are of different natures:

1) Heat flow from the shortwave solar radiation. It is calculated separately in the "radiosity" module.

2) Longwave radiative fluxes traveling toward other elements of the scene or to the atmosphere. They are proportional to the difference of fourth power of temperatures.

3) Convective flow proportional to the temperature difference between the surface of the solid and a reference point of the fluid in which it merges [ERE 11].

4) Any other heat flow that may be estimated directly or expressed in terms of temperatures, e.g. evapotranspiration.

In summary, the solid subjected to these heat flows and where the temperature is known at least at one point will suffer modifications because of internal heat conduction and the ability of materials to store heat. In finite element calculation, it is a classical problem, the theory of which was developed in the 1970s [FRA 72].

The time component is calculated by a finite difference method. At the level of discretization, we must ensure that the temporal pattern is consistent with the spatial discretization.

In this problem, the main difficulty is the need for view factors of the surfaces brought into contact. It may be assumed that these factors were calculated in the previous step (shortwave). If these view factors must apply for both the analyses, the two meshes have to coincide.

To calculate the convective exchanges, we must know the temperature of the air, which requires, in principle, including the modeling of the fluid.

The evaluation of the quality of the discrete solution of a system of partial differential equations or a system of differential equations is still valid. It has been the subject of special attention from users and developers of finite element analysis programs. The convergence of the solutions was discussed in numerous publications, almost since the beginning of development of the method.

In 1965, Fraeijs de Veubeke [FRA 65] proposed a double analysis (primal and dual) to guide the exact solution. This had been particularly successful when the discretization error calculation was proposed [LAD 01, SZA 91].

## 10.6. Conclusion

The calculation of thermal interactions in the city encompasses three major phases: the definition of the geometry, which must be structured and allow processing of very large volumes of data; the view factors calculation, which involves the effective detection of hidden or viewed parts; and finally, the solution of the equations of transient heat conduction in the coupled problem conduction–radiation.

The methods proposed to solve these problems are qualified, but it is still necessary to verify that the computation time is acceptable.

Treatment of massive geometric data takes advantage of advances in procedural methods and in "LOD". The calculation of view factors can take advantage of the progress made in the Monte Carlo methods or in the effective treatment of hemispheric and stereographic projections.

For the solution of the coupled system, the choice of the finite element method is motivated by its ability to provide a temperature map that can be compared to telemetry. Today, finite elements are widely used to solve nonlinear problems of millions of degrees of freedom and benefit from the attention of programmers who have optimized algorithms. It may be accused of producing an enormous amount of results. The task of identifying the relevant information is reduced through visualization techniques. The use of well-known optimization techniques and sensitivity calculation is an essential asset to assist in the understanding and interpretation of the analyzed phenomena.

## 10.7. Bibliography

[BAU 89] BAUM D.R., RUSHMEIER H.E., WINGET J.M., "Improving radiosity solutions through the use of analytically determined form-factors", *Computer Graphics*, vol. 23, no. 3, pp. 325–334, 1989.

[BEC 07] BECKERS B., MASSET L., BECKERS P., "Enrichment of the visual experience by a wider choice of projections", *Proceedings of the 2007 11th International Conference on Computer Supported Cooperative Work in Design*, CSCWD 2007, Melbourne, Australia, pp. 355–360, 2007.

[BEC 11a] BECKERS B., MASSET L., BECKERS P., "The universal projection for computing data carried on the hemisphere", *Computer-Aided Design*, vol. 43, no. 2, pp. 219–226, 2011.

[BEC 11b] BECKERS B., "Urban outlines 2D abstraction for flexible and comprehensive analysis of thermal exchanges", Cisbat 2011, Lausanne, Switzerland, 14–16 September, 2011, http://cisbat.epfl.ch.

[BEC 12] BECKERS B., BECKERS P., "A general rule for disk and hemisphere partition into equal-area cells", *Computational Geometry - Theory and Applications*, vol. 45, no. 7, pp. 275–283, 2012.

[BES 11] BESUIEVSKY G., PATOW G., "A procedural modeling approach for automatic generation of LoD building models", *Proceeding Cisbat*, Lausanne, Switzerland, 2011.

[CAM 98] CAMPBELL G.S., NORMAN J.M., *An Introduction to Environmental Biophysics*, 2nd ed., New York, Springer, 1998.

[COL 08] COLLIN O., Facteur de ciel: un paramètre d'évaluation des masques en architecture, Master Thesis, University of Liège, 2008.

[COM 04] COMPAGNON R., "Solar and daylight availability in the urban fabric", *Energy and Buildings*, vol. 36, pp. 321–328, 2004.

[CRA 01] CRAWLEY D.B., WINKELMANN F.C., LAWRIE L.K., PEDERSEN C.O., "Energyplus: new capabilities in a whole-building energy simulation program", *7th International IBPSA Conference*, Rio de Janeiro, Brazil, 13–15 August 2001.

[DUF 06] DUFFIE J.A., BECKMANN W.A., *Solar Engineering of Thermal Processes*, John Wiley, 2006.

[ERE 11] ERELL E., PEARLMUTTER D., WILLIAMSON T., *Urban Microclimate – Designing the Spaces between Buildings*, Earthscan, London, pp. 304, 2011.

[FRA 65] FRAEIJS de VEUBEKE B., "Displacement and equilibrium models in the finite element method", in ZIENKIEWICZ O.C., HOLISTER G.S. (eds), *Stress Analysis*, Chapter 9, John Wiley & Sons, pp. 145–197, 1965.

[FRA 72] FRAEIJS DE VEUBEKE B., HOGGE M., "Dual analysis for heat conduction problems by finite elements", *International Journal for Numerical Methods in Engineering*, vol. 5, no. 1, pp. 65–82, September/October 1972.

[GEB 61] GEBHART B., *Heat Transfer*, McGraw-Hill, 1961.

[GEO 98] GEORGE P.-L., BOROUCHAKI H., *Delaunay Triangulation and Meshing: Application to Finite Elements*, Hermes, 1998.

[HOW 10] HOWELL J.R., SIEGEL R., MENGUC M.P., *Thermal Radiation Heat Transfer*, 5th ed., Taylor and Francis/CRC, New York, 2010. Reference is also made to: *A Catalog of Radiation Heat Transfer Configuration Factors*, available at http://www.engr.uky.edu/rtl/Catalog/, 2010.

[KRI 98] KRISTENSEN L.K., "Astronomical refraction and airmass", *Astronomische Nachrichten*, vol. 319, no. 3, pp. 193–198, 1998.

[LAD 01] LADEVEZE P., PELLE J.P., *La maîtrise du calcul en mécanique linéaire et non linéaire*, Hermes, 2001.

[LAM 60] LAMBERT J.H., "Photometria sive de mensura et gradibus luminis, colorum et umbrae", 1760, German translation by ANDING E., in Ostwald's *Klassiker der Exakten Wissenschaften*, vol. 31–33, Leipzig, 1892. Cited by SCHRÖDER P. and HANRAHAN P., A closed form expression for the form factor between two polygons, Research Report CS-TR-404-93, January 1993.

[LEW 96] LEWIS R.W., MORGAN K., THOMAS H.R., SEETHARAMU K.N., *The Finite Element Method in Heat Transfer Analysis*, John Wiley & Sons, 1996.

[LIS 51] LIST R.J. (ed.), *Smithsonian Meteorological Tables*, 6th revised ed., p. 422, available at http://amsglossary.allenpress.com/glossary/search?id=optical-air-mass1, 1951.

[LIU 60] LIU B.Y.H., JORDAN R.C., "The interrelationship and characteristics distribution of direct, diffuse and total solar radiation", *Solar Energy*, vol. 4, no. 3, pp. 1–19, 1960.

[MEY 99] MEYER R.X., "Elements of space technology for aerospace engineers", *Spacecraft Thermal Design*, Academic Press, 1999.

[MÜL 95] MÜLLER M., "Equation of time – problem in astronomy", *Acta Physica Polonica A*, 88 Supplement, S-49, 1995.

[NUS 28] NUSSELT W., "Graphische bestimmung des winkelverhaltnisses bei der wärmestrahlung", *Zeitschrift des Vereines Deutscher Ingenieure*, vol. 72, no. 20, p. 673, 1928. (See: BECKERS B., MASSET L., BECKERS P., Commentaires sur l'analogie de Nusselt, Rapport Helio_004_fr, 2009, available at http://www.heliodon.net/.)

[PER 93] PEREZ R., SEALS R., MICHALSKY J., "All-weather model for sky luminance distribution – preliminary configuration and validation", *Solar Energy*, vol. 50, no. 3. pp. 235–245, 1993

[PLA 98] PLANAS P., FLETT D.C., "ESARAD: From R&D to industrial utilisation", *ESA Bulletin*, vol. 93, no. 93, pp. 61–67, February 1998.

[ROB 11] ROBINSON D., *Computer Modelling for Sustainable Urban Design. Physical Principles, Methods & Applications*, Earthscan, London, 2011.

[SZA 91] SZABO B., BABUSKA I., *Finite Element Analysis*, John Wiley & Sons, Inc., 1991.

[TRE 87] TREGENZA P.R., "Subdivision of the sky hemisphere for luminance measurements", *Lighting Research and Technology*, vol. 19, no. 1, pp. 13–14, 1987.

[VAN 09] VANEGAS C., ALIAGA D., BENES B., WADDELL P., "Interactive design of urban spaces using geometrical and behavioral modeling", *ACM Transactions on Graphics*, vol. 28, no. 5, pp. 10, 2009.

[WAR 94] WARD G.J., "The RADIANCE lighting simulation and rendering system", *SIGGRAPH '94 Proceedings of the 21st Annual Conference on Computer Graphics and Interactive Techniques*, Orlando, 1994.

[WIT 97] WITTMANN A.D., "Astronomical refraction formulae for all zenith distances", *Astronomische Nachrichten*, vol. 318, no. 5, pp. 305–312, 1997.

[ZIE 71] ZIENKIEWICZ O., *The Finite Element Method in Engineering Science*, McGraw-Hill, 1971.

Chapter 11

# Radiation Modeling Using the Finite Element Method

In this chapter, the coupled radiation-conduction problem is discussed, and an implementation of the non-gray radiation problem, using the finite element method, is worked out. The discussed implementation is used today in SAMCEF to solve thermal problems in aerospace applications.

## 11.1. Basic assumptions

Every body emits radiation (electromagnetic) energy, depending on its temperature and material properties. The kind of radiation energy that is referred to as heat radiation, is situated in the wavelenghs between 0.1 μm (ultraviolet) and 100 m (mid-infrared). In Figure 11.1, a definition of the complete electromagnetic spectrum is given. A body that has maximum radiation emission for a given temperature is called a blackbody. We first define the emission of a blackbody over the wavelength spectrum and for a given temperature. This definition is referred to as Planck's law:

$$E_b(\lambda, T) = \frac{2\pi h c_0^2}{n^2 \lambda^5 \left[ e^{\frac{h c_0}{n \lambda R T}} - 1 \right]} \qquad [11.1]$$

If the blackbody emissive power $E_b$ multiplied by the emissivity $\varepsilon^\lambda$ is integrated over the entire spectrum, we obtain the total emissive power of a body. This emissive

Chapter written by Tom VAN EEKELEN.

*Solar Energy at Urban Scale* Benoit Beckers

power depends on total emissivity $\varepsilon$, the Stefan–Boltzmann constant $\sigma$ ($= 5.6696^{-8}$ $\mathrm{Wm^{-2}K^{-4}}$) and the temperature.

$$E(T) = \int_0^\infty E_\lambda(\lambda, T)\, d\lambda = \int_0^\infty \varepsilon^\lambda E_b\, d\lambda = \varepsilon\sigma T^4 \qquad [11.2]$$

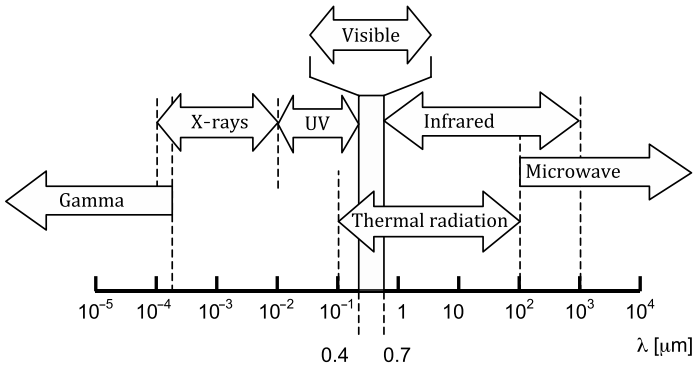


**Figure 11.1.** *Electromagnetic spectrum*

Real bodies emit less than a blackbody does and their emission is normally described as a fraction $\varepsilon$ of blackbody emission.

In this chapter, we limit ourselves to the radiation between the opaque bodies where there is no participating media between the bodies, i.e. the radiation will travel (with the speed of light) in straight lines between the facets. When radiation energy arrives on a real surface, it may be reflected or absorbed, thus leading to the following relation between absorptivity ($\alpha$), diffuse reflectivity ($^d\rho$), and specular reflectivity ($^s\rho$):

$$^s\rho^\lambda + {}^d\rho^\lambda = 1 - \alpha^\lambda \qquad [11.3]$$

The sum of the absorptivity and reflectivities, for a given wavelength, always equals 1, a property that will be exploited for the ray-tracing algorithm. To finalize the description of the basic concepts, we introduce Kirchhoff's law. This law states that for a given wavelength, the emissivity of a body equals the absorptivity.

$$\alpha^\lambda = \varepsilon^\lambda \qquad [11.4]$$

Kirchoff's law seems at odds with the idea of an infrared emissivity and solar absorptivity. The reason for this is that the emissivity and absorptivity in this case refers to different wavelengths, and in reality the solar absorptivity will equal the solar emissivity (body emissivity in the solar wavelength band).

## 11.2. Visibility and view factors

Because radiation travels in straight lines between bodies, without interruption from participating media, the heat exchanged between two bodies will depend on the mutual visibility of the two bodies. A measure for this visibility is the view factor, which will be defined first and a method to calculate it is shown next.

### 11.2.1. *Definition*

For the heat exchange balance between the bodies, we are interested in calculating the radiative heat, emitted by one body $i$ and absorbed by another body $j$. A definition for this so-called radiative exchange factor is given by:

$$dF_{dA_i-dA_j} = \frac{\text{Diffuse energy leaving } dA_i \text{ intercepted by } dA_j, \text{by direct travel}}{\text{Total diffuse energy leaving } dA_i} \quad [11.5]$$

where we assume that all the radiative energy is diffusely emitted and reflected. This means that the energy has no preferred direction of emission or reflection. This assumption is very common for emitters, but obviously too limiting for reflection in general (think of reflection on a mirror surface). Because light travels in straight lines, the diffuse radiative exchange factor only accounts for exchange via direct visibility. In Figure 11.2(a), we see the visibility between the two facets $i$ and $j$. With the right assumptions (diffuse emission, isothermal facets, etc.) the energy balance between the two facets can be reduced to a geometric relation of the visibility between the two facets. A full derivation of this so-called geometrical view factor is given in standard radiation textbooks like [MOD 03] and [HOW 11]. One of the geometric relations introduced is the solid angle, which gives the projection of facet $j$ onto a sphere with radius $d$. The solid angle is hence defined as:

$$d\Omega = \frac{\cos\theta_j \, dA_j}{d^2} \quad [11.6]$$

From the relation between the total radiative intensity and emissive power from Modest [MOD 03]

$$E_b^\lambda = \pi I_b^\lambda \quad [11.7]$$

we can obtain the total emitted power of an infinitesimal facet $i$

$$dq_i = \pi I \, dA_i \quad [11.8]$$

The diffuse view factor between two infinitesimal facets $i$ and $j$ can now be defined as the energy emitted into the solid angle $\Omega$ divided by the total emitted energy.

$$dF_{dA_i-dA_j} = \frac{I\cos(\theta_i) dA_i d\Omega}{\pi I \, dA_i} = \frac{\cos\theta_i \cos\theta_j}{\pi d^2} \, dA_j \quad [11.9]$$

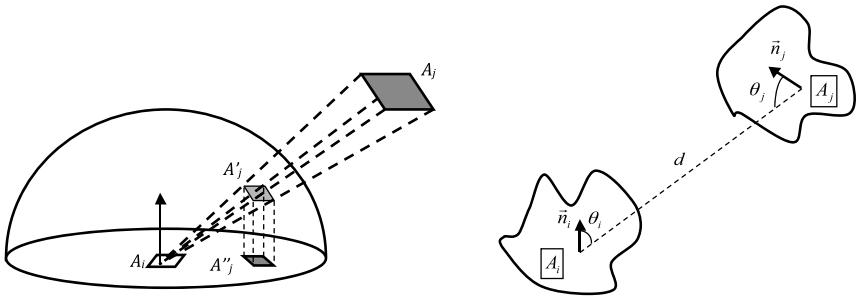


**Figure 11.2.** *(a) Projection of facet $j$ onto the unit sphere around facet $i$, (b) definition of the diffuse view factor for isothermal facets*

The energy balance can now be expressed as the view factors between two facets $i$ and $j$, given in Figure 11.2(b)

$$F_{ij} = \frac{\iint I dF_{dA_i - dA_j}\, dA_i}{\pi \int_{A_i} I\, dA_i} \qquad [11.10]$$

Here, an isothermal facet is assumed, so that the radiative intensity can be taken outside the integrals yielding

$$F_{ij} = \frac{1}{A_i} \int_{A_i} \int_{A_j} \frac{\cos\theta_i \cos\theta_j}{d^2}\, dA_i\, dA_j \qquad [11.11]$$

To complete the definition of the diffuse view factors, the reciprocity and the closure relation have to be introduced:

$$A_i F_{ij} = A_j F_{ji} \qquad [11.12]$$

The closure relation can be geometrically interpreted, namely that all the facets ( $j$), that are seen from facet $i$, will fill the entire unit sphere, as shown in Figure 11.2(a)

$$\sum_{j=1}^{n} F_{ij} = 1 \qquad [11.13]$$

These relations are valid for diffuse emissions and reflection, but this is a too limiting case for practical situations. A more general definition of a radiative exchange factor is given by the specular exchange factor defined by:

$$dF^s_{dA_i - dA_j} = \frac{\text{Diffuse energy leaving } dA_i \text{ intercepted by } dA_j, \text{ by direct travel or any specular reflection}}{\text{Total diffuse energy leaving } dA_i} \qquad [11.14]$$

where the rays that arrive at a facet $j$ can be either absorbed or specularly (like a mirror) reflected. This results in indirect visibilities, which is a much more difficult geometrical concept. For this kind of exchange factor, it is better not to introduce the equivalent geometrical view factor but to directly use the ray-tracing method that can be directly applied to the energy balance expression. The ray-tracing method is the subject of the following section.

### 11.2.2. *Monte Carlo-based ray-tracing method*

For the evaluation of the diffuse view factor, given by the expression of equation [11.5], several numerical methods exist. These methods consist of numerical quadrature rules, and are given in detail in [MOD 03]. Numerical quadrature methods have two main disadvantages. The first is that the calculation cost goes up substantially with the complexity of the models. The second is that the quadrature rules cannot be easily extended to more general radiation cases.

A very important example is the case where specular reflection is included. The general definition of the view factor for this case was given by equation [11.14]. A method that is ideally suited for this kind of radiation case is the so-called ray-tracing method. In this method, rays are launched from every surface and the rays are followed when they travel through the model, where they are reflected and finally absorbed. One of the assumptions is that every ray has the same amount of energy attached to it, i.e. that the energy of a ray equals the total emitted power divided by the total number of emitted rays:

$$\Delta E_i = \frac{\varepsilon \sigma T_i^4 A_i}{N_i} \qquad [11.15]$$

If we define the energy emitted form surface $i$ arriving on surface $j$ after any number of reflections as $\Delta E_{ij}$, the view factor is defined as:

$$F_{ij}^{*} = \lim_{N_i \to \infty} \frac{\Delta E_{ij}}{E_i} = \lim_{N_i \to \infty} \frac{N_{ij}}{N_i} \qquad [11.16]$$

where $N_i$ equals the number of emitted rays and $N_{ij}$ the number of rays emitted by facet $i$ and absorbed by facet $j$. These relations are valid both for the entire spectrum and per wavelength band. In this definition, we have implicitly assumed the use of the collision-based ray-tracing method, which is further described in the following.

In a collision-based Monte Carlo ray-tracing method, we loop over all the facets of the model, and for every facet the following actions are performed:

1) The total number of emitted rays $N_i$ is determined.

2) Four vectors of independent random numbers $[\mathbf{R_x}, \mathbf{R_y}, \mathbf{R_\Psi}, \mathbf{R}_\theta]$, with a uniform distribution, are generated.

3) A ray $\Delta E_i$ is launched from a random initial position $[R_x, R_y]$ and random direction $[R_\Psi, R_\theta]$.

4) The ray is traced through the model until it is intercepted by a facet $j$, after which a new random number $[R_\rho]$ is generated to decide if:

i) the ray is specularly reflected, after which the ray is traced further through the structure,

ii) the ray is absorbed by the facet and counted as $\Delta E_{ij}$, or more directly as a contribution of $N_{ij}$, after which a new ray will be launched by facet $i$.

5) The ray is continued until it is finally absorbed by a facet, or absorbed by the environment.

6) After all rays of facet $i$ have been launched, the next $i + 1$ facet will be treated until all facets have launched their rays.

The random numbers can be generated using random number generators. These generators are numerical algorithms that will generate a (deterministic) sequence of numbers that has specific statistical properties. The random numbers that will be used here will have a uniform random distribution, and all sequences are independent. To launch a ray, a position has to be determined. For a finite element (facet), the position can be easily obtained for the case of an isothermal surface with constant emissivity (see [MOD 03]). The natural coordinates of the finite element facet can now be simply obtained by the following expression:

$$\xi = 2R_x - 1 \quad \eta = 2R_y - 1 \qquad [11.17]$$

where the uniform random numbers $0 \leq R \leq 1$ are transformed into the natural coordinate $-1 \leq \xi, \eta \leq 1$. The actual coordinate of the origin of the ray can now be obtained by using the finite element shape functions (see equation [11.53]) and the coordinates of the facets corner nodes.

$$x = \sum_i N_i(\xi, \eta) X_i \quad y = \sum_i N_i(\xi, \eta) Y_i \qquad [11.18]$$

Once the position of the emission point has been determined, the direction of the ray has to be obtained with the help of the two directional random numbers $[R_\psi, R_\theta]$. The angles $\psi$ and $\theta$ are defined in Figure 11.3 and are respectively the angle in the plane of the facet and the angle with respect to the normal of the facet. Here, again the assumption of an isothermal facet with uniform emissivity is made, resulting in two independent angles. Because all the in-plane directions of emission are equally probable, the in-plane angle $\Psi$ is obtained by simply multiplying the random number by $2\pi$:

$$\Psi = 2\pi R_\Psi \qquad [11.19]$$

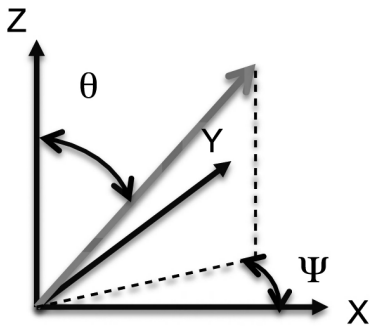


**Figure 11.3.** *Direction of emission of the ray*

For the $\theta$ angle, the situation is slightly more complicated. In case of a diffuse emitter, the radiation intensity $I$ is direction independent, but the emitted energy $E$ follows *Lambert's law*, which states

$$E^{\lambda} = I^{\lambda} \cos(\theta) \qquad [11.20]$$

From the above assumptions, the expression for $\theta$ can be derived, as shown in [MOD 03] and [HOW 11].

$$\theta = \sin^{-1}(\sqrt{R_{\theta}}) \qquad [11.21]$$

Now that both the emission point and direction are known, the ray can be traced through the model. In Figure 11.4, we consider a two-dimensional (2D) model together with a uniform so-called *voxel* distribution. The voxels are not absolutely necessary for the functioning of the ray-tracing method, but are instrumental in decreasing the cost of the algorithm. Every voxel will have a list of finite element facets that are geometrically situated inside. Besides the emission point, the emission voxel will also be determined.

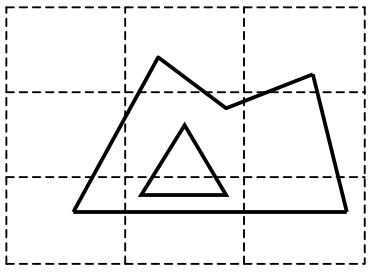

**Figure 11.4.** *Two-dimensional (2D) model plus voxel distribution*

Within this voxel, all the facets are tested to see if they intersect with the ray. If this is not the case, the ray is traced until the next voxel, where again it is tried to find

the intersection between the ray and all the facets within the voxel. This algorithm is continued until an intersecting facet is found.

Now that the intersection between the ray and a facet is found, the next action has to be decided. Will the ray be absorbed by the facet or will it be reflected. Since we consider only two types of view factors in this chapter, namely diffuse or specular view factors (diffuse and specular reflection), the reflection that will take place will only be specular (no diffuse reflection because the energy balance formulation chosen includes the diffuse reflection contribution). To decide what to do next, a random number $0 \leq R_\rho \leq 1$ will be generated, and a choice will be made depending on the value of $R_\rho$. The $R_\rho$ values are split into three subdomains, the first represents the absorption, the second the diffuse reflection, and the third the specular reflection.

$$R_\rho = [[0, \ldots, \alpha[, [\alpha, \ldots, \alpha + \rho^d[, [\alpha + \rho^d, \ldots, \alpha + \rho^d + \rho^s]] \quad [11.22]$$

If $R < \alpha$, the ray will be absorbed, while if $R \geq \alpha + \rho^d$ the ray will be specularly reflected. Whenever a ray is absorbed, its contribution is added to the $N_{ij}$ value. Owing to this discrete nature of tracing the energy parcels through the model, the method gets its name of collision-based ray-tracing method. Once all the rays have been launched and traced through the model, the view factor can be calculated:

$$F^*_{ij} = \frac{N_{ij}}{N_i} \quad [11.23]$$

In case of diffuse reflection, the $F^*_{ij}$ view factor is identical to the diffuse view factor $F_{ij}$. However, when the (partially) specular facets are included in the model, the specular view factor is defined as:

$$F^s_{ij} = \frac{1}{1 - {}^s\rho_j} F^*_{ij} = \frac{1}{1 - {}^s\rho_j} \frac{N_{ij}}{N_i} \quad [11.24]$$

which reduces to the diffuse view factor in case of a diffuse facet ${}^s\rho_j = 0$.

After calculating all the view factors, a final step needs to be performed, namely applying reciprocity and reclosure. The reciprocity of the view factors is expressed by:

$$A_i F^s_{ij} = A_j F^s_{ji} \quad [11.25]$$

or in a slightly more appropriate form for reciprocity calculations:

$$(1 - {}^s\rho_i) A_i F^*_{ij} = (1 - {}^s\rho_j) A_j F^*_{ji} \quad [11.26]$$

To impose reciprocity, several methods exist and descriptions are given in [ZEE 02, TAY 95]. A rather straightforward method proposed by [MAS 10] is an iterative method that uses the following estimator from [ZEE 02]:

$$\overline{F}^*_{ij} = \frac{1}{(1 - {}^s\rho_i) A_i} \frac{b - \sqrt{b^2 - 4ac}}{2a} \quad [11.27]$$

The values of $a$,$b$, and $c$ are defined by:

$$\begin{aligned} a &= N_i + N_j \\ b &= (1 - {}^s\rho_i)A_i(N_{ij} + N_j) + (1 - {}^s\rho_j)A_j(N_{ji} + N_i) \\ c &= (1 - {}^s\rho_i)(1 - {}^s\rho_j)A_iA_j(N_{ij} + N_{ji}) \end{aligned} \quad [11.28]$$

Once the reciprocity has been applied, the cavity has to be reclosed, i.e. no rays can leave the cavity. This requirement can be expressed by the following expression:

$$\sum_{j=1}^{N}(1 - {}^s\rho_j^{\lambda})F_{ij}^s = 1 \quad [11.29]$$

This relation together with the reciprocity is iteratively applied. First the reciprocity is applied, after which the sum of all the view factors (as defined above) is calculated. If this value is not equal to one, all the view factors with the same index $i$ will be divided by the calculated value. After this step, the reciprocity relation is applied and the sum of the view factors is again calculated. This algorithm is applied iteratively until the relative closure error is smaller than a user-defined value.

In case a solar flux is applied to the structure, the solar rays will be traced through the structure in the same way as the view factor rays, but in this case every ray has an energy content that will be directly applied to the (conductive) facet where it is finally absorbed.

## 11.3. Thermal balance equations

Because we are interested in solving general thermal problems including conduction, we describe both the conductive thermal balance and the radiation thermal balance equations.

### 11.3.1. *Conductive thermal balance*

The conductive thermal balance equation can be obtained by performing a heat flow balance for a control volume. The balance is between the incoming/outgoing conductive flux and the internal energy of the body. The derivation of this balance equation can be found in many standard works on thermal analysis [ÖZI 85] and also in standard finite element books [BAT 96], and will not be repeated here, but only the end result will be given.

$$\rho c\frac{\partial T}{\partial t} = \nabla.(\lambda\nabla T) \quad [11.30]$$

where $c$ is the capacity, $\rho$ the density, and $\lambda$ the conductivity. The constitutive equation is given by Fourier's law:

$$\overline{q}_c = -\lambda\nabla T \quad [11.31]$$

where $\overline{q}_c$ is the conductive heat flux and the minus sign is due to the fact that heat flows from higher to lower temperatures.

To complete the definition of a transient thermal problem, the initial conditions (temperature at time zero) and the boundary conditions need to be defined. The boundary conditions can be either imposed temperatures or imposed heat flux, where the heat flux can take different forms. The heat flux can be a convection, a simple flux, or a radiation with an environment at a given temperature $T_r$. If we look at the simple case of gray radiation, a body will emit a radiation flux depending on its temperature. If we assume that the body radiates to a blackbody, all the emitted radiation will be absorbed by this blackbody. The blackbody will emit $\sigma T_r^4$ but only a fraction $\alpha$ will be absorbed by the structure:

$$q_{\text{emitted}} = -\varepsilon\sigma T_i^4 \quad q_{\text{absorbed}} = \alpha\sigma T_r^4 \qquad [11.32]$$

Also, the assumption is made that the body can only see the environment at temperature $T_r$, thus the view factor equals one. If we now use Kirchhoff's law, we can write the radiation balance on the outer surface as:

$$\overline{q}_c.\overline{n} = \sigma\varepsilon\left[T_r^4 - T_i^4\right] \qquad [11.33]$$

where the applied radiation flux (positive when applied to the body) will be in equilibrium with the (perpendicular component) conductive flux at the boundary.

### 11.3.2. *Radiation thermal balance*

In this section, the radiation balance equations are derived for the radiation exchange between opaque facets with a non-participating medium between them. The balance equations will be valid for a closed cavity, i.e. a cavity where every facet can only see other (participating) facets. This assumption will let us use the closure relation in the derivation of the equations. This assumption of closure is not very restrictive, because any cavity can be closed by including the environment into the radiation balance (outer space as a blackbody, with $F_{is} = 1 - \sum_j F_{ij}$).

The radiation exchange takes place at the speed of light; therefore, it is not necessary to take any time dependence into account for engineering structures (small dimensions, small time delays). The heat balance equations are derived for a given wavelength $\lambda$, with the thermo-optical properties ($\alpha^\lambda, \varepsilon^\lambda, {}^d\rho^\lambda, {}^s\rho^\lambda$) depending on wavelength.

If we look at the radiation exchange of an opaque surface in Figure 11.5, we see that *emission* of the surface can be split into two components. The first is a specular component, which models the specular reflection of the incident radiation (from the other facets). The second component consists of two components, namely the diffusely

reflected flux and the emitted flux. The diffuse component can be defined by the following expression, and is called the radiosity $R_i^\lambda$ of facet $i$:

$$R_i^\lambda = E_i^\lambda + {}^d\rho_i^\lambda H_i^\lambda \quad [11.34]$$

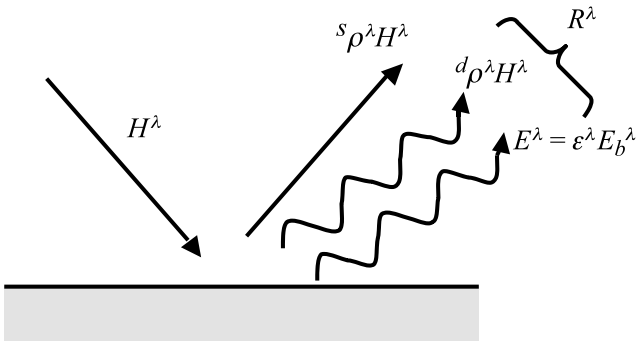


**Figure 11.5.** *Radiation balance at an opaque surface*

The incident heat flux $H_i^\lambda$ on facet $i$ consists of the sum of all emitted heat fluxes. This can be expressed as a sum of all the emitted powers $R_j^\lambda.A_j$ of facets $j$ multiplied by the view factors from facet $j$ toward $i$:

$$H_i^\lambda = \frac{\sum_{j=1}^{N} R_j^\lambda A_j{}^\lambda F_{ji}^s}{A_i} \quad [11.35]$$

This relation can be simplified by using the reciprocity relation for view factors:

$$A_i{}^\lambda F_{ij}^s = A_j{}^\lambda F_{ji}^s \quad [11.36]$$

which yields

$$H_i^\lambda = \sum_{j=1}^{N} R_j^{\lambda\lambda} F_{ij}^s \quad [11.37]$$

The radiation balance can now be expressed in two different ways. First, with the help of Figure 11.5 we can write the resultant heat flux $q_i^\lambda$ for facet $i$ as the resultant of the incident flux minus the diffuse and specular component.

$$\begin{aligned} q_i^\lambda &= H_i^\lambda - R_i^\lambda - {}^s\rho_i^\lambda H_i^\lambda \\ &= (1 - {}^s\rho_i^\lambda) H_i^\lambda - R_i^\lambda \end{aligned} \quad [11.38]$$

With the previously derived expression for $H_i^\lambda$, we now obtain:

$$q_i^\lambda = (1 - {}^s\rho_i^\lambda) \sum_{j=1}^{N} R_j^{\lambda\lambda} F_{ij}^s - R_i^\lambda \quad [11.39]$$

Introducing the closure relation for specular view factors:

$$\sum_{j=1}^{N}(1-{}^{s}\rho_j^{\lambda})^{\lambda}F_{ij}^{s}=1 \qquad [11.40]$$

yields the final expression for the heat balance for facet $i$, which only depends on the radiosities of all the facets of the model:

$$q_i^{\lambda}=\sum_{j=1}^{N}{}^{\lambda}F_{ij}^{s}\left[(1-{}^{s}\rho_i^{\lambda})R_j^{\lambda}-(1-{}^{s}\rho_j^{\lambda})R_i^{\lambda}\right] \qquad [11.41]$$

The second way to express the resultant heat flux $q_i^{\lambda}$ for facet $i$ is given in the following equation, where the difference between the absorbed flux and the emitted flux is taken:

$$q_i^{\lambda}=\alpha_i^{\lambda}H_i^{\lambda}-E_i^{\lambda} \qquad [11.42]$$

Here, the resultant flux is rewritten in such a way that the final expression will be expressed as a function of the facet emitted flux and its radiosity. For this, equations [11.34] and [11.3] are used:

$$q_i^{\lambda}=\alpha_i^{\lambda}\frac{R_i^{\lambda}-E_i^{\lambda}}{{}^{d}\rho_i^{\lambda}}-E_i^{\lambda}=\frac{1-{}^{s}\rho_i^{\lambda}}{{}^{d}\rho_i^{\lambda}}\left(\frac{\alpha_i^{\lambda}R_i^{\lambda}}{1-{}^{s}\rho_i^{\lambda}}-E_i^{\lambda}\right) \qquad [11.43]$$

We now have two equations for the resultant heat flux on facet $i$, one expressed as a function of all the facets radiosities and the other as a function of the local emitted flux and radiosity. With these two results, we can write the thermal balance for a facet relating one facet $i$ with all the other facets $j$, by simply equating the two expressions:

$$\sum_{j=1}^{N}{}^{\lambda}F_{ij}^{s}\left[(1-{}^{s}\rho_i^{\lambda})R_j^{\lambda}-(1-{}^{s}\rho_j^{\lambda})R_i^{\lambda}\right]=\frac{1-{}^{s}\rho_i^{\lambda}}{{}^{d}\rho_i^{\lambda}}\left(\frac{\varepsilon_i^{\lambda}R_i^{\lambda}}{1-{}^{s}\rho_i^{\lambda}}-E_i^{\lambda}\right) \qquad [11.44]$$

For this equation, the boundary conditions are the imposed values of the emitted energy $E_i$ of the facets of the cavity or, stated differently, the imposed temperatures of the cavity facets. In the next section, we will see that this is not really a limitation and that the temperature of the facets can become unknowns of the problem. The above balance equates the heat flux, which can be transformed into the following expression for the power:

$$\sum_{j=1}^{N}(1-{}^{s}\rho_i^{\lambda})(1-{}^{s}\rho_j^{\lambda})A_i{}^{\lambda}F_{ij}^{s}\left[\frac{R_j^{\lambda}}{1-{}^{s}\rho_j^{\lambda}}-\frac{R_i^{\lambda}}{1-{}^{s}\rho_i^{\lambda}}\right]$$
$$=\frac{(1-{}^{s}\rho_i^{\lambda})A_i}{{}^{d}\rho_i^{\lambda}}\left(\frac{\varepsilon_i^{\lambda}R_i^{\lambda}}{1-{}^{s}\rho_i^{\lambda}}-E_i^{\lambda}\right) \qquad [11.45]$$

There is no difference in principle between the two aforementioned equations, but the latter is retained for practical computer implementations. This is due to the fact that in that case we only need to store the symmetric view-factor matrix $A_i F_{ij}^s$, instead of the non-symmetric $F_{ij}^s$ matrix.

The equations derived so far are valid for any wavelength $\lambda$, where all the thermo-optical properties can vary continuously over the wavelength domain. Trying to solve the above equations in this form proves intractable and additional assumptions are needed. Two additional assumptions are discussed in the following subsections, namely the gray approximation and the multiband approximation.

11.3.2.1. *Gray approximation*

For the gray approximation, we assume that the thermo-optical properties do not depend on wavelength $\lambda$, and are unique values for the entire wavelength domain. With this assumption, the emitted heat $E_i$ flux of facet $i$ can be obtained via the following integral:

$$E_i = \int_0^\infty \varepsilon_i^\lambda E_b^\lambda(\lambda, T)\, d\lambda = \varepsilon_i E_b = \varepsilon_i \sigma T_i^4 \qquad [11.46]$$

If we substitute the above expression for a gray (diffuse) emitter into the radiation heat balance equation, we obtain:

$$\sum_{j=1}^{N} (1 - {}^s\rho_i)(1 - {}^s\rho_j) A_i F_{ij}^s \left[ \frac{R_j}{1 - {}^s\rho_j} - \frac{R_i}{1 - {}^s\rho_i} \right] = \frac{(1 - {}^s\rho_i) A_i}{{}^d\rho_i} \left( \frac{\varepsilon_i R_i}{1 - {}^s\rho_i} - \varepsilon_i \sigma T_i^4 \right) \qquad [11.47]$$

where we see that the facet temperature $T_i$ appears explicitly in the equation. This temperature will be one of the unknowns in a finite element model. Because the thermo-optical properties are constant, the view factors do not have to be calculated as a function of $\lambda$.

11.3.2.2. *Non-gray (multiband) solution*

Again an assumption has to be made about the variation of the thermo-optical properties with $\lambda$. The assumption of the multiband approximation is that the thermo-optical properties are constant for different bands of wavelengths. Therefore, the emitted energy of a facet $i$ is again integrated over the entire spectrum, with constant emissivities $\varepsilon_i^k$ for wavelength band $k$ and facet $i$. Thus, the emitted flux of facet $i$ for wavelength band $k$ can be expressed by:

$$E_i^k = E^{\lambda_{k+1} - \lambda_k} = \int_{\lambda_k}^{\lambda_{k+1}} \varepsilon_i^\lambda E_b^\lambda(\lambda, T)\, d\lambda = \varepsilon_i^k \left[ f(\lambda_{k+1} T) - f(\lambda_k T) \right] \sigma T_i^4 \qquad [11.48]$$

Integrating Planck's function [11.1] from $\lambda_k$ to $\lambda_{k+1}$ yields a fraction of the blackbody emissive power that depends on the wavelengths $\lambda_{k,k+1}$ and the facet temperature $T_i$. The integrals

$$f(\lambda T) = \int_0^{\lambda} E_b^{\lambda}(\lambda, T)\, d\lambda \qquad [11.49]$$

can be found in tabulated form in books like [HOW 11] and [MOD 03]. To carry out the complete integral over the entire spectrum, we have to replace the $\lambda$ superscript by the $k$ wavelength band identifier. Also, a sum over all the wavelength bands needs to be performed. Because of the use of the blackbody emissive power function $f(\lambda T)$, the sum of the emitted heat flux per band remains equal to the total emitted heat flux. The solution of the radiation problem $R_i^k$ depends on the imposed boundary conditions $E_i^k$.

$$\sum_{k=1}^{m}\left[\sum_{j=1}^{N}(1-{}^{s}\rho_i^k)(1-{}^{s}\rho_j^k){A_i}^{k}F_{ij}^{s}\left[\frac{R_j^k}{1-{}^{s}\rho_j^k}-\frac{R_i^k}{1-{}^{s}\rho_i^k}\right]\right]$$
$$=\sum_{k=1}^{m}\left[\frac{(1-{}^{s}\rho_i^k)A_i}{{}^{d}\rho_i^k}\left(\frac{\varepsilon_i^k R_i^k}{1-{}^{s}\rho_i^k}-\varepsilon_i^k\left[f(\lambda_{k+1}T)-f(\lambda_k T)\right]\sigma T_i^4\right)\right] \qquad [11.50]$$

The boundaries are correctly weighed depending on the number of bands, and thus so is the solution of $R_i^k$. Contrary to the gray approximation, here we will have to calculate the view factors for different wavelength bands. Only in the case of diffuse reflection do all the wavelength bands have the same view factors.

A special and important case of the multiband approximation is the two-band approximation. This is very useful in the application of satellites. When a satellite is in orbit around the Earth, it radiates in the longwave infrared field, while it is loaded by the solar flux in the visible (shortwave) wavelength. It is from this two-band approximation case that the nomenclature of infrared emissivity and solar absorptivity is derived, and makes sense without violating Kirchhoff's law.

## 11.4. Finite element formulation

To solve the coupled radiation-conduction problem, the finite element method is used. This method is described in great detail in many standard textbooks by Bathe or Zienkiewicz [BAT 96, ZIE 89], and only some points specific to our problem are highlighted here. The general approach of the method is that any continuum problem is split up into finite elements where all the equations are expressed as a function of the nodal degrees of freedom. To obtain the finite element equations, we discretize the continuum problem differential equation via Galerkin's method, and for the radiation problem we simply introduce the appropriate nodal degrees of freedom.

Because of the nonlinear nature of the radiation problem, a nonlinear solution method needs to be applied. Here we concentrate on a steady-state problem, but the formulation can be easily extended to a transient problem by including the capacity of the conductive elements. The general nonlinear problem can be written simply as:

$$\overline{F}(T) = F^{int}(T) - F^{ext}(T) = 0 \qquad [11.51]$$

where $F^{int}$ signifies the internal power vector and $F^{ext}$ the external power vector. The first vector includes the contribution of the elements themselves (conductive or radiative), and the second vector contains contributions of the external boundary conditions (applied flux, convection, etc.). This problem can be solved by Newton's method, to obtain the nodal temperatures:

$$\left|\frac{\partial \overline{F}}{\partial T}\right| . |\Delta T| = - |R| \qquad [11.52]$$

where $R$ is the residue that needs to go to zero and $\Delta T$ the temperature correction.

For the conductive problem, we have to define a finite element discretization with the appropriate shape functions. If we take, for example, a four-node membrane element, the four shape functions attached to the four nodes are:

$$N_1(\xi,\eta) = \frac{1}{4}(1-\xi)(1-\eta) \quad N_2(\xi,\eta) = \frac{1}{4}(1+\xi)(1-\eta)$$
$$N_3(\xi,\eta) = \frac{1}{4}(1+\xi)(1+\eta) \quad N_4(\xi,\eta) = \frac{1}{4}(1-\xi)(1+\eta) \qquad [11.53]$$

where the variables $\xi$ and $\eta$ are the natural coordinates of the finite element. The relation between the natural coordinates and the physical coordinates can be obtained from any finite element textbook and given by equation [11.18]. The temperature in the element is related to the nodal temperatures via the standard relation:

$$T = \sum_i T_i N_i(\xi,\eta) \qquad [11.54]$$

The internal and external power vector for the conductive elements are expressed by the following simple integrals (see [ZIE 89, BAT 96]). For the internal power vector, we integrate the conductive flux vector $q_c$ over the volume using the $B$ matrix

$$F_i^{int} = \int B_i^T \overline{q}_c \, dV \qquad [11.55]$$

The $B$ matrix contains the spatial derivatives of the element shape functions.

$$B_i = \begin{vmatrix} \frac{\partial N_i}{\partial x} & 0 \\ 0 & \frac{\partial N_i}{\partial y} \end{vmatrix} \qquad [11.56]$$

The external power vector is obtained by integrating the boundary conditions (applied flux, convection, etc.) over the external surface, using the shape functions of the outer surface:

$$F_i^{ext} = \int N_i q_{ext}\, dS \qquad [11.57]$$

To perform the above integrals, some details need to be worked out. First of all, a relation needs to be defined between the element's natural coordinates and the physical coordinates. In addition, the element should be able to have arbitrary shapes (isoparametric deformation). For all these topics, the reader is referred to standard finite element textbooks. To perform the integrals, numerical integration rules (Gauss rules) are used.

This leads to the finite element discretization of the radiation balance equation. The radiation between two (2D) facets is given in Figure 11.6, where the two so-called radiosity nodes are introduced. These radiosity nodes model the value of the facets' radiosities. In case of a multiband approach, this node will have $k$ degrees of freedom, and every degree of freedom is the radiosity of the appropriate wavelength band. To formulate the entire problem as a thermal problem, we replace the unknown radiosity by the unknown radiosity "temperature" $T_{ai}$.

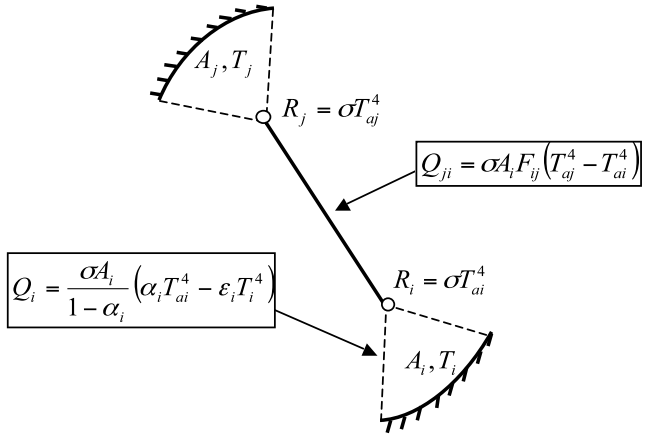


**Figure 11.6.** *Finite element discretization of the radiation balance equation*

If we now introduce the radiosity node expression into the gray approximation ($k = 1$) for diffuse reflection, we obtain a simpler form of the radiation balance equation:

$$R_j^k = \sigma^k T_{aj}^4 \qquad [11.58]$$

This simplification is only performed to facilitate the understanding of the reader, and the extension to the general case is straightforward:

$$\sum_{j=1}^{N} A_i F_{ij} \sigma \left[T_{aj}^4 - T_{ai}^4\right] = \frac{\sigma \varepsilon_i A_i}{{}^d\rho_i} \left(T_{ai}^4 - T_i^4\right) \quad [11.59]$$

The reader should note that the radiation problem of Figure 11.6 has been split into three separate finite elements: one element between the two radiosity nodes and two elements that are each between the face of a conductive element and the radiosity nodes.

The total power going through the element between the radiosity nodes depends on the unknown radiosity temperatures:

$$Q_i = A_i F_{ij} \sigma [T_{ai}^4 - T_{aj}^4] \quad [11.60]$$

The internal power vector for this element can be written in the same way as the internal force vector of a simple 1D spring element, namely

$$F^{int}(T) = \left| \begin{array}{c} Q_i \\ -Q_i \end{array} \right| \quad [11.61]$$

The expression of the "boundary" elements between the conductive facet and the radiosity node is slightly more complicated. The total power on the radiosity node has to be in equilibrium with the integrated flux over the conductive surface. Here, we therefore introduce the heat flux through this element:

$$q_i = \frac{\sigma \varepsilon_i}{{}^d\rho_i} \left(T_{ai}^4 - T_i^4\right) \quad [11.62]$$

Further, the internal power vector can now be obtained by simply integrating the heat flux over the conductive face with the appropriate shape functions.

$$F^{int}(T) = \left| \begin{array}{c} -\int q_i N_1 \, dA_i \\ -\int q_i N_2 \, dA_i \\ q_i A_i \end{array} \right| \quad [11.63]$$

For the radiation problem, the external power vector only has a contribution of the solar flux. The absorbed solar flux is calculated by the ray-tracing algorithm and added directly to the conductive facets. It can thus be added to the external power vector $F^{ext}$ of the conductive element.

Now that the element nodal power vectors are obtained for all the nodal degrees of freedom, they only need to be assembled into the global power vector according to their node numbers. To complete the Newton solution algorithm, we not only need the nodal power vectors but also their temperature derivatives. These derivatives can be obtained either analytically or by a finite difference scheme, but are not given here.

## 11.5. Example problems

As an example, the temperature distribution is calculated in a satellite-like structure, exposed to outer space and subjected to a solar heat flux. All the equations of the previous sections are implemented in the finite element program SAMCEF THERMAL, which is used here for the calculations. The outer space has a temperature of 4 K and the solar heat flux has an intensity of 1,500 $\mathrm{Wm}^{-2}$. The satellite cavity is closed by the outer space, and a view factor is calculated between all facets and the outer space ($F_{is} = 1 - \sum_j F_{ij}$). The solar heat flux comes out of the direction $\vec{v} = [\ 1\ 1\ 2\ ]$, in structural axis system as shown in Figure 11.7(a). Furthermore, the base plate of the satellite has an imposed temperature of 293 K, because it is connected with the rest of the spacecraft. The structure is given in Figure 11.7(b), where we see two distinct groups, namely a group containing the support structure and a group containing the instruments and the electronic boxes. All the objects in the satellite have a constant thickness of 5 mm, and are made of aluminum ($\lambda = 126$ W $(\mathrm{mK})^{-1}$).

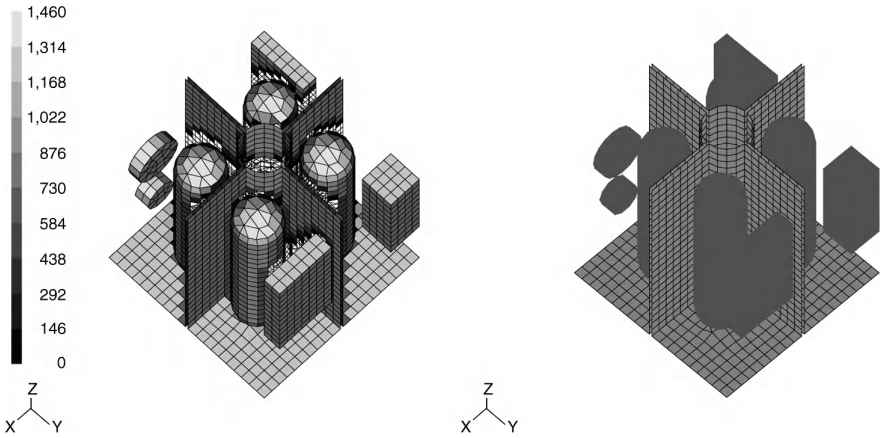


**Figure 11.7.** *(a) Incident solar heat flux, (b) group definition*

In this section, a total of four steady-state calculations of increasing complexity is performed, to show the effect of certain hypotheses on the results.

– Example 1: Gray diffuse radiation heat balance ($\lambda = 10^{-6}$ W$(\mathrm{mK})^{-1}$);

– Example 2: Gray diffuse radiation-conduction heat balance ($\lambda = 126$ W$(\mathrm{mK})^{-1}$);

– Example 3: Two-band diffuse radiation-conduction heat balance;

– Example 4: Two-band diffuse/specular radiation-conduction heat balance.

For both Examples 1 and 2, the same gray diffuse emissivity of $\varepsilon = 0.7$ is used, and the only difference is the value of the conductivity that is used in the

calculation. In Figure 11.8, we see the temperature distribution of Examples 1 and 2, respectively, and we can see the diffusion effect of the conductivity results in a more uniform temperature distribution. As a consequence, the maximum and minimum temperatures are closer together, resulting in lower thermal gradients. The effect of conductivity on the results can be multiple, but not including it will generally result in an overestimation of the thermal gradients.

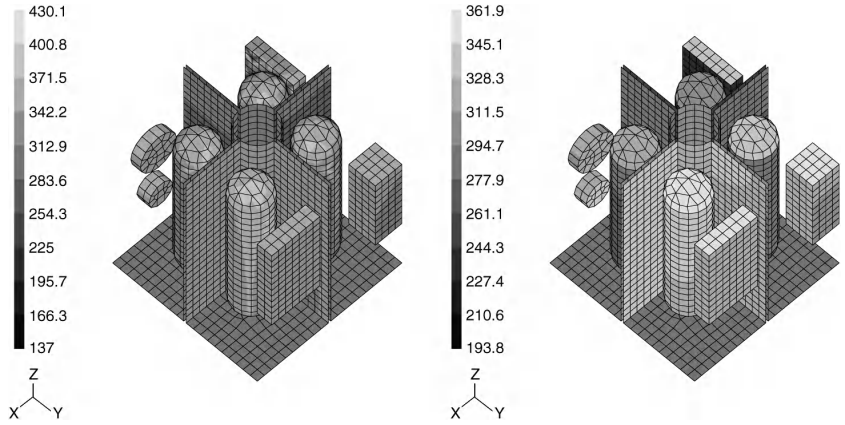


**Figure 11.8.** *Temperature distribution: (a) radiation problem, (b) radiation-conduction problem*

The calculations of Examples 3 and 4 are more complex as the gray approximation is replaced by a two-band approximation. For space applications, the two-band approximation is indispensable because the radiation inside the satellite takes place in the infrared (due to the low temperatures), while the main heat source is the solar heat flux. The energy content of the solar heat flux is mainly situated in the visible domain. Because of this, a two-band approximation with the possibility of different thermo-optical properties per wavelength band is necessary. The two wavelength bands are defined as band 1 from 0 μm till 4 μm, which models the ultraviolet and visible domain, and band 2, which extends from 4 μm until infinity to model the infrared part of the spectrum.

In Example 3, for the support structure, we use the diffuse emissivity of $\varepsilon = 0.7$ for both wavelength bands (gray approximation). For the instruments and electronic boxes, a paint is applied to the surface that has an infrared emissivity $\varepsilon = 0.7$ and a visible diffuse reflectivity of ${}^{d}\rho = 0.5$. This results in a solar absorptivity (in the visible domain) of $\alpha = \varepsilon = 1 - {}^{d}\rho = 0.5$, which is not equal to the infrared emissivity. A paint with a reduced solar absorptivity was applied to reduce the absorption of the solar heat flux, and to reduce the maximum temperature of the satellite. When we compare the temperature distribution of Example 2 (Figure 11.8(b)) and Example 3 (Figure 11.9(a)), we can see that not only the temperature distribution has changed, but

also more importantly the maximum temperature has decreased around 30 K. From this, we can see that for space applications the choice of thermo-optical properties is an important tool to regulate the temperature. In Example 4, we add specularity in the view factor definition. We thus again change the thermo-optical properties, but this time to the detriment of the satellite. The support structure retains the infrared emissivity $\varepsilon = 0.7$, while the visible properties change to ${}^{d}\rho = 0.1$ and ${}^{s}\rho = 0.2$ resulting in a visible emissivity of $\varepsilon = 1 - {}^{d}\rho - {}^{s}\rho = 0.7$. When we compare the temperature distributions of Examples 3 and 4 in Figure 11.9, we see that the minimum and maximum temperatures have hardly changed. However, what has changed is the maximum temperature of the cylindrical instrument. This is due to the fact that the support structure behind the cylindrical instrument acts as a partial mirror (${}^{s}\rho = 0.2$) in the visible domain, i.e. part of the solar heat flux is reflected off the support structure onto the cylindrical instrument, and thus increases its temperature.

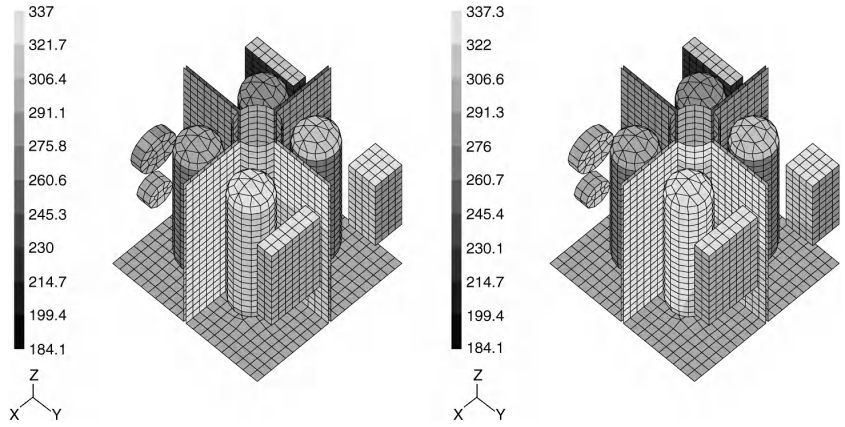


**Figure 11.9.** *Temperature distribution: (a) two-band diffuse model, (b) two-band diffuse-specular model*

The examples shown here were only steady state, while for real satellite applications transient calculations are performed. For the transient calculation, the maximum and minimum temperatures are not allowed to surpass certain values during the lifetime of the satellite. Additionally, active controls can be used to regulate the temperature of the satellite. Nevertheless, choosing the thermo-optical properties (via the application of paint, for example) is an important tool for the thermal control of a satellite. The aforementioned examples are, therefore, certainly instructive of real satellite applications.

## 11.6. Bibliography

[BAT 96] BATHE K.J., *Finite Element Procedures*, Prentice Hall, 1996.

[HOW 11] HOWELL J.R., SIEGEL R., MENGÜÇ M.P., *Thermal Radiation Heat Transfer*, CRC Press, 5th ed., 2011.

[MAS 10] MASSET L., Iterative reciprocity and closure for view factors, Personal communications, 2010.

[MOD 03] MODEST M.F., *Radiative Heat Tranfer*, Academic Press, 2nd ed., 2003.

[ÖZI 85] ÖZIŞIK M.N., *Heat Transfer A Basic Approach*, McGraw-Hill International Editions, 1985.

[TAY 95] TAYLOR R., LUCK R., "Comparison of reciprocity and closure enforcement methods for radiation view factors", *Journal of Thermophysics and Heat Transfer*, vol. 9, no. 4, pp. 660–666, 1995.

[ZEE 02] ZEEB C.N., Performance and accuracy enhancements of radiative heat transfer modelling via Monte Carlo, PhD Thesis, Colorado State University, Fort Collins, CO, 2002.

[ZIE 89] ZIENKIEWICZ O., TAYLOR R., *The Finite Element Method*, McGraw-Hill Book Company, 4th ed., 1989.

# Chapter 12

# Dense Cities in the Tropical Zone

## 12.1. Introduction

A well-known conversation between a scientist and a high-ranking government officer goes like this:

*Scientist*: it is therefore important that we design the buildings in our city properly so that people can still enjoy the availability of diminishing daylight.

*Officer*: Tell me, without daylight, will people die?

*Scientist*: No, they won't die, at least not in the term of one's office. However, with respect, the consequences of one not dying may be worse.

*Officer*: Interesting, maybe somebody needs to do something then.

(post meeting note: 6 months later, new building regulations were implemented.)

The conversations aptly sum up the state of affairs of many high-density megacities – most of them are now springing up in the Asia-Pacific rim. Many government officials face key questions such as, how dense can we go? What could happen if we go beyond the threshold? How can we balance the need for urbanization and the wishes for a quality of life environment? The irony is that there is currently no textbook to rely on and no example to follow. The so-called high-density city morphologies of all the European and American cities are simply too low to be of any reference. There is a need for new understanding, new methods,

Chapter written by Edward NG.

*Solar Energy at Urban Scale* Benoit Beckers

and new guidelines. In short, nothing short of a paradigm shift may be necessary to tackle the issue at hand.

**Figure 12.1.** *The cityscape of Hong Kong: closely packed buildings with high H/W ratio in the city can seriously limit the available daylight and solar access to indoor and outdoor spaces*

The issue of dealing with density from the planning perspective is not new. Taylor's Manhattan gridiron plan in 1796 and Haussman's Paris plan in 1850 can be regarded as two attempts. There are quite a number of high-density megacities in the tropical and subtropical zone in the Asia-Pacific region: Hong Kong, Guangzhou, Singapore, Taipei, Bangkok, Manila, Kuala Lumpur, Jakarta, to name but a few. These cities have urban densities of 100,000 person per kilometer, or above. A quick calculation based on 50% buildable per land area, 50% of residential per total built volume, and 25 $m^2$ per person of living space will give a land development plot ratio of 10. With this kind of site plot ratio, the building height to street width ratio (H/W) will be in the order of 2 to 3 to 1, or higher. We have very few references in the literature that cope with this kind of living density at the city scale.

Buildings that are closely packed receive diminished daylight and solar access potentials. This is a known factor, but that which is less known is the degree of impact it has on the human lives. How should we quantify the needs? for what? to whom? and when? These are just a few of the biophysiologically related questions we need to answer. Without proper impact assessment, any cry to politicians for a better living environment will go unnoticed.

The understanding between the sky and the living condition on ground for human habitation can be best summarized as (1) the need to perceive the sky, (2) the

need for daylight, and (3) the need for solar access, both for open spaces and for indoor spaces. This chapter elaborates on them one by one.

## 12.2. Access to the sky

Density denotes the proportional amount of units of certain phenomena in a defined volume in time and space. It is a measure of "some quantity per unit measure". Density is synonymous with "intensity"; intensity is perceived. Clever design can sometimes disguise the perceived intensity and hence reduce the impact of density [MAR 73, RAP 75, UNW 12]. Rapoport also argues that low perceived density is a pre-requisite of high-quality living [RAP 77]. The perception of spaciousness (lower density) can be related to the experienced sky view [FIS 03]. Psychologically, we feel less density when we have better access to nature – typically, this means access to the sky [RAT 02]. Sky view factor (SVF) is a scientific way to quantify it.

Fisher-Gewirtzman *et al*. [FIS 03] have suggested that the relations between density and living quality should be established based on "morphological perceptual criteria". SVF, often denoted by $\psi_{sky}$, indicates the ratio of the sky unobstructed by a planar surface from the sky to the entire hemispheric sky [WAT 87].

$$\psi_{sky} \frac{1}{\pi R^2} \int_{S_v} \cos \Phi dS \qquad [12.1]$$

With a three-dimensional (3D) GIS-based dataset, and employing an ArcGIS-embedded computer program, the point SVF values for an entire urban environment can be generated [CHE 10] (Figure 12.2). For a point Po, as discussed in section 2.1.4, the algorithm divides the hemisphere with radius $R$ into equal slices by a rotation angle $\alpha$ and searches for a pixel Pi with the largest elevation angle $\beta$ along a particular direction. $\beta$ is determined by $\tan^{-1}$ ($h$(Pi)/$r$), where $h$(Pi) is the height difference between Pi and Po, and $r$ is the distance from Pi to Po. In case Pi is found, the surface $S$, which is a slice of an enclosed basin, is considered to be obstructed. The view factor of S is VF($S$) = (1 − cos2 $\beta$) ($\alpha$/360) = sin2 $\beta$ ·($\alpha$/360), so the SVF of Po can be calculated by summing up the VF($S$) for all the directions and subtracting the sum from unity

An SVF plot of a dense area in Hong Kong is plotted. Sky views of narrow streets are in the order of 0.3, meaning that most of the sky vault is obstructed (Figure 12.3). An example of the sky view obstruction of an urban space surrounded by tall buildings, using Ecotect, is illustrated in Figure 12.4. In this case, the SVF is around 0.5.

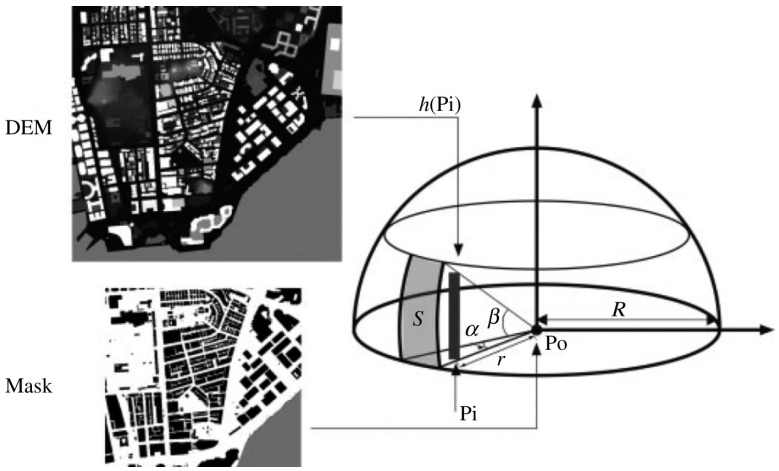


**Figure 12.2.** *Illustration of the algorithm for calculating SVF. The mask layer defines the pixels whose SVFs are to be calculated (Po) and the DEM layer stores height information of the urban surface [h(Pi)]. α is the rotation angle and R is the searching radius. Pi is the pixel with the largest elevation angle β along a certain direction. Surface S is the segment of the sky obstructed by Pi*

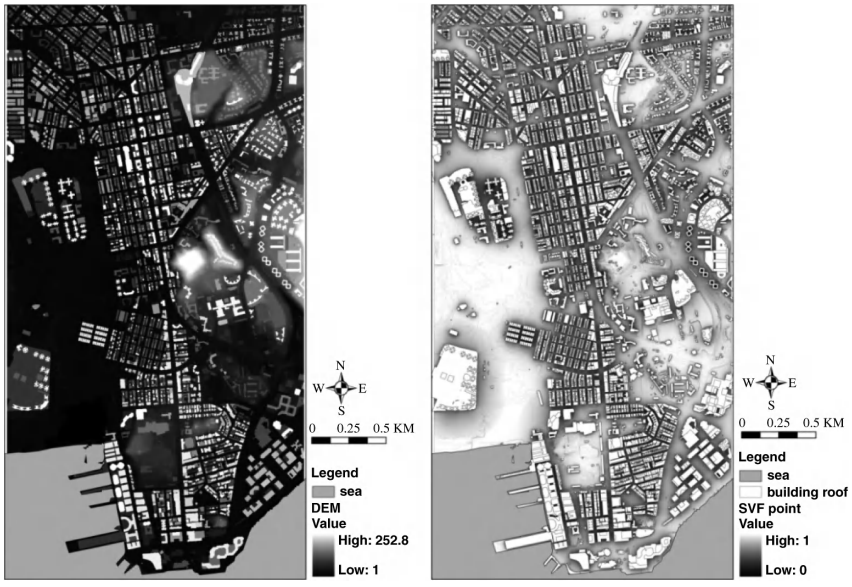


**Figure 12.3.** *An SVF plot of an urban area in Hong Kong. Note the low SVF of narrow streets due to high H/W ratio. The density (plot ratio) of the area is around 5–8*

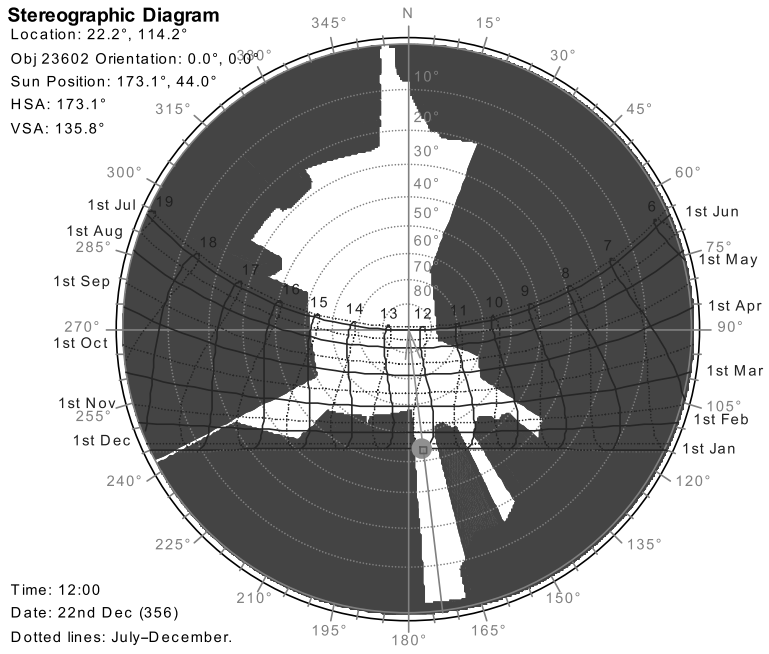


**Figure 12.4.** *The sky view of an open space (measured 80 m × 80 m) in urban Hong Kong. Low SVF of 0.5 can be reported. This is due to the very tall buildings, nearly 9 (around 100–150 m), around the site. The lack of sky view means higher density perceived*

Urban SVF can be further understood by plotting the SVF against the ground cover, an indication of urban spaciousness, and the building volume (BV) density, an indication of physical built density. Figure 12.5 illustrates (from left to right) the point SVF, the ground coverage (GC), and the BV of an urban area in Hong Kong. The relationships between SVF and GC and between SVF and BV are plotted in Figures 12.6 and 12.7.

However, on the other hand, the relationship between SVF and BV is not that obvious. Areas A4B6, A1B6 and A2B7 have high BV and high SVF, whereas areas A1B1, A3B8, A2B2 and A2B3 have lower SVF with high BV. The difference is in the order of 0.3 SVF. Examine the map in Figure 12.5, it is obvious that areas A1B6 and A2B7 have tall buildings and low GC. A2B2 and A2B3 have tall buildings and high GC. That is to say, it is possible to design the city morphologically speaking to maintain the high BV and at the same time maintain a higher SVF – and hence lower the perceived density. It seems that the way to do this is to optimize GC.

In general, based on Figure 12.6, SVF and GC are inversely (weakly) related. Higher GC can lead to lower SVF. A number of urban morphological cases,

e.g. A2B2 and A1B1 with high GC and low SVF, are worth noting. They both have narrow streets and little open space. On the other hand, A4B6 with high GC and yet high SVF have spaced out tall towers on a podium. The difference between the worst- and best-case SVF scenarios given the same GC can be doubled indicating the importance to optimizing the design of building morphology.

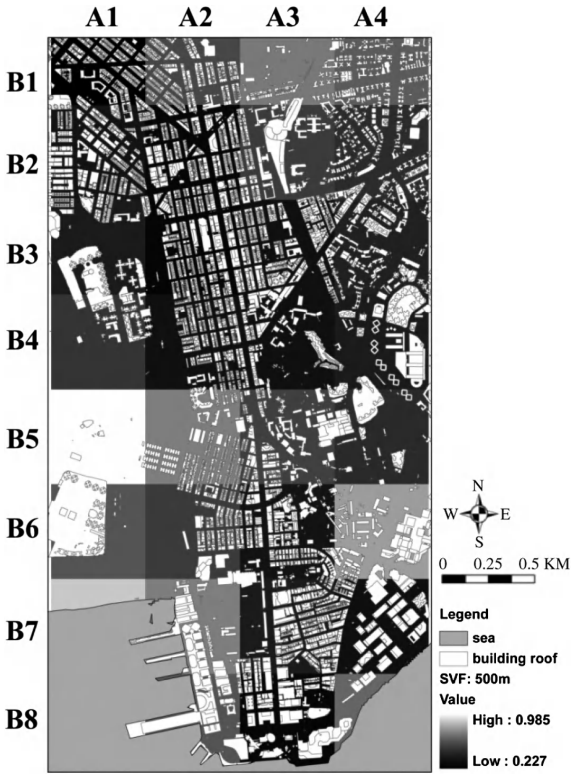


**Figure 12.5.** *SVF of an urban area in Hong Kong. Value area averaged and gridded at 500 m × 500 m*

Furthermore, in general, based on Figure 12.7, SVF and BV are inversely (weakly) related. Higher BV can lead to lower SVF. A number of urban morphological cases, e.g. A2B3 and A2B2 with high GC and low SVF, are worth noting. They both have narrow streets and little open space and with tall towers. On the other hand, A2B7 with high BV and yet high SVF have tall towers but with large open spaces. The difference between the worst- and best-case SVF scenarios given the same BV can be more than doubled indicating again the importance to optimize the design of building morphology.

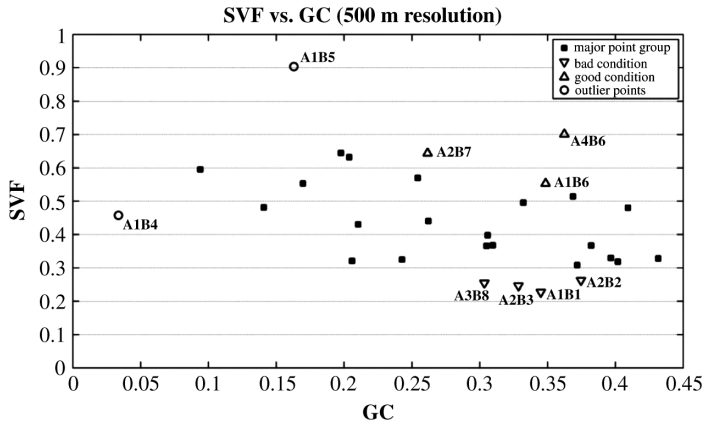


**Figure 12.6.** *SVF versus ground coverage (GC) on a 500 m × 500 m area average basis*

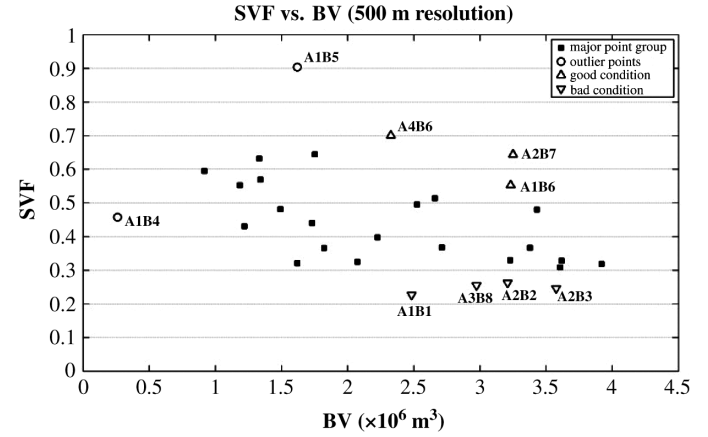


**Figure 12.7.** *SVF versus building volume (BV) on a 500 m × 500 m area average basis. Samples with low SVF and high BV, as well as high SVF and high BV, are highlighted*

High density can be understood with high BV and low building GC. To understand further, SVF, BV, and GC values are sorted , and SVF versus BV/GC plot is drawn, which is illustrated in Figure 12.8. The data can be sorted into four quadrants. For cities that have high density, based on SVF, Class 2 quadrant of Figure 12.8 can be considered to be an optimized one. Therefore, we can see that A1B6 and A2B7, both with tall towers and large open spaces, may optimize SVF for "density" understanding.

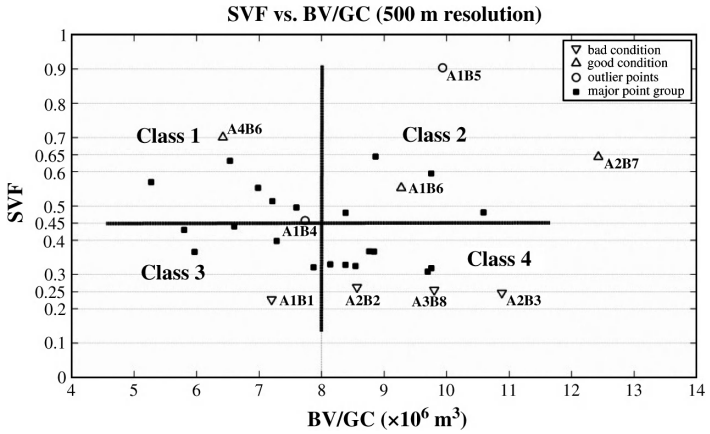


**Figure 12.8.** *SVF versus building volume (BV)/ground coverage (GC) on a 500 m × 500 m area average basis*

On the basis of the in-house GIS database and taking note of the above study, it will be quite easy for local government planners to quickly visualize the issue of urban density of the city. Reliefs, like open spaces, can then be planned into the land use zoning map to ensure that the visual access to the sky can be maintained at key points of the city. Proper urban typology can also be designed, or even regulated, at the project development level to ensure that the perception of high density is optimized.

## 12.3. Designing for daylight

Naturally lit buildings are not only energy efficient, but also psychologically more pleasant and potentially more comfortable for their inhabitants, as well as being "green" and "sustainable". In high-density cities, buildings are fighting with each other for natural light. Finding ways to optimize the natural agent without compromising development density is a task for architects and engineers. Daylight design for high-density urban conditions is more complicated than that for lower density cities.

Natural lighting of an interior space, lit by side windows, is influenced not only by the indoor illumination, but also by how it relates to the outdoor illumination. The ratio, expressed in percentage, between the illuminance at a point indoors and the horizontal illuminance under an unobstructed hemisphere of sky outside is known as the daylight factor (DF). Average DF is defined as the ratio of average interior illuminance (a spatial average over the working plane) to external horizontal

illuminance under standard overcast sky conditions. A simplified version of the formula by Crisp and Littlefair [CRI 84], as in the CIBSE Applications Manual – Window Design, may be written as follows:

$$DF_{\text{average}} = \frac{tA_w\theta}{A(1-\rho^2)} \quad (\%) \qquad [12.2]$$

The equation takes into account obstructions that form a horizontal band. It was claimed that the equation gives a standard error of ±10% of the measured values under certain controlled conditions.

Equation [12.2] has been used to design terrace-type or slab-like building blocks where external obstructions could be estimated based on a horizontal band. Some commercial consultants have also used it to estimate daylight availability of high-rise tower block-type designs in Hong Kong. As an illustration, with a typical high-density urban residential development in Hong Kong, given $A_w$ = 10% of $A_f$ and $\theta$ = 40°, $\text{DF}_{\text{average}}$ is estimated to be 0.9%. There is, however, a problem in using Tregenza's more accurate modified split flux formulas. From equations [12.3]–[12.8] [HOP 54, LON 75, TRE 89], with $\theta$ = 40°, $\text{DF}_{\text{average}}$ is estimated to be 0.4%. Further studies by Ng [NG 01] confirmed that when $\theta$ < 60°, equation [12.2] becomes less reliable. Therefore, while equation [12.2] may be comfortably applied to low- and mid-density cities like London, its use for high-density cities like Hong Kong is doubtful.

$$\text{IRC}_{\text{mean}} = t\frac{A_w}{A}\frac{C\rho_{fw} + D\rho_{cw}\rho_g}{1-\rho} \qquad [12.3]$$

$$\text{DF}_{\text{average}} = tA_w\frac{C}{A_{fw}} + \text{IRC}_{\text{mean}}(\%) \qquad [12.4]$$

$$C = \frac{9}{7\pi} f\left(1 + \frac{\rho_b}{\pi(1-\rho_o)} g\right) \times 100\% \qquad [12.5]$$

$$D = \frac{E_g}{2E_h} \times 100\% \qquad [12.6]$$

where

$$f = \frac{1}{3}(\sin\varphi_L + \sin\varphi_R) \times \left( \frac{\theta_H - \theta_L}{2} + \frac{\sin 2\theta_H - \sin 2\theta_L}{4} - \frac{2\cos^3\theta_H - 2\cos^3\theta_L}{3} \right) \qquad [12.7]$$

and

$$g = \frac{\pi}{2} - (\sin\varphi_L + \sin\varphi_R) \times \left( \frac{\theta_H - \theta_L}{2} + \frac{\sin 2\theta_H - \sin 2\theta_L}{4} \right) \qquad [12.8]$$

The understanding can be best illustrated with the help of Figure 12.9. The amount of SC available to a window when the vertical obstruction angle is from 0° to 55° is between 0.10 and 0.16. However, when the vertical obstruction angle is greater than 60°, SC drops drastically, with the range between 0.00 and 0.06. The relationship between the vertical obstruction angle and the available SC is not linear. Therefore, finding ways to secure the necessary tool to design for high-density cities, like Hong Kong, is a task.

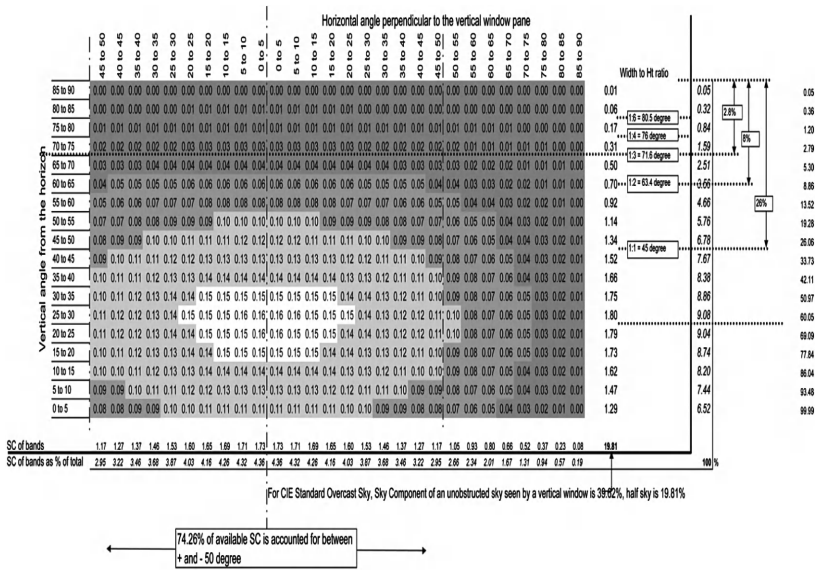


**Figure 12.9.** *Sky component (SC) at 5° band of the CIE overcast sky as calculated using Tregenza's formulas*

Hong Kong is the most densely populated city in the world [NG, 01]. It boasts a development density of some 2,500 person per hectare. Typically, residential buildings are built to a plot ratio of eight and above with site coverage of 100%. This leads to very tall buildings built very close together. Daylight is diminished and solar access is compromised. The Building (Planning) Regulation 1959 of Hong Kong introduced an approach based on "prescribed window" and "rectangular horizontal plane (RHP)". This method made reference to the "imaginary line"

method of London Buildings Act 1930. It was developed primarily for windows not facing the street, i.e. windows facing rear open space within the site. An angle of 71.5° (1:3) was used to regulate windows of habitable space facing "external air". For a window facing an enclosed courtyard with a 71.5° obstruction opposite, the amount of light in terms of DF, arriving at the vertical window plane – hence vertical daylight factor (VDF) – was about 1%. For a window facing a parallel street with a 71.5° obstruction opposite, the amount of light arriving at the vertical window plane (VDF) was about 7% – mostly from reflected light (Figure 12.10).

**Figure 12.10.** *High density means very tall buildings built very close together. The street width to building height ratio in this case is 1:3. The tapering at the top of the towers follows the 71.5° obstruction limiting angle based on the Building Regulations of Hong Kong*

The problem of the building regulations regulating daylight availability using the vertical obstruction angle has been illustrated above with the shortcoming of equation [12.2]. When $\theta > 60°$, the vertical obstruction angle ceases to be an effective parameter for safeguarding daylight availability. The urban cityscape of contemporary Hong Kong, with its higher tower-like buildings, higher density, and complicated site planning, is very different from the low-rise terrace-type tenement buildings of 40 years ago. The antiquated laws could not guarantee any desirable performance of light (Figure 12.11). Better rules must be developed to "encourage" better design.

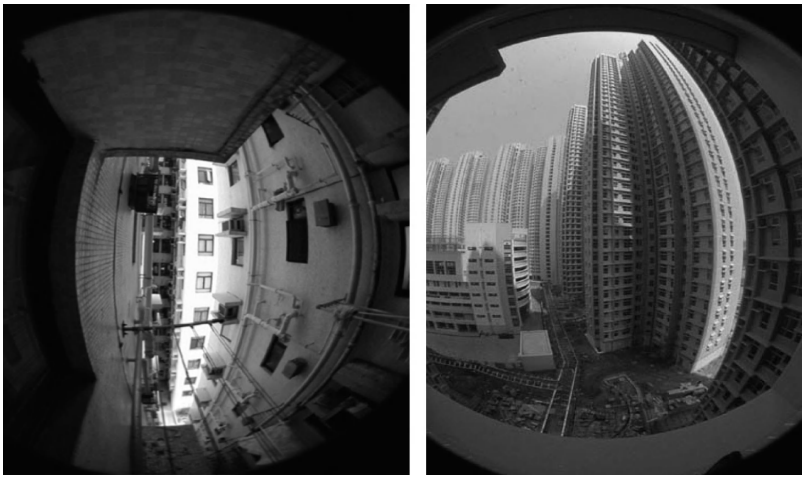

**Figure 12.11.** *A window facing a restricted space that is legal under the Building Regulations. The bit of remaining sky that is otherwise available is blocked by the air conditioners' shelf (left). A window with a tall tower directly opposite does not satisfy the Building Regulations. This is despite the availability of plenty of daylight from one side (right)*

In 2000, the Hong Kong Government initiated a study to seek new methods to compliment the aging building regulations, which was based on methods originated in the UK over 100 years ago that employed a vertical sustained angle to regulate building heights and spacing.

A minimum daylight performance of spaces based on VDF on the surface of the window of the spaces was established. The concept of VDF is based on the concept of DF. It can be defined as "the illuminance received on the vertical surface of the window plane as a percentage of the simultaneous horizontal outdoor illuminance from the unobstructed sky. Direct sunlight is excluded". Unlike the use of DF, VDF accounts for daylight availability due to the sky and external obstruction only. As far as the design of urban and interbuilding spaces is concerned, VDF is more appropriate.

Using scale models and computational studies of real and hypothetical cases, a design and regulatory measure based on "Unobstructed Vision Area" (UVA) was developed. Crosschecking with other daylight prediction methods indicated that the UVA method is reasonably accurate for high-rise high-density conditions. Findings and recommendations of the study, completed in 2002, have been presented to Buildings Department HKSAR to adopt as a way to safeguard the provision of daylight in residential buildings. Subsequent to that, Buildings Department

promulgated a practice note (PNAP 278) allowing authorized architects to employ the UVA method to demonstrate compliance to the building regulations.

Based on a study of the current building regulations in Hong Kong, the basis and assumptions underlining the use of Rectangular Horizontal Plane (RHP) [HKG 11] are no longer valid. Research studies indicate that windows designed to satisfy the building regulations can perform very differently [NG 03]. It is necessary to find better methods. Various design tools exist [TRE 98]. As demonstrated above, the design tools recommended for use in the CIBSE guides and in BS8206 can result in vastly overestimated predictions [LEE 92, NG 01]. A design and regulatory method for Hong Kong has to be developed from first principles.

Based on an older "gaps between buildings" method by R. G. Hopkinson [MHL 66], a method based on 2D "the visible area in front of the window" is speculated. For high-density environments where surrounding buildings are high, the sky component (SC) above the buildings can be assumed to be very small. Light from gaps of buildings can then be approximated using the plans. Reflected light depends largely on how the surrounding surfaces are illuminated and thus the openness of these surfaces to the sky. It is possible to devise a design method based only on 2D plan information [NG 03]. The UVA method (Figure 12.12) is a simple and practical method suitable for high-rise high-density development (Figure 12.13).

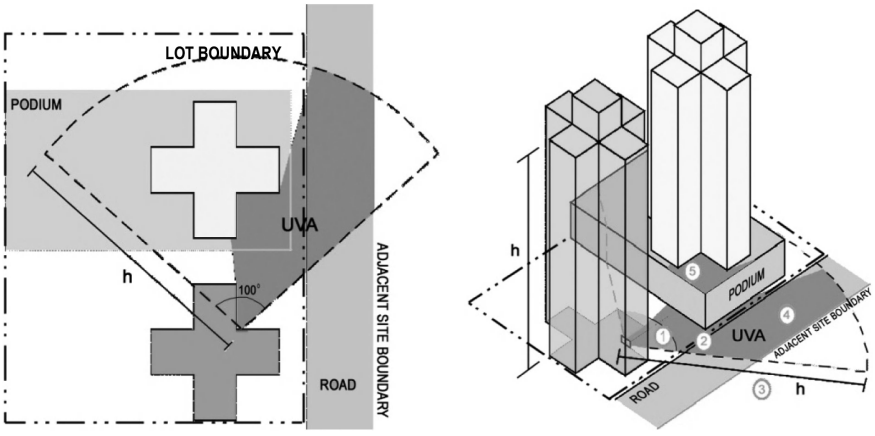


**Figure 12.12.** *The fundamental principles of the unobstructed vision area (UVA) method. Step 1: set angle of measurement from the window, up to 100°, symmetrical and perpendicular to the window pane. The radius of the UVA fan is H, H being the height of the building. Step 2: calculate UVA, count UVA up to the boundary of the adjacent property, and include road and permanent open space*

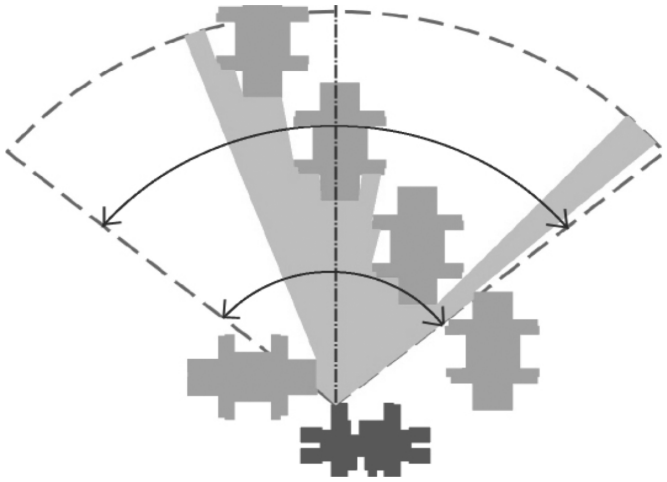

**Figure 12.13.** *UVA in practice. Architects can shift the building blocks in the estate to optimize UVA for better daylight design*

The limitations of the UVA method must be borne in mind when it is applied. Again, it is always meaningless to apply a simplified design tool beyond its context and purpose. The misinterpretation of a design tools for a scientific tool is unnecessary [CHU 06]. Furthermore, design tool by nature of its practical application needs to be simple and user-friendly to designers. Making it overtly difficult for precision is not useful [CHU 06].

## 12.4. Designing for solar access

> Sunlight should be admitted (to a building) unless it is likely to cause thermal or visual discomfort to the users, or deterioration of materials. The controlled entry of sunlight is rarely unwelcome in buildings in the UK. Dissatisfaction can arise at least as much from the permanent exclusion of sunlight as from its excess. However, uncontrolled sunlight is unacceptable in most types of building. [BS 8206]

> People like sunlight. In surveys, about 90% of the interviewed people said they appreciated having sunlight in their homes. The Sun is seen as providing light and warmth, making homes look bright and cheerful, and also having a therapeutic, health-giving effect [LIT 91].

The 1991 publication *Site layout planning for daylight and sunlight* [LIT 91] is the principal reference in the UK for planners and designers. It is a guidance publication that covers daylight (light from all of the sky except the Sun), sunlight, and passive solar heating. It seeks to describe good practice and assumes a holistic view of the environment in and around buildings, recognizing that in practice it is necessary to balance the various environmental requirements against each other and against other building constraints. For this reason, it is not prescriptive. It gives numerical criteria (such as the hours of sunlight that a dwelling should receive), but these are typical values and the planning authority may adopt different values to take local conditions into account. The 1991 publication is based on the British Standard *BS8206 pt 2: Code of practice for daylighting* [BSI 92]. It supersedes an earlier publication of the UK Government Department of the Environment, *Daylight and sunlight indicators*. Neither *Site layout planning for daylight and sunlight* nor the British Standard sets out mandatory requirements, and a local planning authority in the UK may decide whether or not to adopt the recommendations.

The Ministry of Construction for the Peoples Republic of China has published a series of national codes, such as Code of Urban Residential Areas Planning and Design [GB 50180-93] (Table 12.1, Figure 12.14), Standard for daylighting design of buildings [GB/T 50033-2001], Residential building code [GB 50368-2005], and so on. With these codes, the Ministry of Construction for the Peoples Republic of China has clearly prescribed the requirement for the standard of sunlight availability for buildings. The Chinese code is principally referenced to

1) give warmth in cold weather;

2) enhance the brightness of a room or an outdoor space;

3) maintain the health of people who are confined indoors.

It aims to address the problems/issues of inadequate solar access provision in current developments that tend to occur in the following cases:

1) Apartments on the lower floors of housing blocks (on the upper floors, little or no sunlight entry tends to be compensated by increased daylight and more extensive views). The people mostly affected are those who, because of age or infirmity, tend to be confined to the dwelling.

2) Residential homes for older people and those with disabilities.

3) External areas used for recreation, such as children's play spaces, seating areas in pedestrian routes, and areas designated for landscape planting near buildings.

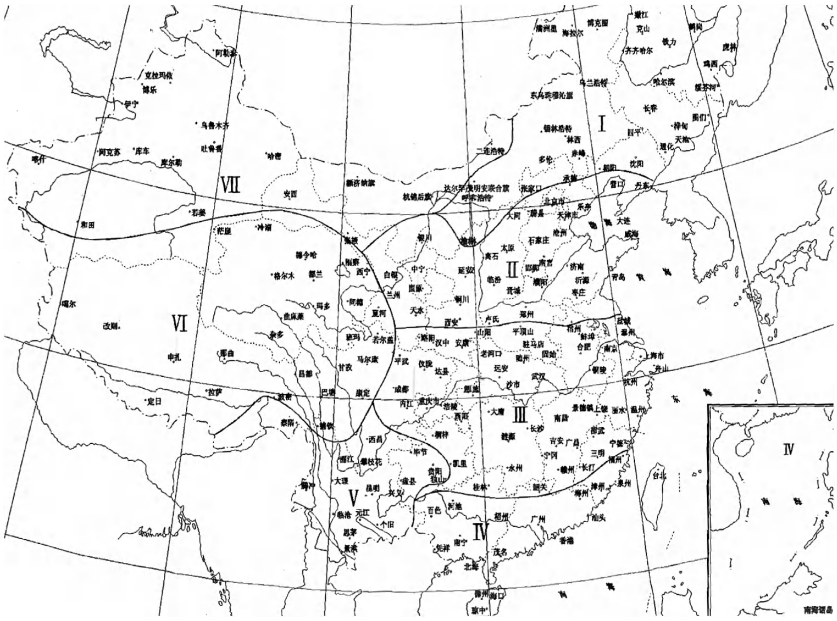


**Figure 12.14.** *Climate zones in China for solar access requirements as in GB 50180-93*

It employs the criterion of

1) sunshine hours received on the winter solstice between 9.00 a.m. and 3.00 p.m.

2) the criterion shall be 2 h possible sunshine hour.

In the USA, solar envelopes have been used (Figure 12.15). The "solar envelope"–based guidelines in the USA emphasize the use of renewable energy [KNO 03]. In Israel, it has also been used for site planning [CAP 03].

In a high-density city like Hong Kong, after the outbreak of the Severe Acute Respiratory Syndrome in 2003, people have become more concerned about their living environment conditions and have been aspiring for a clean, comfortable, and healthy environment. Planning, urban design, and environmental protection are instrumental in bringing about improvements. The issue of sunlight and shadow is one among these factors. Solar access for windows of habitable rooms and for urban open spaces is an important consideration for planning and building design. Especially in the winter months, adequate levels of solar access can greatly enhance the quality of the living environment.

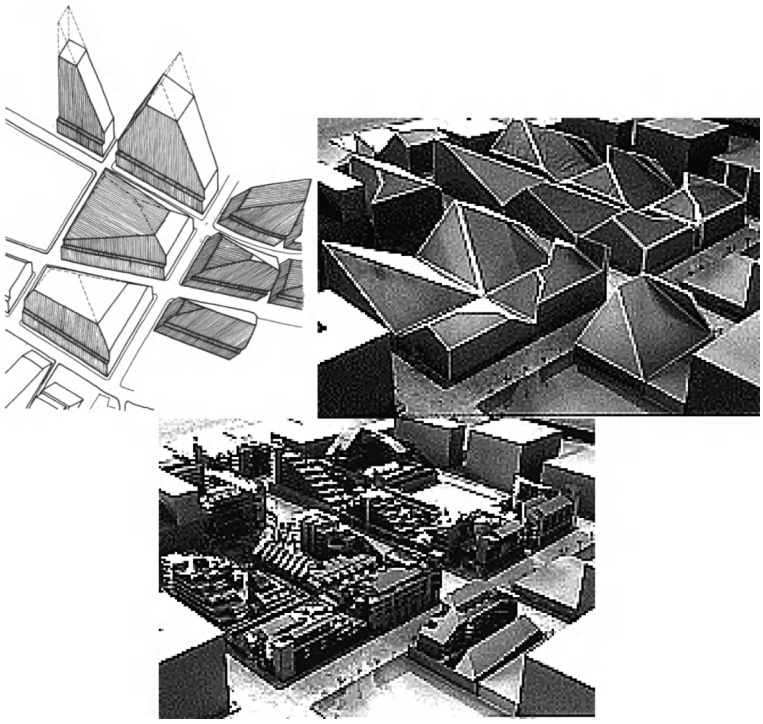

**Figure 12.15.** *Using solar envelope for site planning – from the generic envelope to the actual building design. Reproduced with permission of Ralph L. Knowles*

To meet the increasing desire of the public for a better living environment, and taking into account Hong Kong's unique high-rise and high-density development characteristics, as well as its hot and humid subtropical climate, studies to explore and investigate the application of sunlight and shadow analysis for planning are considered necessary and useful. Based on the literature studied, the following key points are identified for the unique high-density setting of Hong Kong.

1) For assessment parameter, the UK guide uses probable sunlight hours. This gives a more realistic estimate of the sunshine exposure of a place when cloudiness varies between morning and afternoon, or between summer and winter. The Chinese code uses possible sunshine hours. This is a lot more straightforward. The weather for over 70% of the days of the year in Hong Kong is cloudy. Like the UK approach, the use of *probable sunlight hours* as the parameter is more scientifically correct.

However, it is a lot simpler to use *possible sunshine hours* as a parameter. For solar access, the performance criterion should specify the minimum *possible sunlight hours* within a time frame.

2) For the performance criterion, the climate in Hong Kong is different from that in the UK. The Code of Urban Residential Areas Planning and Design (GB-50180-93), especially the required sunshine hours in "south" China, could be taken as a more relevant reference. It is reasonable to reference the local requirements in the same climate zone as Hong Kong, for example Shenzhen and Guangzhou. By reference to Table 12.1, the suggestion for the performance criterion can be 1 or 2 h in the winter on 22 December between 9.00 a.m. and 3.00 p.m. for urban open spaces and windows of habitable spaces.

3) The sunlight availability of the buildings, where the elderly people live, is a more important consideration than other building types. Hence, it is very important to apply any suggested requirement based on an understanding of the kind of activities the open space, or the building, is going to accommodate.

4) For Hong Kong, due to the high-density urban living environment, sunlight availability in open spaces should be considered. Using a MATLAB scientific visualization program, the sunshine hour map of the urban spaces can be generated (Figure 12.16) based on GIS information provided by the Planning Department of HKSAR Government. The characteristics of the open space of a district can be quickly visualized.

5) Unlike in the UK, in Hong Kong, the summer Sun should be shaded and the winter Sun should not be blocked. As such, there may be a need to look at sunlight availability seasonally. While ensuring the minimum *sunlight hours* for building interiors in the winter, controlling devices on building facades to control the sunlight exposure should be coupled to prevent visual or thermal discomfort.

6) The use of solar envelope to control the maximum building bulk so as not to cast shadows on our neighbor's building is a simple-to-use tool. However, given the high-density built environment of Hong Kong, its practical application for Hong Kong is not realistic.

From the key understanding, to assist planners, a set of guidelines are formulated. Some examples of them are illustrated in Figures 12.17–12.19. The guidelines are referenced by city planners and lay members of the Town Planning

Board when making planning-related decisions. Figure 12.17 contains a guideline on land use zoning; planners should not place higher density development sites on the south side of sensitive receivers. Guidelines on street layout are illustrated in Figure 12.18; here diagonally arranged streets, if possible, are preferred. At the street and building design level, the need to cater for the winter Sun with adequate building spacing and the need to provide shading for the summer Sun are elaborated.

| Architectural climate zone (please refer to Appendix 1) | I, II, III, VII Climate zone | | IV Climate zone | | V, VI Climate zone |
|---|---|---|---|---|---|
| | Large city | Medium/ small city | Large city | Medium/small city | |
| Day for sunlight standard | 大寒日 either 20 or 21 January, depending on the year | | | 冬至日 Winter solstice, either 21 or 22 December, depending on the year | |
| Sunlight hour (h) | ≥ 2 | ≥ 3 | | ≥ 1 | |
| Effective sunlight hour | 8 a.m.–4 p.m. | | | 9 a.m.–3 p.m. | |

**Table 12.1.** *Solar access requirements of various climate zones in China as in GB 50180-93.*

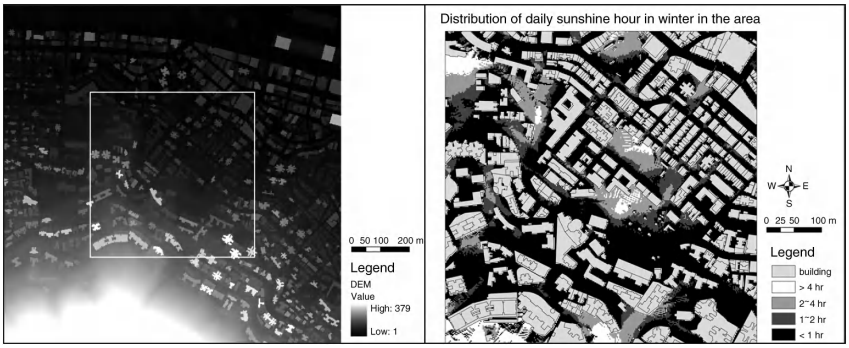


**Figure 12.16.** *Sun-hours distribution simulated by a MATLAB program*

At the estate design level, simulation software is available. Figure 12.20 shows the solar hour distribution of an estate. With this information, open spaces can be better planned. Simulation software can also be used to assess the impact of a development on the neighborhood (Figures 12.21 and 12. 22). More numbers of windows on the two towers to the north of the proposed development will have their solar assessment hours reduced. Some of the windows will have less than 1 h sunlight.

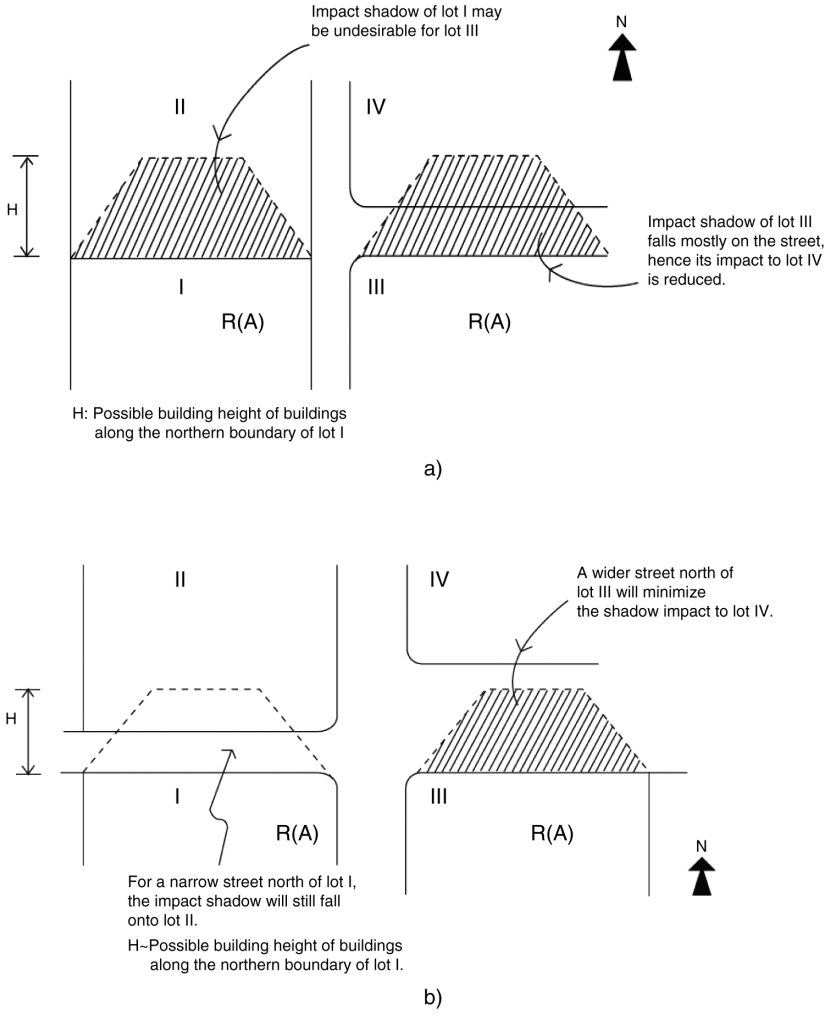


**Figure 12.17.** *An example of the recommended planning guideline. (a) Possible impact of R(A) on other zones. (b) Possible impact of R(A) on other zones and how to minimize it*

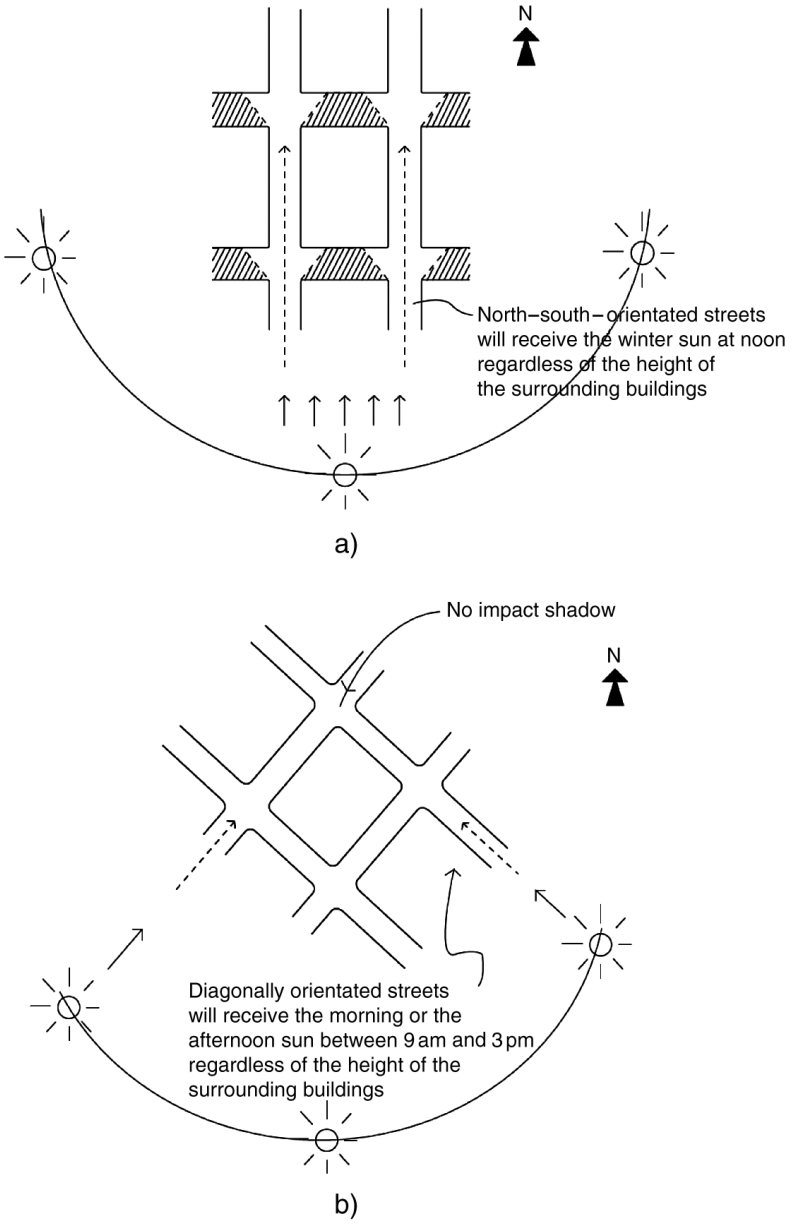


**Figure 12.18.** *An example of the recommended planning guideline. (a) An understanding of shadow area of north–south streets. (b) An understanding of shadow area of diagonal streets*

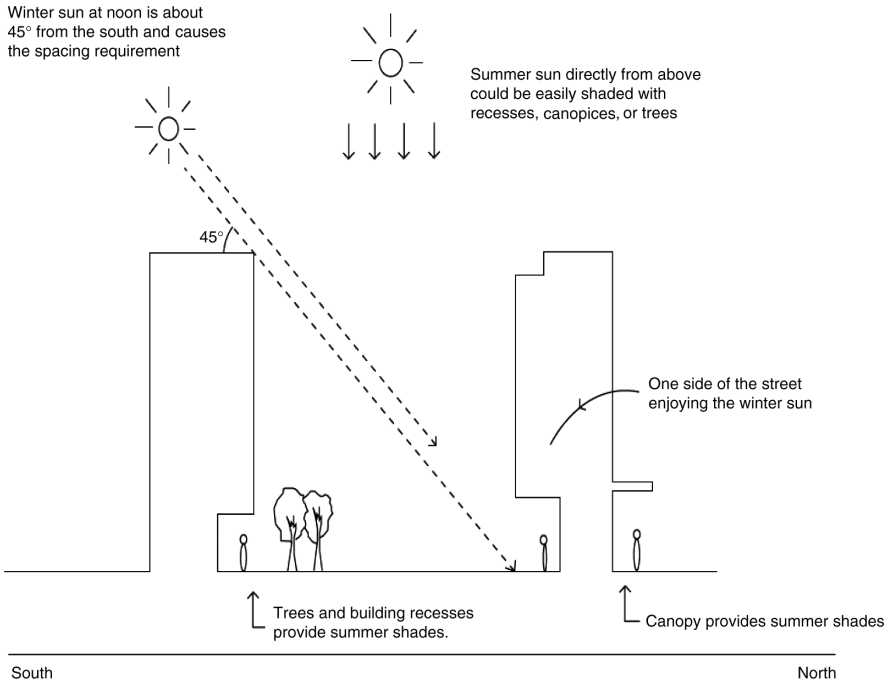


**Figure 12.19.** *An example of the recommended planning guideline. Designing and planning for the summer and the winter Sun; avoid summer Sun by providing shading; and allow winter Sun by spacing buildings properly*

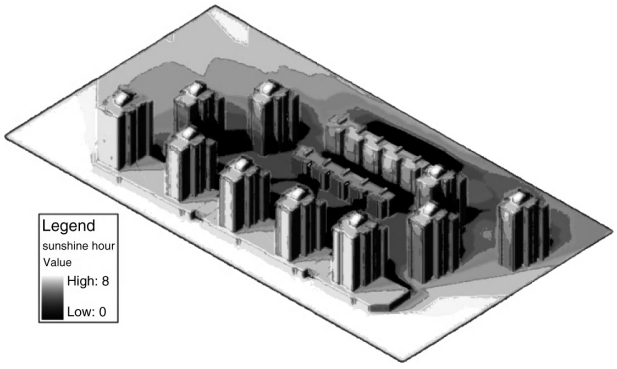


**Figure 12.20.** *Sunshine hour of an estate simulated using SUNLIGHT 2.0*

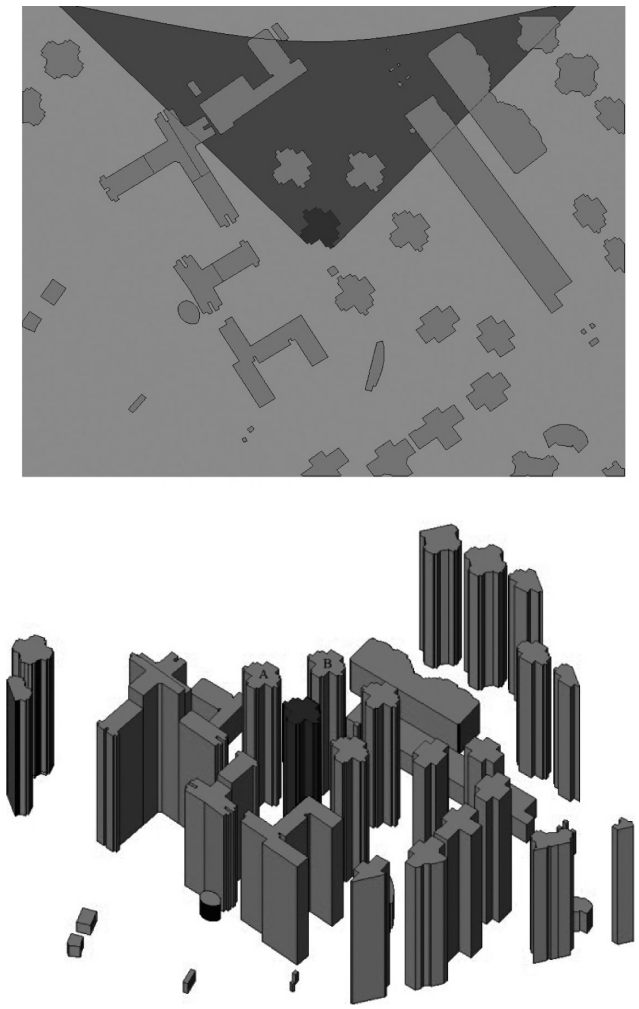


**Figure 12.21.** *Using SUNLIGHT 2.0, the possible shadow impact of the proposed building can be assessed*

## 12.5. Designing with solar renewable energy

For achieving low (zero) energy building, we need to amass the benefits of solar energy. For high-density city, the spirit is one of "every drop counts". The most important thing we need to do while assessing the renewable energy potential of a site in high-density cities is the consideration of obstruction.

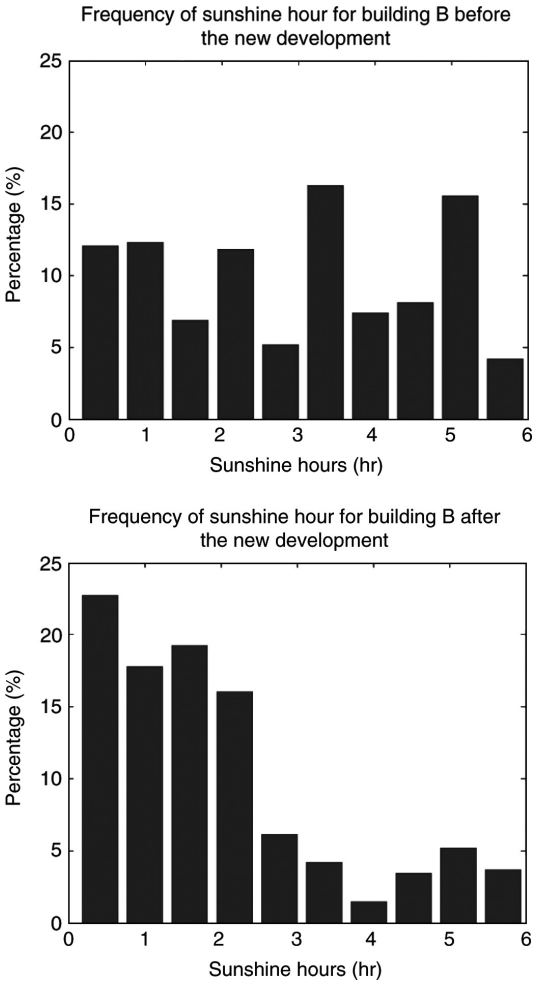


**Figure 12.22.** *A frequency distribution study of solar access of windows of the two towers in the proposed building's shadow zone (top) before the proposed building; and (down) after the proposed building*

The solar energy potential of a site can be estimated by first estimating the direct and the diffuse components separately. The solar radiation on the shaded surface is calculated based on Quaschning's method [QUA 98]. The reduced direct irradiance $E_{es,red}$ on the horizontal surface is given by

$$E_{es,red} = (1 - S_b) E_{es} \sin \gamma_s$$

where $S_b$ is the direct shading factor:

$$S_b = \begin{cases} 0, & \text{if the surface is outside the shadow} \\ 1, & \text{if the surface is inside the shadow} \end{cases}$$

$E_{es}$ (W m$^{-2}$) is the direct irradiance measured in 10-min intervals; $\gamma_s$ is the solar altitude.

The reduced diffuse irradiance $E_{ed,\,red}$ on the horizontal surface is given by

$$E_{ed,red} = E_{ed} \cdot SVF$$

where

$SVF$ is the sky view factor;

$E_{ed}$ is the diffuse irradiance measured by our IDMP station (W m$^{-2}$).

Isotropic sky conditions can be assumed. Quaschning has argued that "the isotropic radiance for the calculation of the shading reduction is sufficient for most applications because the differences between the isotropic and anisotropic models can be neglected if there is shading of the direct irradiance" [QUA 98].

The reduced global irradiance $E_{ed,\,red}$ (W m$^{-2}$) on the horizontal surface is therefore given by

$$E_{eg,red} = E_{ed,red} + E_{es,red}$$

Using a city site (Figure 12.23) in Hong Kong as an example, Figure 12.24 shows the monthly average daily solar radiation on an unshaded horizontal plane. The same for the four points on the boundaries of the site is illustrated in Figures 12.25–12.29. It is apparent that, surrounded by tall buildings, the site has reduced solar energy potential; the reduction is from 3.2 to 2.2 kW h m$^{-2}$ day$^{-1}$ (center of the site). More importantly, the solar energy potentials of various locations of the site itself are different. It ranges from 2.4 to 1.6 kW h m$^{-2}$ day$^{-1}$. With this understanding, architects have therefore been advised to position the building and the PV panels at the northwest corner of the site. Further refinements as to the angle of tilt of the PV panels can be further optimized using the same method and equations as above.

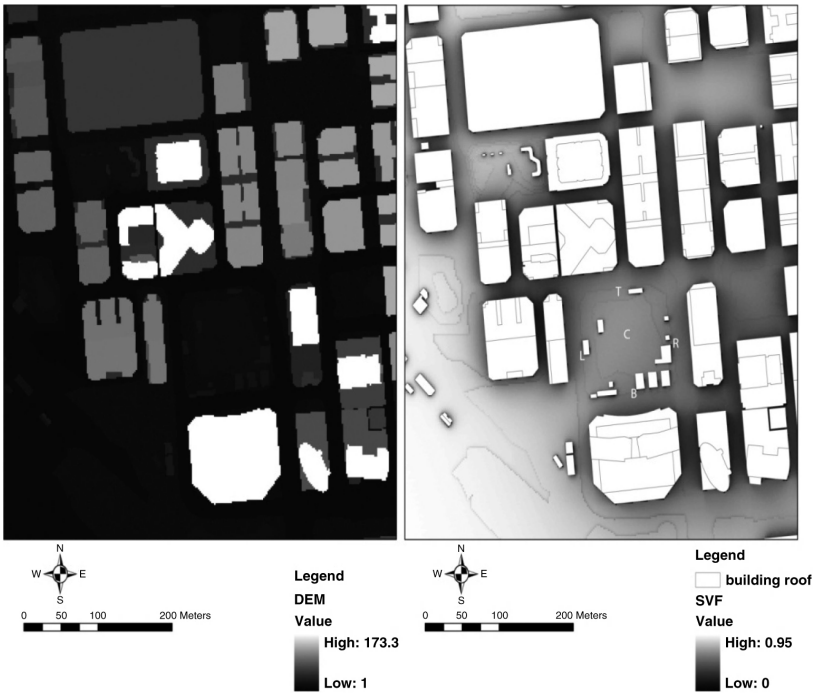


**Figure 12.23**. *A site in Hong Kong where a zero-energy building will be located. The boundaries are denoted by T, R, B, and L. Surrounding buildings are up to 173.3 m height (left). Three tall buildings are on the south side of the site. The sky view factors (right) of the site are 0.696 in the center, 0.616 (T), 0.534 (R), 0.548 (B), and 0.538 (L)*

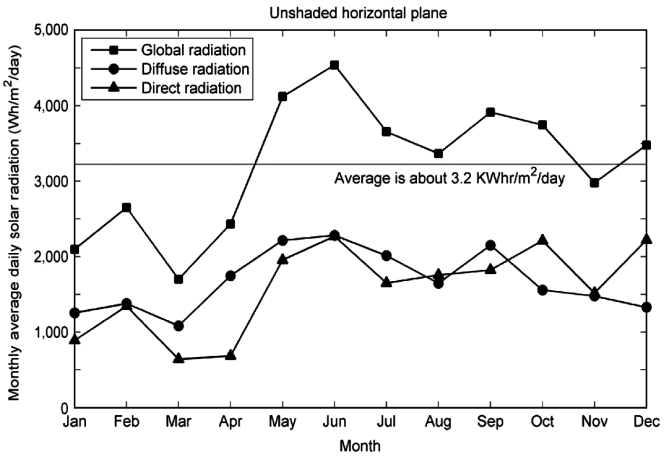


**Figure 12.24.** *Monthly average daily solar radiation of an unshaded horizontal plane*

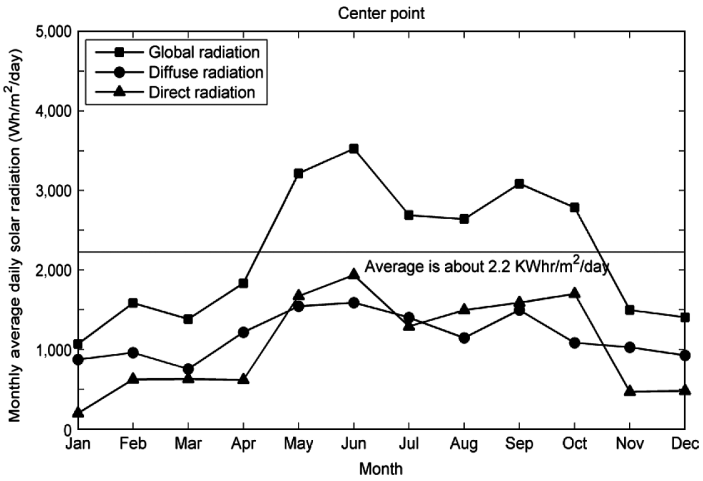


**Figure 12.25.** *Monthly average daily solar radiation of the center (C) point considering shading reduction*

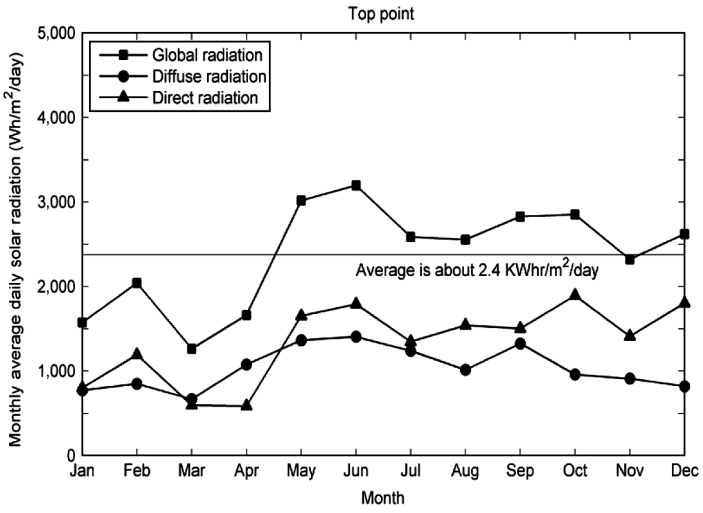


**Figure 12.26.** *Monthly average daily solar radiation of the top (T) point considering shading reduction*

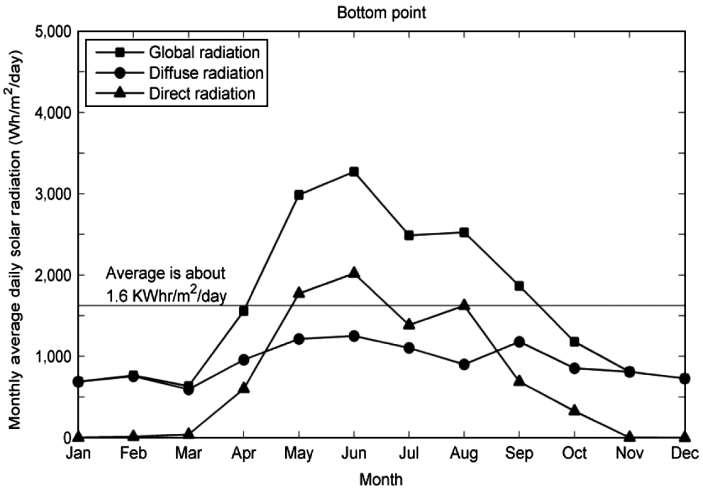


**Figure 12.27.** *Monthly average daily solar radiation of the bottom (B) point considering shading reduction*

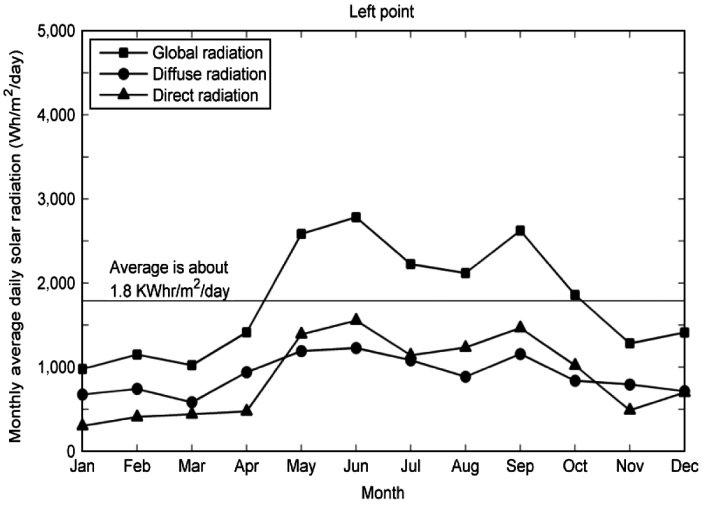


**Figure 12.28.** *Monthly average daily solar radiation of the left (L) point considering shading reduction*

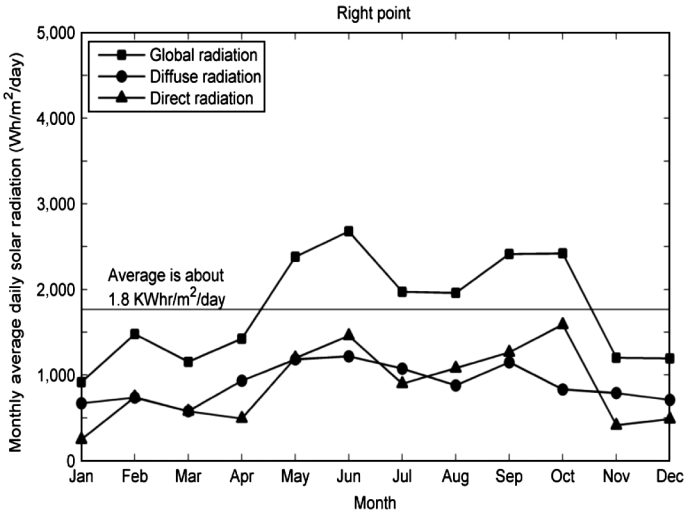


**Figure 12.29.** *Monthly average daily solar radiation of the right (R) point considering shading reduction*

## 12.6. Conclusion

Various design issues relating to solar access, solar energy availability and daylight in the high-density city context are elaborated. Psychologically, the principal issue of seeing the sky and distant views is important to be optimized, so as to lessen the impact of perceived density. Methods and procedures for daylight design in high-density cities can be very different from that for low-density settings. The need to have gaps and open spaces is fundamental. The UVA methodology provides an easy way for designers. Even for the subtropical regions, winter Sun is welcomed. City planners and architects need to design their plans to, on the one hand, gain access to the winter Sun and, on the other hand, provide shade from the summer Sun. Last but not the least, for zero-energy design, solar energy may be harvested. It is important to carefully consider site obstructions.

The journey toward better solar energy design for high-density cities in the tropical regions has just begun. It is still necessary to understand the sky and its types [NG 07a, NG 07b]. Unlike temperate regions with lower Sun altitudes, the summer Sun in the tropics can be directly above the head. Models that have been developed in the temperate regions may not work in the tropics [HE 10]. Research efforts are needed. In addition, how human habitation responds to the Sun, in terms of daylight provision and solar access, needs further study [LAU 11]. The

questions such as where, when, how long, and for what purpose the Sun is needed are poorly understood at the moment. Without this understanding, it is impossible to develop assessment criteria to objectively evaluate whether a design is satisfactory or not.

When it boils down to it, the important issue is application. Can our scientific understanding find any easy way to impact practice? For that to happen, simple tools and guidelines are needed. Without crossing this threshold, scientists can only continue to talk about numbers, models, and the need for precision; yet at the same time, none of those really matter. That should be the last thing we wish to see.

## 12.7. Bibliography

[BSI 92] BSI 1992, British Standards Institution, BS 8206: Part 2: 1992 Code of Practice for Daylighting, BSI, London, 1992.

[CAP 03] CAPELUTO I.G., YEZIORO A., SHAVIV E., "Climatic aspects in urban design – a case study", *Building and Environment*, vol. 38, pp. 827–835, 2003.

[CHE 10] CHEN L., NG E., AN X.P., REN C., HE J., LEE M, WANG U, HE J., "Sky view factor analysis of street canyons and its implications for intra-urban air temperature differentials in high-rise, high-density urban areas of Hong Kong: a GIS-based simulation approach", *International Journal of Climatology*, 2010.

[CHE 06] CHEUNG H.D., CHUNG T.M., "Calculation of the vertical daylight factor on window façades in a dense urban environment", *Architectural Science Review*, vol. 48, pp. 81–92, 2006.

[CHU 06] CHUNG T.M., CHEUNG H.D., "Assessing daylight performance of buildings using orthographically projected area of obstructions", *Journal of Light and Visual Environment*, vol. 30, no. 2, pp. 74–80, 2006.

[CRI 84] CRISP V.H.C., LITTLEFAIR P.J., "Average daylight factor prediction", *Proceedings of the CIBS National Conference 1984*, University of Cambridge, London, CIBSE, 16–18 April 1984.

[FIS 03] FISHER-GEWIRTZMAN D., BURT M., TZAMIR Y., "A 3-D visual method for comparative evaluation of dense built-up environments", *Environment and Planning B: Planning and Design*, vol. 30, pp. 575–587, 2003.

[GB 50180-93] GB 50180-93, Code of Urban Residential Areas Planning and Design, The Ministry of Construction, People's Republic of China, 2002.

[GB 50368-2005] GB 50368-2005, Residential Building Code, The Ministry of Construction, People's Republic of China, 2005.

[GB/T 50033-2001] GB/T 50033-2001, Standard for Day-Lighting Design of Buildings, The Ministry of Construction, People's Republic of China, 2001.

[HE 10] HE J., NG E., "Using satellite-based methods to predict daylight illuminance for subtropical Hong Kong", *Lighting Research and Technology*, vol. 42, no. 2, pp. 135–147, 2010 [P098527].

[HKG 11] HKG., http://www.hklii.org/hk/legis/en/reg/123F/s31.html, accessed on 30 March 2011.

[HOP 54] HOPKINSON R.G., LONGMORE J., PETHERBRIDGE P., "An empirical formula for the computation of indirect component of daylight factor", *Transactions of the Illuminating Engineering Society*, vol. 19, no. 7, pp. 201–219, 1954.

[KNO 03] KNOWLES R.L., "The solar envelope: its meaning for energy and buildings", *Energy and Building*, vol. 35, pp. 15–25, 2003.

[LAU 11] LAU K., NG E., HE J., "Residents' preference of solar access in high-density sub-trophical cities", *Solar Energy*, vol. 85, pp. 1878–1890, 2011.

[LEE 92] LEE F.W.K., "Insights into the daylighting effect of external obstructions", *CIBSE National Lighting Conference*, pp. 235–243, 1992.

[LIT 91] LITTLEFAIR P.J., Site layout planning for daylight and sunlight: a guide to good practice. BRE report BR 209, Building Research Establishment, Garston, 1991.

[LON 75] LONGMORE J., "Daylighting: a current view", *Light and Lighting*, vol. 68, no. 3, pp. 113–119, 1975.

[MAR 73] MARTIN L., MARCH L., (eds), *Urban Space and Structures*, Cambridge University Press, Cambridge, 1973.

[MHL 66] MHLG, "Daylight Code, Ministry of Housing and Local Government in the UK", Cited in HOPKINSON R.G., *et al*. (eds.), *Daylighting*, Heinemann, London, 1966.

[NG 01a] NG E., "A simplified daylight design tool for high density urban residential buildings", *Lighting Research and Technology*, vol. 33, no. 4, pp. 259–272, 2001.

[NG 01b] NG E., "Green architecture in Hong Kong, the densest city in the world", in EDWARDS B. (ed.), *Green Architecture – A International Comparison*, Architectural Design Monograph Academy ed., John Wiley & Sons Inc., London, 2001.

[NG 03] NG E., "Studies on daylight design of high density residential housing in Hong Kong", *Lighting Research and Technology*, vol. 35, no. 2, pp. 127–140, 2003.

[NG 07a] NG E., GADI A., JUN M., LEE, M., "Predicting daylight availability based on forecast of a weather observatory", *Lighting Research and Technology*, vol. 39, no. 1, pp. 69–77, 2007a.

[NG 07b] NG E., CHENG V., GADI A., JUN M., LEE M., "Defining standard skies for Hong Kong", *Building and Environment*, vol. 42, pp. 866–876, 2007b.

[QUA 98] QUASCHNING V., HANITSCH, R., "Irradiance calculation on shaded surfaces", *Solar Energy*, vol. 62, no. 5, pp. 369–375, 1998.

[RAP 75] RAPOPORT A., "Toward a redefinition of density", *Environment and Behaviour*, vol. 7, no. 2, pp. 133–158, 1975.

[RAP 77] RAPOPORT A., *Human Aspects of Urban Form: Towards a Man-Environment Approach to Urban Form and Design*, Pergamon Press, New York, 1977.

[RAT 02] RATTI C., Urban analysis for environmental prediction, PhD Thesis, University of Cambridge, Cambridge Reference 91, 2002.

[TRE 89] TREGENZA P.R., "Modification of the split-flux formulae for mean daylight factor and internal reflected component with large external obstructions", *Lighting Research Technology*, vol. 21, no. 3, pp. 125–128, 1989.

[TRE 98] TREGENZA P., LOE D., *The Design of Lighting*, E & FN Spon, London, 1998.

[UNW 12] UNWIN R., *Nothing Gained by Overcrowding!*, Garden Cities and Town Planning Association, London, 1912.

[WAT 87] WATSON I.D, JOHNSON G.T., "Graphical estimation of sky view factors in urban environments", *International Journal of Climatology*, vol. 7, pp. 193–197, 1987.

Chapter 13

# Dense Cities in Temperate Climates: Solar and Daylight Rights

## 13.1. Introduction

### 13.1.1. *Urban form and thermal comfort*

In cities with a temperate climate, open spaces, gardens, and streets can provide a vital place for public urban realm during the whole year. There is a clear relationship between the buildings and the quality of the spaces adjacent to them. Successful and enjoyable use of these places by the public depends heavily on microclimatic conditions that affect thermal comfort.

The geometry of the urban grid affects the wind conditions and shading zones created in buildings and open areas. Consequently, it determines whether these places will be thermally pleasant or uncomfortable during different hours of the day and throughout the year. Streets and other public open spaces that allow solar exposure during winter and shading during the hot season provide the proper conditions to sustain urban life.

Summer shading may be achieved by dynamic shading solutions, like deciduous trees or by pergolas with a light cover that can be folded or removed in winter, or even by the building form itself as will be presented later in this chapter. On the other hand, insolation cannot be added in winter if the buildings around streets and open spaces block the Sun completely.

---

Chapter written by Guedi CAPELUTO.

*Solar Energy at Urban Scale* Benoit Beckers

The important aforementioned effects of appropriate solar design of streets and open spaces were recognized more than 40 years ago by Olgyay and Olgyay [OLG 76]. The energy crisis of 1973 accelerated attempts to find advanced methods and tools for the design and evaluation of suitable insolation and shading of open spaces and buildings. Moreover, various studies and recommendations for solar rights in special cases were suggested by researchers using different methods and design tools, as will be presented later.

This chapter presents the concept of solar and daylight rights as a way of determining the urban form with the aim of providing solar access during the cold period for passive solar heating of buildings and thermal comfort in open spaces, self-shading of buildings in summer, and daylight access throughout the year. Furthermore, it presents simple methods of application and guidelines to allow designers to consider these important design factors right from the beginning of the design process.

## 13.2. Solar rights in urban design

The consideration of solar rights in urban design is essential to improve the comfort conditions of people in the streets, on sidewalks, and open spaces. Moreover, it is important to consider passive heating of buildings in winter and solar exposure of solar systems during the whole year. A design that considers these factors may reduce the energy consumption of buildings, while insolation of exterior spaces may create climatically comfortable areas that can be used for outside activities in winter. On the other hand, shading should be provided to avoid overheating of buildings and create pleasant spaces during summer.

The idea of ensuring solar access is not new; the Roman Empire had solar access laws; the “Leyes de Indias” (The Law of the Indies) that were applied on the foundation of new towns in America considered block layout and street orientation to allow solar access; and the Doctrine of Ancient Lights protected the landowners’ rights to light in 19th Century Britain. Additionally, several US communities adopted solar access regulations in response to the energy crisis and as a way to save energy and to reduce air pollution and costs. In these examples, daylight and solar radiation are considered significant factors in the determination of urban development policies.

Interest in the building integration of solar systems, like solar water heating that is compulsory for residential buildings in Israel, or photovoltaic panels, where these systems actually become an integral part of the building envelope often serving as the exterior weather skin, is growing worldwide. The local urban environment, and the location of collectors on different building surfaces and with different tilt angles,

may seriously affect the system performance, and as well the period of time over the year that they will be exposed to direct solar radiation. Since the amount of unobstructed solar radiation is critical to the efficient operation of solar systems in new or existing buildings as a part of roofs or building facades, the solar access to the collectors and the solar rights must be assured year-round.

As a result, a design that does not consider the solar rights of buildings and open spaces may cause uncomfortable conditions inside the buildings and in the streets and other public open spaces. During the schematic design stages of urban "quarters", the designer deals mainly with geometrical characteristics of the buildings, i.e. their proportion, height, distance between each building, and so on, that have crucial influence on the future performance and quality of the built environment. These parameters are related to the profile, dimensions, and orientation of streets and open spaces. Various research works have proposed different computer-based methods to deal with this issue – from evaluative tools that analyze the performance of a given design alternative, like shadow cast programs or Sun's view axonometric projections [KRO 85, YEZ 94], to generative tools that aid in obtaining a proper geometry to achieve the required performance, like the solar envelopes. However, the use of such tools depends on profound knowledge of computer programs, or on the hire of expert consultants, both of which are not always affordable by architects during the early stages of the design process. In the next sections, a simple design tool that can be used by designers as a design guide for solar rights consideration from the very schematic design stages, without the need of using computer models or defining a large amount of input data, is presented.

The design tool was developed through the generative computer model SustArc developed by Capeluto and Shaviv [CAP 96, 97]. SustArc allows the generation and evaluation of different building configurations, ensuring solar rights of each neighboring building, and open spaces like sidewalks, gardens, and squares. The model presents the maximum available volume in which it is possible to build without violating the solar rights of any existing building, as well as the designed one.

## 13.3. Solar envelopes as a design tool

Different research works dealt with the determination of solar envelopes for various design purposes: Shaviv [SHA 75] proposed a computerized model for the design of fixed external sunshades. The method was extended later on for the generation of solar rights envelopes (SRE) for the design of solar communities [SHA 84]. Arumi [ARU 79] developed a computerized model that determines the maximum allowed height of a building that does not violate the solar rights of the existing neighboring buildings. Knowles [KNO 81] suggested a method for assuring

solar access to each residential unit in a community. De Kay [DEK 92] made a comparative analysis of various envelopes allowing daylight access. Schiler and Uen-Fang [SCH 93] developed a computer program for the generation of solar envelopes for flat-rectangular sites based on Knowles' work, and Koester [KOE 94] presented energy armatures using passive resources like winds and rainwater for urban sustainable development.

Capeluto and Shaviv [CAP 96, CAP 97, CAP 01] suggested the creation of two different types of solar envelopes, which are "the solar rights envelope" and "the solar collection envelope" (SCE). These envelopes are defined for a built area as follows:

The SRE presents the maximum buildings' heights that do not violate the solar rights of any existing buildings, during a given period of the year.

The SCE presents the lowest possible locus of windows and passive solar collectors on the considered building's envelope so that they are not shaded by the existing neighboring buildings, during a given period of the year.

Clearly, it is possible to determine the volume between both envelopes. This volume is called the "solar volume" (SV), and can be defined as follows:

The SV contains the maximum buildings' volume to be designed so that these buildings allow solar access to all the surrounding buildings, and at the same time are not shaded by them, during a given period of the year (Figure 13.1).

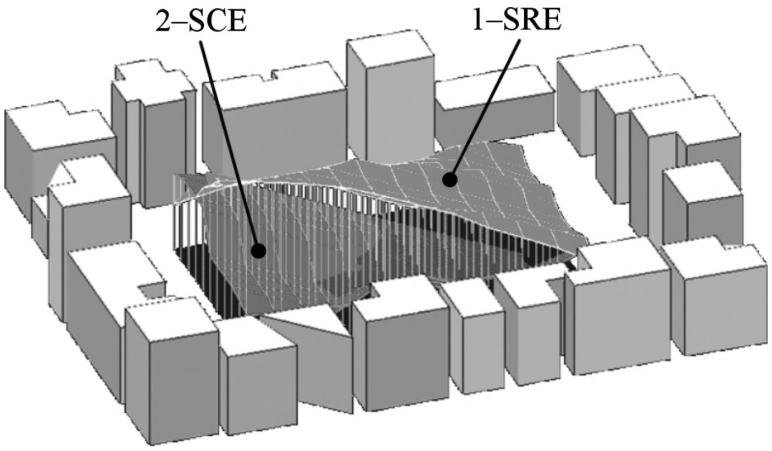


**Figure 13.1.** *Solar envelopes: solar rights envelope, 1-SRE; solar collection envelope, 2-SCE; and the resulting solar volume, SV*

In a non-built area, we can define lines on the ground to border each subdivision, and calculate the SRE in a way that ensures that shades produced by the buildings are not trespassing. In this case, the SRE obtained for each subdivision is also the SV. If all buildings' heights are designed below the SRE, the solar rights of each building will be ensured and there will be no negative influence from adjacent buildings (Figure 13.2).

## 13.4. Solar envelopes as a tool for urban development

Many cities and countries in the world defined regulations to keep solar rights. Some were created from a public point of view to keep open spaces and sidewalks insolated as defined in cities such as New York [NYC 12], San Francisco [SFG 12], Toronto [BOS 95], and Tel Aviv [CAP 03a]. In other places, regulations were defined to ensure the full use of private properties such as private open spaces and solar collectors. The cities also differ in their approach for application of the regulations.

The solar envelopes may also be implemented by city-planning authorities as a means of controlling development. As an example, the solar envelopes were adopted recently by the planning authorities of the municipality of Tel Aviv for the development of a 250,000-$m^2$ new business district [CAP 03a].

Solar exposure is undesired in Tel Aviv during the summer, but it may transform any open space and park to a very pleasant and enjoyable place in winter. Therefore, permanent shading, even if needed in summer, compromises winter exposure and thermal comfort achievement. A dynamic solution, such as planting deciduous trees in open spaces and sidewalks to allow shading in the summer and solar insolation in winter, is preferred. In general, at least one pedestrian sidewalk should be exposed to winter Sun to provide thermal comfort in winter. The other sidewalk, which is shaded in winter by the building itself, can be protected from the high summer Sun by permanent shading devices, or by evergreen trees. In addition, to motivate the usage of solar systems to produce hot water and electricity, their exposure should be achieved year-round as well.

In this case, the requirement was to achieve solar access during the entire winter, between 8.00 a.m. and 3.00 p.m. in the existing residential neighborhood, as well as in the main avenue that is the only available existing green open area. The solar envelope that fulfills the above requirement was accepted as a design ordinance for the relocation or reshaping of the tall buildings in the business district. Although the requirements were only to ensure solar access to the residential neighborhood, the demand that the main two avenues from west to east will be exposed to the Sun during the same period was considered. This was to ensure that the morning and afternoon walk from the railway station to work could be along sunny sidewalks. Moreover, it was suggested that the main inner street parallel to the main green

avenue would have solar access during lunchtime, from noon to 1.00 p.m. These requirements will allow people to enjoy walking in the Sun through the two avenues that lead them to the main green avenue, to have lunch in the garden, or in the planned restaurants along the green avenue.

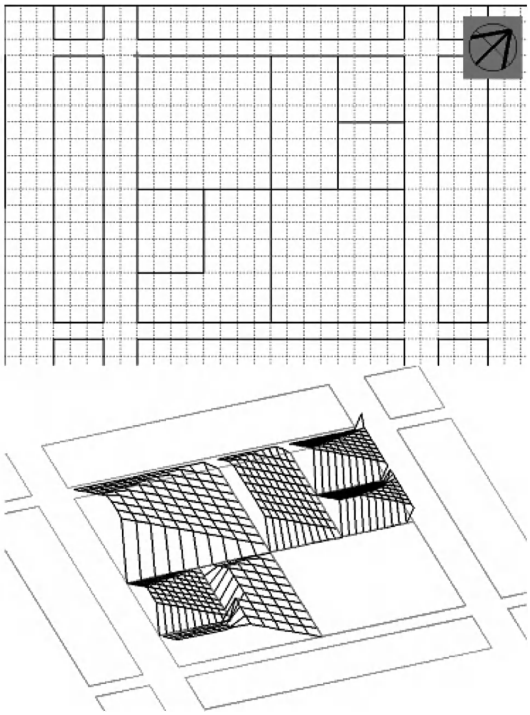

**Figure 13.2.** *The solar volume for a non-built area*

Figure 13.3 presents the solar envelope that fulfills these comprehensive requirements as determined by SustArc. All buildings higher than this envelope (these are the buildings that can be seen above the net of the envelope) must be displaced to another location, or should be reshaped. This is a descriptive approach in which all possible consistent solutions are given in advance. However, we combined this descriptive approach with a performance one, by allowing some exceptions, as long as the shading caused by these buildings is not above a given standard. The determination of such a standard should be done considering the influence of solar radiation on the overall energy performance of the buildings as well as taking into account pedestrians' comfort conditions in open spaces. Until now, several tall buildings have already been relocated and reshaped so that they will not exceed the given solar envelope.

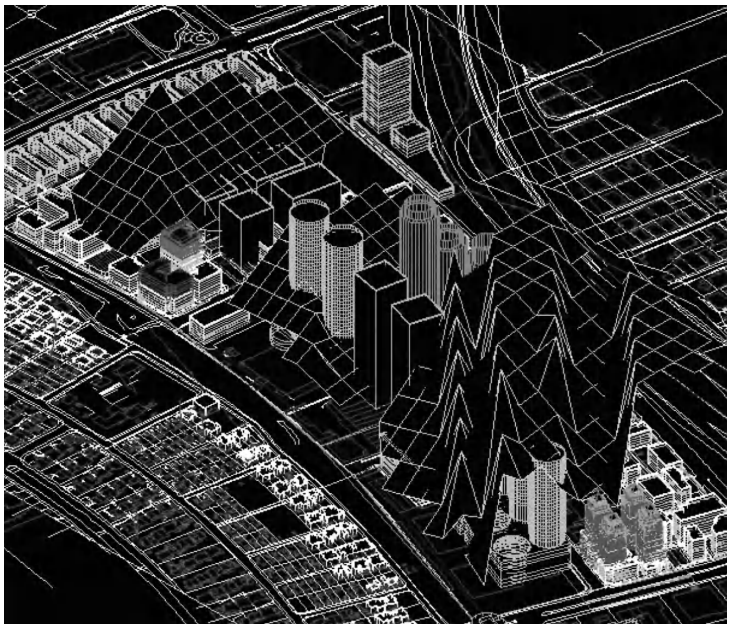

**Figure 13.3.** *The solar envelope that ensure solar rights in the existing residential neighborhoods as well as in the main avenues and streets*

A new green buildings standard SI5281 approved in Israel [SII 11a] included requirements regarding solar rights and solar access for buildings, solar systems, and open spaces. These requirements are based on regulations about windows' insolation that were used as a basis for the determination of objective criteria regarding solar exposure, which is described in the next section.

## 13.5. Regulations and applications

The Israeli Standard SI5282-1: Energy rating of buildings, residential buildings, defines the percentage of solar insolation needed in winter, as can be seen in Table 13.1. [SHA 02, SII 11b]. The standard was based on a study that examined the effect of solar insolation on energy consumption in buildings. The study showed that exposure to the winter Sun may reduce energy consumption significantly. The effect of insolation depends on the orientation of the facade, and was found especially important for all southern orientations (SE, S, and SW) and to some extent on the east and west facades (Figure 13.4). The energy consumption was only slightly influenced by the amount of insolation on the northern facades.

| | | Azim=90 | | Azim=135 | | Azim=180 | | Azim=225 | | Azim=270 | |
|---|---|---|---|---|---|---|---|---|---|---|---|
| | | Periphery | Center | Periphery | Center | Periphery | Center | Periphery | Center | Periphery | Center |
| Tel-Aviv | Total | 0.68 | | 1.76 | | 2.51 | | 2.09 | | 0.78 | |
| | SC(%) | 50 | 30 | 60 | 40 | 70 | 50 | 60 | 40 | 50 | 30 |
| | **required** | **0.34** | **0.20** | **1.06** | **0.70** | **1.76** | **1.26** | **1.25** | **0.84** | **0.39** | **0.23** |
| BeerSheva | Total | 0.70 | | 1.81 | | 2.59 | | 1.94 | | 0.82 | |
| | SC(%) | 50 | 40 | 60 | 45 | 70 | 55 | 60 | 45 | 50 | 40 |
| | **required** | **0.35** | **0.28** | **1.09** | **0.81** | **1.81** | **1.42** | **1.16** | **0.87** | **0.41** | **0.33** |
| Jerusalem | Total | 0.70 | | 1.81 | | 2.59 | | 1.94 | | 0.82 | |
| | SC(%) | 50 | 40 | 70 | 55 | 80 | 65 | 70 | 55 | 50 | 40 |
| | **required** | **0.35** | **0.28** | **1.27** | **1.00** | **2.07** | **1.68** | **1.36** | **1.07** | **0.41** | **0.33** |
| Eilat | Total | 0.68 | | 1.74 | | 2.47 | | 1.84 | | 0.78 | |
| | SC(%) | 60 | 30 | 50 | 30 | 50 | 30 | 50 | 30 | 50 | 30 |
| | **required** | **0.34** | **0.20** | **0.87** | **0.52** | **1.24** | **0.74** | **0.92** | **0.55** | **0.39** | **0.23** |

**Table 13.1.** *Required radiation for each orientation, urban location, and climatic zone. Requirements for Jerusalem in frame (radiation values are in kWh m$^{-2}$)*

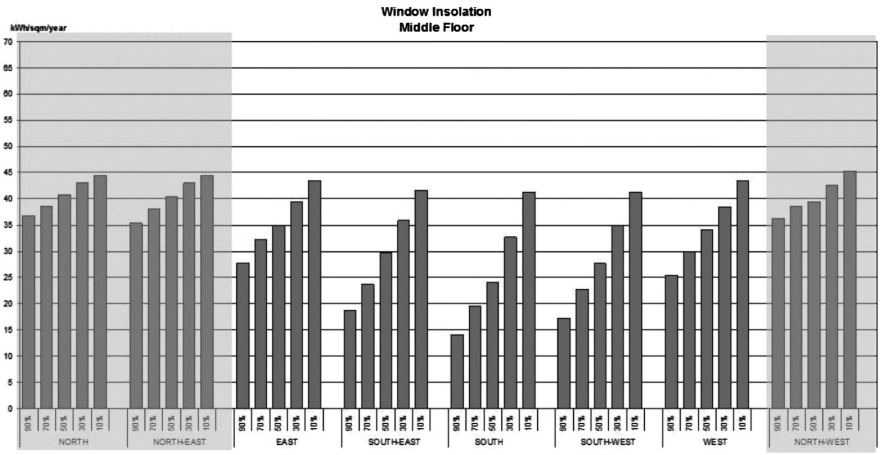


**Figure 13.4.** *The effect of winter solar insolation for different orientations for a middle floor apartment in Jerusalem. The northern orientations that are nearly unaffected are given in gray*

The amount of effective insolation was different for each of the four climatic zones in Israel. Therefore, the energy standard defines different requirements for each of these zones.

The energy rating standard also defined several levels of energy conservation: from a basic level to a high ("green") one. The requirements relate to these levels as well and indicate full and partial exposures. It is suggested that full exposure will be implemented for the city's peripheral areas to achieve better climatic comfort, while partial exposure will satisfy the requirements for more central areas where high density is desirable.

## 13.6. Methods of application

There are two approaches to apply solar rights regulations:

1) The performance method that defines the number of insolation hours needed [MEL 95, MEL 98].

2) The descriptive method in which the geometry of the buildings that meet the requirements is defined by regulating the building heights as in San Francisco [SFG 12].

This chapter suggests three levels of application for the regulations defined by the energy standard, based on the two aforementioned approaches [CAP 04, SHA 05]:

1) The basic level is based on the performance approach. It defines the required amount of radiation for each orientation, urban location, and climatic zone (Table 13.1). This method allows freedom in design, but is complicated in terms of implementation by designers and also for validation by authorities.

2) The second level, also based on the performance approach, indicates the insolation hours that meet the radiation requirements (Table 13.2). Validation of fulfilling the demands is possible, but still requires specific knowledge and the use of specific software.

3) The third level is a descriptive method, based on the insolation hours indicated. It presents the use of solar section lines that were developed from the solar envelope by using SustArc. These section lines serve as a simple tool for solar rights design (Figure 13.5). This method is easy to validate since designing according to these lines will always fulfill the requirements.

| | Periphery | Center | Periphery | Center | Periphery | Center | Periphery | Center | Periphery | Center |
|---|---|---|---|---|---|---|---|---|---|---|
| JERUSALEM | Azim=90 | sc50/40 | Azim=135 | sc80/65 | Azim=180 | sc80/65 | Azim=225 | sc80/65 | Azim=270 | sc50/40 |
| | sc 50 | sc 40 | sc70 | sc55 | sc 80 | sc65 | sc 70 | sc55 | sc 50 | sc 40 |
| required | 0.35 | 0.28 | 1.267 | 0.9955 | 2.072 | 1.68 | 1.358 | 1.067 | 0.41 | 0.33 |
| December | 9.30-11 | 10-11 | 9.30-13 | 10.30-14 | 9-14 | 10-13.30 | 10-14 | 9-13 | 12-14 | 12-13.30 |
| 6:00 | 0 | 0 | 0 | 0 | 0 | 0 | 0 | 0 | 0 | 0 |
| 7:00 | 0.05 | 0.05 | 0.05 | 0.05 | 0.03 | 0.03 | 0 | 0 | 0 | 0 |
| 8:00 | 0.17 | 0.17 | 0.22 | 0.22 | 0.14 | 0.14 | 0 | 0 | 0 | 0 |
| 9:00 | 0.23 | 0.23 | 0.37 | 0.37 | 0.29 | 0.29 | 0.04 | 0.04 | 0 | 0 |
| 10:00 | 0.18 | 0.18 | 0.4 | 0.4 | 0.38 | 0.38 | 0.14 | 0.14 | 0 | 0 |
| 11:00 | 0.07 | 0.07 | 0.34 | 0.34 | 0.42 | 0.42 | 0.24 | 0.24 | 0 | 0 |
| 12:00 | 0 | 0 | 0.24 | 0.24 | 0.39 | 0.39 | 0.31 | 0.31 | 0.05 | 0.05 |
| 13:00 | 0 | 0 | 0.14 | 0.14 | 0.34 | 0.34 | 0.35 | 0.35 | 0.15 | 0.15 |
| 14:00 | 0 | 0 | 0.05 | 0.05 | 0.29 | 0.29 | 0.36 | 0.36 | 0.22 | 0.22 |
| 15:00 | 0 | 0 | 0 | 0 | 0.21 | 0.21 | 0.31 | 0.31 | 0.23 | 0.23 |
| 16:00 | 0 | 0 | 0 | 0 | 0.1 | 0.1 | 0.19 | 0.19 | 0.17 | 0.17 |
| 17:00 | 0 | 0 | 0 | 0 | 0 | 0 | 0 | 0 | 0 | 0 |
| 18:00 | 0 | 0 | 0 | 0 | 0 | 0 | 0 | 0 | 0 | 0 |
| 19:00 | 0 | 0 | 0 | 0 | 0 | 0 | 0 | 0 | 0 | 0 |
| Total | 0.7 | 0.7 | 1.81 | 1.81 | 2.59 | 2.59 | 1.94 | 1.94 | 0.82 | 0.82 |
| *obtained* | *0.365* | *0.25* | *1.305* | *0.97* | *2.11* | *1.675* | *1.4* | *1.08* | *0.42* | *0.31* |

**Table 13.2.** *Required hours of insolation for mountain zone (Jerusalem) (in gray). Dotted pattern represents a half-hour (radiation values are in kWh $m^{-2}$)*

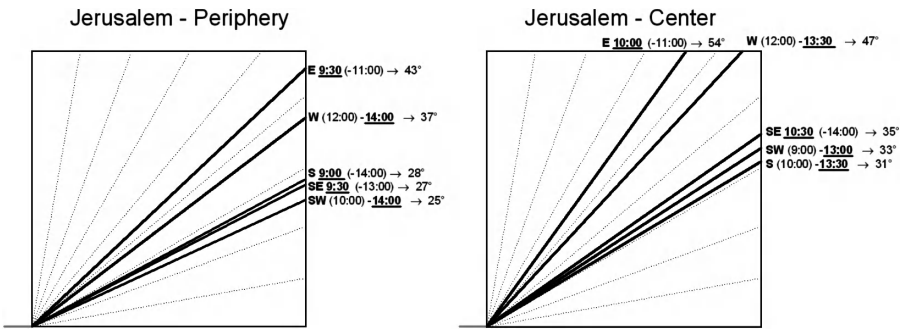


**Figure 13.5.** *Section lines for the temperate-cold mountain zone (Jerusalem), for central and peripheral locations. The hours of insolation required are indicated next to each line. The critical hours are in bold and underlined*

The solar rights requirements defined by the energy standard refer to residential buildings only, but this chapter extended the applications for the design of open spaces such as streets, sidewalks, and parks as well. When designing open spaces, the amount of radiation is irrelevant, thus one must keep either the required insolation hours or use the section lines.

## 13.7. A simple design tool

The section lines defined for the descriptive method are based on solar envelopes such as those described in the previous sections. The solar envelopes were created to keep the required insolation hours for each orientation, climatic zone, and urban location. Each section line represents the critical (lowest) slope of the relevant envelope.

Buildings that are lower than the section lines will keep the required hours of insolation for the relevant orientation. The section lines are used in three ways:

– To keep solar rights of neighboring residential buildings by defining a base point at the lower part of the first residential floor and using it to create the section lines to limit the building's height (Figure 13.6).

– To keep solar rights of sidewalks, it is required to expose at least 1–2 m of the sidewalk on one side of the street (1 m for central locations and 2 m for peripheral). Therefore, the base point of each section line is defined accordingly (Figure 13.7).

– To keep solar rights of other public open spaces, we must follow the three listed steps (Figure 13.8):

- Defining a triangle of the area needed to be insolated in the northeast and northwest sides (30% for central locations and 40% for peripheral [YEZ 05]). The hypotenuse should be parallel to the diagonal of open space.

- Defining the base points of the section lines in the middle of the triangle's hypotenuse.

- Creating the section lines using the angle of the south to limit buildings on the east, south, and west sides.

In cases where the open space is positioned at 45° from the main orientations, there would be only one triangle in the north. The section lines of the south will limit the buildings on the southeast and southwest sides.

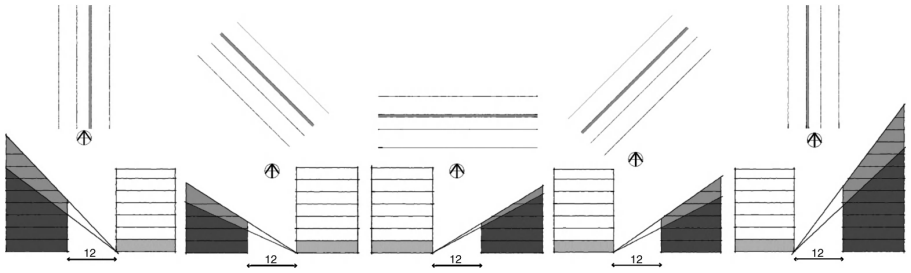


**Figure 13.6.** *Keeping solar rights of facades: defining base points at the lower part of the first residential floor and using the section lines from these points to limit building heights. Example for a 12 m-wide street in Jerusalem*

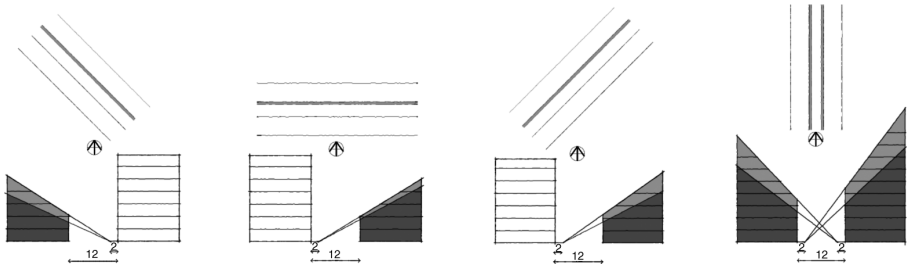


**Figure 13.7.** *Keeping solar rights of sidewalks: defining base points at 2 m from the edge of the sidewalk and using the section lines from these points to limit building heights. Example for a 12 m-wide street in Jerusalem*

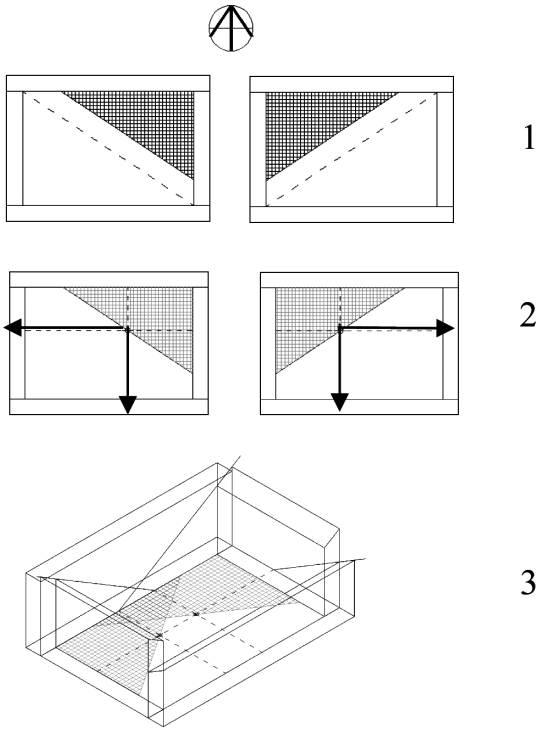


**Figure 13.8.** *Three steps for keeping solar rights in open spaces: 1) defining the area of exposure, 2) defining base points of section lines, and 3) limiting heights on the east, south, and west sides*

## 13.8. Modeling the building shape for self-shading using the solar collection envelope

The use of the SCE concept can be extended to protect building facades from overheating during the hot period of the year [CAP 03b]. In this section, we demonstrate the possible use of the SCE for the generation of the building shape to achieve self-shading, as mentioned above [CAP 96, CAP 97, CAP 01].

We can find examples of architectural solutions trying to achieve shading of pedestrian sidewalks by means of modeling a street profile or building shape that helps to protect the sidewalks from summer solar radiation.

There are also examples where designers tried to shape buildings in a way that enhances their thermal performance. This was done by determining the building's

form in a manner that allows both partial self-protection from solar radiation during a required period and its insolation in winter to achieve passive heating of the building.

Examples of such buildings are the Bank of Israel in Jerusalem (A. and E. Sharon), the Blue Cross and Blue Shield part of Connecticut Building in North Haven, Connecticut (Ellenzweig Associates, Inc.), and the city hall buildings of Bat Yam (Hecker, Sharon, Neuman), Boston (Kallmann, McKinnel, Knowles), and Tempe (Michael and Kemper Goodwin). The last example is rotated by 45° from the north–south axis. In these examples, an inverted pyramid-shaped structure was created so as to achieve self-shaded facades during a certain period in summer. It must be stated that a building with an inverted pyramidal geometry may increase its roof area as in the Tempe City Hall. Therefore, additional design solutions should be considered, avoiding very inclined walls, such as the use of deep windows as proposed in the Bank of Israel building (Figures 13.9 and 13.10). In this example, the combination of sloped walls with deep windows avoids the need for a greater depth in windows. The depth as proposed in the Bank of Israel is also appropriate for the placement of shelves under the windows. Moreover, installing the windows in the sloped surface, like in the Tempe City Hall, increases the window size. The stepped inverted pyramid as proposed for the Bank of Israel, the Blue Cross and Blue Shield of Connecticut Building, and the city hall buildings of Bat Yam and Boston, leaves the windows in a vertical position avoiding their oversize, as in Tempe.


**Figure 13.9.** *Bank of Israel, Jerusalem: Free view (left) and section (right). (A. and E. Sharon Architects)*

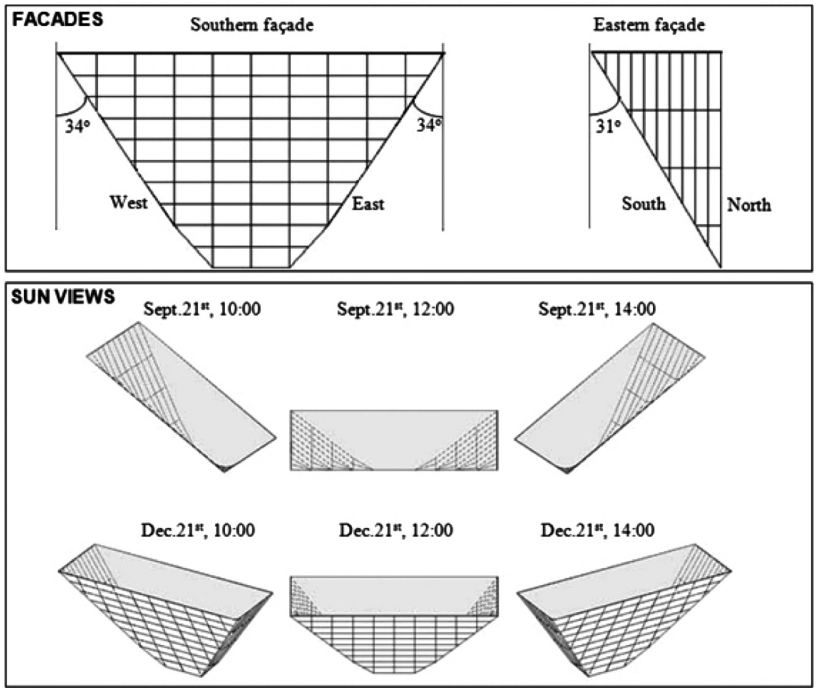


**Figure 13.10.** *The solar collection envelope for a north–south–oriented building. Required period: May to September, 10:00–14:00. Top: Facades. Bottom: SCE visual evaluation in September and December. The critical month is September. The critical time for south is noon, for east is 10:00, and for west is 14:00*

The SCE presents the lowest possible locus of windows and passive solar collectors on the elevations of a building so that they will be exposed to the Sun during a given period at winter, thus avoiding shading by existing buildings (Figure 13.1). In fact, this envelope represents the shading cones cast by existing buildings that constitute the built environment during the entire period as defined by the designer. It is also possible to determine the SCE produced by a building's roof during a required period at summer. In this case, the resulting surfaces will be shaded during that period by the building's roof. We can, therefore, use the SCE to determine the building's shape in a way that guarantees the building's elevations will be self-shaded during the required period. Since the SCE is, in this case, defined for a summer period when the Sun is high in the sky, the resulting surfaces will also be exposed to the lower winter Sun. In addition to that, the open areas adjacent to the building will be exposed to the winter Sun as well [CAP 03b] (Figure 13.11).

The required period for self-shading must be limited, particularly during the early morning and late afternoon hours, to avoid extremely sloped walls. Since solar gains during these hours could be significant in summer, an additional shading program must be determined for each of the facades.

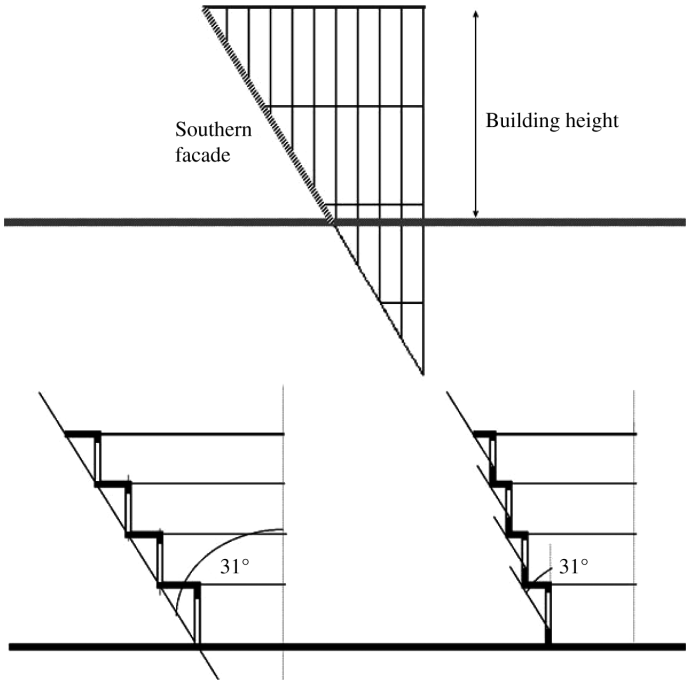


**Figure 13.11.** *Two possible design alternatives for the southern facade profile according to the SCE*

The design potential of these SCE makes them a useful design tool for the architect in the early stages of the design process, when a self-shaded building is expected to achieve an energy-saving design of the building. Designers and planners may get immediate graphic and numeric output for the design of different geometric variations based on the SCE, in an accurate and easy way. This tool can also be used at an urban level with the purpose of determining the profile of the streets so as to obtain shadowed sidewalks and facades during a required period at summer and expose them to the winter's Sun. The use of this design tool does not lead to a unique final design and hence the freedom of the architect is not limited.

## 13.9. Daylight rights

Building occupants prefer natural light and an outside view. In a well-designed space, daylight reduces energy costs, enhances the visual quality, and offers psychological benefits that are hard and expensive to imitate with electrical lighting. It has been shown that naturally lit spaces increases occupant satisfaction and improves worker productivity [NEE 70].

Lighting is responsible for 30–50% of all the energy utilized in commercial and office buildings. Daylight can be used to reduce lighting energy use and the heat gains associated with electric lighting. The efficient utilization of daylighting can dramatically reduce the total electricity load and the peak demand.

However, the availability of daylighting in certain areas of the city can be difficult due to the influence of the external built environment. In medium-and high-density zones, where office buildings are generally located, the lack of light from the sky at street level can cause design problems for the architect who wishes to use daylight to provide a high-quality working environment and as an energy efficient design strategy. Tall buildings and elongated obstructions can dramatically affect the amount of light received and its distribution inside the building [CAP 03c]. Given that only the upper floor in multistorey buildings can eventually make use of skylights, the only source of daylighting inside the office space is through side windows. In addition, the provision of side-daylit offices places limitations on building depth and interior organization. In dense urban areas, the arrangement of buildings is the most important factor affecting daylighting as well as the thermal comfort of public and private open spaces. The surrounding built environment can seriously affect the possibility of using daylight inside offices.

For this reason it is imperative that the development of new design guidelines for the design of the built environment considers not only the conditions of the open spaces between the buildings but also the internal daylighting implications and results.

## 13.10. Daylight access

The sky solid angle (SSA) presents the solid angle subtended by the patch of the sky visible from a point located at the center of the studied window. The SSA was proposed by Capeluto [CAP 03c] as a way to assess the influence of the external obstructions on the availability of daylighting inside a room.

Since a vertical window can potentially see only half of the hemisphere, the maximum possible value of the SSA for a completely unobstructed window, measured

in the external wall layer, is $\pi$ steradians. The SSA can be related to the average daylight factor inside a room. The SSA may be estimated easily by the architect in very early design stages using SunTools [CAP 11] as can be seen in Figure 13.12. In this way the architect can understand and assess from the beginning the potential and limitations of the selected site for the design of an energy conscious building and the design implications of the space location in the building.

The correlation between the obtained SSA values and average daylight factors (DFave) is presented in Figure 13.13. It can be seen that an SSA value of at least 1.4 sr is needed to obtain a DFave of about 3% and 2.2 sr to obtain DFave of 5%. As can be seen in Figure 13.13, this is, in particular, difficult to achieve in the lower floors if daylight access is not considered at the urban design level, and no special attention is given by the architect in the design of the building envelope and its internal organization.

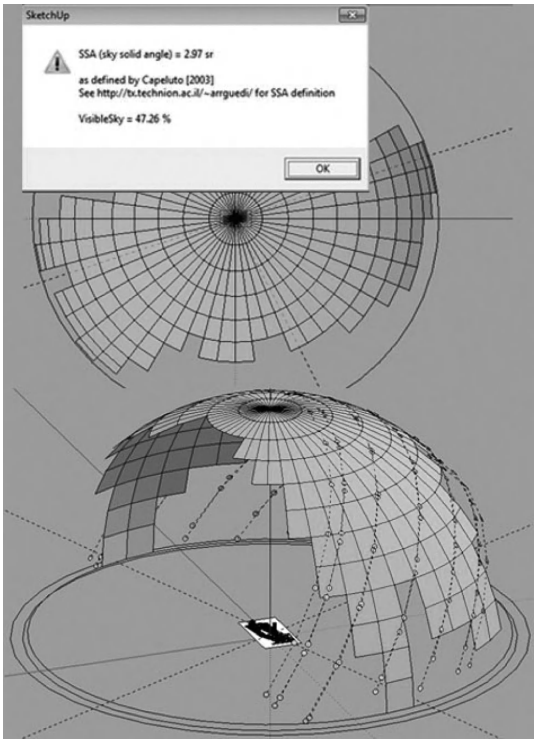


**Figure 13.12.** *The sky solid angle (SSA) as determined by SunTools*

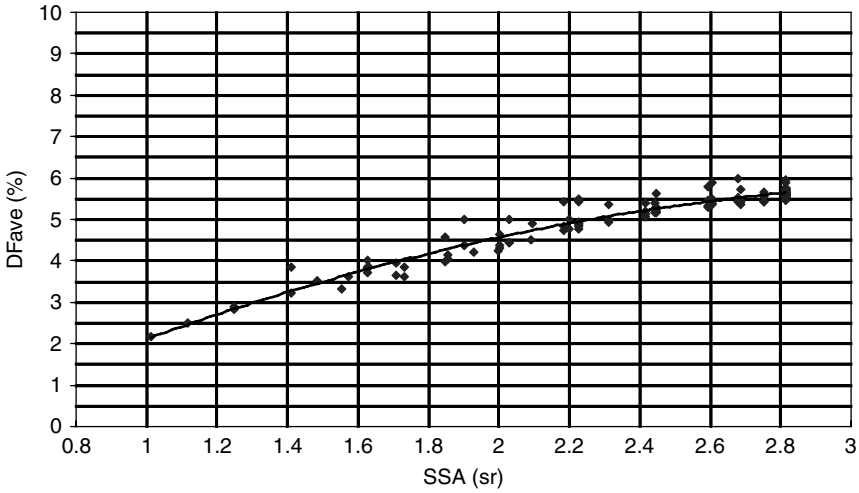


**Figure 13.13.** *Dependence of average daylight factor (DFave) for office spaces on the solid angle subtended by the visible patch of sky (SSA) from the center of the window*

## 13.11. Conclusions

There is no doubt that climate is among the important factors influencing the quality of the architectural solution from the energy and thermal comfort points of view and should be taken into consideration during the design process. The determination of the urban fabric should be made according to the specific climatic conditions of the site, allowing exposure of building facades and open spaces to the Sun during winter and of solar systems year-round, as well as providing shaded facades and open areas in summer. Since availability of natural light in dense areas of the city can be difficult due to the influence of the externally built environment, daylight access should also be considered. Appropriate comprehensive planning should consider ways of bringing together the different urban components to make use of renewable energy sources for passive heating and cooling of buildings, and create enjoyable streets and open spaces that sustain urban life.

This chapter presented the concept of solar and daylight rights as a way of helping designers in the determination of the building form. Furthermore, it demonstrated the possible use of solar envelopes as a design tool for urban development. The method proposed here can help architects to consider, evaluate, and, as a consequence, make informed design decisions by bearing in mind the solar and daylighting potential and limitations of the site, and its implications on building design. It can also provide valuable information to authorities trying to regulate

development in a way that considers solar and daylight access as a key for successful urban development.

## 13.12. Bibliography

[ARU 79] ARUMI F., "Computer-aided energy design for buildings", in WATSON D. (ed.), *Energy Conservation through Building Design*, McGraw-Hill, New York, 1979.

[BOS 95] BOSSELMANN P., ARENS E., DUNKER K., WRIGHT R., "Urban form and climate: case study, Toronto", *Journal of the American Planning Association*, Spring, pp. 61–62, 1995.

[CAP 96] CAPELUTO I.G., Architecture and environment-modeling a sustainable architecture, DSc Thesis, Technion-Israel Institute of Technology, Haifa, Israel, 1996.

[CAP 97] CAPELUTO I.G., SHAVIV E., "Modeling the design of urban grids and fabric with solar rights considerations", *Proceeding of the ISES 1997 Solar World Congress*, Taejon, Korea, pp. 148–160, 1997.

[CAP 01] CAPELUTO I.G., SHAVIV E., "On the use of solar volume for determining the urban fabric", *Solar Energy*, vol. 70, no. 3, pp. 275–280, 2001.

[CAP 03a] CAPELUTO I.G., YEZIORO A., SHAVIV E., "Climatic aspects in urban design – a case study", *Building and Environment*, vol. 38, no. 6, pp. 827–835, 2003.

[CAP 03b] CAPELUTO I.G., "Energy performance of the self-shading building envelope", *Energy and Buildings*, vol. 35, no. 3, pp 327–336, 2003.

[CAP 03c] CAPELUTO I.G., "The influence of the urban environment on the availability of the daylighting in office buildings in Israel", *Building and Environment*, vol. 38, no. 5, pp. 745–752, 2003.

[CAP 04] CAPELUTO I.G., YEZIORO A., BLEIBERG T., GAT D., SHAVIV E., Climatic and energy aspects of urban design in a temperate-cool climate region of Israel (in Hebrew), Technion Research and Development Foundation Ltd, sponsored by the Ministry of National Infrastructures, 2004.

[CAP 11] CAPELUTO I.G., "The meaning and value of information for energy-conscious architectural design", *Building Simulation BS2011, 12th International Conference of the International Building Performance Simulation Association*, Sidney, Australia, 2011.

[DEK 92] DE KAY M., "A comparative review of daylight planning tools and a rule-of-thumb for street width to building height ratio", *17th National Passive Solar Conference ASES*, Boulder, CO, 1992.

[KNO 81] KNOWLES R., *Sun Rhythm Form*, The MIT Press, Cambridge, MA, 1981.

[KOE 94] KOESTER R.J., "Energy armatures – ordering an integration of passive energy resources for community sustainability", *19th National Passive Solar Conference ASES*, San Jose, CA, 1994.

[KRO 85] KRONER W.M., ABREY D., "From the sun's point of view", *Proceedings of the 10th National Passive Solar Conference*, Raleigh, NC, 1985.

[MEL 95] MELBOURNE CITY COUNCIL, *Building Design Planning Requirements*, 1995.

[MEL 98] MELBOURNE CITY COUNCIL, *Melbourne Planning Scheme*, Clause 22 – Urban Design, 1998.

[NEE 70] NE'EMAN E, HOPKINSON R.G., "Critical minimum acceptable window size: a study of window design and provision of a view", *Lighting Research and Technology,* vol. 2, no. 1, pp. 17–27, 1970.

[NYC 12] NYC DEPARTMENT OF CITY PLANNING, http://www.nyc.gov/html/dcp/ (accessed 2012).

[OLG 76] OLGYAY A., OLGYAY V., *Solar Control and Shading Devices*, University Press, Princeton, NJ, 1976.

[SCH 93] SCHILER M., UENG-FANG P., "Solvelope: an interactive computer program for defining and drawing solar envelopes", *18th National Passive Solar Conference – ASES*, Washington, DC, 1993.

[SFG 12] SFGOV – SAN FRANCISCO CITY AND COUNTY, http://www.ci.sf.ca.us/planning (accessed 2012).

[SHA 75] SHAVIV E., "A method for the design of fixed external sunshades", *Build International*, Applied Science Publishers, UK, vol. 8, pp. 121–150, 1975.

[SHA 84] SHAVIV E., "Design tools for solar rights and sun-shades determination", *Proceedings of the 9th National Passive Solar Conference – ASES*, Boulder, CO, pp. 14–19, 1984.

[SHA 02] SHAVIV E., CAPELUTO I.G., YEZIORO A., BECKER R., VARSHAVSKY, A., Thermal performance of buildings and the development of guidelines for energy conscious design, part A – residential buildings (in Hebrew), sponsored by the Ministry of National Infrastructures, 2002.

[SHA 05] SHAVIV E., CAPELUTO I.G., YEZIORO A., BLEIBERG T., Solar rights in high density urban development (in Hebrew), technion Research and Development Foundation Ltd, sponsored by the Ministry of Housing and Construction, 2005.

[SII 11a] THE STANDARDS INSTITUTION OF ISRAEL, SI 5281, Sustainable buildings (Green buildings): requirement for residential buildings, 2011.

[SII 11b] THE STANDARDS INSTITUTION OF ISRAEL, SI 5282-1, Energy rating of buildings: residential buildings, 2011.

[YEZ 94] YEZIORO A., SHAVIV E., "A design tool for analyzing mutual shading between buildings", *Solar Energy*, vol. 52, no. 1, pp. 27–37, 1994.

[YEZ 05] YEZIORO A., CAPELUTO I.G., SHAVIV E., "Design guidelines for appropriate insolation of urban squares", *Renewable Energy*, Elsevier Ltd, vol. 31, no. 7, pp. 1011–1023, 2005.

# Chapter 14

# Solar Potential and Solar Impact

Urban engineering, more specifically urban environmental engineering, is an emerging field that is in its early stages of development. The urban system is complex; the scale of analysis is difficult to define, and simple and robust quantitative methods of evaluation are still limited. In a context where energy is of central importance, the issue of solar potential and its impact on a city or, more specifically, on an urban district, becomes a crucial question. The solar potential of a neighborhood varies according to the geographical latitude or even between cities at the same latitude, considering the fact that weather conditions fluctuate. The orientation of a neighborhood also impacts its solar potential.

Furthermore, with increasing world populations and the migration of rural populations to cities, engineers, architects, and city planners are confronted with the problems of building densification. Thus, how can urban districts be modified without unduly interfering with the solar potential in a context where environmental policies encourage the construction of low- or zero-energy buildings?

The issue of the solar potential applied at a neighborhood level certainly needs to be better understood. This chapter provides some answers for urban engineering practitioners. It is organized around a case study initially corresponding to some typical streets of the Plateau Mont-Royal district, in Montreal. Montreal is at latitude 45, midpoint between the Equator and North Pole, as are Lyon and Bordeaux (France), Torino and Milan (Italy), and Harbin (China). Besides, winters are much colder on the eastern coast of America than in Europe. So, it was decided to situate

Chapter written by Frédéric MONETTE and Benoit BECKERS.

*Solar Energy at Urban Scale* Benoit Beckers

the same typical street in five different cities to better estimate the influence of the different temperate and northern climates in Europe and America.

Solar radiation at the urban scale has been a source of studies since the end of 19th Century. It is noteworthy that this was already a concern of design for architects at the beginning of last century [NOB 22]. The main initiatives related to this problem were initially to arrange the buildings of a new district to avoid the effects of masks for natural light [LIT 98], or to analyze the solar and luminous contributions in existing neighborhoods [RAT 04]. Further work describes the sensitivity of solar radiation (heat and light) compared to the building density [STR 11] or evaluates the gain in consumption obtained, thanks to efficient constructions in urban canyons [ESC 12, NG 11].

## 14.1. Methodological considerations

The chapter is organized into five major sections as described in the following diagram (Figure 14.1). First, we make a selection of five major cities of the Northern Hemisphere, which have both similarities and important differences. The main criterion is to identify residential areas with the same typology in these five cities. The goal is to be able to identify the parameters that allow us to discriminate the different situations.

The second section consists of defining the geometry with the appropriate level of detail (LOD) and to introduce the geometrical quantities that have to be evaluated: sky solid angle (SSA), sunshine periods, and sky view factor (SVF). Sky models are used to calculate the effective solar irradiation taking into account the climatic data.

In the third section, the energy needs have to be quantified as well as the possible recovery of the solar energy for heating or for producing energy through photovoltaic (PV) panels. This section is mainly based on classical evaluations performed by thermal engineers to classify the behaviors of the buildings or of the urban districts.

In the fourth section, the results are discussed. Finally in the fifth Section, we present some conclusions and try to forecast future developments.

## 14.2. Definition of the residential area

The analysis focuses on cities with different climatic conditions, but with comparable urban geometry. The availability of climate data was a determinant prerequisite. The choice of the cities (Table 14.1) was made following these criteria:

three cities were located at middle latitudes (45°) – Montreal, Bordeaux, and Lyon; one city in southern latitude – San Francisco; and one city in northern latitude – Stockholm.

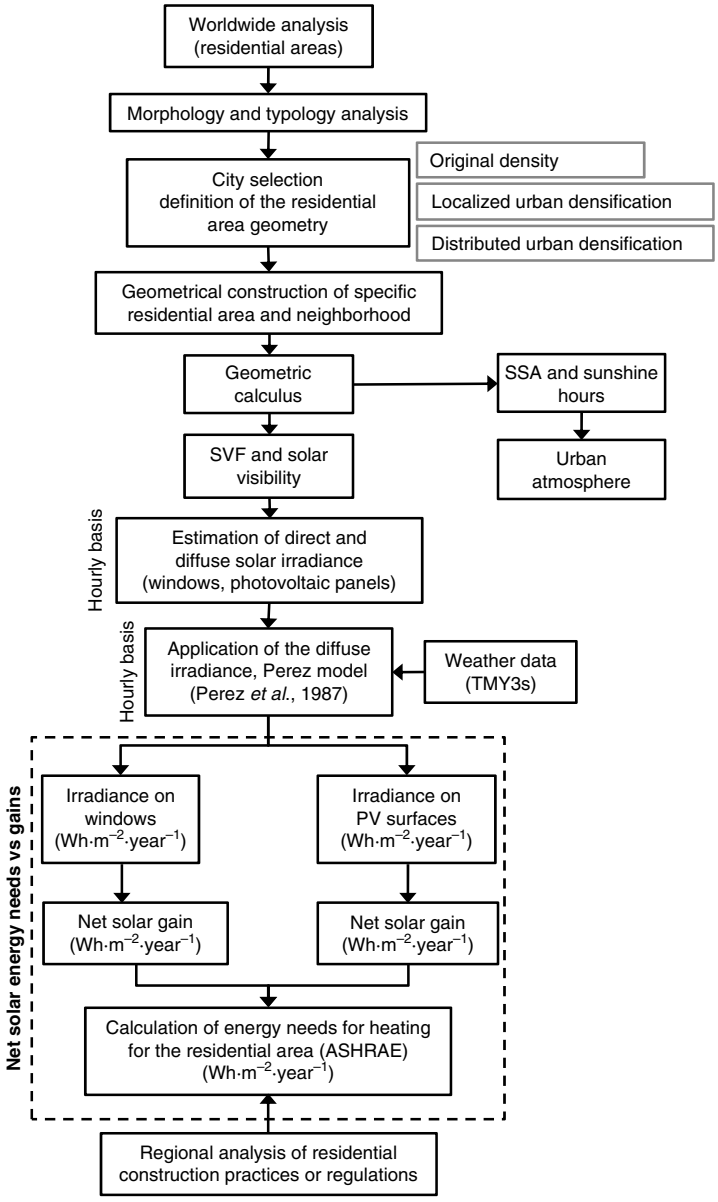


**Figure 14.1.** *Methodological approach*

| City | Latitude | Climate | Köppen climate classification |
|---|---|---|---|
| Montreal, Canada | 45°30′ | Humid continental | Dfb |
| Bordeaux, France | 44°50′ | Oceanic climate Mediterranean | Cfb |
| Lyon, France | 45°45′ | Oceanic climate | Cfb |
| San Francisco, USA | 37°47′ | Dry-summer sub-tropical | Csb |
| Stockholm, Sweden | 59°21′ | Limit between the humid continental climate and oceanic zone | Dfb/Cfb |

**Table 14.1.** *Climatic information of the five cities*

The geometrical model is based on a typology of urban form. For its definition, three cities of reference have been chosen (Montreal, Bordeaux, and Lyon), which present sufficiently similar morphologies as to propose an idealized street representative of each. Such a street is very similar to the streets of some particular districts of Stockholm and San Francisco.

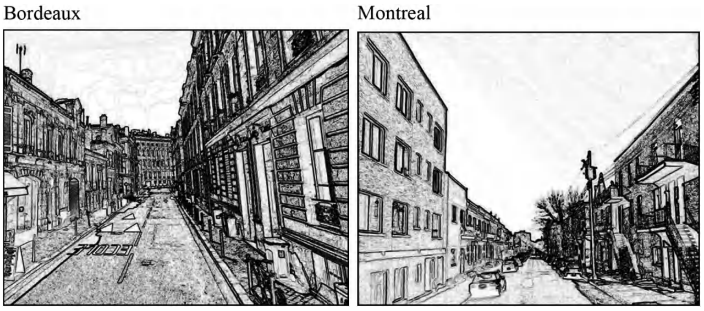


**Figure 14.2.** *Similar streets in two different cities*

Numerical simulation of physical phenomena at the urban scale requires a drastic simplification of the geometry, to preserve a compromise between accuracy and reasonable computing time [BEC 10]. The LOD of the geometrical model is similar to LOD 01 of the CityGML official OGC Standard, where buildings are represented as simple prisms with flat roofs [GRÖ 08], but with the difference that windows are included.

The street width is 12 m, which is the average of the existing streets. The block has fixed width and depth (W = 135 m, D = 45 m) and consists of different building

types. The aim is to reproduce the diversity of the real cases. We decided to set the buildings aligned to the width of the street, to have only N–S orientation. The presence of buildings inside the courtyard of the block is avoided (Figure 14.3).

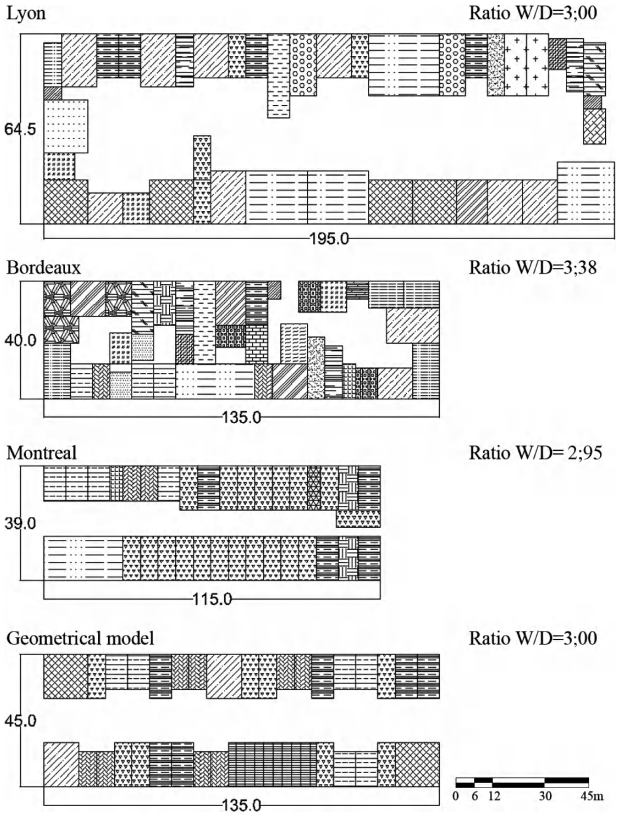


**Figure 14.3.** *Definition of the block*

The building types were defined after the analysis of the characteristics of the real buildings. There are buildings of two, three, and four floors. A representative 3-m floor height has been adopted. We added 1.5 m at the top. There is only one type of window (1.2 m width and 1.5 m height). The wall thickness, the frame, and the existence of doors are neglected (Figure 14.4).

The most representative characteristics of the buildings (depth, width, height, and number of floors) and windows (number, dimensions, position, and glazing ratios) were used as reference for the definition of 10 building types (see Figure 14.5).

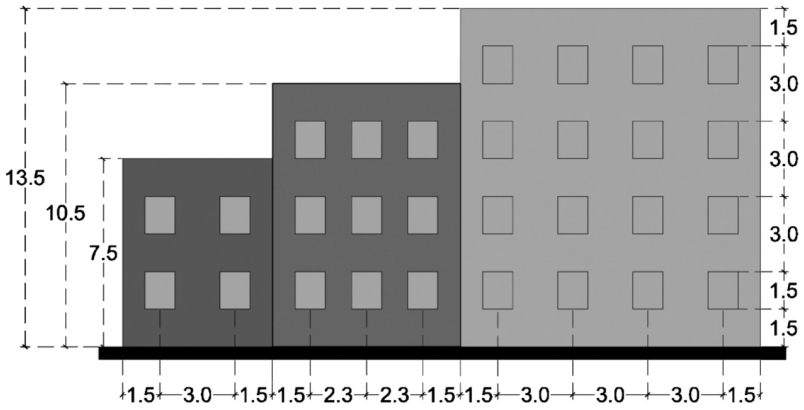


**Figure 14.4.** *Determination of the height and position of the windows*

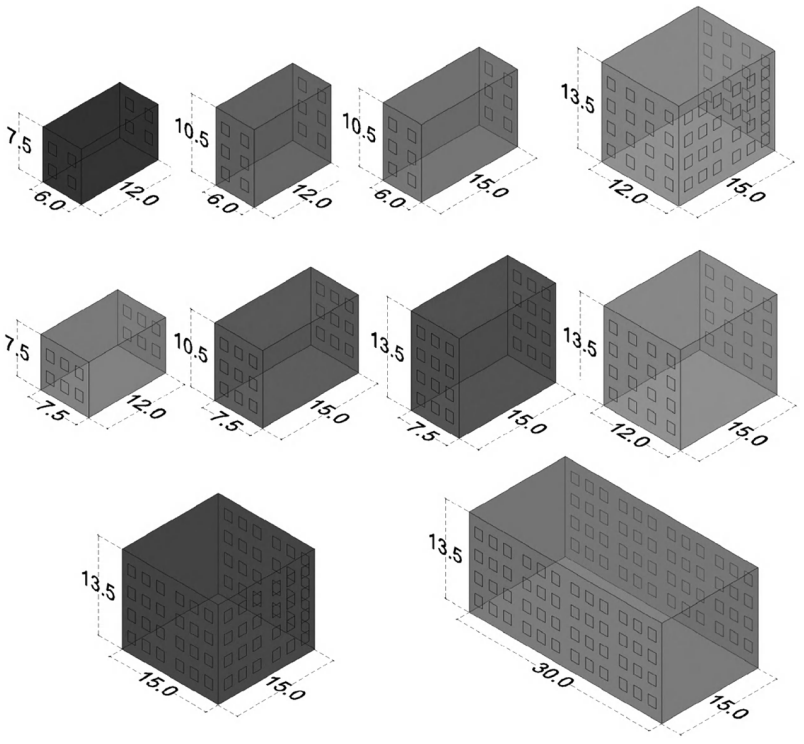


**Figure 14.5.** *Building types*

The definition of the window types, their number, and the position in each facade of the building types was carried out after the analysis of the most representative actual buildings found in the three cities (see actual facades of Figure 14.6). Owing to the deformations caused by the perspective of the photography, it is necessary to design a simplified facade without the decorative elements, to set the measures, proportions, and glazing ratios (see simplified facades). We can notice that there is a big diversity in the characteristics of the windows; however, a "realistic" reproduction of this diversity will not allow us to interpret and compare the results because of the exceeding number of variables. For this reason, the number and position of the windows in the buildings types was settled similar to the real facades. The dimension and proportion of the most common window was adopted as the window type. The most important parameter to maintain is the real glazing rates (%).

It is obvious that some glazing rates do not match exactly in each building, but as we study the whole street section, it is sufficient to consider only the total facade glazing rate (Figure 14.6).

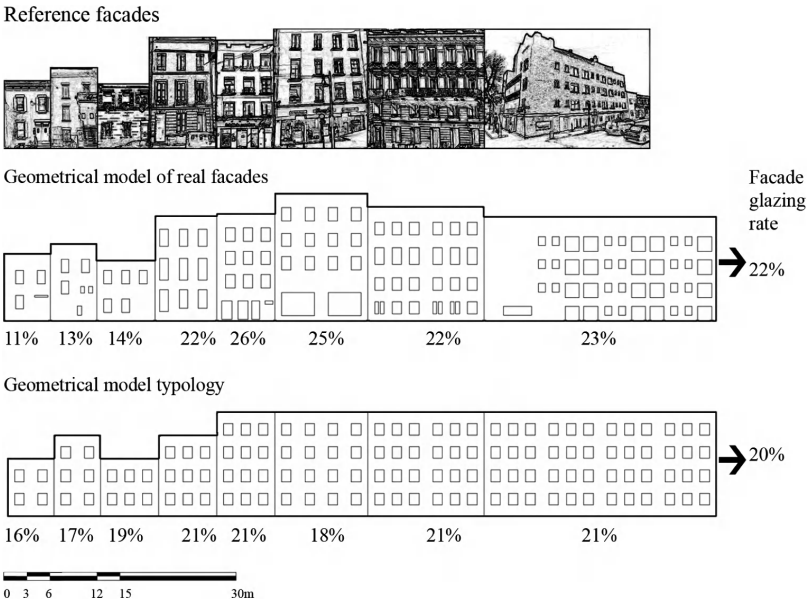


**Figure 14.6.** *Definition of the facades of buildings types*

The block consists of 33 buildings. The buildings are used for housing purposes. The LOD of the neighborhood corresponds to [LOD 01]. The average height of the constructions is 10.5 m. The width of the street is uniform. The distance between the buildings in the courtyard varies between 15 and 21 m (Figure 14.7).

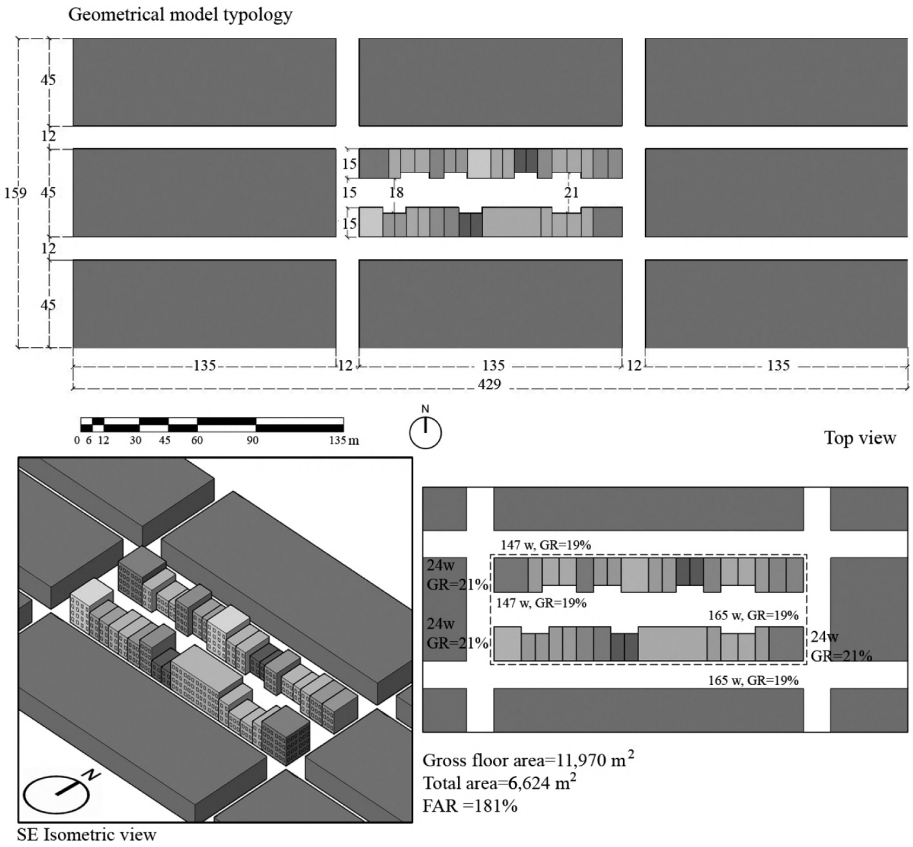


**Figure 14.7.** *Geometrical model typology* (*GR = glazing rate; w = numbers of windows)*

Different density measures such as building density, population density, and city density [FOR 03] can be used. We have chosen to use the building density because it is more appropriate for the scale used for the study. Building density can be estimated using the floor area ratio (FAR), also known as plot ratio. It is the ratio of the built floor area on all floors divided by the parcel area [FOR 03, PAN 08].

We decided to increase the original density of 30% in two scenarios:

– Distributed densification: It consists of adding one floor to each building of the block and of the neighborhood.

– Localized densification: It consists of adding the equivalent area to two existing buildings.

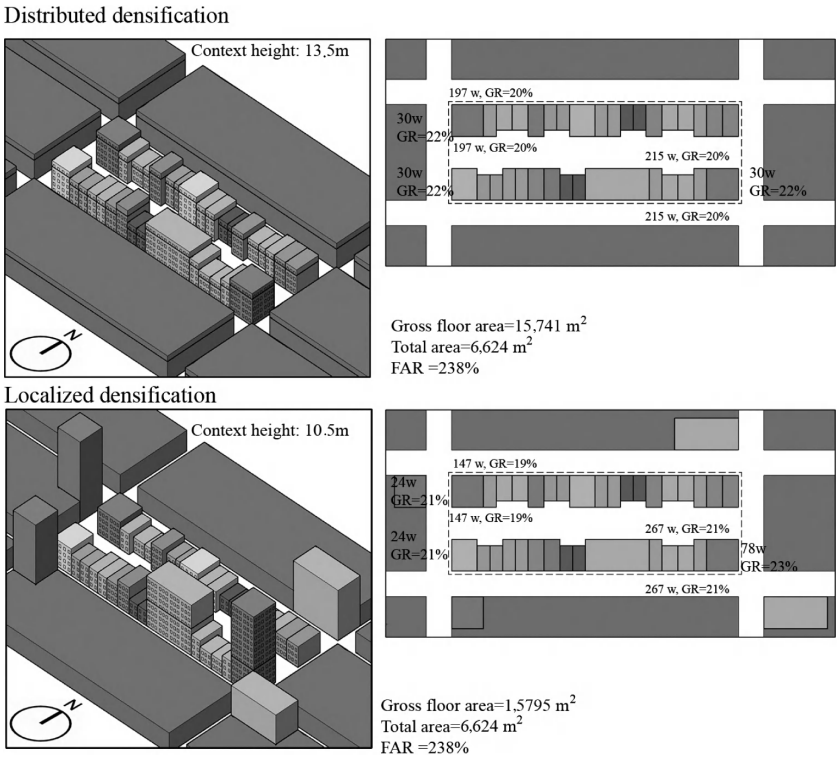


**Figure 14.8.** *Densification scenarios (GR = glazing rate; w = numbers of windows)*

## 14.3. Estimation of irradiance and solar gains

The SSA is the solid angle of the part of the sky seen from a point as compared to the solid angle of the hemisphere surrounding the point. The calculations were performed with the tool Heliodon 2 [BEC 06]. The visibility of the Sun is presented with two kinds of graphs: stereography and number of hours of Sun exposure. These indicators are purely geometric and depend only on the urban shape for the sky form factor, orientation and latitude for the visibility of the Sun. In this step, the evaluations are performed without considering diffuse input or climatology.

This calculation step is performed to estimate the solar energy received by the window surfaces of each of the buildings in the modeled area (and its variants) or the inclined surfaces of PV panels. As appropriate, the estimates were made either on an annual basis or on the heating period, when building energy needs are greater and the angle of incidence of the Sun is lower.

On the basis of the detailed definition of each building, each window was represented by a single point at its center. This approximation is valid given the limited size of the windows. Moreover, it also reduces significantly the computation time.

The visibility of the Sun is then calculated for all points on an hourly time scale. This scale consists of following the Sun's path and to check for each point that the Sun is not hidden. The SVF, which represents the portion of the flux emitted by the celestial sphere (assumed isotropic) captured by the point (diffuse energy), is calculated for each evaluation point.

The Perez model applicable to inclined surfaces [PER 87] is then used to represent the diffuse solar radiation. The value 0.7 of visible light transmittance of glazing is applied to the incoming flow. The Perez model has been included in a large number of buildings and solar conversion system simulation programs.

Owing to its simplicity and worldwide applicability, we have chosen to use this model. To simulate the climate conditions of the entire year, we used the typical meteorological year (TMY3) data sets derived from National Solar Radiation Data Base update. TMY3 provides files for each city. The TMY3s are data sets of hourly values of solar radiation and meteorological elements for a 1-year period. Their intended use is for computer simulations of solar energy conversion systems and building systems to facilitate performance comparisons of different systems, configurations, and locations [WIL 08].

The reflections from surfaces in the vicinities have not been considered, which means that the results of solar energy on the windows are slightly underestimated. Similarly, the impact of the trees was not taken into account. However, since the calculations were made for the heating period, that is to say when the foliage is generally not present, the impact on the results is potentially insignificant.

Solar gain in $Whm^{-2}$ on various inclined surfaces of the PV panels was calculated using the same calculation steps as for the windows. The calculations take into account both direct and diffuse contributions, and consider the climatic data, but they exclude the effects of reflections from adjacent surfaces. For purposes of estimating the solar gains, the panels were installed on the roof surfaces receiving direct sunlight annually on at least 90% of their surface. In practice, the working surface layout of the panels on roofs was considered equivalent to 90% of their surfaces.

For estimation purposes, panels of about 1 $m^2$ (1.5 m × 0.7 m) were placed in their optimal orientation over the year on the various exploitable roofs. The choice of spacing between the panels is a compromise between the energy received on the roof area and production per square meter of panel [BAY 10]. These authors propose as a criterion, in the city of Zaragoza (41°39′), that the panels do not shade

off a row over the other on December 21 at 12:00 noon. At the latitude of Stockholm, where the Sun is 6° high at this date, this criterion imposes a too large spacing between the panels and therefore a misuse of available space for the symbolic winter solar flux. To limit losses by taking into account the latitude, we placed the panel in a way that the lower 10 cm of each panel is receiving at least 95% of direct solar radiation over the year.

PV panel on facades covers all the available south-oriented walls of the towers when they are free of Sun mask. For the final calculation, we assume that all the panels are fully exposed to the Sun.

An electric conversion rate of 15% was used for calculations, although the latest commercial technologies give rates close to 20%. The panels were considered new, knowing that rates of deterioration of the panels less than 1% per year are observed in practice. Yield losses for fouling or accumulation of snow, about 3.5% on an annual basis, have been neglected. It is the same with respect to heat loss, or spectral reflectance, or other specific losses of around 5% [THE 11]. These approximations are considered acceptable given the scale of study in which magnitudes are rather sought after.

Progress on technology panels and the drop of their cost of production suggest a wider use during the next decade. Yields over 30%, or higher, will be certainly achieved within two decades.

## 14.4. Estimation of energy needs for heating

The heating requirements of buildings of five residential areas (San Francisco, Montreal, Bordeaux, Lyon, and Stockholm) were estimated using the method of the American Society of Heating, Refrigerating, and Air-Conditioning Engineers (ASHRAE). The method of calculation, based on residential load factor, is a simplification of the method detailed in [ASH 09] that incorporates the dynamics of the internal contributions (residential heat balance, RHB).

In the simplified method, we consider all the losses of the building and the annual degree-days heating for a given city according to a balance point temperature (outside temperature) of 18.3°C. The annual values of degree-days (provided by the statistics of ASHRAE based on 20–30 years of data) are obtained by considering the sum of the difference between the reference value of 18.3°C and that of the average daily outdoor temperature. For simplicity, below 18.3°C, we consider that the internal energy inputs (human, bulbs, etc.) are no longer sufficient to maintain a comfortable temperature of 20°C inside the building, which then causes the starting of the heater. The magnitude of the values obtained is sufficient in the context of this

study since it is primarily designed to contextualize the results of solar contributions to the neighborhood level. Moreover, according to ASHRAE, "A climate's severity can be concisely characterized in terms of degree-days".

Needs (losses) on heating were evaluated for two reference years, 1960 and 2010 (renovated buildings). Regionalization of the building materials and their heat transfer coefficient (leading to losses) were selected on the basis of various existing regulatory documents or standards from local agencies. Thus, on the basis of a unit area, the product of the heat transfert coefficient (walls, roofs, windows, doors, etc.) in W $K^{-1}$ and degree-hours in K-h yields the need for heating in Wh. Finally, the heating times for selected cities are October 15 to May 15 for Montreal, Bordeaux, and Lyon; from October 1 to April 30 for San Francisco; and from October 1 to May 31 for Stockholm.

## 14.5. Results analysis

We are interested primarily in urban environments. Figure 14.9 shows the SSA calculated at the street level and on the facades for the three proposed configurations. The distributed densification is giving the major reduction of the sky view.

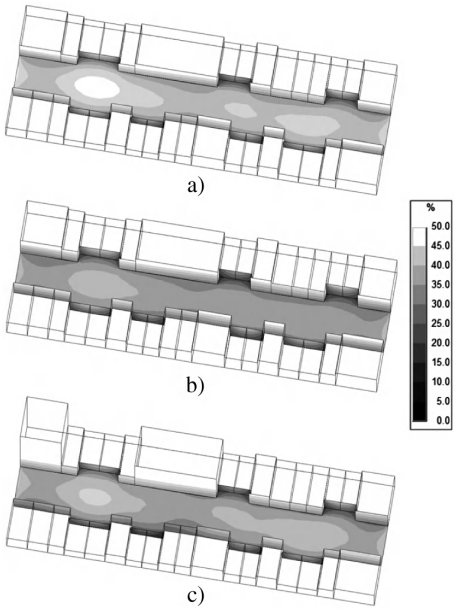


**Figure 14.9.** *Sky solid angle for (a) original density, (b) distributed densification, and (c) localized densification*

In Figure 14.10, we show the sunshine of the original configuration for the orientations of the east–west street at 45° and north–south. In the figure, the three solar diagrams are calculated in the center of the street. The east–west orientation, which is the best, as we shall see, for the buildings (themselves north–south) is the worst from the urban point of view: only the summer Sun reaches the ground. At 45°, the possibility of having the Sun in winter depends on the environment of the street. With a north–south orientation, sunshine is guaranteed. The three charts below show the number of hours of sunlight at the equinoxes, when the Sun is particularly likely to cause overheating and glare. Again, the east–west orientation causes problems because the entire south facade receives considerable sunshine, while the north facades are constantly in the shade. We should add that this effect can be utilized for through-ventilation, which explains the lack of agreement between specialists on urban environments [ERE 11] and bioclimatic architecture [ESC 12].

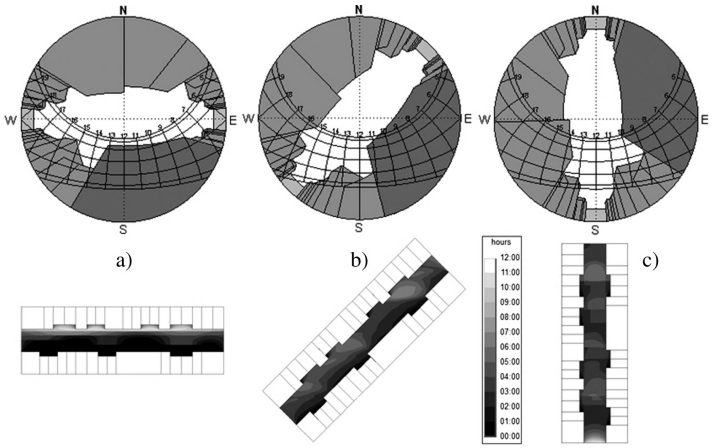


**Figure 14.10.** *Stereographic view (from the center of inner courtyard) and sunshine hours (equinox day) at Montreal, for the original density case rotated at (a) 0°, (b) 45°, and (c) 90°*

Figure 14.11 shows the variation of the total radiation received on a yearly basis depending on the orientation of the surface area and taking into account the diffuse component of solar radiation and climatic conditions. In accordance with their respective latitudes, the figure shows the extreme values of minimum and maximum, respectively, in Stockholm and San Francisco. In addition, a leftward shift of the maxima is observed between Stockholm and San Francisco, which is also consistent with the incidence angle of the Sun at the different latitudes.

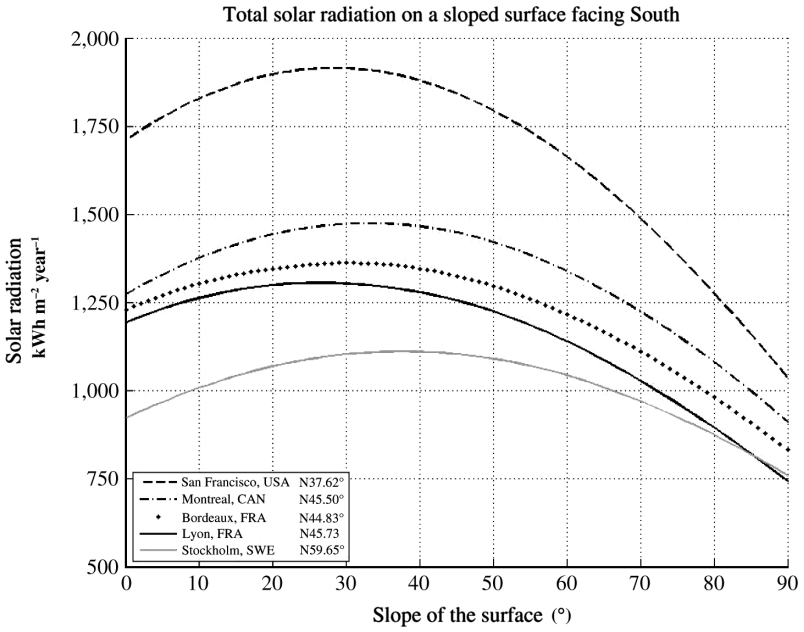


**Figure 14.11.** *Annual solar irradiation on a tilted surface facing south, for a slope angle varying from 0° (horizontal) to 90° (vertical)*

The curves obtained for cities of similar latitudes show significant unexpected differences. Indeed, the maxima move up to a tilted angle of nearly 26° in Lyon, 30° in Bordeaux, and almost 33° in Montreal. The values obtained for the cities of Lyon, Bordeaux, and Montreal are, respectively, 1,304, 1,361, and 1,474 $kWhm^{-2}$ $year^{-1}$. Hence, despite its climate in winter, Montreal, clearly more northerly, has an advantageous position in terms of solar field with a value greater than 13%, compared to Lyon.

This means that the temporal sequencing of cloud cover or the cloud characteristics is sufficiently different between cities to generate a translation of the maxima depending on the tilt of the panel and a differentiation of the values of the obtained fields. This type of result means in practice that necessarily Lyon enjoys a climatic advantage in summer, because a lower tilt is observed at the optimum. However, Montreal enjoys a climatic advantage in winter, because a higher tilt is observed at the optimum.

Furthermore, analysis of all curves shows little variation near the extremes. From a technical point of view, this means that there are few issues related to the accuracy

of the tilt angle of a panel. Indeed, a variation of ±5° in the installation of the panel shows no significant differences in the final solar field. The variation in the vicinity of the maximum for San Francisco is however higher than that for other cities, but still insignificant, within inside a gap in the ±5°. In the case of Montreal, in practice, the results indicate that the panel could be adjusted to an angle slightly greater than that corresponding to the maximum to limit the accumulation of snow.

Figure 14.12 shows the same curves, but calculated on the heating period presented above. In Stockholm with a warm-up period that is 1 month longer, it is normal to observe a relative increase. Displacements of the peaks confirm the observations made previously.

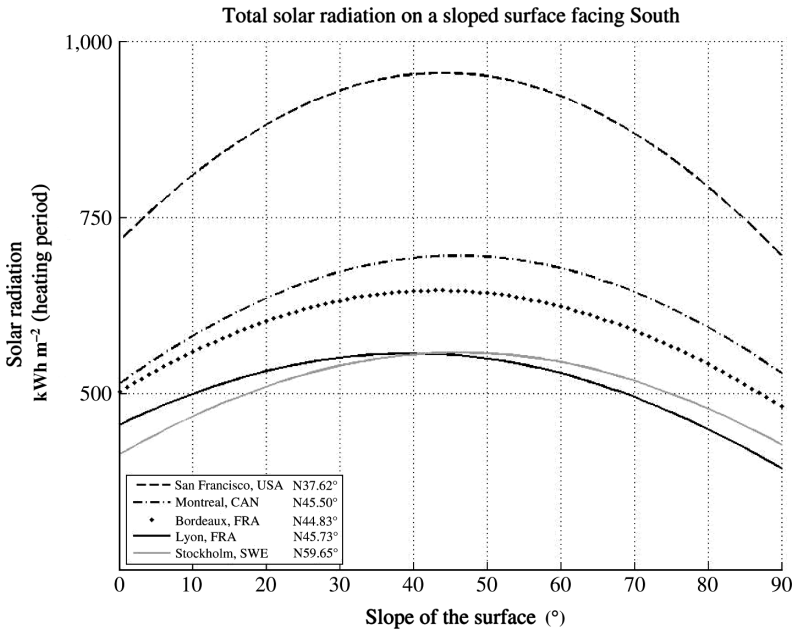


**Figure 14.12.** *Solar irradiation on a tilted surface facing south during the heating period, for a tilt varying from 0° (horizontal) to 90° (vertical)*

Figure 14.13 shows the variation in solar inputs on all the windows for the five cities, in function of the orientation (initial configuration, east–west oriented, then rotated anticlockwise by increments of 10°).

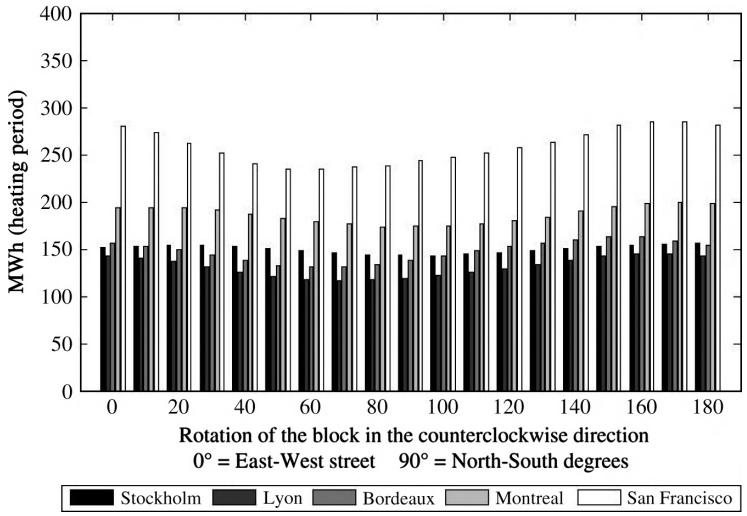


**Figure 14.13.** *Solar heat gain during the heating period in the original configuration*

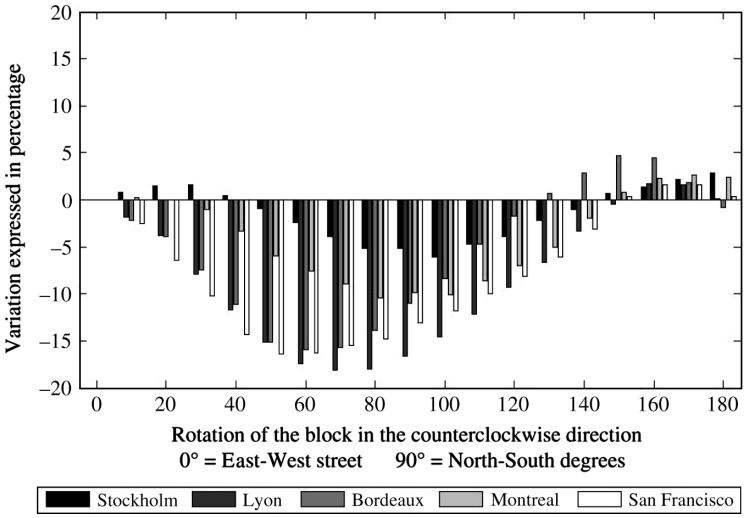


**Figure 14.14.** *Solar heat gain during the heating period in the original configuration, expressed as a variation of the original east-to-west orientation of the street*

Figure 14.14 shows the variations from the initial configuration in percentage. As expected, the first rotations reduce the solar gain. Indeed, the east–west street orientation and therefore the north–south building is the optimal one. However, we

note that, from 140°, there is an improvement for some cities. This result is due to the asymmetry of the street and buildings that line it. Further analyzes are needed to better understand the influence of the geometry and its LOD on the results, as well as climate and average changes in cloud cover throughout the day and the heating period. These results also show that San Francisco receives the most important solar gains, followed by Montreal. Stockholm, despite a longer period of integration, is the same as Bordeaux. Lyon, where winter is cloudier, brings up the rear.

Figure 14.15 shows the solar gains, compared to the heat losses for buildings that meet the thermal standards of 1960 and 2010, depending on the configurations (original, distributed, or localized), for the five cities. Here, the Nordic character of the Montreal winter is obvious, with input counterbalancing only 20% of the heat losses for new buildings (like in Stockholm), while these gains reach almost 30% in Lyon, 40% in Bordeaux, and over 80% in San Francisco.

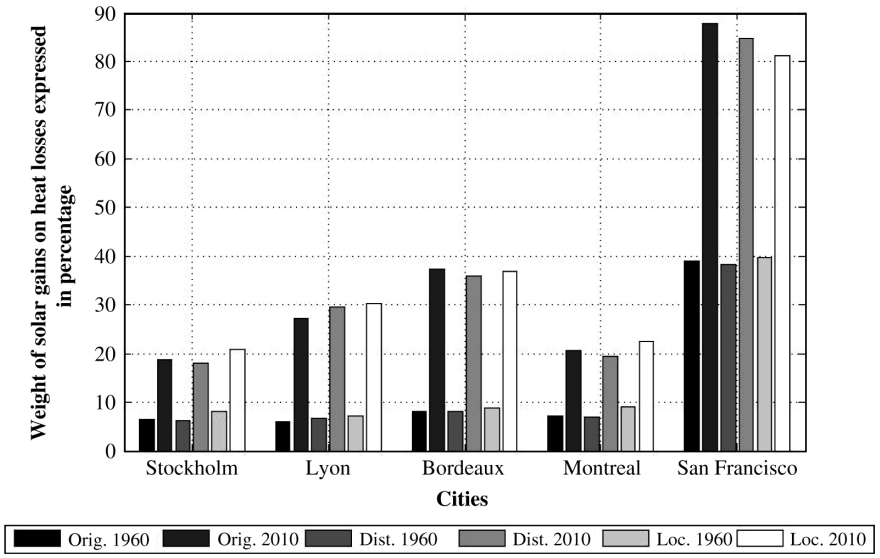


**Figure 14.15.** *Solar heat gain during the heating period: East–west orientation for original configuration, distributed densification, and localized densification*

These results change a little depending on whether the buildings are oriented north–south or east–west (Figure 14.15 vs. Figure 14.16). Densification, which brings both new obstructions and new glass surfaces, has also a small influence.

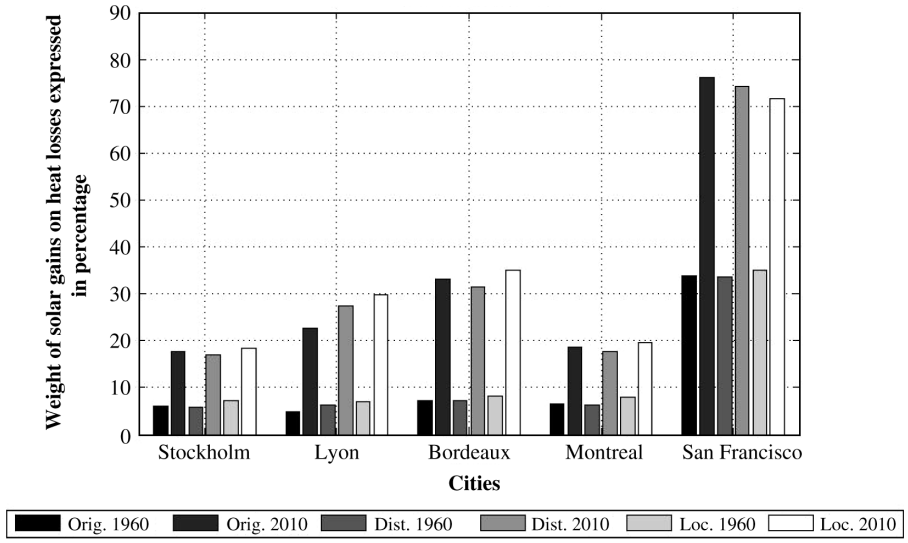


**Figure 14.16.** *Solar gains during the heating period, north–south orientation*

Table 14.2 shows PV results for the initial urban configuration and the localized densification (yearly and during the heating period). In the case of the initial urban densification, the results related to the total energy contribution for the roofs are practically in agreement with the optima presented in Figures 14.11 and 14.12. This result was expected given the fact that the surfaces of installed PV panels are the same for four of the five studied cities, a slight loss of surface being observed for Stockholm. This conclusion also applies to the distributed densification, because adding a floor to each building does not involve loss of exploitable areas.

The results for the localized densification show a non-negligible loss of usable surfaces (compared to initial urban densification), and consequently of surfaces equipped with PV panels. Energy losses produced by the panels are equal to 57% in Stockholm, Lyon, Bordeaux, and Montreal and at nearly 53% in San Francisco. Thus, localized densification strongly influences the energy produced by the panels, but the geographical location of the cities (latitude) does not significantly impact the magnitude of losses in PV energy since they remain in the vicinity of 55%. These conclusions are valid for yearly periods and during the heating period (Figure 14.17).

To compensate for losses from a localized densification, a strategy lies in the installation of PV panels on south-oriented vertical walls of the two high buildings (716 m² available). Indeed, the results show that this strategy would fully compensate the losses observed after the localized densification during the heating period (Figure 14.17), despite the fact that the south-oriented vertical walls show

energy per unit area (kWhm$^{-2}$) reaching only 72–78% of the optimally tilted panels (surface facing south).

| Parameters | Stockholm | Lyon | Bordeaux | Montreal | San Francisco |
|---|---|---|---|---|---|
| Exploitable surfaces (roofs), m$^2$ | | | | | |
| – Initial urban configuration | 2,255 | 2,255 | 2,255 | 2,255 | 2,255 |
| – Localized densification | 968 | 968 | 968 | 968 | 1,058 |
| Optimal panel tilt (surface facing south) | 38 | 26 | 30 | 33 | 28 |
| Installed panels areas, m$^2$ | | | | | |
| – Initial urban configuration | 808 | 1,012 | 1,012 | 1,012 | 1,012 |
| – Localized densification | 352 | 440 | 440 | 440 | 480 |
| Energy per unit area, optimal tilt, kWh·m$^{-2}$ | | | | | |
| – Yearly | 1,110 | 1,304 | 1,361 | 1,474 | 1,914 |
| – Heating period | 553 | 544 | 631 | 680 | 922 |
| Potential of solar energy on PV surfaces on roofs, MWh | | | | | |
| – Yearly | | | | | |
| - Initial urban configuration | 897 | 1,320 | 1,377 | 1,492 | 1,937 |
| - Localized densification | 391 | 574 | 599 | 649 | 919 |
| – Heating period | | | | | |
| - Initial urban configuration | 447 | 551 | 639 | 688 | 933 |
| - Localized densification | 195 | 239 | 278 | 299 | 443 |
| Energy per unit area, south vertical wall, kWh·m$^{-2}$ | | | | | |
| – Yearly | 758 | 741 | 831 | 910 | 1,036 |
| – Heating period | 427 | 393 | 481 | 528 | 696 |
| Potential of solar energy on PV surfaces on south facades (716 m²), localized densification case, MWh | | | | | |
| – Yearly | 543 | 531 | 595 | 652 | 742 |
| – Heating period | 306 | 281 | 344 | 378 | 498 |

**Table 14.2.** *Photovoltaic results*

The analysis on an annual basis shows that this strategy would not fully compensate the losses observed after the localized densification, except for the city of Stockholm, where a surplus of nearly 4% would be produced with respect to the original urban densification. The strategy would still produce for the cities of Lyon, Bordeaux, Montreal, and San Francisco, respectively, 84%, 87%, 87%, and 63% of

PV energy produced by the initial urban densification. The opposite results obtained for Stockholm and San Francisco are due to the angle of incidence of the Sun that benefits the city of Stockholm for the contributions of PV panels on the south-oriented walls. The energy per unit area ($kWhm^{-2}$) of south-oriented vertical walls stands indeed at 68%, 57%, 61%, 62%, and 54% of the optimally tilted panels (surface facing south) for the cities of Stockholm, Lyon, Bordeaux, Montreal, and San Francisco, respectively.

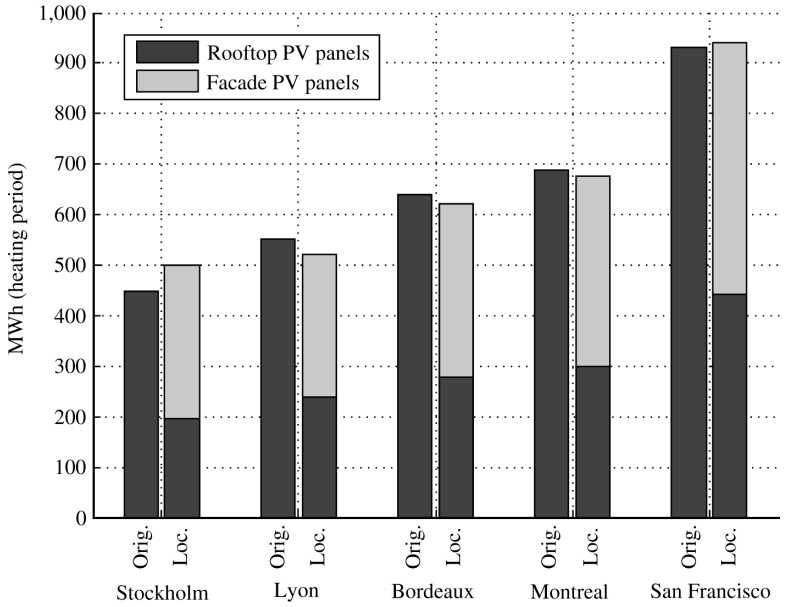


**Figure 14.17.** *Solar potential on PV surfaces for original density and localized densification*

In terms of values, the energy produced by PV panels during the heating period (assumed yield of 15%) would fill nearly, respectively, 8.3%, 15.7%, 22.9%, 11.0%, and 43.7% of the heat losses of buildings in the district for the cities of Stockholm, Lyon, Bordeaux, Montreal, and San Francisco (original configuration, thermal standards of 2010). Thus, in agreement with Figure 14.16, contributions to PV power generation would be proportionately less than those related to solar gain, but the two contributions would theoretically fill a total of around 27.1%, 42.8%, 60.2%, 31.6%, and 131.4% of the heat losses. The buildings in the districts of the city of San Francisco would have the most positive energy. According to this study, solar energy (passive and PV) would cover more than half of the heat losses for Bordeaux. For this city, with the hypotheses that have been made in the calculation process, PV yields of 41% would balance all heat losses. For Lyon, Montreal, and Stockholm, it would be necessary to combine with other renewable energies (solar

thermal, geothermic, etc.), or to take a better advantage of passive solar energy, with enhanced insulation of the buildings envelope.

## 14.6. Perspectives and conclusions

The results allowed for highlighting the issue related to solar contribution in neighborhoods located in three cities of similar geographic latitudes – Lyon, Bordeaux, and Montreal – with a well-argued comparison with the cities of Stockholm and San Francisco. Differentiated results were obtained, even in the three cities at the same latitude. Climate plays a significant role, but the study of the rotation of the district also has shown a distinct evolution and variations with respect to solar gain. So, Montreal, with a cold but sunny winter, shows an advantage with respect to solar gains and relative gains in PV and is less influenced by the rotation of the neighborhood. The performance of PV panels, however, has to greatly increase to compensate for very low temperatures during the heating period.

From the perspective of urban engineering, on the basis of this exercise, it is not easy to predict the look that will be made based on the results. Localized densification is one example. The LOD of the 3D representation of buildings (dimensions W L H, variation of these dimensions, layout of buildings relative to each other, etc.) plays a role whose weight on the evaluation of solar gain of a neighborhood remains difficult to assess.

In practice, it is rare to see a precise repetition of the typology from one neighborhood to another: we see significant changes in the dimensional characteristics of buildings, their arrangement, the pattern of windows, etc. Thus, conclusions about the solar gain of a district seem at first not easily transferable to another. This conclusion justifies the need for further research in modeling, to minimize the computation time, and make more accessible simulation tools for engineers by integrating the different stages. This conclusion also justifies that we carry on developing tools for 3D modeling of the city to reduce work effort and time.

The notion of densification impact, and also of possible compensation, both for the solar gain and the PV energy production, following for instance the construction of tall buildings within an existing neighborhood, will certainly incorporate the work approach of the urban engineer. In the coming years or decades, issues of pooling energy and the quest will probably also concern urban designers. With consensual basis between building owners and following the implementation of targeted regulatory measures, we could indeed see a sharing of solar panel's available spaces, and the creation of easements to access spaces to maximize the overall gains at the neighborhood and possibly the city levels. Optimization techniques could then emerge.

Regardless of the issues related to energy prices, we can predict with quite a good level of confidence that the next two or three decades will lead to significant changes in construction techniques and building insulation. The thermal evolution of some regulations around the world gives warning signs. Similarly, technology and consequently the yields of PV panels will change significantly, in parallel, with a probable substantial decrease of purchase prices. In this context, cities located in northern climates such as Montreal and Stockholm would receive substantial benefits of solar gain. Moreover, the cities farther south could soon achieve energy independence based solely on solar energy.

## 14.7. Acknowledgments

The authors would like to thank Ms. Diana Rodriguez de Santiago and MM. Luis Merino, Thibaut Vermeulen, and Laurent Chénard (graduate students) for their substantial contribution to this work. Their interest in urban engineering is stimulating and particularly promising for the future.

## 14.8. Bibliography

[ASH 09] American Society of Heating, Refrigerating and Air-Conditioning Engineers (ASHRAE), 2009 ASHRAE Handbook Fundamentals, ASHRAE, 2009.

[BAY 10] BAYOD-RÚJULA A.A., ORTEGO-BIELSA A., MARTÍNEZ-GRACIA A., "Photovoltaics on flat roofs: energy considerations", *Energy*, vol. 87, pp. 3625–3631, 2010.

[BEC 06] BECKERS B., MASSET L., "Heliodon 2", software and user's guide, www.heliodon.net, 2006.

[BEC 10] BECKERS B., RODRÍGUEZ D., ANTALUCA E., BATOZ J.-L., "About solar energy simulation in the urban framework: the model of Compiègne", *3rd International Congress Bauhaus SOLAR*, Erfurt, Germany, 10–11 Novembre 2010.

[ERE 11] ERELL E., PEARLMUTTER D., WILLIAMSON T., *Urban Microclimate – Designing the Spaces Between Buildings*, Earthscan, 304 pp, 2011.

[ESC 12] VAN ESCH M.M.E., LOOMAN R.H.J., DE BRUIN-HORDIJK G.J., "The effects of urban building design parameters on solar access to the urban canyon and the potential for direct passive solar heating strategies", *Energy and Buildings*, vol. 47, pp. 189–200, 2012.

[FOR 03] FORSYTH A., Measuring Density: Working Definitions for Residential Density and Building Intensity, Design Brief, Number 8/July 2003, Minneapolis Design Center for American Urban Landscape, 2003.

[GRÖ 08] GRÖGER G., CZERWINSKI A., NAGEL C., OpenGIS® City Geography Markup Language (CityGML) Encoding Standard, Open Geospatial Consortium Inc., 2008.

[LIT 98] LITTLEFAIR P.J., "Passive solar urban design: ensuring the penetration of solar into the city", *Renewable and Sustainable Energy Reviews*, vol. 2, pp. 303–326, 1998.

[NG 11] NG E., YUAN C., CHEN L., REN C., FUNG J.C.H., "Improving the wind environment in high-density cities by understanding urban morphology and surface roughness: a study in Hong Kong", *Landscape and Urban Planning*, vol. 101, no. 1, pp. 59–74, 2011.

[NOB 22] NOBBS P.E., "Planning for Sunlight", *Journal of the Town Planning Institute*, vol. 1, no. 9, pp. 6–7 1922.

[PAN 08] PAN X., ZHAO Q., CHEN J., LIANG Y., SUN B., "Analyzing the variation of building density using high spatial resolution satellite images: the example of Shanghai City", *Sensors*, vol. 8, pp. 2541–2550, 2008.

[PER 87] PEREZ R., INEICHEN P., STEWART R., MENICUCCI D., "A new simplified version of the Perez diffuse irradiance model for tilted surfaces", *Solar Energy*, vol. 39, no. 3, pp. 221–231, 1987.

[RAT 04] RATTI C., BAKER N., STEEMERS K., "Energy consumption and urban texture", *Energy and Buildings*, vol. 37, pp. 762–776, 2005.

[STR 11] STROMANN-ANDERSON J., SATTRUP P.A., "The canyon and building energy use: urban density versus daylight and passive solar gains", *Energy and Buildings*, vol. 43, pp. 2011–2020, 2011.

[THE 11] THEVENARD D., PELLAND S., "Estimating the uncertainty in long-term photovoltaic yield predictions", *Solar energy*, In Press, 2011.

[WIL 08] WILCOX S., MARION W., Users Manual for TMY3 Data Sets, Technical report, NREL/TP-581-43156, 2008. Available at: http://www.nrel.gov/docs/fy08osti/43156.pdf. Accessed in March 2011.

# Conclusion

The sponsor of a new tower boasts of bright apartments with stunning views of the city. The neighbors find that the new building spoils the landscape and plunges them into shadow. In a dense city, indeed, every new building is constrained by an environment that, in turn, is being transformed. This observation was made for the first time with modern acuity in the 1920s in Manhattan, and the answer given by the urban planners was to define a "building envelope", which would limit the size of any new building to not only preserve sunshine but also reduce the congestion. At the same time, new tools, such as heliodons and solar diagrams, came into existence to better control the distribution of solar radiation in the design of buildings and in urban neighborhoods. It was not until the end of the century that advances in computer technology and CAD allowed the widespread use of these methods and tools.

Today, for each new urban building project, we should define an upper solar envelope – limiting the size of the building so that it does not harm the environment – and a lower envelope, defined by this environment, and under which there is not enough access to the Sun and sky for the new building to reach minimum luminous and thermal efficiency. In practice, the required 3D urban models are very expensive, or unsuitable, which means that the offices of town planners and architectures have an overload of manual work that they can rarely afford.

If this difficulty were overcome, the next step would naturally lead to the optimization algorithms that automatically search configurations to better meet the different energy and light criteria, for example, when creating a new neighborhood. Actually, the architectural project is already an optimization process that is carried out manually, and often intuitively. The use of digital techniques involves defining

---

Written by Benoit BECKERS.

*Solar Energy at Urban Scale* Benoit Beckers

the constraints and objectives. It allows us to work on a larger scale – a block of buildings or an urban district – where intuition is no longer sufficient.

A first difficulty is that the city is a poorly known object. The planner does not know what transpires behind the windows. The right level of detail is difficult to specify. Often, the city is changing faster than the patiently reconstructed geometric models. Finally, the uses of buildings are also variable and difficult to grasp. The parameterized geometric models, easier to change, seem necessary, and behavioral patterns described in this book should provide new opportunities for the simulation, especially for developing scenarios of possible evolutions of the city and its usages.

The second complication comes from the criteria to be considered and the underlying physics. For years, designers restricted themselves to think about the natural light throughout the building. The tighter regulations and higher prices for thermal energies, and the greater diffusion of thermal and photovoltaic panels, led to better quantifying of solar gain, including at the urban scale. The radiative exchanges in the longwaves are much less known, although the diffusion of thermal cameras (including at urban scale, by airborne photography) today educates researchers in this field.

Since the 1960s, the atmospheric and the environmental sciences have contributed to a better understanding of the urban physics, and in particular the exchange of matter and energy between the city and the atmosphere. Increasingly ambitious measurement campaigns were conducted in urban areas. However, the extreme difficulty of carrying out such campaigns only reinforces the need for numerical simulation.

A key problem for the numerical simulation remains the acquisition of input data. Certainly, great advances have been made in defining the sky models and detecting clouds from air and land, with the production of more complete and better-documented databases. The quality of these data still varies, because of the distribution of measuring stations on the globe, a problem that should partly be compensated by the substantial progress of satellite observation. The descriptions of longwave emissions from the sky are more exceptional. However, another difficulty encountered is the growing uncertainty about the data as we enter into the city and lose the vision of the sky. An evaluation of this uncertainty and the errors induced by the simulation will be a fundamental contribution to the improved credibility of urban simulations. For this, a deeper collaboration between the specialists of satellite imagery and urban physics is required.

The effectiveness of simulation techniques has been widely proven in other areas (realistic rendering, satellite thermal simulation, etc.). However, at the urban scale, the challenges are the size of the model and the amount of input data. Depending on

the required calculations, it becomes essential to better understand the reasonable assumptions that will control the computation time. Is it enough to just consider the first reflection? Should we consider the specular component? Should we use an anisotropic sky model? What level of detail is required for windows, roofs, chimneys? How accurate is the mesh for shortwave and longwave? All these questions require specific studies and implementation of test cases to compare the different software, as has been done in other areas.

In the near future, we will without doubt have software adapted to the urban scale, capable of exchanging information (in particular, air and surface temperatures) with the weather and climate models, on the one hand, and with the tools for physical simulation of buildings, on the other. We will then be able to consider multilevel optimization, allowing us to better control the mutual influences of buildings and cities and of cities and atmosphere.

Demand is now beginning to be felt. In some cities, roofs are repainted in white to reduce the urban heat island. In others, it was decreed that all buildings must be of the same height and, elsewhere, massive tree planting or expansion of green areas is planned. But today, we are not able to accurately assess the result of such initiatives. Therefore, for this book, we have chosen to limit the area to solar radiation, so as to be able to show all components of the problem, from satellite imagery to urban planning and regulation.

Multidisciplinary work is essential in this field. This book shows that a community is emerging, and that excellent work is underway in Europe, North America, and South-East Asia. Other parts of the world such as Africa, Latin America, and, in general, the Southern Hemisphere – where urban growth will be very important in the coming decades – are still less represented.

We hope this book will be an opportunity to strengthen this community and deliver its initial findings to city stakeholders, in order to achieve together a better understanding and better utilization of solar energy at the urban scale.

# APPENDICES

*Solar Energy at Urban Scale* Benoit Beckers

Appendix 1

# Table of Europe's Platforms (Micro- and Minisatellites) for Earth Observations

| Platform | In orbit mass (power) | Proposed payload (mass) | Current missions (in orbit since) [in development for] |
|---|---|---|---|
| ALMASAT BUS | From 12.5 to 40 kg (from 40 to 100 W) | Multispectral camera (from 5 to 25 kg) | ALMASat-1 [2012], ALMASat-EO [2013] |

**Table A1.1.** *ALMASpace (Italy)*

| Platform | In orbit mass (power) | Proposed payload (mass) | Current missions (in orbit since) [in development for] |
|---|---|---|---|
| ASTROBUS-C /MYRIADE /ASTROSAT-100 | 120–135 kg (up to 180 W) | NAOMI (New AstroSat Observation Modular Instrument): high-resolution panchromatic and medium-resolution multispectral imager with Korsch telescope (up to 50 kg) | Alsat-2A (July 2010) and 2B (2011) for Algeria, SSOT for Chile (December 2011), VNREDSAT-1 for Vietnam (2013) |

**Table A1.2.** *Astrium Satellites* (*France, Germany, UK*)

Written by Théo PIRARD.

| Platform | In orbit mass (power) | Proposed payload (mass) | Current missions (in orbit since) [in development for] |
|---|---|---|---|
| ASTROBUS-L/ ASTROSAT-250 | 200–500 kg (from 0.5 to 1 kW) | Enhanced NAOMI (New AstroSat Observation Modular Instrument): optical sensors with Cassegrain telescope (100–200 kg) | Formosat-2 for Taiwan (May 2004), THEOS for Thailand (October 2008), KOMPsat-3 [2012] and -3A [2013] for South Korea, Ingenio/SEOsat for Spain [2013], AstroTerra or SPOT-6/-7 for SPOT Image [2012–2014], ERS SS-HRES for Kazakhstan [2013], Sentinel-2 for EU-GMES [2013], Sentinel-5P for EU-GMES [2015] |
| ENHANCED ASTROBUS-L /FLEXBUS-LEOSTAR/ ASTROSAT-500 | From 500 kg to 1 t (up to 1.5 kW) | 2 NAOMI (New AstroSat Observation Modular Instrument)-type imagers, Optical sensors with Cassegrain telescope (300–400 kg), multispectral imager | Pleïades HR-1 and HR-2 [2011–2012] and (MUSIS) Composante Spatiale Optique/2 satellites [2016–2018] |
| ASTROBUS-G /EUROSTAR 3000 /ASTROSAT-1000 | Up to 3 t (several kW) | Multispectral camera, high-resolution imager (up to 1 t) | Geosynchronous multipurpose satellites, such as COMS-1/Chollian for South Korea (June 2010) |

**Table A1.2.** *(Continued) Astrium Satellites* (*France, Germany, UK*)

| Platform | In orbit mass (power) | Proposed payload (mass) | Current missions (in orbit since) [in development for] |
|---|---|---|---|
| TET BUS/ TET-XL BUS | ~120 kg (220 W) | Infrared CCD cameras among technological experiments (up to 80 kg) | TET-1 demonstrator for DLR OOV (On-Orbit Verification) program [2012], TET-2 project or AsteroidFinder [2014?] |

**Table A1.3.** *Astro-und Feinwerktechnik Adlershof (Germany)*

| Platform | In orbit mass (power) | Proposed payload (mass) | Current missions (in orbit since) [in development for] |
|---|---|---|---|
| LEOS-50 | 55 kg (60 W) | 6 m HD video imager, 15 m multispectral imager (20 kg) | DLR-TUBsat (May 1999), Maroc-TUBsat (December 2001), LAPAN-TUB-sat (January 2007, still in operation) |
| LEOS-100 | 95 kg (120 W) | 1.5 m HD video imager with Dobson Space Telescope, high-resolution multispectral imager (35 kg) | LAPAN-A2 for Indonesia [2013], LAPAN-ORARI for Indonesia [2013], LISAT for Indonesia [2016] |

**Table A1.4.** *BST (Berlin Space Technologies, Germany) – see also Theta Aerospace*

| Platform | In orbit mass (power) | Proposed payload (mass) | Current missions (in orbit since) [in development for] |
|---|---|---|---|
| CGS BUS | 120 kg (120–150 W) | High-resolution panchromatic camera, multispectral spectrometer (50 kg?) | MIOsat [2012], ESEO [2014] |

**Table A1.5.** *Carlo Gavazzi Space* (*Italy*)

| Platform | In orbit mass (power) | Proposed payload (mass) | Current missions (in orbit since) [in development for] |
|---|---|---|---|
| SI-100 BUS /SPACEEYE-10 | 80–150 kg (up to 200 W) | Medium-resolution multispectral imager (30 kg) | International partnership with South Korea's Satrec Initiative: Xsat-1 for Singapore [2011], Rasat for Turkey [2011] |
| SI-200 and -300 BUS /SPACEEYE-1 and -2 | 150–300 kg – up to 500 kg (330–450 W) | High-resolution multispectral imager (60–100 kg) | Razaksat-1 (July 2009), Dubaisat-1 for Dubai (July 2009), Dubaisat-2 for Dubai [2012], Göktürk-2 for Turkey [2013], Deimos-2 for Spain [2013] |

**Table A1.6.** *Deimos Space* (*Spain*)

| Platform | In orbit mass (power) | Proposed payload (mass) | Current missions (in orbit since) [in development for] |
|---|---|---|---|
| SENTRY XL (CUBESAT) SENTRY XP (NANOSAT) | From 2–10 kg for XL to 20–40 kg for XP (10–20 W to 40–60 W) | Multispectral sensors, multipurpose detectors, data relay systems (from 1 to 20 kg?) | TBD [starting in 2012] |

**Table A1.7.** *ISIS (Innovative Solutions in Space, The Netherlands) with Andrews Space (USA)*

| Platform | In orbit mass (power) | Proposed payload (mass) | Current missions (in orbit since) [in development for] |
|---|---|---|---|
| LEOBUS-1000 | From 600 kg to 1.3 t (up to 2.2 kW) | High-resolution X-band SAR, hyperspectral imager (from 250 to 450 kg) | SAR-Lupe (five satellites launched from 2006 to 2008, in operation), EnMAP [2012], Galileo FOC [2013–2014], SARAH [2016–2018] |

**Table A1.8.** *OHB Technology Group and Kayser-Threde (Germany)*

| Platform | In orbit mass (power) | Proposed payload (mass) | Current missions (in orbit since) [in development for] |
|---|---|---|---|
| PROBA | From 95 to 160 kg (up to 140 W) | High-resolution camera, hyperspectral imaging spectrometer, multispectral imager, wide angle camera, (from 25 to 50 kg) | PROBA-1 with hyperspectral sensor (October 2001, still in operation), PROBA-V(egetation) [early 2013], VNREDSAT-1B for Vietnam [2016] |

**Table A1.9.** *Spacebel/QinetiQ Space (Belgium)*

| Platform | In orbit mass (power) | Proposed payload | Current missions (in orbit since) [in development for] |
|---|---|---|---|
| SSTL-100 | 100–120 kg (up to 50 W) | 32 m/22 m and wide-field multispectral imager | DMCII (Disaster Monitoring Constellation) microsatellites: Alsat-1A for Algeria (2002), Nigeriasat-1 for Nigeria (2003), Bilsat-1 for Turkey (2003), UK-DMC1 for UK (2003), Deimos-1 for Spain (2008), UK-DMC2 for UK (2008), Nigeriasat-X [2011], EarthMapper [2013] |
| SSTL-150 | 150–200 kg (up to 60 W) | 2.5 m panchromatic and 5 m multispectral imager, hyperspectral imager, space surveillance optical sensor | Beijing-1 for China (2005), TOPsat (2005), 4 RapidEye microsatellites (August 2008), Sapphire for Canada [2011], KGS-MRES for Kazakhstan [2013], HIRes-100 [2013] |
| SSTL-300 | From 300 to 400 kg (up to 200 W) | 1 m panchromatic and 2 m multispectral imager | Nigeriasat-2 [2011], S1 Constellation/DMC-3 [3 minisatellites to be launched in 2014, with the partnership of Chinese AT21/BLMT] |
| SSTL-300i | 400 kg (200–250 W) | S-band SAR for 5–30 m resolution observations | NovaSAR-S [2014] |

**Table A1.10.** *Surrey Satellite Technology Ltd. (SSTL, UK*)

| Platform | In orbit mass (power) | Proposed payload | Current missions (in orbit since) [in development for] |
|---|---|---|---|
| PRIMA | From 1.5 to 2.3 t/up to 5 kW | High-resolution X-band or C-band SAR, radar altimeter, surface temperature radiometer, microwave radiometer, ocean and land color instrument | 4 Cosmo-SkyMed for Italy (launched from 2007 to 2010, in operation), Radarsat-2 for Canada (December 2007), Kompsat-5 for South Korea [2011], Sentinel-1 for EU GMES [2013], Sentinel-3 for EU GMES [2013] |
| PROTEUS | From 500 to 700 kg (up to 600 W) | High-precision altimeter, high-resolution imager (from 250 to 300 kg) | Jason-1 (December 2001), CALIPSO (April 2006), Jason-2 (June 2008), SMOS (November 2009), Göktürk-1 for Turkey [2013], Jason-3 [2013] |

**Table A1.11.** *Thales Alenia Space/Telespazio* (*France, Italy*)

| Platform | In orbit mass (power) | Proposed payload | Current missions (in orbit since) [in development for] |
|---|---|---|---|
| THETASAT | 100–150 kg (120 W) | spaceCam s1450 and c4000, LISA II multispectral sensor for high-resolution imagery (30–40 kg) | High-resolution optical systems for LAPAN-A2 [2012] and LAPAN-Orari [2012], Flying Laptop with IRS/University of Stuttgart [2013], LISAT [2015], confidential contract for educational EO satellite in China [2013] |



**Table A1.12.** *Theta Aerospace (Germany)*

Appendix 2

# Commercial Operators of Earth Observation (EO) Satellites (as of January 1, 2012)

*Europe is among the leaders for operational remote sensing satellites, and is largely in advance of India, which owns and operates the Indian Remote Sensing Satellite (IRS) constellation, and of China, which is developing national systems of Earth observation (EO) spacecraft for dual-use (civilian and military) purposes.*

In the business of remote sensing satellites in Europe, Infoterra Global, a group of EADS companies in Germany, UK, and France, is expanding worldwide with the purchase of SPOT Image, and is becoming the leader for Earth imagery from space with new products and services dedicated to Geographic Information Systems, through the new entity Astrium Geo-Information Systems. Radar observations with SAR satellites (German TerraSAR, Italian COSMO-SkyMed) become available for commercial products and services. Italy collects and markets radar data and images through the e-GEOS company, a joint venture of Agenzia Spaziale Italiana (ASI) and Telespazio (Finmeccanica), which operates the COSMO-SkyMed constellation of four satellites. The Disaster Monitoring Constellation International Imaging Ltd (DMCii), established by Surrey Satellite Technology Ltd (SSTL ), is renewing its Landsat-type microsatellites with new candidates in the constellation, such as Deimos of Spain. With the partnership and support of a Chinese public company, it is going ahead with the DMC-3 constellation of minisatellites for 1 m resolution images anywhere in the world.

---

Written by Théo PIRARD.

*Solar Energy at Urban Scale* Benoit Beckers

New Europe-based private operators are developing business with EO satellites: RapidEye with a constellation of five optical minisatellites, Deimos Space contracting a second satellite with South Korean Satrec Initiative. The European operators of EO satellites in Europe are the members of the European Association of Remote Sensing Companies (EARSC), which is lobbying the EU institutions for the correct establishment of the operational Global Monitoring for Environment and Security (GMES) system with "made in Europe" Sentinel observatories to propose continuous civilian products and public services in EO applications – http://www.earsc.org/.

| Company (Country)<br>Address (Website) | Main characteristics |
|---|---|
| *Astrium GEO-Information Services (France/UK/ Germany)*<br>15, avenue de l'Europe,<br>F-31522 Ramonville Saint Agne,<br>France<br>(www.infoterra-global.com) | Company integrating, since December 2010, Infoterra and SPOT Image services and products, leader in Europe for optical and radar observations from space. Looking for governmental contract for geo-information data (two optical and two SAR satellites in operation, two optical satellites in construction for launches in 2012 and 2014, one SAR satellite in preparation) |
| *Deimos Imaging (Spain)*<br>Edificio Galileo, Modulo Gris, Oficina 103,<br>Parque Technologico de Boecillo,<br>Boecillo-Valladolid, Spain<br>(www.deimos-imaging.com) | Subsidiary of Deimos Space (Spanish Elecnor Group) to participate to the DMC (Disaster Monitoring Constellation) through contract with SSTL. Private provider of images for all parts in the world. Building a satellite integration and test center in Castilla La Mancha with the technical assistance of South Korea's Satrec Initiative, prime contractor of Deimos-2 (one remote sensing microsatellite in operation, one high-resolution EO minisatellite in construction) |

**Table A2.1.** *Commercial operators of EO satellites (as of January 1, 2012)*

| Company (Country)<br>Address (Website) | Main characteristics |
|---|---|
| *DigitalGlobe (USA)*<br>1601 Dry Creek One, Suite 260, Longmont, Colorado 80503, USA<br>(www.digitalglobe.com) | Earth imaging and information company providing highest resolution (0.60 m) and multispectral (2.4 m) imagery with QuickBird satellite since October 2001, with the pair of more agile and fully operational WorldView satellites – WorldView-1 and WorldView-2 since September 2007 and October 2009 – able to produce 0.50 m resolution (panchromatic) images. ClearView and EnhancedView contracts for high-resolution imagery with National Geospatial-Intelligence Agency (NGA). Distribution agreement with European Space Imaging (EUSI) in Munich (Three satellites in orbit, one more advanced high-resolution satellite in construction for launch in 2014). |
| *Disaster Monitoring Constellation International Imaging (UK)*<br>Tycho House, Surrey Research Park, 20 Stephenson Road, Guildford, Surrey, GU2 7YE, UK<br>(www.dmcii.com) | Constellation consisting of medium-resolution remote sensing microsatellites designed and built by SSTL; individually owned and operated by Algeria, Nigeria (two satellites), Turkey (no longer operational), UK (one), China, Spain (Deimos Imaging) in 2009. (Six satellites in operation, two in construction for Nigeria, one in project for Algeria and Sri Lanka, three minisatellites with 1 m resolution sensors for the DMC-3 constellation system, with Chinese support) |

**Table A2.1.** *(Continued) Commercial operators of EO satellites (as of January 1, 2012)*

| Company (Country)<br>Address (Website) | Main characteristics |
|---|---|
| *e-GEOS (Italy)*<br>Via Cannizzaro, 71, I-00156 Roma, Italy<br>(www.e-geos.it) | Joint venture between Agenzia Spaziale Italiana (ASI) and Telespazio to promote and commercialize radar imagery of the COSMO-SkyMed X-SAR satellites for geospatial applications. Strategic alliance with 4C Satellite Images & Technologies in the Middle East. EO centers in Matera and Neustrelitz. Cooperation with GeoEye for high-resolution optical imagery. Contract with Lockheed Martin for US National Geospatial-Intelligence Agency (NSA) (constellation of four satellites in orbit, two in construction for launch in 2015–2016). |
| *EUMETSAT (Germany)*<br>Am Kavalleriesand 31<br>D-64295 Darmstadt, Germany<br>(www.eumetsat.int) | Intergovernmental organization (18 member states and 12 cooperating states) to establish, maintain, and exploit European systems of operational satellites for meteorology, climate monitoring, global change observations, and oceanography. Cooperation with NOAA for exchange of meteorological images and data. Optional program of Jason satellites for oceanography data with precise altimeter. Contract with Thales Alenia Space (with OHB-System) for the Meteosat Third Generation (MTG) system. Study of the polar satellites for Metop/EPS (EUMESTAT Polar System) Second Generation possible operator of Sentinel-3 satellites (Three geosynchronous + one polar + one in-inclined-orbit satellites, five in construction for operations until 2020, two Sentinel satellites in construction, four imager satellites + two sounder satellites in construction within MTG/Meteosat Third Generation program for operations until 2035, 4 or 6 EPS-Second Generation in project for first launch in 2020). |

**Table A2.1.** *(Continued) Commercial operators of EO satellites (as of January 1, 2012)*

| Company (Country) Address (Website) | Main characteristics |
|---|---|
| *Euromap (Germany)* Kalkhorstweg 53, D-17235 Neustrelitz, Germany (www.euromap.de) | Euromap Satellitendaten-Vertriebsgesellschaft mbH, subsidiary of GAF AG to process and to provide imagery covering Europe, collected by Indian Remote Sensing Satellites, following commercial agreement with Antrix Corp and through cooperation with DLR (IRS-1C/1D, IRS-P5 and -P6, Resourcesat-1/-2, Cartosat-2/-2A/-2B in orbit; up to four in construction for launches until 2013). |
| *ESA/European Space Agency (France) for the European Commission*<br><br>European Space Agency, Directorate of EOP/Earth Observation, ESRIN, Via Galileo Galilei, Casella Postale 64, I-00044 Frascati (Roma). (http://www.esa.int/esaMI/ESRIN_SITE/ | Development of EO satellites as technological demonstrators (open and free data) and for operational systems of EUMESTAT (Meteosat, Metop) and of the European Union (Sentinel observatories). Family of scientific Earth explorers to test advanced remote sensing instruments. Constellation of Sentinel satellites: Sentinel-1 with SAR, Sentinel-2 with multispectral imager, Sentinel-3 for sea- and land-surface survey, Sentinel-5p for atmospheric analysis. Sentinel payload with EUMESTAT satellites: Sentinel-4 on Meteosat Third Generation and Sentinel-5 on Metop Second Generation (five in orbit/one Envisat + one PROBA + three Earth Explorers, three Earth Explorers in construction, seven Sentinel satellites + one PROBA Vegetation in construction, 4 in project). |
| *GeoEYE (USA)* Orbimage/Space Imaging. 21700 Atlantic Boulevard Dulles, VA 20166, USA (www.geoeye.com) | Result of Space Imaging merged with Orbimage: the world's largest commercial satellite imagery company, to operate a current constellation of three remote sensing satellites. Global provider of geospatial imagery products and services with digital remote sensing satellites, complemented by data from other optical, aerial, and radar sources. GeoEye-1 launched in September 2008 for 0.41 m resolution imagery. ClearView and EnhancedView contracts for high-resolution imagery with National Geospatial-Intelligence Agency (NGA) (OrbView-2, Ikonos and GeoEye-1 in orbit, GeoEye-2 in construction for 2013). |

**Table A2.1.** *(Continued) Commercial operators of EO satellites (as of January 1, 2012)*

| Company (Country)<br>Address (Website) | Main characteristics |
|---|---|
| *ImageSat International (Israel)*<br>2 Kaufman Street, 17th Floor, Tel Aviv 61500, Israel<br>Imagesat Cyprus:<br>45 Ayias Paraskevis, Office 1A, Yermasoyia, Limassol 4044 Cyprus<br>(www.imagesatintl.com) | Commercial provider – registered as Netherlands Antilles company – of high-resolution black and white imagery collected by its family of Earth Remote Observation Satellites (EROS). Exploitation of EROS-A in orbit since December 2000 and collecting 1.9 m resolution images. Financial partnership with Serbia. EROS-B launched in April 2006 for 0.70 m resolution images (Two satellites in orbit, one in project). |
| *Infoterra (Germany/UK/France)*<br>– InfoTerra GmbH, D-88090 Immenstaad, Germany<br>– InfoTerra Ltd, Atlas House, 41 Wembley Road, Leicester, Leicestershire, LE3 1UT, UK<br>– InfoTerra SAS, 15, avenue de l'Europe, F-31522 Ramonville Saint-Agne, France<br>(www.infoterra-global.com) | Remote sensing companies of Astrium Geo-Information Services (subsidiary of Astrium Services) to provide geographical information solutions – in digital form and for dual use – by acquiring and processing of airborne and satellite data. Developing the TerraSAR system of commercial radar satellites to enhance Earth observations (One optical microsatellite [Topsat] and two radar satellites [TerraSAR, Tandem-X] in operation, third radar satellite in preparation for 2015). |
| *NOAA (USA)*<br>1401 Constitution Avenue, NW, Room 5128<br>Washington, DC 20230, USA<br>(www.noaa.gov, www.nesdis.noaa.gov) | National Oceanic and Atmospheric Administration of USA, conducting research and gathering data about global situation of oceans, atmosphere, environment, managing the National Weather Service, the National Environmental Service Data and Information Service, and the National Ocean Service. Partnership with EUMETSAT for exchange of images and data, for the oceanography program of Jason satellites (Five satellites in geostationary orbit + five in polar orbit + Metop of EUMETSAT; in construction: two geostationary for operations until 2028, up to eight – with the DOD weather satellites – in polar orbit). |

**Table A2.1.** *(Continued) Commercial operators of EO satellites (as of January 1, 2012)*

| Company (Country)<br>Address (Website) | Main characteristics |
|---|---|
| *RADARSAT International/MDA's Geospatial Services (Canada)*<br>MDA, 13800 Commerce Parkway<br>MacDonald Dettwiler Building, Richmond,<br>British Columbia V6V 2J3, Canada<br>(www.rsi.ca or http://gs.mdacorporation.com,<br>www.radarsat2.info) | Provider of information solutions combining EO data from optical remote sensing satellites and from its Radarsat system that offers all-weather, day-and-night C-band SAR (Synthetic Aperture Radar) monitoring. Radarsat-2 launched in December 2007. Distributor of RapidEye images. Partnership with ESA (Two in orbit for combined observations, Radarsat Constellation of three minisatellites in construction for launch in 2014–2015). |
| *RapidEyeYE (Germany)*<br>Molkenmarkt 30,<br>D-14776 Brandenburg an der Havel,<br>Germany<br>(www.rapideye.de) | Satellite-based Geo-Information System, combining daily revisit and multispectral observations, due to an operational constellation of remote sensing minisatellites for 6.5 m resolution images. Cooperation with MDA in Canada (payload) and SSTL (platform and integration) in the UK. Contract with the Joint Research Centre of the European Commission (five identical satellites in orbit, launched in August 2008 by the same Dnepr rocket). |
| *Spot Image (France)*<br>5, rue des Satellites,<br>BP 14 359<br>F-31030 Toulouse Cedex 4, France<br>(www.spotimage.com) | Part of Astrium of Astrium Geo-Information Services. Worldwide supplier of geographic information products and services derived from the multispectral imagery of French SPOT EO satellites. Owned and operated by Astrium Services, along with Infoterra. Distribution agreements with KARI in South Korea for Kompsat-2 data, with NSPO in Taiwan for Formosat-2 data (Two satellites in operation, two Pleïades in construction for launches in 2011–2012, SPOT-6 and SPOT-7 in construction for launches in 2012 and 2014). |

**Table A2.1.** *(Continued) Commercial operators of EO satellites (as of January 1, 2012)*

| Company (Country)<br>Address (Website) | Main characteristics |
|---|---|
| *Telespazio Satellite Imaging (Italy)*<br>Via Tiburtina, 965,<br>I-00156 Roma, Italy (www.telespazio.it) | Subsidiary of the Italian–French Group Finmmeccanica-Alcatel, specialized in satellite applications, including Earth observations from space. Offering a complete range of solutions from acquiring and processing space data to the distribution of specific products and services (via Eurimage). Operating company for the COSMO-SkyMed constellation of radar satellites, with e-Geos subsidiary. Agreement with GeoEye for the exclusive marketing of Ikonos and GeoEye imagery. Contract with Lockheed Martin to provide radar images to US National Geospatial-Intelligence Agency (NGA). Cooperation with Turkey for the Göktürk system (four satellites in orbit, four in study) |
| *TÜBITAK UZAY (Turkey)*<br>Space Research Technologies Institute,<br>ODTÜ Yerleskesi, 06531 Ankara, Türkey<br>(www.uzay.tubitak.gov.tr) | Indigenous development, with international support, of the RASAT microsatellite (93 kg) for Earth observations, regional mapping, and disaster monitoring (one in orbit but decommissioned, one in construction for launch in 2011, one Göktürk in preparation for 2013). |
| *Vito/Pegasus (Belgium)*<br>VITO-TAS (Teledetectie en aardobservatieprocessen)<br>Boeretang 200<br>B-2400 Mol, Belgium<br>(www.vito.be) | International center – for the European Commission – to process and to archive vegetation images from SPOT-4 and SPOT-5 satellites. Delayed development of the ultralight Mercator UAV (unmanned aerial vehicle) for low-altitude and long-duration remote sensing missions to complement observations from space. Operator of "made in Belgium" PROBA-V(egetation) minisatellite to continue Vegetation observations (One in construction for launch in 2013, through ESA GSTP/General Support Technology Programme with Belgian funding). |



**Table A2.1.** *(Continued) Commercial operators of EO satellites (as of January 1, 2012)*

Appendix 3

# Earth's Annual Global Mean Energy Budget

| | [ROT 74][1] % | [HAR 94][2] % | [KIE 97] $Wm^{-2}$ | [TRE 09] $Wm^{-2}$ | [TRE 09] % |
|---|---|---|---|---|---|
| Incoming solar radiation | 100 | 100 | 342 | 341.3 | 100 |
| Reflected solar radiation | 28 | 30 | 107 | 101.9 | 30 |
| Reflected by clouds and atmosphere | 25 | 26 | 77 | 79 | 23.1 |
| Reflected by surface | 3 | 4 | 30 | 23 | 6.7 |
| Absorbed by surface | 47 | 50 | 168 | 161 | 47.2 |
| Absorbed by atmosphere | 20 + 5 | 20 | 67 | 78 | 22.9 |
| Thermals (sensible) | 5 | 5 | 24 | 17 | 5 |
| Latent heat | 24 | 24 | 78 | 80 | 23.4 |
| Surface radiation | 114 | 110 | 390 | 396 | 116 |
| Surface radiation to atmosphere | 109 | 98 | 350 | 356 | 104 |
| Surface radiation to sky | 5 | – | 40 | 40 | 11.7 |
| Outgoing longwave radiation | 67 | 70 | 235 | 239 | 70 |
| Emitted by atmosphere | | 60 | 165 + 30 | 169 + 30 | 58.3 |
| Back radiation | 96 | 89 | 324 | 333 | 97.6 |

1 Cited in [OKE 87]
2 Cited in [WAL 06]

Written by Benoit BECKERS.

*Solar Energy at Urban Scale* Benoit Beckers

## A3.1. Bibliography

[HAR 94] HARTMANN D.L., *Global Physical Climatology*, Academic Press, 1994.

[KIE 97] KIEHL J.T., TRENBERTH K.E., "Earth's annual global mean energy budget", *Bulletin of the American Meteorological Society*, vol. 78, no. 2, pp. 197–208, 1997.

[OKE 87] OKE T.R., *Boundary Layer Climates*, 2nd ed., Methuen & Co, New York, 1987.

[ROT 74] ROTTY R.M., MITCHELL J.M., "Man's energy and the world's climate", *67th Annual Meeting of American Institute of Chemical Engineers*, Washington D.C., 1974.

[TRE 09] TRENBERTH K.E., FASULLO J.T., KIEHL J., "Earth's global energy budget", *Bulletin of the American Meteorological Society*, vol. 90, pp. 311–323, 2009.

[WAL 06] WALLACE J.M., HOBBS P.V., *Atmospheric Science: An Introductory Survey*, 2nd ed., Elsevier, 2006.

# List of Authors

Daniel G. ALIAGA
Purdue University
USA

Viorel BADESCU
Candida Oancea Institute
Polytechnic University of Bucharest
Romania

Benoit BECKERS
Avenues – Urban Systems Engineering Department
Compiègne University of Technology
France

Pierre BECKERS
University of Liège
Belgium

Grega BIZJAK
Laboratory of Lighting and Photometry
Faculty of Electrical Engineering
University of Ljubljana
Slovenia

Philippe BLANC
Center for Energy and Processes
Mines ParisTech
France

*Solar Energy at Urban Scale* Benoit Beckers

Guedi CAPELUTO
Faculty of Architecture and Town Planning
Technion – Israel Institute of Technology
Israel

Tom VAN EEKELEN
Samtech
Belgium

Bella ESPINAR
Center for Energy and Processes
Mines ParisTech
France

George M. JANES
George M. Janes and Associates
New York
USA

Pierre KASTENDEUCH
Faculty of Geography and Planning
University of Strasbourg
France

Matej KOBAV
Laboratory of Lighting and Photometry
Faculty of Electrical Engineering
University of Ljubljana
Slovenia

John MARDALJEVIC
De Montfort University
Leicester
United Kingdom

Frédéric MONETTE
École de Technologie Supérieure de Montréal
Canada

Marjorie MUSY
CERMA "Laboratory of Architectural and
Urban Ambient Environment"
and
Institute for Research on Urban Sciences and
Techniques (IRSTV)
Nantes
France

Edward NG
Chinese University of Hong Kong (CUHK)
China

Marius PAULESCU
Physics Department
West University of Timisoara
Romania

Théo PIRARD
Freelance chronicler
Belgium

# Index




*Solar Energy at Urban Scale* Benoit Beckers